JOURNEY OF BINARY BLACK HOLES: FROM SUPERCOMPUTERS TO LIGO TO UNIVERSE

A Dissertation
Presented to
The Academic Faculty

By

Karan Jani

In Partial Fulfillment
of the Requirements for the Degree
Doctor of Philosophy in the
School of Physics

Georgia Institute of Technology

May 2017

JOURNEY OF BINARY BLACK HOLES: FROM SUPERCOMPUTERS TO LIGO TO UNIVERSE

Approved by:

Dr. Deirdre Shoemaker, Advisor
School of Physics
Georgia Institute of Technology

Dr. Laura Cadoanti
School of Physics
Georgia Institute of Technology

Dr. Alexander Endert
School of Interactive Computing
Georgia Institute of Technology

Dr. John Wise
School of Physics
Georgia Institute of Technology

Dr. Tamara Bogdanovic
School of Physics
Georgia Institute of Technology

Date Approved: March 7, 2017

"તુજ નામનો મહિમા ઋષિઓ કૈંક ભક્ત કવિ કથે,
હું તો બિચારું રાંકડું તે શું કથી કથીને કથે ?
જ્યમ સૂર્ય આગળ આગિયો, દરિયા કને ખાબોચિયું;
હીરા કને જ્યમ કાચ એવો સાવ હું નાદાન છું."

-- પૂ. શ્રીમોટા

"पैरों की बेड़ियाँ ख्वाबों को बांधे नहीं रे, कभी नहीं रे
मिट्टी की परतों को नन्हे से अंकुर भी चीरे, धीरे-धीरे"

-- उड़ान (२०१०)

"It takes a village to discover gravitational waves."

– Gabriela Gonzalez

To

Dadu, Maa, Pappa

and Shreyas Parivar

ACKNOWLEDGEMENTS

All the work presented in this doctoral thesis have been possible due to the trust, patience and vision of my adviser, Deirdre Shoemaker. Without her guidance, I would have been lost in pursuing too many activities in a finite research life of my graduate studies.

I am privileged to have Laura Cadoanti as my mentor for the LIGO project, results from which played a crucial role in this doctoral thesis. I am also thankful to Pablo Laguna, who pushed me to pursue rigorous numerical investigations in my research.

The suggestions from my thesis committee members, Tamara Bogdanovic, John Wise, Alexander Endert, has ensured this manuscript showcases my contributions in the studies conducted as part of large collaboration, and I am indebted to them for that.

The numerical relativity investigations in this thesis have based upon library of scripts and documentations written by previous members of our group at Georgia Tech. I am particularly indebted to James Healy, who taught me to run the `Maya Code` and have been answering my queries even after leaving Georgia Tech. I am also thankful to Lionel London, Larne Pekowsky, Michael Clark and Mathew Kinsey for helping me resolve N number of computing issues.

The search for gravitational waves in the Advance LIGO (since 2015) data have been primarily conducted using the `Coherent Wave Burst` algorithm. I am indebted to Claudia Lazzaro, Francesco Salemi and Sergey Klimenko for training me in using this algorithm and helping me to configure it for the binary black hole search in Advance LIGO. The interface of my numerical relativity simulations with LIGO data analysis were made in collaborations with my colleagues at Georgia Tech, James Clark and Juan Calderon Bustillo, and Richard O'Shaughnessy. I am very thankful to Aycin Aykutalp for our many discussion over coffee on the astrophysical implications of the binary black hole searches in LIGO.

The experience I gained as a resident fellow at the LIGO Livingston Observatory has

been crucial for narrating the interface of instrumental noise with astrophysics in this thesis. For this I am grateful to Brian O'Reilly, Janeen Romie, Adam Mullavey and Jess McIver, and also Stan Whitcomb for convincing me to go as a fellow at the site. I am also thankful to the very supportive chairs of the burst group in LIGO-Virgo Collaboration, Jonah Kanner and Ik Siong.

I had a rare privilege of collaborating with friends from arts background, all of whom have contributed to the aesthetics of the various plots and figures presented in this thesis. In particular, I am thankful to Naveen Sabesan, Khushnam Mirza, Vrunda Kansara and Saloni Dangarwala. I am also immensely thankful to the Graduate Student Government Association at Georgia Tech for granting me a travel award and supporting with conference funds.

Also, if it was not for my advisers and mentors during undergraduate studies at Penn State - Paul Sommers, Lee Sam Finn, Michael Eracleous, Abhay Ashtekar, Richard Robinett - I would not have pushed myself to pursue a doctoral study in gravitational wave physics.

Finally, I am thankful to every member of our LIGO family. It is an honor for life to be a part of the historic first direct detection of gravitational waves and the first observation of a binary black hole merger.

The work presented in this thesis has been supported by National Science Foundation grants 1505824, 1333360, and XSEDE TG-PHY120016.

TABLE OF CONTENTS

Acknowledgments v

List of Tables xi

List of Figures xii

Chapter 1: Introduction 1

1.1 Historical Context 1

1.2 Two-Body Problem in General Relativity 5

1.2.1 Stages of a Binary Black Hole Coalescence 8

1.2.2 Birth of Numerical Relativity 10

1.3 Astrophysical Origins of Black Holes & Their Binaries 12

1.4 Binary Black Holes in this Era of Gravitational Wave Astronomy 16

1.4.1 Detecting Gravitational Waves 17

1.5 This Thesis: An End-to-End Investigation of Binary Black Holes 23

I Binary Black Holes in Supercomputer **27**

Chapter 2: Numerical Relativity Simulation of Binary Black Holes 28

2.1 Interface with Gravitational Wave Astronomy 30

2.2 Overview of Infrastructure 31

2.3 Generating Initial Data 32
2.4 Running on Supercomputers 36
2.5 Post-Processing Stage 39
2.5.1 Gravitational Waveform 39
2.5.2 Extracting Radiated Energy and Momentum 43
2.5.3 Information Regarding Individual Black Holes 46
2.5.4 Parameters of Remnant Black Hole 47

Chapter 3: Georgia Tech Catalog of Binary Black Hole Simulations 50
3.1 BBH Parameter Space Covered by GT Catalog 53
3.2 Analysis of Numerical Errors in BBH Simulations 58
3.3 Testing Accuracy of GW Data- Analysis Tools 60
3.3.1 Approximate Models of GWs from BBH 60
3.3.2 Phenomenological Fits of Final BH 62

Chapter 4: Dynamics of Massive, Precessing Binary Black Holes 65
4.1 The Many Difficulties With Precessing-Spin BBH 68
4.2 Three Cases of Precession 70
4.3 Spin-Orbit Coupling in Non-Linear Regime 78
4.4 Future Work 82

Chapter 5: Applications of Information Visualization to General Relativity . . . 83
5.1 Motivations 83
5.2 Patterns Between Pre- and Post-Merger States of Binary Black Holes 85

5.3 Conservative Quantities in Binary Black Holes With Precessing Spins . . . 87

II Binary Black Holes in LIGO 93

Chapter 6: Transient Burst Search of Binary Black Holes in LIGO 94

6.1 Binary Black Hole Searches in LIGO 95

6.2 First Science Observation Run of Advanced LIGO 99

6.3 Overview of Coherent Wave Burst Algorithm 100

6.3.1 Input and Output 101

6.3.2 Search Configurations 103

6.4 Estimating Background Rate of Noise Events in LIGO 104

6.5 Impact of Background Noise on Binary Black Hole Search 106

Chapter 7: Sensitivity to Detect Binary Black Hole Coalescence 112

7.1 Quoting Sensitivity Towards a Gravitational Wave Source 113

7.2 Sensitive Distance for Heavy-Stellar to Intermediate Mass Binary Black Holes 115

7.2.1 Impact of Data Quality on Sensitive Distance 120

7.3 Sensitive Distance Towards a Generic Binary Black Holes 120

7.4 Hardware Injections of Intermediate Mass Black Holes 122

III Binary Black Holes in The Universe 127

Chapter 8: GW150914: Role In The First Gravitational Wave Detection 128

8.1 Numerical Relativity Simulations 129

8.1.1 Comparison with Reconstructed Signal From Transient Burst Search 134

8.1.2 Direct Comparison with LIGO Data 136

8.2 Estimating Sensitive Distance Based on Chirp-Mass 137

Chapter 9: Search for Intermediate Mass Black Hole Binaries in the First Science Run of Advanced LIGO Detectors 142

9.1 Scope of The Search 143

9.2 Search Technique 146

9.3 Upper-Limits on Merger Rates 148

9.4 Discussions 149

9.5 Astrophysical Implications of Results 150

Chapter 10: Binary Black Holes in the Next Generation of Gravitational Wave Experiments 152

10.1 Motivations 153

10.2 A Science Case For Next Detectors 153

10.3 Challenges From Gravitational Wave Data Analysis 157

Chapter 11: Conclusion and Summary 160

Appendix A: Glossary of Binary Black Hole Parameters 166

References 182

LIST OF TABLES

2.1 Initial data of the follow-up numerical relativity simulations of first binary black hole candidate, GW150914. 33

3.1 GT catalog waveform classification 55

3.2 Numerical errors in GW strain for GT catalog due to finite computational grid. Here mismatch are computed for the advance LIGO noise curve. The numbers refer to the waveforms showcased in figure 3.6. 59

3.3 Typical numerical errors in phase and amplitude of GW strain for GT catalog. The numbers refer to the waveforms showcased in figure 3.6. . . . 59

3.4 GT BBH simulations used for comparison with approximate GW models. The results are shown in figure 3.5. 62

4.1 **Three Cases of Precession:** The initial and final parameters of our three test cases of precession is stated. The first two configuration refers to, what is known in literature as, *simple precession*, while the last case is of *transitional precession* (notice the direction of initial $\mathbf{J}$ and $\mathbf{a_F}$). Here the vectors are listed as (magnitude, polar angle measured from +Z-axis, azimuthal angle measured from +X-axis) 71

8.1 Numerical relativity simulations of binary black holes conducted as a followup on GW150914. 131

8.2 Total mass and chirp-mass of GW150914 obtained from the numerical relativity comparison with reconstructed waveforms from transient burst searches (cWB and BW), and similar values obtained from conventional parameters estimation studies using approximant models (LALInference) . 136

LIST OF FIGURES

1.1 Effect of the plus and cross polarization of gravitational waves on an orange. 3

1.2 Cartoon representation of a binary black hole system in General Relativity. The arrows refer to the spin direction of the individual black holes. 8

1.3 Stages of BBH coalescence. The upper-panel shows the morphology of emitted GWs for the two polarization. The bottom-panel shows the energy emitted at each stage and the corresponding trajectories and horizon shapes of individual black holes. The plot utilized data from the publicly available numerical relativity simulation `GT0901` [21]. 9

1.4 Three three categories of black hole candidates in the universe as noted by electromagnetic observations. The possibilities of stellar and intermediate mass black holes are obtained from tidal disruption of regular stars while for super-massive (galactic) black holes from heuristic arguments. All three images are copyrights of NASA. 13

1.5 The three end stages of a star as a function of the initial mass. Notice, that we do not expect formation of any remnant object for a star with initial mass between $140 - 260\ M_{\odot}$. Image credit [28]. 14

1.6 Confirmed masses of black holes through x-ray observations and gravitational wave detections in LIGO. Image credit: LIGO Labs 16

1.7 Schematic diagram of the Advance LIGO detectors. Plot (a) shows the location of the two LIGO detectors. Plot (b) shows the average noise as a function of detectable GW frequency in both the detectors. Image credit [20] 19

1.8 The next two decades in gravitational wave band, spanning from ground based to space based experiments, as well as using pulsar to detect GWs. The black curves refer to the sensitivity of the listed experiments next to it. Binary black holes emit GWs all the way from nano-Hz (super-massive BBHs) to milli-Hz (IMBH binaries) to kilo-Hz (stellar BBHs) 22

1.9 Conceptual overview and flow of this thesis. Images utilized from [21, 20, 41], AEI and Sloan Digital Sky Survey 24

1.10 The two methods used in this thesis to conduct investigations. Image of waveform obtained from [43] 26

2.1 Steps involved in conducting a numerical relativity simulation of binary black hole systems 29

2.2 Trajectories of individual black holes of GW150914 from $r_0 = 50M$ to $r^{\rm initial} = 12M$ obtained by PN equations. The x-y axes are scaled in Schwarschild units $R_s = 2M \approx 206$ km. The circles refers to the two event horizon of two black holes (dotted being the bigger black hole). The plot on the left is for the first orbit starting at a binary separation of r_0. The plot on the right is for orbital separation at $r^{\rm initial}$. The BBH made 356 orbits around the center of mass from r_0 to $r^{\rm initial}$. The total time spent by BBH in this plot is $\Delta t = 537576M \approx 185$s. 35

2.3 Refinement levels in a NR simulation. The finest grids are moving and resolve the black holes. The fixed grids resolve the radiation zone. Image credit: James Healy [67] 36

2.4 Resolving individual black holes in a numerical relativity simulation based on their mass-ratio and spins 37

2.5 Evolution of Ψ_4 at an extraction radius $R = 75M$ for the NR simulation of GW150914. Different harmonic modes of radiation are shown. 40

2.6 Gravitational wave strain $h(t)$ computed from the NR simulation of GW150914. The strain utilizes all the radiated modes of Ψ_4 ($\ell = 2 : 6$) and extracted at $R \to \infty$. To get the physical units, the strain is scaled for a total mass $70M_\odot$ and source placed in an optimal sky-location (north pole) at a distance of 450 Mpc. Both the $+$ and $\times$ polarization are stated, as well as the amplitude of waveform $|h|$. The x-axis are scaled in the physical units of time and centered around the instance of BBH merger. Notices, the LIGO detectors needed a minimum sensitivity of $\delta l/l \sim 10^{-21}$ to detect this signal 42

2.7 Gravitational wave amplitude obtained from NR simulation of GW150914 at different sky-locations values at polar angle θ (0 implies directly above the detector). Here dashed lines refer to amplitude obtained from dominant modes $\ell = 2, m = 2$, while straight lines refer to all combination of modes upto $\ell = 2 : 6$. Notice that when system is pointing at an angle $\theta > 0$, the higher modes show more features, hence allowing us to break degeneracy in the parameter space of the system 43

2.8 Radiated energy and luminosity derived from ψ_4 of the NR simulation of GW150914 45

2.9 Radiated total angular momentum (left) and linear momentum (right) derived from ψ_4 of the NR simulation of GW150914 45

2.10 Trajectories of individual black holes, orbital separation and relative speed obtained from the NR simulation of GW150914. 48

2.11 Apparent horizon shapes of the black holes for the NR simulation of GW150914. The two black holes at top form the binary at the start of the simulation, the black hole at bottom is the remnant at the end of our simulation at the start of the simulation and remnant black hole at the end of the simulation 49

3.1 Flowchart showing the applications of GT Catalog to GW data-analysis (Chapter 3) and investigating dynamics of BBH in extreme gravity (Chapter 4, 5) 51

3.2 Coverage of binary black hole parameter space by the GT catalog. The vertical axis in both plots denotes the mass ratio q. The plot on the left is for non-spinning and aligned-spin systems, and on the right for precessing binaries. 54

3.3 Magnitude of the spin of the final BH $|\vec{\chi}_F|$ as a function of the percentage of total mass radiated, i.e. $(1 - M_F/M) \times 100\%$ 55

3.4 The histogram showing the distribution of the $M\omega$. For Advanced LIGO, the x-axis limit scales to $[50, 110]\ M_\odot$ as range of minimum total mass M. The numbers on the top of each bar corresponds to the total unequal-mass precessing simulations in the stated range. 56

3.5 Mismatches of NR waveforms in Table 3.4 with approximant GW models. 57

3.6 Numerical errors in the amplitude and phase of the GW strain, $h(t)$, for $\ell = 2:6, m = -\ell:\ell$ radiated modes. Left panels show results for the GT0582 case and right panels for the GT0560. Top panels depicts the strain $h(t)$ at face-on location from detector. The middle and bottom panel shows the errors in phase and amplitude, respectively. 59

3.7 Percentage relative errors predicting the mass and spin of the final BH from the RIT and BR fitting formulas when applied to our catalog. The red line in each box is the median value of the errors. The colored region within each box denote the $25-75$ percentile of relative error in each case. 63

4.1 Overview of Chapter-4. 66

4.2 Diagrammatic representation of a generic spin configuration of a binary black hole. 67

4.3 Diagrammatic representation of the spin and mass-ratio configuration of three cases 71

4.4 **Trajectories of BBH:** In the inertial frame of initial total angular momentum, $\mathbf{J}_i = \mathbf{J}(t=0)$, the trajectories of BBH of cases C-1 (top), C-2 (center) and C-3 (bottom) is shown. The yellow lines refer to trajectory of smaller BH, blue line refers to trajectory of bigger BH. Notice that the direction of $\mathbf{J}(t=0)$, from where most energy is radiated, is perpendicular to the plane at $z=0$ for the first two cases. 73

4.5 **Gravitational-Wave Polarization:** For the BBH source at distance $D = 100$ Mpc, total binary mass $M_{Tot} = 200M_\odot$ and sky location face on with LIGO detector, the GW strain of plus-polarization for C-1 (top), C-2 (center), and C-3 (bottom) is showcased for multiple radiated modes: $\ell = 2:4, m = -\ell:\ell$ (dashed green), $\ell = 2, m = 2$ (blue), $\ell = 2, m = 2$ (blue), $\ell = 3, m = 3$ (yellow). Note that energy in dominant mode, $\ell = 2, m = \pm 2$ is twice that of shown in $\ell = 2, m = 2$. 75

4.6 **Energy Radiated in dominant modes**: For the test cases (C-1)-blue , (C-2)-yellow, (C-3)-green, the radiated energy in corotating frame is shown for dominant modes $m = \pm\ell$ for $\ell = 2:5$. The total radiated energy (stated in legend) is obtained $\sum_{\ell=2}^{6} E_{RAD}(\ell, m)$. 76

4.7 Angles between intrinsic parameters of BBH that impact the non-linear behavior and observation of the systems with precessing spins. 77

4.8 **Evolution of Radiated Quantities:** The dynamics of the three cases , C-1 (top-left), C-2 (top-right), and C-3 (bottom), on a particular extraction sphere for $\psi_4(r = 75M)$ is shown. The orbital angular momentum $\mathbf{L}$ (green arrows) and spins $\mathbf{S_1}$, $\mathbf{S_2}$ (blue and yellow vectors) and $\mathbf{S} = \mathbf{S_1} + \mathbf{S_2}$ (blue thick line) are plotted from start of the run (at $D = 10M$) till merger (at $D = 2M$). The total angular momentum $\mathbf{J}$ (grey arrows) and averaged radiated angular momentum $\frac{-d\mathbf{J}}{dt}$ (thick green line) are plotted from the start until the system relaxes to its final BH configuration. Note that the direction of dJ/dt and $L(t)$ remain nearly parallel until merger. 79

4.9 For configurations (C-1), (C-2), (C-3), the evolution of angles is stated from the start of the simulation (after first cycle that gets rid of junk radiation) to *merger*. The first row refers to the binary separation, and the z-coordinates of the two BHs. The second row refers to the change in spin geometry angles : $\delta(\theta_1), \delta(\theta_2), \delta(\Delta\phi)$. The third row refers to conservation angles: $\delta(\beta), \delta(\beta_{EF}), \delta(\gamma)$. The fourth row refers to angles that affect detection : $\delta(\iota), \delta(\zeta), \delta(\alpha)$. Notice the varying y-axis scale and scaling of the quantities in the legends of rows 2-4. 80

5.1 Map between input data, ouput and final state for a generic binary black hole simulation in numerical relativity 84

5.2 Parallel coordinate plot between initial and final values of non-spinning binary black hole simulations. The only input parameter of importance in these simulations is mass-ratio $q = m_1/m_2 \geq 1$ (axis 2 from left). There are four outputs - recoil velocity remnant black hole as a thousandth fraction of speed of light $|v_F|$ (axis-1), energy radiated in all the modes (axis-3), fraction of total energy radiated in dominant modes (axis-4) and final spin of remnant black hole $|a_F|$ (axis-5). The two thick black lines refer to our limits on q. The color refer to the correlation between q and $|v_F|$ 89

5.3 Parallel coordinate plot between initial and final values of aligned-spinning binary black hole simulations. The input parameter of these simulations are the effective spins $a_{\rm Eq}$ (axis 1) and mass-ratios $q = m_1/m_2 \geq 1$ (axis 5 from left). There are three outputs - energy radiated in all the modes (axis-3), fraction of total energy radiated in dominant modes (axis-4) and final spin of remnant black hole $|a_F|$ (axis-2). The two thick lines refer to our limits on final spins in these set of simulations. The color refer to the value of mass-ratio q. 90

5.4 Parallel coordinate plot between initial and final values of precessing-spins binary black hole simulations. The input parameter of these simulations are the effective spins $a_{\rm Eq}$ (axis 1) and mass-ratios $q = m_1/m_2 \geq 1$ (axis 5 from left). There are three outputs - energy radiated in all the modes (axis-3), fraction of total energy radiated in dominant modes (axis-4) and final spin of remnant black hole $|a_F|$ (axis-2). The two thick lines refer to our limits on radiated energy from these set of simulations. The color refer to the value of mass-ratio q. 91

5.5 Parallel coordinate for the standard deviation of the evolution of 8 distinct angles that govern dynamics of an equal mass, precessing spins binary black holes. The colors refer to the azimuthal angles between the spins at the start of the simulation. 92

5.6 Parallel coordinate for the standard deviation of the evolution of 8 distinct angles that govern dynamics of an unequal mass, precessing spins binary black holes. The colors refer to the azimuthal angles between the spins at the start of the simulation. 92

6.1 Steps involved in conducting a transient gravitational wave search for binary black hole merger 96

6.2 Fourier frequencies of an binary black hole waveform of different total masses. The two black holes are non-spinning and of equal masses. Binary is placed at an optimal orientation and at a distance of 1 Gpc. The BBH waveform is obtained from the Georgia Tech Numerical Relativity catalog. The noise curves refer to the sensitivity of Advanced LIGO during first observation run (black line), and for its design stage (dashed lines). 97

6.3 Difference between a modeled and unmodeled search of gravitational waves from binary black holes merger. Image credit: [97] 98

6.4 A heuristic sketch of binary black hole sensitivity for matched-filtering vs. transient burst search in a LIGO-like experiment. At higher total-mass, only the merger and ringdown signal is within the sensitivity band. 99

6.5 Total observation time in during the first science run of Advanced LIGO. Pie-chart obtained from the online summary pages of LIGO detector characterization studies. 100

6.6 Output of cWB for GW150914 with the search configuration defined in this chapter. 'L' and 'H' refer to output specific to the two LIGO detectors. Images obtained from the report page generated by cWB algorithm. 102

6.7 A representative diagram for generating artificial time shifting in cWB algorithm. Zero-lag is the coincident data $T = 44.8$ days during O1. Non-zero lag is the artificial time-shifting to generate a background of $B = 1,100$ years using coincident data of length T. A true gravitational wave signal lies in zero-lag, while non-zero lag is used for estimating rate of background noise. 105

6.8 Estimating rate of background noise in O1. The left column refers to quality of 1,100 years of background after applying production cuts, while right column is the background after post-production cuts. Both these cuts are mentioned in section 6.3.2. The first row is a measure of ρ (half of SNR) of glitches as a function of GPS time in Livingston. The second row is ρ vs. the frequency range. The third row represents the False Alarm Rate as function of ρ. Images obtained from the report page generated by cWB algorithm. 107

6.9 A blip glitch (left) compared to a heavy mass binary black hole system with anti-align spins (right). Image for blip glitch obtained from [100], while time-frequency map of binary is from from cWB report page. 108

6.10 Simulated injections of binary black holes of generic masses and spins in the coincident (zero-lag) data of O1. The cWB algorithm then looks for the simulated signals just like an actual search. If a signal is found, an output page as shown in figure 6.6 is generated. The time-frequency map displayed here is from [101]. 109

6.11 Diagrammatic representation of the steps involved for computing sensitive distances for injected binary black hole waveform. 110

7.1 Horizon distance for binary black hole systems during First Observation Run of Advanced LIGO. Thetwo curves refer to horizon distance for binaries with equal masses of individual black holes (no-spin, and maximally align spin). The sensitive total-mass range for two distinct transient burst searches are highlighted. 114

7.2 Recovery of simulated injections of binary black holes using cWB algorithm configured for the `IMBH Search`. The plot on the top demonstrates the missed-found injections for total-mass vs. distance, while bottom plot refers to effective spin vs. distance. Red are the missed injections and blue are the recovered signals by this search. About 1/10th of 350,000 simulated injections of binary black holes are recovered. The plots have been generated using the CBC_PLOTS plugin within cWB infrastructure. 116

7.3 Search distance for binary black holes using cWB algorithm configured for the `IMBH Search`. The plot on the top demonstrates the search distance as a function of individual black hole masses (m_1, m_2), while bottom plot refers to search distance as a function of effective spin χ_z and total-binary mass M. Colors indicate the values of search distance at an Inverse False Alarm Rate of half year. The error bars depends on the ratio of missed and found injections. The plots have been generated using the CBC_PLOTS plugin within cWB infrastructure. 118

7.4 Average sensitive distance as a function of false alarm rate for binary black holes systems using cWB algorithm configured for the `IMBH Search` for heavy-stellar to intermediate mass black hole mergers in the total mass-range $50 - 600 M_{\odot}$. The plots have been generated using the CBC_PLOTS plugin within cWB infrastructure. 119

7.5 Sensitive distance to binary black holes computed using cWB algorithm at different operational stages of in LIGO data between June 2015 to January 2016. 119

7.6 Recovery of simulated injections of stellar binary black holes using the *all-sky* search of cWB. The plot on the top demonstrates the missed-found injections for total-mass vs. distance, while bottom plot refers to effective spin vs. distance. Red are the missed injections and blue are the recovered signals by this search. About 1/5th of 460,000 simulated injections of binary black holes are recovered. The plots have been generated using the CBC_PLOTS plugin within cWB infrastructure. 123

7.7 Search distance to stellar binary black holes using the *all-sky* search of cWB. The plot on the top demonstrates the search distance as a function of individual black hole masses (m_1, m_2), while bottom plot refers to search distance as a function of effective spin χ_z and total-binary mass M. Colors indicate the values of search distance at an Inverse False Alarm Rate of half year. The error bars depends on the ratio of missed and found injections. The plots have been generated using the CBC_PLOTS plugin within cWB infrastructure. 124

7.8 Hardware injections of two distinct types on intermediate mass black hole systems in Advanced LIGO and recovery using low-latency transient burst search. Dotted green line shows the region of the injected signal reconstructed by cWB. Time-frequency maps and reconstructed signal obtain from cWB report pages. 126

8.1 Overview of this chapter. 130

8.2 GW150914 as observed in the LIGO detectors. The top panel is the measured GW strain. The bottom panel is the time-frequency map as computed by transient burst searches. The middle plot is a comparision between the reconstructed waveform and numerical relativity simulations. [20] 131

8.3 Visualization of GW150914 for `GT0901`. Image Credit: M. Kinsey, M. Clark, K. Jani for the Georgia Tech NR Group. 132

8.4 Distribution of initial parameters Georgia Tech NR simulations utilized to directly compare with the LIGO data from GW150914. 133

8.5 Histogram of Georgia Tech NR simulations for minimum salable chirp-masses in the range of GW150914. Any NR waveforms of $\mathcal{M}_c \leq 35M_\odot$ can be scaled for GW150914. 133

8.6 Reconstructed signal of GW150914 in both the LIGO detectors from the two transient burst searches - COHERENT WAVE BURST (cWB) and BAYESWAVE. The light grey lines refer to the strain measured in LIGO. . . 134

8.7 Fitting factors between NR waveforms and the reconstructed waveform from COHERENT WAVE BURST (left) and BAYESWAVE (right). Each dot is a distinct NR simulation from the Georgia Tech Catalog. A total of 104 such BBH simulations are showcased in this plot. The x-axis represents mass-ratio of NR simulation, while the two y-axes refers to the component of spin aligned with the orbital angular momentum at the start of NR simulation. Color refers to the scale of FF - yellow being best match, black being list match. 136

8.8 Direct comparison of NR simulations with the strain data from the LIGO detector at the GPS time of GW150914. Each dot is a distinct NR simulation from four different groups. There are 406 BBH simulations from the Georgia Tech Catalog in this plot. The plot on the top highlight the values of effective spin and total mass of GW150914 as constrained using this study. The plot on the bottom highlight the values of effective spin and mass-ratio of GW150914 as constrained using this study. The colors refer to a likelihood parameter of match between NR waveform and LIGO data (black being the highest match, orange being a medium match, purple being the least match). The black contour lines refer to the constrain obtained from an independent parameter estimation study. The blue and green contour lines refer to the constraints obtained through this study. Image credit: Richard OShaughnessy [43]. 138

8.9 Possible values for the masses of individual black holes of GW150914 for the recorded chirp-mass by three different algorithms (cWB, BW, CBC). Circles highlight the sensitive distance to which we can detect these systems using the cWB algorithm 139

8.10 The parameter space of BBH injections in five chirp-mass bins are shown. . 140

8.11 Effective chirp-mass on the sensitive distance as recovered by transient burst search. The center plot showcase the sensitive distance for each bin. The bottom plot displays the error between injected and recovered chirp mass of BBH with cWB algorithm. 141

9.1 Horizon distances at optimal orientation for equal-mass BBH systems with a detection threshold of SNR=8 in O1. Comparison curves are also given for the previous S6 run. 144

9.2 Search range in Gpc and 90%-confidence rate density upper limits in $\mathrm{Gpc}^{-3}\,\mathrm{yr}^{-1}$ for IMBH binary mergers in the first science run of Advanced LIGO. Each circle represents an all-sky injection of IMBH binary with component masses (m_1, m_2) and their corresponding upper limit rates. The lines represent constant mass-ratios $q = m_1/m_2$. The impact of spin (χ_{eff}) in search sensitivity is reported for 100–$100M_{\odot}$ system. For comparison, the binary neutron star search range is reported as the red circle at center. All reported quantities are in the source frame. 147

9.3 Increase in sensitive volume it the total mass range of intermediate mass black holes while utilizing gravitational waveforms with higher harmonic modes of radiation $\ell > 2$. 150

10.1 Sensitivity curves of the current and proposed ground-based gravitational wave experiments. Details about the listed experiments can be found in [120]. Timeline of the experiments are speculative. 154

10.2 Horizon distance for equal-mass, non-spinning binary black hole systems in the current and proposed ground-based gravitational wave experiments. Here 'aLIGO First Run' refers to sensitivity of Advanced LIGO during detection of GW150914. The total-mass is computed in the source frame of BBH by taking into account the redshift corrections (dashed line is to interpret mass measured in detector frame). Circles refer to the remnant black holes produced from the binary black hole events published from the First Observation Run of Advanced LIGO (O1). The star refers to an intermediate mass black hole candidate from electromagnetic observations. 155

10.3 Horizon distances in Cosmic Explorer (2028+) for binary black holes with unequal masses. The plot is an extension of the sensitivity studies of Cosmic Explorer show in figure 10.2. 156

11.1 Apparent horizon tubes of a binary black hole system from the start to end of a numerical relativity simulation. The data has been obtained from the the Georgia Tech Catalog. 164

A.1 Diagrammatic representation of a generic spin configuration of an relevant components of binary black hole in numerical relativity simulations. 166

SUMMARY

The detection of gravitational waves from the coalescence of binary black holes has inaugurated the era of gravitational wave astronomy. The mergers of binary black holes in stellar and intermediate mass range will continue to remain one of the most promising astrophysical sources in the current generation and future ground-based gravitational wave experiments, with detection sensitivity up to cosmological distances.

This study presents an end-to-end investigation of binary black hole systems in extreme gravity from a theoretical, observational and astrophysical perspective. The theoretical investigations have been conducted by numerically solving the Einstein's Equations on supercomputers; the observational search for the transient burst of gravitational waves was carried in the coincident data from the two Laser Interferometer Gravitational Wave Observatories (LIGO), and the astrophysical constraints were applied on the mergers of heavy-stellar and intermediate mass black hole binaries ($50 - 600\ M_{\odot}$).

In doing so, the author presents his contributions to the first direct detection of gravitational waves, GW150914 and describe the results from the search for intermediate mass black holes binaries during the inaugural science observation run of Advance LIGO (2015-2016). We also present the Georgia Tech public catalog of numerical relativity simulations of binary black holes and highlight its applications to gravitational wave data analysis, spin-orbit coupling in strong gravity and information visualization to General Relativity. We conclude by narrating the science case of massive binary black holes systems in the next two decades of gravitational wave experiments.

Chapter 1

INTRODUCTION

1.1 Historical Context

On November 1915, Dr. Albert Einstein concluded a lecture series at the Prussian Academy of Sciences in Berlin by deriving a set of equations that exhibit the interplay of matter with the four-dimensional geometry of space and time [1]. The goal of these equations was to generalize the behavior of moving bodies - a special case of which Einstein had published in 1905 to demonstrate the principal of relativity in electrodynamics and the universal constancy for the speed of light [2]. Known as the *Einstein's Equations*, these set of 10 independent, highly non-linear hyperbolic-elliptic, partial differential equations (eq. 1.1) are a manifestation of a theoretical framework called the **General Theory of Relativity**, or simply General Relativity (GR). In geometrical units ($G = c = 1$), the Einstein's equations are written in a compact form as,

$$\boxed{G_{\mu\nu} = 8\pi T_{\mu\nu}} \tag{1.1}$$

where, the *Einstein tensor* $G_{\mu\nu}$ captures the second derivative of spacetime coordinates, and stress-energy tensor $T_{\mu\nu}$ on the right hand side represents the 'potential energy' of the system ($\mu\nu$ refer to the elements in a 4×4 matrix).

This pursuit of generalization led to a complete departure from the Newtonian concept of a gravitational "force". Unlike the interchange between magnetic and electric force for different observers that was demonstrated by Special Theory of Relativity, the gravitational force cannot be *shielded* by coordinate transformation, and therefore will be felt by *all observers*. In the 1915 paper on GR, Einstein noted [1],

> "Gravitation occupies an exceptional position in this theory compared to any other force, since the 10 functions representing the gravitational field at the same time define the metrical properties of the space measured"

or, more figuratively, as remarked by John Wheeler, *"Mass tells space-time how to curve, and space-time tells mass how to move"*, and gravity is simply a geometrical property of curved spaces.

Within just a few months, Einstein further demonstrated that for a weak-field limit (i.e., slowly varying perturbations to a flat spacetime metric η), the approximate solution to equation 1.1 resulted in transverse waves of amplitude $|h|$ that traveled on the spacetime fabric at the speed of light [3]. This was the first theoretical prediction of **gravitational waves (GWs)**. The spacetime metric for GWs ($h_{\mu\nu}$) can be written as a linear approximation as,

$$\boxed{g_{\mu\nu} = \eta_{\mu\nu} + h_{\mu\nu}} \tag{1.2}$$

Conceptually, GWs are similar to electromagnetic (EM) waves. The latter is caused by acceleration of charged particles, while the former is caused by acceleration of masses. The EM waves travel on spacetime, while GWs are movement of spactime. Furthermore, like the two E and B polarization vectors of EM radiation, the gravitational radiation is composed of plus ($+$) and cross ($\times$), which periodically *stretch and shrink*

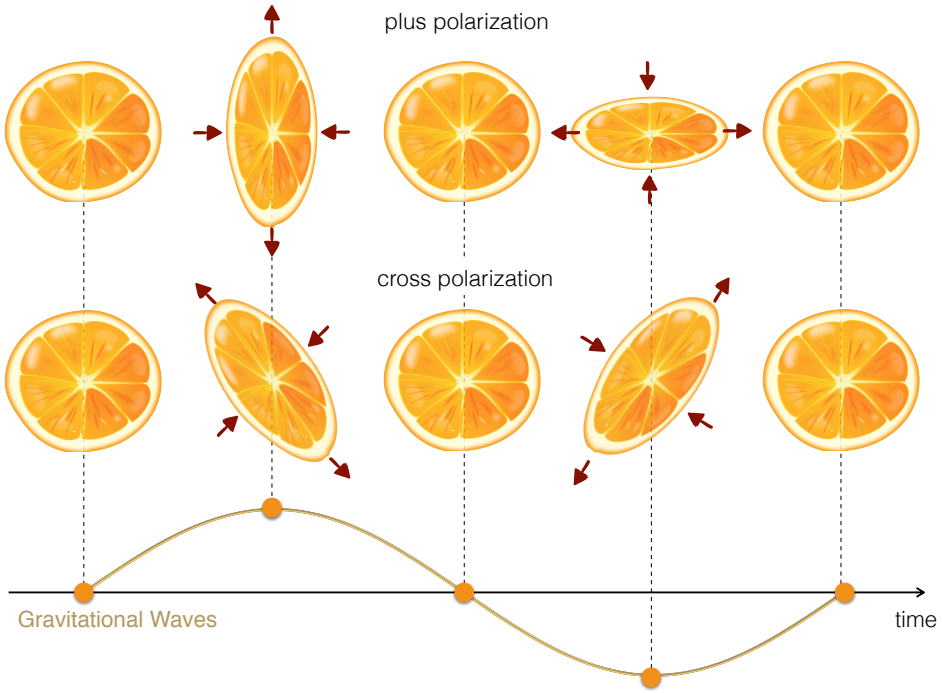

Figure 1.1: Effect of the plus and cross polarization of gravitational waves on an orange.

the spactime with a geometry represented by their names (see figure 1.1). In EM, the E and B polarization vectors are always perpendicular to each other and the direction of propagation, while the plus and cross polarizations maintain an angle $\pi/4$ between each other. These GWs are do not couple with any matter in the universe, making them practically invisible and to Einstein and other physicists of his time, it was thought to be impossible to detect them.

Later in 1916, when the World War-I was at the peak, a weatherman from the German military wrote a famous letter to Dr. Albert Einstein [4], "the war treated me kindly enough, to allow me to get away from it all and take this walk in the land of your ideas." With just four lines of math in the letter, this weatherman - Karl Schwarzschild - described the first analytic solution of equation 1.1 for a point object in vacuum $(T \equiv 0)$. This mathematical solution is referred today as a spacetime of a non-spinning, stationary **black hole** [5] (also referred in literature as *Schwarzschild black hole*).

The simplest explanation of a black hole is a surface which is so dense that even light

cannot escape from it, hence it will not emit any form of EM radiation. But the density of such an object was easy to calculate even within the Newtonian concept of gravity. What made Schwarzschild's solution of a black hole exceptional was that it produced a physical singularity in the spacetime fabric, a *puncture* of some sort in the fabric. In Schwarzschild coordinates, the singularity exists at $r = 2GM/c^2 = 2.95(M/M_\odot)$ km, where M can be treated as a mass of black hole. Just like gravity cannot be shielded, all observers, under any coordinate transformation, will always find this point of singularity in the spacetime fabric. In 1963, Roy Kerr extended this solution of Schwarzschild for the case of rotating black hole with constant angular momentum [6].

In 1958, David Finkelstein (later a professor at the Georgia Institute of Technology) found that along with a singularity, the Schwarzschild solution produces a one-way membrane around the origin $r = 0$, i.e. if you travel inside a black hole, you cannot return back [7]. This sphere of radius $r = 2GM/c^2$ in Schwarzschild coordinates is called an *event horizon*. In 1970, as a graduate student, C. V. Vishwesvara provided the first rigorous proof for the stability of a black hole, which meant that if such an object was indeed formed in the universe, then according to GR it will maintain its properties till eternity [8, 9]. The same year, he also demonstrated the emission of GWs if an aloof black hole was *perturbed* from its equilibrium [10].

The work of S. Chandrasekhar from 1930 already provided a limit for the mass of a star to gravitationally collapse to form an astrophysical black hole [11].. But it was only in 1967, when physicist John Wheeler first coined the term 'black hole'. Later, his doctoral student Kip Thorne demonstrated the observational aspects of GWs from various astrophysical sources, of which the most dominant and promising were the coalescence of compact binaries formed by a combination of black hole and neutron stars [12]. In the meantime, by 1972, Rai Weiss and others demonstrated the conceptual design of an interferometric setup to detect GWs from such astrophysical sources [13]. By 2000s, several groups successfully obtained the exact numerical solution to Einstein's

equation 1.1 for the coalescence of a binary black hole, thus providing the most accurate gravitational waveform to detect such systems [14, 15, 16, 17, 18]. The combined efforts of experimental, theoretical and computational work in detecting a compact binary system of black holes and neutron stars charted the field of **gravitational wave astronomy**.

The field of GW astronomy was built on three promises: (i) a direct detection of GWs (ii) tests for GR in the extreme gravity limit (iii) survey of the universe that was not accessible by EM observations (such as collision of a binary black hole system).

The construction of the first large scale experimental network to detect gravitational waves - the **Laser Interferometer Gravitational Wave Observatory (LIGO)** - begun in the United Stated in 1990 [19]. Two LIGO detectors, one at Livingston, LA and other at Hanford, WA became operational in the year 2000. 15 years later, on September 14, 2015 these two LIGO detectors recorded the first direct observation of gravitational waves, having originated from a merger of two black holes a billion years ago, and was found to be consistent with the numerical solutions to Einstein's equations [20].

This thesis builds on the 100 years of scientific persistence - from Albert Einstein to LIGO - in our quest to understand gravity and black holes in the universe.

1.2 Two-Body Problem in General Relativity

In Newtonian mechanics, the dynamics between two objects of mass m_1 and m_2 in absence of any other form of matter can by expressed with the inverse-square law,

$$F = G\frac{m_1 m_2}{|r_1 - r_2|^2}, \tag{1.3}$$

where $r \equiv |r_1 - r_2|$ is the relative separation between the objects.

A particular feature of the inverse-square law is the conservation of angular momentum, $\mathbf{L}$. An immediate consequence of this is that relative separation r between the two objects remain constant, i.e. after each orbit around the center of mass, the objects will come back to same position. Until the 20th century, the only exception to this behavior known was the orbit of planet Mercury, which exhibited a curious precession around theSun. In his 1915 paper [1], Einstein examined the two-body problem in GR for the case of Mercury and the Sun. Under the criteria of the *weak-gravity limit* [1] to equation 1.1, he found linear correction terms of the order $\mathcal{O}(v/c)$ to the Newtonian equation 1.2. These higher order corrections terms to Einstein's equation in weak-field limit are called **post-Newtonian (PN)** equations of motions. The zeroth order term in PN is equation 1.2. Einstein noticed that the first order terms of PN naturally explained the orbital precession. This provided the first confirmation of GR in the weak-gravity limit. The higher order terms of $\mathcal{O}(v/c)$ in PN shows that the separation between two objects, $|r_1 - r_2|$ shrinks with each orbit. To conserve angular momentum, the system thus has to be radiating away its rest mass energy $(E = \delta(m_1 + m_2)c^2)$. This phenomenon is due to the emission of gravitational radiation via GWs. Each orbit around center of mass releases two cycles of GWs.

In the *strong-gravity limit* [2], the PN equations will break down and the linear expression of GWs (equation 1.1) will no longer be valid. The simplest solution of a two-body system in the strong-gravity regime in GR is that of two black holes in vacuum. This solution is dynamic, i.e. even if two black holes are separated by a mathematical infinity, the distance between them will eventually shrink to 0 due to the emission of GWs. In context of this thesis, a configuration of two black holes that are gravitationally bound with each other, and orbiting around their common center of mass, is defined as a **binary black hole (BBH)** system.

[1] weak-gravity is defined when relative velocity $v \ll c$

[2] strong-gravity is defined when relative velocity $v/c \sim 1$

A spacetime around a black hole can be fully described by only two parameters: mass m, and Kerr parameter of spin $\chi \in [0, 1]$. For an observer at the center of mass of a BBH system, however, the spacetime at a given evolution time t_0 will be defined by all the 20 parameter space of a classical two-body problem:

m_1, m_2 rest masses of the two black holes

$\vec{\chi_1}, \vec{\chi_2}$ dimensionless-spin vectors of the two black holes

$\vec{r_1}, \vec{r_2}$ position vectors of the two black holes

$\vec{p_1}, \vec{p_2}$ linear momenta of the two black holes

As we are considering BBHs in a quasi-circular orbit (orbital eccentricity $e \approx 0$), the information about the two momenta vector can be incorporated within in the binary separation $r = r_2 - r_1$. Further, as the separation between two black holes decreases monotonically with time due to emission of GWs, we can describe the entire dynamics of a BBH system at a given separation $r(t)$ as an 8-dimensional family of intrinsic parameters,

$$\Lambda(r) = \Lambda(m_1, m_2, \vec{\chi_1}(r), \vec{\chi_2}(r)) \tag{1.4}$$

Notice, the only intrinsic parameter that does not change with time t or separation r are the black hole masses. This is because we are considering the BBH system in vacuum, and there is no exchange of mass. Figure 1.2 showcases a cartoon representation of BBH systems.

The evolution of a BBH system can be divided in two states: before $r > 0$, which we define as *pre-merger* and after $r = 0$, which is called *post-merger*. Mathematically, the merger of two black holes will always lead to a formation of a single black hole. Thus, the evolution of simplest two-body problem in GR always results in a single black hole spactime. The parameters of these final black hole (also referred in literature as remnant black hole), can be defined in the center of mass frame of BBH with 5-dimensional

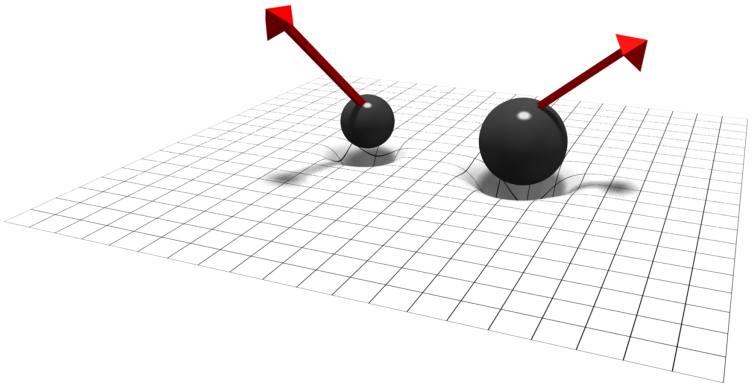

Figure 1.2: Cartoon representation of a binary black hole system in General Relativity. The arrows refer to the spin direction of the individual black holes.

parameters

$$\Lambda_F = \Lambda(m_F, \vec{\chi_F}, |\vec{v_F}|) \tag{1.5}$$

where m_F is the mass ($\equiv m_1 + m_2 - \Delta_{\rm Rad}$), $\vec{S_F}$ is the spin-vector and $\vec{v_F}$ refers to the kick velocity (also called recoil velocity) of final black hole. We typically quote only the magnitude of recoil velocity. If we shift from the center of mass frame to the remnant frame, the final black hole can be described simply by two parameters: m_F and $|\vec{S_F}|$.

1.2.1 Stages of a Binary Black Hole Coalescence

To investigate the evolution of BBH systems from $\Lambda(r)$ to Λ_F, we require observers at two spatial limits:

i. *an observer in the of center of mass frame*, through whom we measure the dynamics of individual black holes - their trajectories, spins, horizon shapes, evolution of spacetime near their vicinity. This *local* observer is important to quantify the effect of extreme gravity;

ii. and *an observer at spatial and temporal infinity*, through whom we extract the GWs emitted during the evolution of BBHs. The information from this *global* observer is

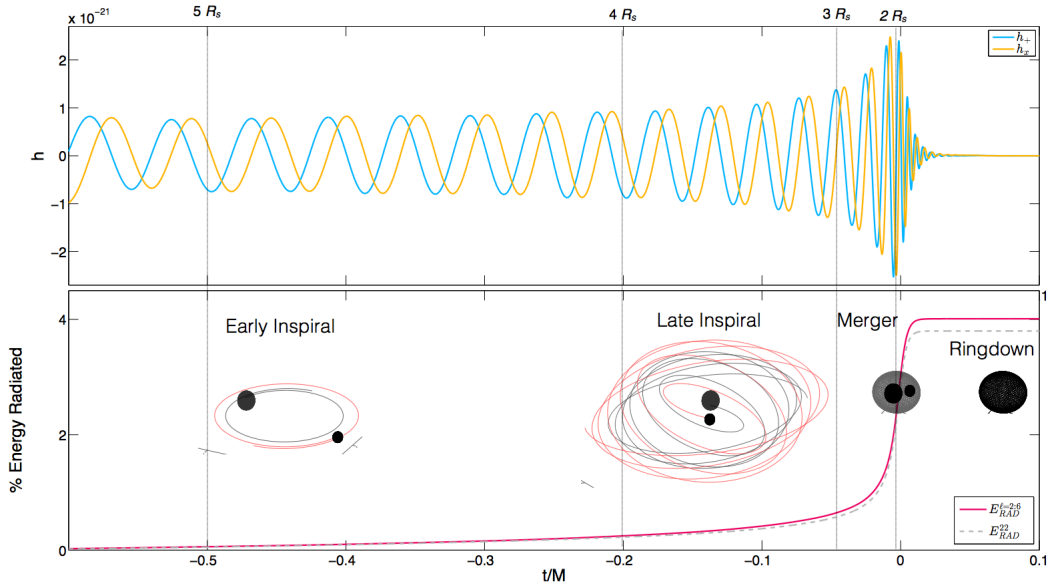

Figure 1.3: Stages of BBH coalescence. The upper-panel shows the morphology of emitted GWs for the two polarization. The bottom-panel shows the energy emitted at each stage and the corresponding trajectories and horizon shapes of individual black holes. The plot utilized data from the publicly available numerical relativity simulation `GT0901` [21].

utilized in building tools for detection of of GWs of cosmic origins.

From the perspective of these two observers, the pre- and post-merger state of BBH system can be further dissected into into four stages of coalescence, which are narrated in figure 1.3 and the text below. The coalescence stages are arranged is descending order of the binary separation r.

I. Early-Inspiral: When the separation between black holes is much larger than Schwarzschild radius, $r \gg 2Gm_{1,2}/c^2$ of either black holes, and their relative speed $v/c \ll 1$, we can treat the BBH in the PN limit. Using PN equations, one can derive the trajectories and spins of individual black holes, as well as their emitted GW morphology. The early-inspiral is the longest stage in a BBH coalescence, starting from the very instance the two black holes are gravitationally bounded as a binary. Based on the initial parameters of BBH, the early-inspiral stage defined by PN equations is valid all the way up to ~ 10 orbits before the collision of two black holes. Also, orbital eccentricity that existed at the

start of the early-inspiral stage tends to be emitted via GWs. Therefore, by end this stage, the BBH is assumed to be in a quasi-circular orbit.

II. Late-Inspiral: When the separation between black holes is comparable to their Schwarschild radius, $r \sim 2Gm_{1,2}/c^2$ and their relative velocity is near the speed of light, the BBH experiences highly non-linear dynamics from extreme gravity. To compute the trajectories and spins of black holes and the emitted GWs in this late-inspiral stage, we need to compute the exact solution to the Einstein's Equations. The BBH coalescence in this stage evolves very fast, and the corresponding emitted GWs carry the signature about the pre-merger parameters of BBH ($\Lambda(r)$) with much higher energy. This stage is essential in testing deviations from GR in strong gravity.

III. Merger: The maximum energy in GWs is emitted when the two black holes collide and form a single black hole. This *merger* is an extreme gravity phenomenon and lasts only for a fraction of a second. The horizon shapes of black holes, the behavior of spacetime and the morphology of emitted GW during merger can be computed only by the exact numerical solution to Einstein's Equations. This merger of BBH is the one of the most energetic events in the universe and plays a crucial role in our search for GWs in current generation of experiments.

IV. Ringdown: The single black hole formed after the merger of BBH takes some time to reach an equilibrium solution. During this time, this remnant black hole emits GWs just like ringing of a bell, hence the term *ringdown*. This stage can be computed by using perturbation techniques on single black hole solution.

1.2.2 Birth of Numerical Relativity

To understand the evolution of BBH systems of generic intrinsic parameters $\Lambda(r)$ during the last three stages of coalescence - *late inspiral, merger, ringdown* - requires sophisticated

numerical infrastructure. The field developed to numerically solve the Einstein's Equations to study underlying physics in extreme gravity is called **numerical relativity (NR)** .

The fundamental goal of NR is to solve Einstein's equations as an initial data value problem. The Maxwell's equations in electromagnetism and the Schrodinger wave equation in quantum physics can be evolved for an initial data, as time is an independent variable that does not couple with the spatial coordinates. However, the Einstein's equations are designed such that the 4D spacetime variables are coupled with each other. Hence, NR codes relies on a mathematical framework called the ADM formalism (named after Richard Arnowitt, Stanley Deser and Chales W. Misner)[22], which splits equation 1.1 into a $3+1$ setup of space and time, and yet maintains the conservation of energy and momenta at each iteration. The NR code utilized in this thesis is based on a modification of ADM formalism, called BSSN formalism (jointly developed by Baumgarte, Stuart L. Shapiro, Masaru Shibata and Takashi Nakamura) [23]. It is important to note that a NR simulation requires evolving the *every spatial path in the grid* at each iteration, thus making such simulations computationally very expensive.

In this thesis, we only showcase applications of NR simulations to a vacuum BBH system. This means we evolve an initial data for a spatial manifold containing two punctures (black holes) that satisfies the Einstein's equations,

$$G_{\mu\nu} = 0. \tag{1.6}$$

The goal of NR, however, goes beyond just analyzing dynamics of BBH coalescence in vacuum and computing corresponding GWs. One can utilize these NR simulations of BBHs to gain insights into differential geometry and mathematical properties of black hole horizons. One can further test exotic scenarios of deviations from conventional GR, such as effect of cosmological scalar field on the evolution of BBH [24].

When regular matter is exposed to extreme gravity, such as a collision of neutron star with black hole, or there is an accretion of gaseous disk around a black hole [25], the right-hand-side of Einstein's equations is no longer zero. Solving such systems with matter leads to magnetohydrodynamics simulations in NR. These simulations are yet in a stage of active development of numerical infrastructure (initial data, equation state of matter) [26].

The central idea of this thesis is to compute the emission of gravitational waves for generic binary black hole coalescence using numerical relativity.

1.3 Astrophysical Origins of Black Holes & Their Binaries

> "Black holes of nature are the most perfect macroscopic objects that are in the universe: the only elements in their construction are our concepts of space and time." – S. Chandrasekhar [27]

Black holes are in abundance in our universe. Based on the total mass, an astrophysical Black hole (BH) can be classified in one of these three bins (see figure 1.4):

Stellar Black Holes: The end stage product of a star, which is defined as a phase when the thermonuclear radiation from the core at the center is unable to counter the gravitational collapse of the outer surface, is strictly dependent on the initial mass of the star (see figure 1.5). The stars with initial masses smaller than $\sim 10M_{\odot}$ will collapse to form a white-dwarf of $1.4M_{\odot}$ [11]. The white-dwarfs maintain an equilibrium between gravity and the electron pressure. The stars with initial masses in the range $10 \sim 25M_{\odot}$ will collapse to form a neutron star of $1.4 \sim 3M_{\odot}$. These neutron stars maintain an equilibrium between gravity and the neutron pressure. For stars higher than $\sim 30M_{\odot}$, there is no known phenomena in quantum physics that can balance the gravitational collapse of the star. This collapse ultimately leads to a mathematical solution equivalent to black holes in GR.

In our universe, stars are typically born as twins. Nearly $\sim 75\%$ of all stars in the local universe and about 35% star at higher red-shift are found to be in a gravitationally bound binary [29]. Therefore, stellar evolution could naturally produce a binary system with one of the objects being a *stellar black hole* of mass $3 \sim 50 M_{\odot}$. The other component of the binary could either be a regular star, a neutron star, or an another stellar black hole. This later configuration is called a **stellar binary black hole** system. Prior to detection of BBHs by LIGO, the only confirmation regarding the existence of a black hole in a binary came from the disruption of a regular star. In such case, the material from the star gets accreted by the black hole. This causes electromagnetic radiation in the X-ray band. As this binary is revolving around its center of mass, there is a periodic variation observed in the X-ray emission, which helps determine the mass of the black hole. One of the strongest cases of such BH binary is Cygnus X-1, shown in figure 1.4. A binary with a black hole and neutron star is hypothesized to be a progenitor for the observed short gamma ray burst [30].

Super-Massive Black Holes: At the center of almost all massive galaxies reside an object with mass $10^4 \sim 10^10 M_{\odot}$, which are on heuristic grounds termed as *super-massive black holes*. We have determined masses of these super-massive black holes via the orbital

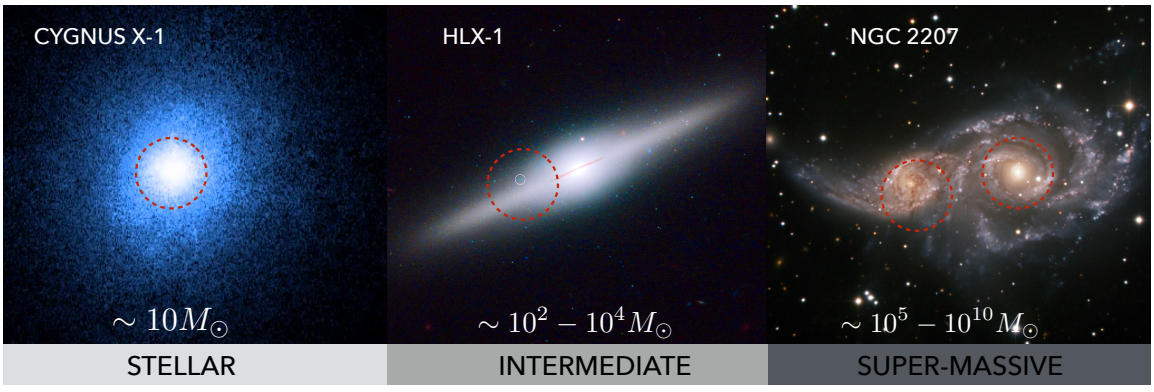

Figure 1.4: Three three categories of black hole candidates in the universe as noted by electromagnetic observations. The possibilities of stellar and intermediate mass black holes are obtained from tidal disruption of regular stars while for super-massive (galactic) black holes from heuristic arguments. All three images are copyrights of NASA.

period of stars around the center of our own Galaxy [31], as well through the accretion of material resulting in quasar or AGNs. In our cosmic history, the collision between two spiral galaxies are of common occurrence, with a peak of such events between red-shift $z = 2$ to 3. The last stage of such merger would hence form a **super-massive binary black hole** systems. As of now, there is no strong electromagnetic confirmation about mergers of these binaries.

Intermediate-Mass Black Holes: The mass range between stellar and galactic, i.e. $100-10^4 M_\odot$, is reserved for a hypothetical class of astrophysical objects called *intermediate*

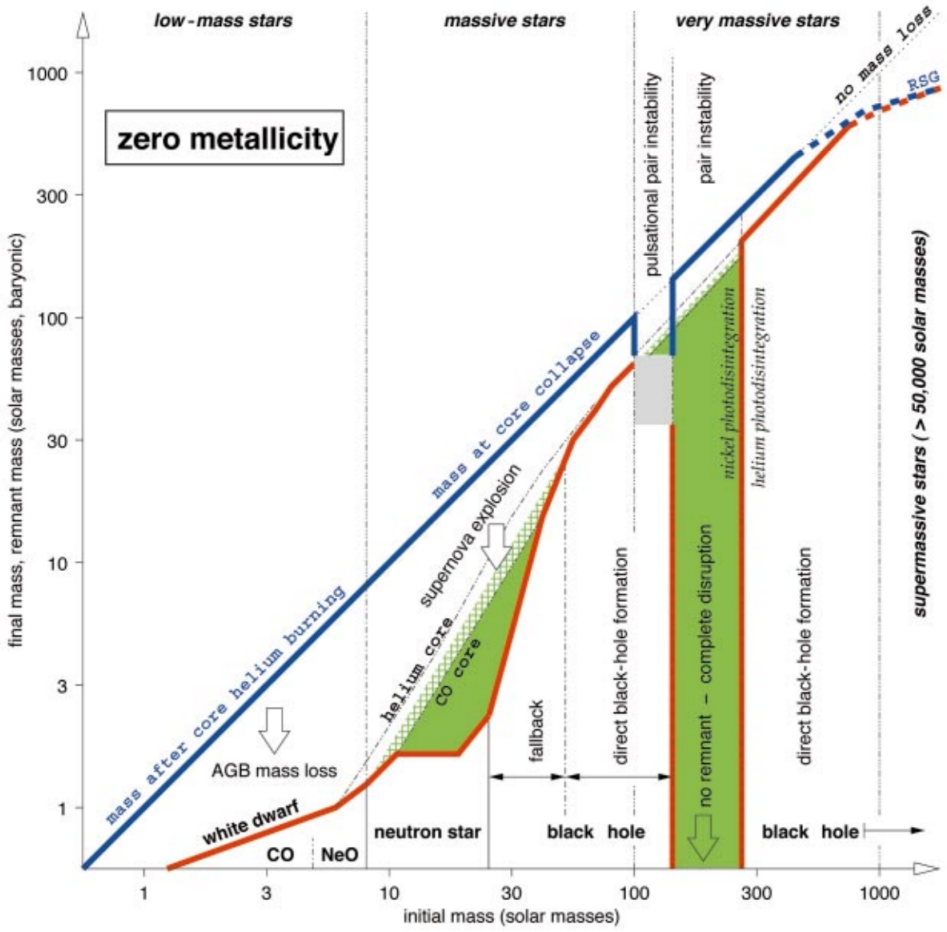

Figure 1.5: The three end stages of a star as a function of the initial mass. Notice, that we do not expect formation of any remnant object for a star with initial mass between $140 - 260\ M_\odot$. Image credit [28].

mass black hole (IMBH). One way to form such black holes is through collapse of very massive stars ($> 300M_{\odot}$). However, there are only few known for existence of cases of such massive stars [32]. In recent years, there has been some evidence from the X-ray observation on a possible IMBH acrreting a regular star [33, 34]. One such system is HLX-1 (hyper-luminous x-ray source), where the mass on black hole is constrained to few hundred solar masses [35]. Except in cases of dynamical captures in globular clusters, we do not expect from stellar evolutionary channels to form a binary of two IMBHs or that of a stellar black hole or neutron star coalescing around IMBH. As we will note in Chapter 9-10, GWs offer the first cosmological survey of **intermediate mass black hole binaries** in the universe.

It is important to mention here that until the discovery of GWs from BBH coalescence by LIGO, we could not confirm whether the astrophysical black holes we observe are indeed the one predicted by GR. The electromagnetic observations only provided an indirect constrain on the intrinsic parameters of black holes (like the total mass, rate of accretion). To test whether a dense, massive object in the universe is indeed a black hole as predicted by Schwarzschild in 1916, we have to measure the spacetime curvature around it. The only way the information about spacetime can be analyzed here on earth is via GWs. Figure 1.6 provides our current limits of observed BH masses in the universe.

This thesis focuses on detecting astrophysical binary black hole systems of stellar to intermediate mass range.

1.4 Binary Black Holes in this Era of Gravitational Wave Astronomy

The coalescing binary black holes are a *universal source* of gravitational radiation. For a BBH of total-mass M, the frequency of GWs from the last orbit around the center of mass before the merger of two black holes (the most energetic stage of BBH coalescence), can be approximately expressed as,

$$f_{GW} \approx 2.2\text{kHz} \left(\frac{M_\odot}{M} \right), \tag{1.7}$$

and therefore, a stellar BBH merger would release GWs around $\sim 10^2$ Hz, an IMBH binary would merge between $0.1 \sim 100$ Hz, and all super-massive BBH coalescence would release GWs with frequencies < 0.01 Hz. On the other hand, a binary neutron stars will always merge > 1000 Hz. Therefore, a standard BBH coalescence - consisting of inspiral, merger, ringdown - covers the GW band for 12 orders of magnitude. No other source in astrophysics, which emits electromagnetic or gravitational radiation, cover such a large

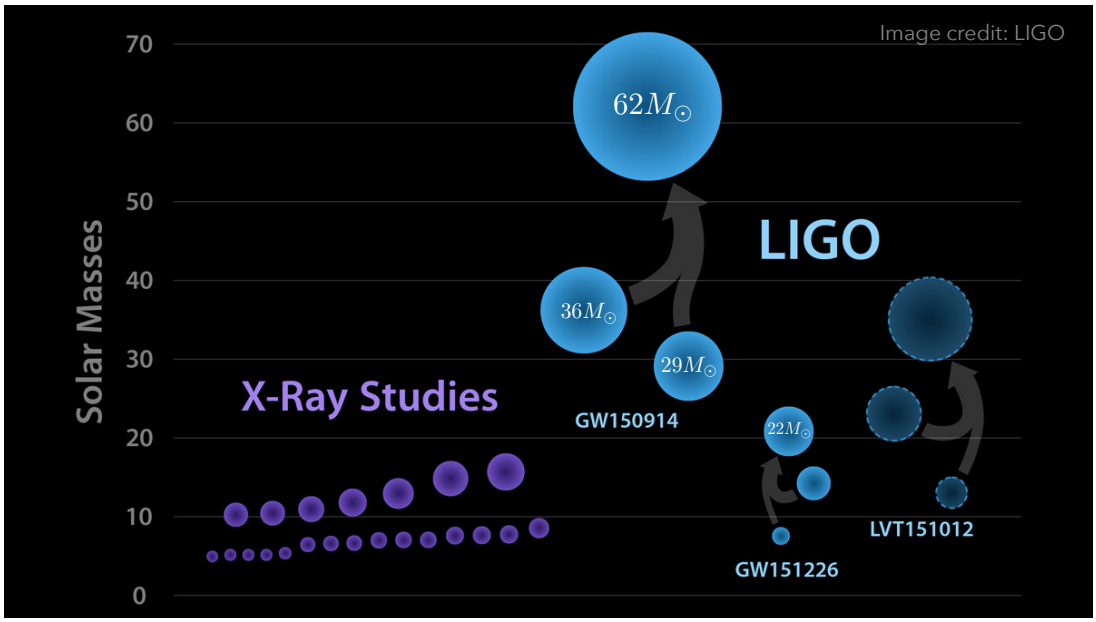

Figure 1.6: Confirmed masses of black holes through x-ray observations and gravitational wave detections in LIGO. Image credit: LIGO Labs

spectrum.

As we noted in figure 1.1, when a GW from such an astrophysical BBH merger arrives at earth, it will *stretch and shrink* the *entire* earth. We can compute a ball-park estimate between the amplitude of the gravitational waves $|h|$ when it arrives on earth from a binary of total mass M, placed at distance D. A coalescence of binary neutron stars, each weighing $1.4M_{\odot}$, from a distance of 100 Mpc (3 million light years) will *distort* an observer on earth (size $l = 1$m) by $\delta l \sim 10^{-23}$ m. Compare that to a BBH coalescence of two non-spinning, $30M_{\odot}$ black holes from a same distance, which will distort an observer by $\delta l \sim 10^{-21}$ m. Now if we repeat the same calculation for a BBH with two $200M_{\odot}$ black holes, and we get $\delta l \sim 10^{-20}$ m.

Now suppose we build a device to measure the distortion of our observer, δl, from the incoming GWs in a frequency range $10 - 2,000$ Hz. As the amplitude of GWs drops linearly with distance, our device can then, in principle, detect a BBH of total mass $60M_{\odot}$ to a distance 100 times more than that of binary neutron stars. Suppose if the universe has an equal population of binary neutron stars and BBHs of this total-mass, then the chances of our device to detect GWs from a BBH are a million times more than that from neutron stars. As the total-mass of black holes can scale between $10 - 10^{10}M_{\odot}$, and the detection volume increases linearly with total mass of binary, the binary black hole coalescence are therefore considered the most promising sources for detecting gravitational waves.

1.4.1 Detecting Gravitational Waves

The guiding physics principles for a *direct detection* of GWs is independent on the astrophysical source. The only impact of frequency and amplitude of GWs is on our chances of detecting a particular system, in our case BBH coalescence. Notice, in figure 1.1, the GWs distort the spatial geometry at every quarter of the wavelength. If you are an observer trying to measure this distortion by a standard ruler or a measuring tape, your experiment will fail as a passing GW will stretch *everything*, including yourself and your

ruler. Thus, there is no reference or a background to measure this distortion against and compare. However, like Einstein one can indulge in the *gedanken* experiment as following:

> Imagine two friends, Amar and Akbar, separated by a distance l and each of them hold a mirror. Let a laser beam bounce between these two mirrors. Now, they ask their third friend, Anthony, to measure the time it takes for the light to finish a round trip between the two mirrors. In a normal case, Anthony will report the round trip time of laser beam to be $t = 2l/c$. Now, if a GW of wavelength $2l$ approaches from a direction perpendicular to the line joining Amar and Akbar, the space between them will stretch and shrink by some δl. No one in the room will realize a GW has passed by. However, a curious Anthony will report the round trip time of laser to have changed for some instance by $t = (2l \pm \delta l)/c$. This is how Amar, Akbar and Anthony will confirm the detection of GWs.
>
> If Anthony wants to detect GWs just by himself, he can arrange two mirrors and beam-splitter in an L-shape Michelson interferometer of arm-length l, such that the laser beam upon arrival from the mirrors produce a dark fringe (i.e. they exactly cancel each other in phase). An incoming GW would stretch the arm-length and result in a periodic shifting between bright and dark fringes, thus making Anthony a proud member of detection of GWs from cosmic origins.

The important thing to note in this thought experiment is the wavelength of GW is comparable to that of the distance between the two mirrors or the arm-length of the interferometer. That means to detect a GW of frequency 100 Hz, the required arm-length of a detector has to be at least of the size $\sim 1000km$. This will make it impossible to build such a detector on earth. However, one can devise a clever interferometer where the laser keeps bouncing between the mirror and the beam-splitter for about hundred times, thus collectively making the arm-length larger by that many factor. This is the guiding principle

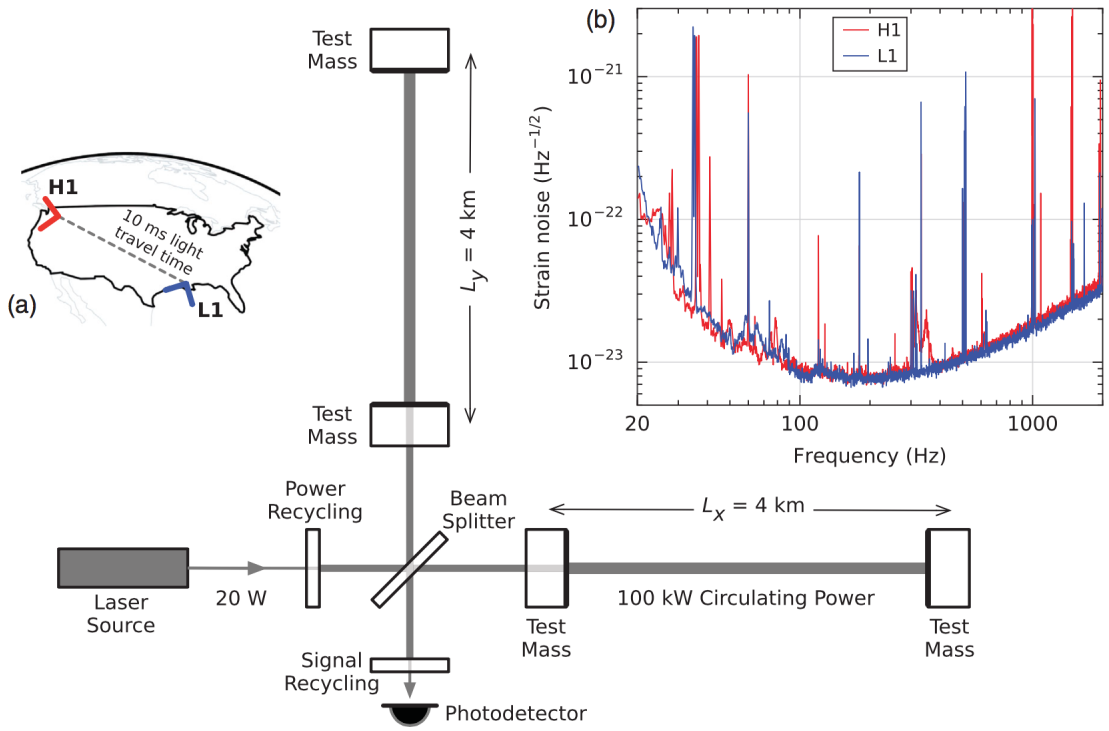

Figure 1.7: Schematic diagram of the Advance LIGO detectors. Plot (a) shows the location of the two LIGO detectors. Plot (b) shows the average noise as a function of detectable GW frequency in both the detectors. Image credit [20]

of the **Laser Interferometer Gravitational Wave Observatory (LIGO)** [13, 19]. The 4 km arm-length of LIGO can detect GWs from a BBH merger between $10 \sim 1000$ Hz (see figure 1.7).

When the GWs from an astrophysical BBH system of $100M_{\odot}$ from 500 Mpc reaches LIGO, it will produce a stretch in the arm-length of the order $|h| \sim \delta l/l \sim 10^{-22}$. That means a minimum sensitivity required for LIGO is $\delta l \sim 10^{-19}$, i.e., about millionth the size of a proton. Such a minuscule change in length can be caused even by terrestrial effects, such as earth quake *any where on planet earth*, and mechanical coupling around the detector.

The primary task even after building a LIGO detector is to identify all possible sources of instrumental and environmental noise that affect sensitivity, and in the cases that are possible, gear the instrument to be more immune towards such noise. The upgrades from

Initial LIGO (2000-2010) to Advance LIGO (2015-Current) were developed with this motivation [36]. The secondary task then is to devise a search technique that can curtail the background noise without affecting our sensitivity to detect GWs. For the case of BBH, there are primarily two classes of techniques, *matched-filtering template bank search* and *unmodeled transient burst search*. The results discussed in this thesis are obtained using the burst search for BBH.

The reason we currently have two exact LIGO detectors (one in Livingston, LA, second in Hanford, WA), separated by about 3,700 km, is to rule out the possibility of any source of noise in one of the detectors that may look identical to a GWs from an astrophysical system. A true GW signal of cosmic origins will be *coincidentally* detected by both LIGO detectors.

The **First Science Observation Run** of the two Advance LIGO detectors (from now on referred as **O1**) begun from September 12, 2015. Two days later, on September 14, 2015 the first GW was detected from BBH merger (officially labeled as GW150914). The O1 run ended on January 19, 2016, with one more GW detection from an another BBH coalescence - GW151226. The Second Science Observation Run, O2, started from December 2016. At the time of writing of this thesis, a total of six GW astrophysical events were recorded and announced by the LIGO team, of which two were confirmed detection of BBHs with 5σ confidence. These detection of BBHs by LIGO inaugurated the era of **Gravitational Wave Astronomy**.

The current sensitivity of Advance LIGO allows detection of GWs of the lowest amplitude of $|h| \sim 1 \times 10^{-23}$. Once the Advance LIGO detector reaches its design sensitivity (by 2020), it will be able to detect $|h| \sim 4 \times 10^{-24}$. LIGO is currently the most sensitive instrument ever constructed. A third LIGO detector is all set to be constructed in India and scheduled to be operational by 2023 [37]. A setup similar to LIGO is adopted in the GW detector in Italy, Virgo, (currently undergoing upgrades) [38, 39], and in the 600m arm-length GEO600 detector in Germany. Another GW detector, KAGRA, is being

currently constructed in Japan and will be operational by 2019. The combination of all these detector form the **ground-based gravitational wave network**.

The same principle of interferometeric setup can be utilized in constructing a space-based GW detector. As space offers a natural vacuum, the arm-length between the two mirrors can be as big as $l = 10^6$ km. This allows detection of GWs in the milli-Hz frequency spectrum for mergers of super-massive BBH and IMBH binaries. The Laser Interferometer Space Antenna (LISA) [40], is the first generation of such space-based GW experiment and is scheduled to launch by 2030. Efforts are also being made to detect GWs using astrophysical interferometer, i.e., using combinations of pulsars separated by thousands of light years as the arm-length. The pulsars emit radio pulses with milli-second accuracy and any deviation in their arrival can be linked with a GW between the earth and the pulsar. These allows detecting GWs up to nano-Hz, which are caused by inspiral of super-massive BBHs. We expect to detect GWs using such pulsar time array (PTA) by 2025. Figure 1.8 showcases the entire BBH spectrum for the upcoming and current experiments in this inaugural decade of gravitational wave astronomy.

This thesis describes the search for binary black holes mergers in the gravitational wave spectrum of LIGO detectors.

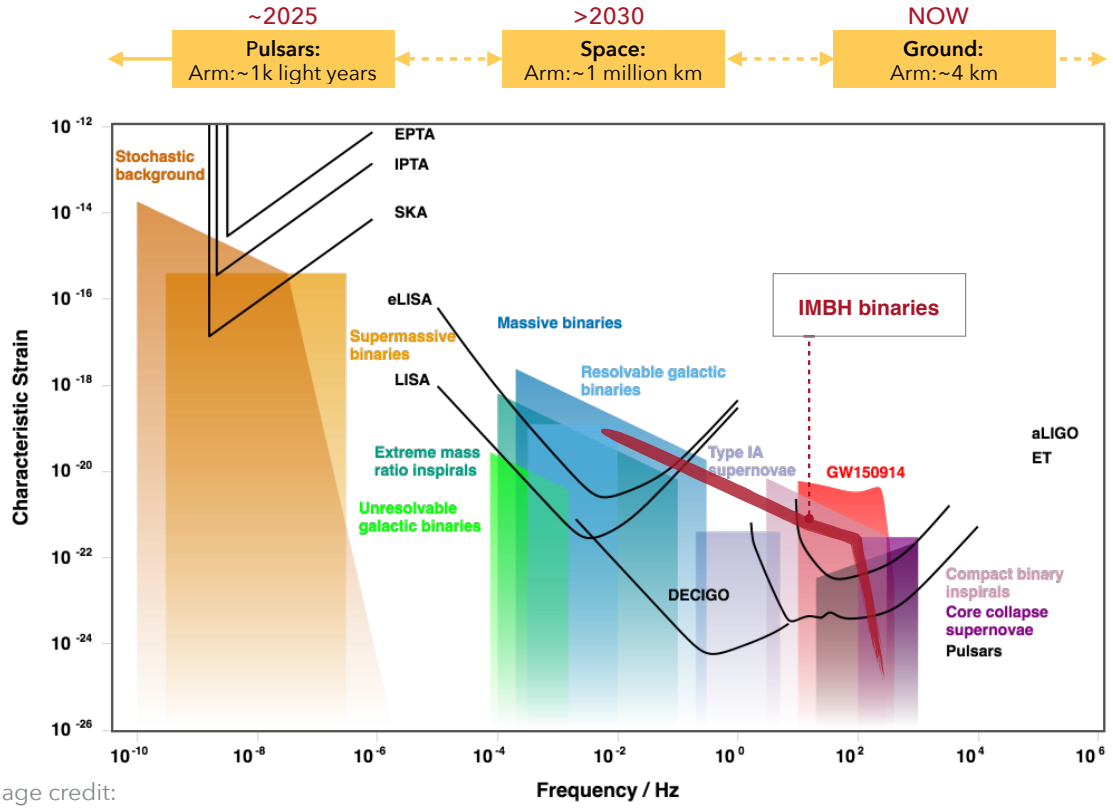

Image credit:
C. Moore, R. Cole, C. Berry

Figure 1.8: The next two decades in gravitational wave band, spanning from ground based to space based experiments, as well as using pulsar to detect GWs. The black curves refer to the sensitivity of the listed experiments next to it. Binary black holes emit GWs all the way from nano-Hz (super-massive BBHs) to milli-Hz (IMBH binaries) to kilo-Hz (stellar BBHs)

1.5 This Thesis: An End-to-End Investigation of Binary Black Holes

The goal of this is to present an end-to-end investigation of BBH systems in extreme gravity from a theoretical, observational and astrophysical perspective. The theoretical investigations have been conducted by numerically solving Einstein's Equations on supercomputers for a BBH system. The observational search for GWs from BBH mergers was conducted in the data from the LIGO detectors since mid-2015. The astrophysical insights about BBHs in the universe were demonstrated from the results of the GW search, and by further integrating them with the numerical simulations. The conceptual overview of the thesis presented in figure 1.5.

The thesis is accordingly divided into three parts, highlighting the specific projects the author conducted using numerical relativity simulations of BBH (Part I), the transient burst search of BBH in LIGO during O1 (Part II), and the results from the GW search for stellar and intermediate mass BBHs (Part III). The outline of the next nine chapter is as follows:

Part I: Binary Black Holes in Supercomputers

- In Chapter 2 we demonstrate the procedure to conduct NR simulations on supercomputers for BBH coalescence (inspiral, merger, ringdown) and extracting the underlying physics of extreme gravity from the output of the simulations.

- Thereafter, Chapter 3, showcases a catalog of GWs obtained for hundreds of such BBH simulations conducted by the Georgia Tech NR group, scattered across the initial parameters space $\Lambda(r)$, and demonstrate their applications to gravitational wave astronomy.

- In Chapter 4, we dissect the dynamics of the late stages of a BBH coalescence with precessing spins and quantify the implications of spin-orbit coupling in strong gravity.

JOURNEY OF BINARY BLACK HOLES

CH: 1
Astrophysical BBHs coalesce & emit detectable GWs

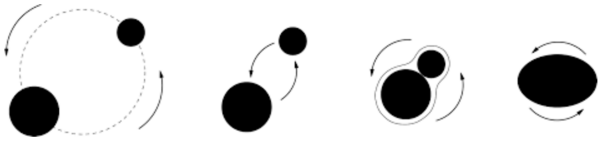

CH: 2, 3
Aid tools for GW data-analysis

PART-1 Compute exact GWs for generic BBH merges by solving Einstein Equations on **supercomputer**

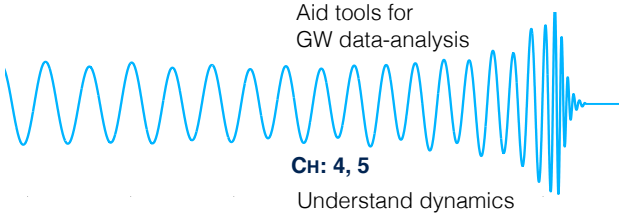

CH: 4, 5
Understand dynamics of BBH in GR

PART-II Hunt for potential GW signals from astrophysical BBH mergers in the **LIGO** detectors

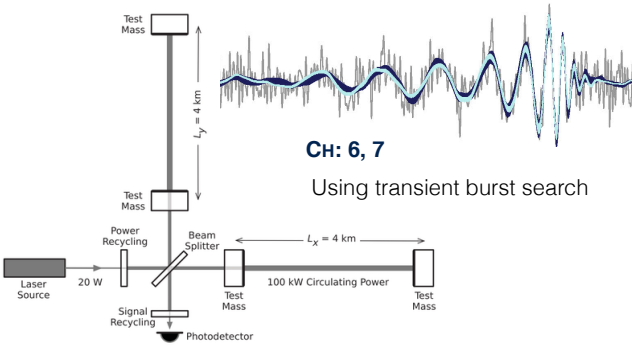

CH: 6, 7
Using transient burst search

CH: 8
GW150914

PART-III Detection of GWs from BBH mergers in our **universe**

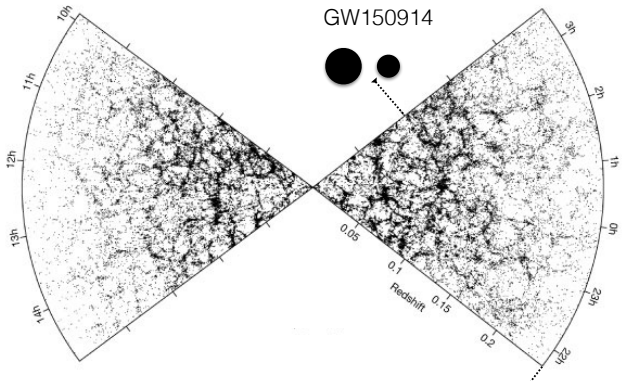

CH: 9, 10
Intermediate-mass BH search limit in LIGO

Figure 1.9: Conceptual overview and flow of this thesis. Images utilized from [21, 20, 41], AEI and Sloan Digital Sky Survey

- With Chapter 5, we present an application of information visualization tools to General Relativity by finding *bulk-features* from the non-linear dynamics of BBHs.

Part II. Binary Black Holes in LIGO

- Along with highlighting the types of BBH search in LIGO and the coincident data during O1, Chapter 6 provides an overview the transient burst search conducted by the author in searching for GWs from BBH mergers.

- In Chapter 7, we demonstrate the sensitivity and readiness to detect BBH systems from stellar to intermediate mass range, without applying any model, in the LIGO data since mid-2015.

Part III. Binary Black Holes in Universe

- Chapter 8 lists the studies conducted by the author in confirming the first detection of GWs, GW150194, as a BBH merger of astrophysical origins.

- Chapter 9 reports the results from the GW search that the author lead in O1 to hunt for the IMBH binaries up to cosmological distances without applying any model.

- Finally, in Chapter 10, we demonstrate the scope of BBH search in the future ground-based GW detectors proposed for next two decades.

A Note on Data and Methods

The results presented in this thesis are obtained using techniques, numerical codes and observational data that were developed by several collaborators and research groups, over decade long efforts. At the heart of this thesis are two types of analysis methods (see figure 1.10), which were developed with an aim to detect BBH using GWs.

- MAYA CODE, EINSTEIN TOOLKIT, GT POST-PROCESSING TOOLKIT:

These codes allow us to perform NR simulations of BBH coalescence on supercomputers, and extract information about their dynamics and emitted GWs. The details about this technique are summarized in Chapter 2.

- COHERENT WAVE BURST, LIGO ANALYSIS LIBRARY:

  These codes allow to conduct a transient burst search for BBHs of cosmic origins in the data from the two Advance LIGO detectors [42]. The details about this technique are summarized in Chapter 6.

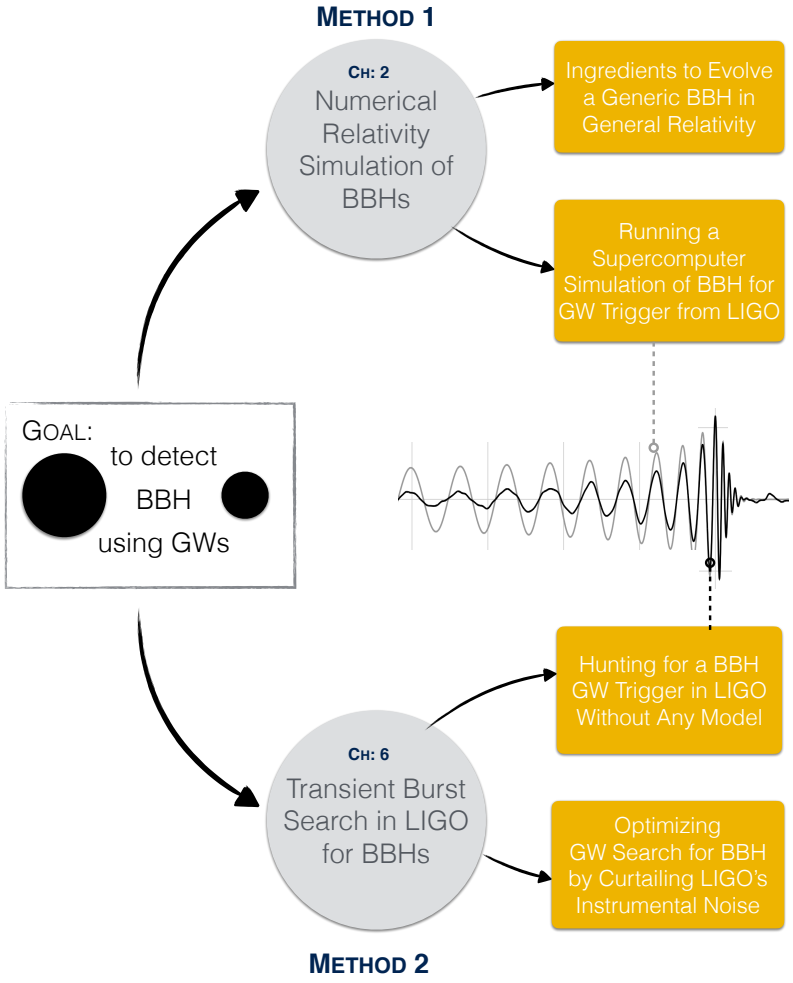

Figure 1.10: The two methods used in this thesis to conduct investigations. Image of waveform obtained from [43]

PART I

BINARY BLACK HOLES IN SUPERCOMPUTER

Chapter 2

NUMERICAL RELATIVITY SIMULATION OF BINARY BLACK HOLES

Overview

This chapter summarizes the methodology followed by the author for conducting numerical relativity simulations of binary black hole coalescence on supercomputers (see figure 2.1). In context of the work presented in this thesis, Section 2.1 highlights the demands from gravitational wave astronomy for conducting these simulations. The primary motivations are to follow-up on binary black holes candidates found by gravitational wave searches in LIGO data, and investigate the dynamics of the late stages of binary black hole coalescence for a generic combinations of masses and spins. Section 2.2 provides an overview of the numerical relativity infrastructure utilized to solve Einstein's equations in vacuum. With the follow-up binary black hole simulation that the author conducted for the first gravitational wave candidate, GW150914, section 2.3 demonstrates the process of generating initial data in numerical relativity, while section 2.4 provides a conceptual overview on the numerical resolutions and required computational resources. In Section 2.5, we showcase the post-processing of the simulation data, with a focus on the extraction of gravitational waves and tracking the dynamics of individual black holes. This chapter is the basis for the studies presented in chapter 3, 4, 5, 8.

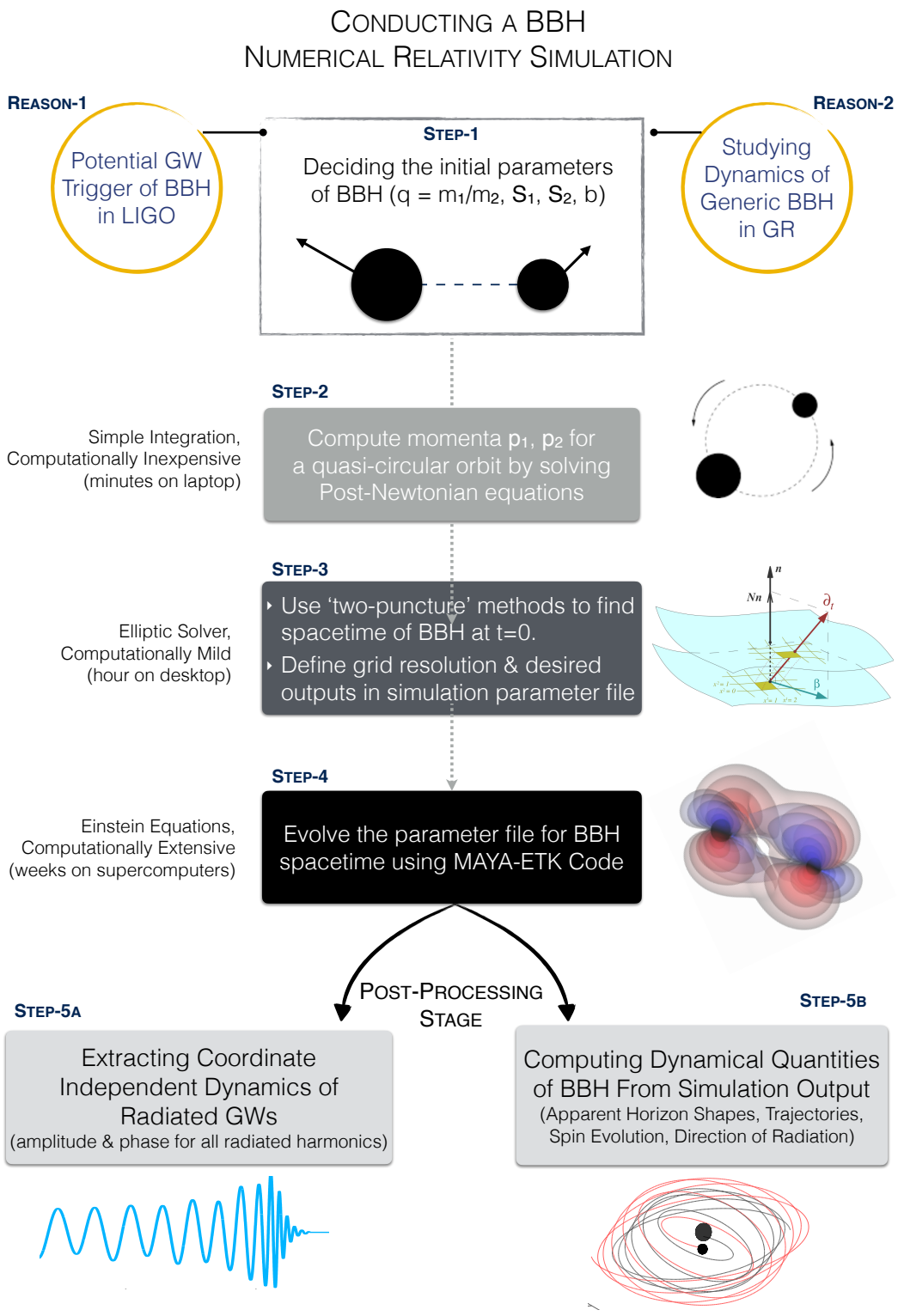

Figure 2.1: Steps involved in conducting a numerical relativity simulation of binary black hole systems

2.1 Interface with Gravitational Wave Astronomy

The binary black hole (BBH) systems are one of the promising sources for detecting gravitational waves (GWs). In the current generation of ground-based GW detectors like LIGO, we can detect all three stages of BBH coalescence - inspiral, merger, ringdown - for systems with total mass $5 \sim 1000 M_{\odot}$. In astrophysics, the BBHs in these mass range correspond to stellar and intermediate mass black holes. Based on the First Observation Run of Advance LIGO (O1), we expect to detect at least ~ 9 stellar BBH mergers within one cubic Gpc every year [44]. Due to the uncertainties in the formation mechanism of BBH in these mass range, we do not have a priori constrains regarding the parameters (masses, spins) we expect to see in these detection. On the other hand, the search for BBH coalescence within the data from LIGO detectors, and future space-based detector LISA, demands a very accurate description of the GW morphology [45]. The only method through which we can computeGWs from BBH coalescences of generic intrinsic parameters of masses ans spins, $\Lambda(r)$ (see equation 1.2) is by numerical solving Einstein's Equations. Therefore, the necessity of conducting numerical relativity (NR) simulations is embodied in the core of gravitational wave astronomy.

Due to practical computing limitations, we can conduct NR simulations only over a discrete points in the intrinsic parameter space $\Lambda(r) = \Lambda(m_1, m_2, \vec{\chi_1}(r), \vec{\chi_2}(r)$. For the purpose of GW data-analysis, we therefore build approximate models of GWs which are tuned to NR simulations [46]. These approximate GW models typically have validity over a small patch of $\Lambda(r)$, mainly limited to quasi-circular orbits of BBH with comparable mass-ratios $q = m_1/m_2$, spins aligned with orbital angular momentum, and can compute only partial of the radiated energy. However, within the sensitivity reach of current detectors like LIGO, we can expect to see BBH systems that could be beyond the reach of these models, such as coalescence of black holes of highly unequal masses, black holes with precessing spins and orbital eccentricities. Accurate GWs from such systems can be obtained only

by conducting NR simulations. Also, our ability to constrain from the GW observation the intrinsic parameters of BBH, $\Lambda(r)$, is crucial in narrowing the astrophysical formation mechanism of these sources. Therefore, every BBH candidate observed in LIGO requires to an extent a targeted followup of NR simulations.

The role of NR simulations was evident for the direct detection of the first GW event and also the first observation of a BBH merger, GW150914. The detection paper [20] showed the best fits of a NR waveform to the data. The estimates on parameters of GW150194 [47], as well as in testing consistency of this signal with GR [48] were obtained by utilizing approximate models of gravitational waveforms and formulas to compare parameters of pre- and post- merger stage of BBH; all of these tools were build using NR simulations of BBHs [49, 50, 51, 52, 53, 54]. Directly relevant to my work, hundreds of BBH simulations from my publicly available Georgia Tech catalog of NR simulations [21] were utilized in constraining the parameters of GW150914 [43], and in confirming this event as binary black hole merger with minimal assumptions [41] (see chapter 8).

2.2 Overview of Infrastructure

All the NR simulations of BBHs that are discussed in this thesis were obtained with MAYA code [55, 56, 57, 58]. The code was developed primarily by the efforts of NR group at Georgia Tech (and formerly at Penn State). This MAYA code is based on the BSSN formulation of the Einstein Equation's [23]. The BBH simulation uses the moving puncture gauge condition [17, 18].

The MAYA code is related to the Einstein code in the open source package of EINSTEINTOOLKIT [59]. The Georgia Tech group has been one of the developers for EINSTEINTOOLKIT. That is, it operates under the CACTUS infrastructure [60], with CARPET providing mesh refinements [61] and thorns (modules) generated by the package KRANC [62]. For time integration, we use fourth Runge Kutta method.

The initial data for each simulation consist of the extrinsic curvature and spatial metric.

The extrinsic curvature has the Bowen-York [63] form, and the spatial metric is conformally flat. The conformal factor is obtained by solving the Hamiltonian constrain using the TWOPUNCTURES spectral solver [64].

The simulations have been performed on the STAMPEDE supercomputer at Texas Advance Computing Center and at on the PACE clusters at Georgia Tech.

2.3 Generating Initial Data

The input information of a NR simulation of BBH entails all the 20 parameters of a classical two-body problem, i.e. normalized black hole masses $m_{1,2}^{\rm initial}$ (and $M^{\rm initial} \equiv m_1 + m_2 \equiv 1$), dimensional black hole spins $\vec{S_{1,2}}^{\rm initial}$[1], momenta $\vec{P_{1,2}}^{\rm initial}$, and positions of black holes $\vec{r_{1,2}}^{\rm initial}$ at an instance of time $t = t^{\rm initial}$. The input information of NR simulations are in geometrical units ($G = c = 1$), so distance and time are measured in the units of M, while momenta are measured as fraction of c.

For all NR simulations presented in this thesis, the initial configuration of BBH is assumed be in a *quasi-circular stage*, i.e. $\vec{P}_1^{\rm initial} = -\vec{P}_2^{\rm initial}$. The assumption is that by the time BBH coalescence enters the LIGO spectrum, it has evolved through millions of orbits, and any eccentricity from its initial stage would have been emitted away by GWs. As described in section 1.2, a quasi-circular BBH in vacuum therefore can be fully described by 8D initial parameters of $\Lambda(r = r^{\rm initial}) = \Lambda(m_1, m_2, \vec{\chi_1}(r), \vec{\chi_2}(r)$.

We decide on the choice of these initial parameters based on whether we are following up on a BBH candidate observed that was observed in the GW searches in LIGO or investigating the effect of an intrinsic parameter on of BBH dynamics in strong gravity.

As an example, we demonstrate the process to generate initial data for the NR simulation `GT0901`, which we conducted as a followup to first GW detection, GW150914. The parameters of the simulation are show in table 2.1. The values of individual black hole masses and spins were obtained from the parameter estimation studies [47].

[1] the dimensional spin relates to Kerr-spin parameter as $\vec{S_{1,2}} = \chi_{1,2}\, m_{1,2}^2$

GT-ID	r_0	$r^{\rm initial}$	m_1/m_2	$\vec{\chi_1}^{\rm initial}$	$\vec{\chi_2}^{\rm initial}$	M_{min}	SU
GT0901	$50M$	$12M$	1.22	$(0, 0, 0.33)$	$(0, 0, -0.44)$	$45M_\odot$	40k

Table 2.1: Initial data of the follow-up numerical relativity simulations of first binary black hole candidate, GW150914.

Using Post-Newtonian Equations To Compute Initial Momenta & Spins: To compute momenta at the start of our NR simulation, $\vec{P}_1^{\rm initial}$, we need to evolve the binary black hole system from some r_0 to $r^{initial}$ using post-Newtonian (PN) equations of motions for a two-body system. Our choice of $r^{\rm initial}$ dictates the length of the NR simulation. The higher the total-mass of the binary, the less time it will coalesce in the LIGO band. Thus, the choice of $r^{\rm initial}$ essentially dictates the lowest total-mass of BBH we can utilize this NR simulation. The followup simulation of GW150914 was started at a generous binary separation of $r^{\rm initial} = 12M1240$ km (assuming total mass of GW150914 $M = 70M_\odot$). Below are the input parameters for the GT-PNEVO code that integrates PN equations [65, 66]. This integration is computationally mild, essentially requires solving only one PDE, and can be performed in few seconds in a regular machine. The trajectories of the two black holes obtained from this integration are shown in fig. 2.2.

```
par.initial_sep = 50.0      # r_0 (in units of M; G=c=1)
par.final_sep   = 12.0      # r-initial
par.MM          = 1.0       # normalized mass, M_0
par.mass_ratio  = 1.22      # mass-ratio m1/m2 = q_0
par.a1x         = 0.0       # chi1x_0
par.a1y         = 0.0       # chi1y_0
par.a1z         = 0.33      # chi1z_0
par.a2x         = 0.0       # chi2x_0
par.a2y         = 0.0       # chi2y_0
par.a2z         = -0.44     # chi2z_0
# Orbital angular momentum L is pointing in +z-axis at t= 0 or r_0
```

The above integration lasted for 356 orbits around center of mass. The total time passed in the center of mass frame of BBHs $\Delta t = t_0$ to $t^{initial} = 537576M \approx 185$s. The above integration gives us with the value momenta $\vec{P}_1^{\rm initial}$ (stated below), such that the BBH simulation has a quasi-circular orbit for intrinsic parameters $\Lambda(r = r^{\rm initial})$. Notice, that at the start of our NR simulation, the black holes already possess a relative velocity of about 8% of speed of light.

```
# momenta at r-initial
$p1x   = -0.000525160055582;
$p1y   = 0.084244835360007;
$p1z   = 0.000000000000000;
```

Apart from the information of momenta, this integration also provides us with the evolution of $\vec{\chi}_1$ and $\vec{\chi}_2$ from $r_0 = 50M$ to $r^{\rm initial} = 12M$, and gives an approximate number of BBH orbits we will see in an NR simulation of these initial parameters (described below).

```
# Dimensional spins s=a*m^2 at r-initial
$s1x   = 0.000000000000000;
$s1y   = 0.000000000000000;
$s1z   = 0.099661553445337;
$s2x   = 0.000000000000000;
$s2y   = 0.000000000000000;
$s2z   = -0.089278467656846;
#-------------------------------------------------
Time to merger from 12.0M to 5.0M is 1856M
Number of orbits over same range: 9.02
```

Note: As $\vec{\chi}_1$ and $\vec{\chi}_2$ are parallel to $\vec{L}$ at r_0, they remain so until $r^{\rm initial}$. If $\vec{\chi}_1$ and $\vec{\chi}_2$ have in-plane components, it will result in spin-orbit precession during PN evolution. In such case, the spin components will be drastically different at $r^{\rm initial}$ than the one we define at

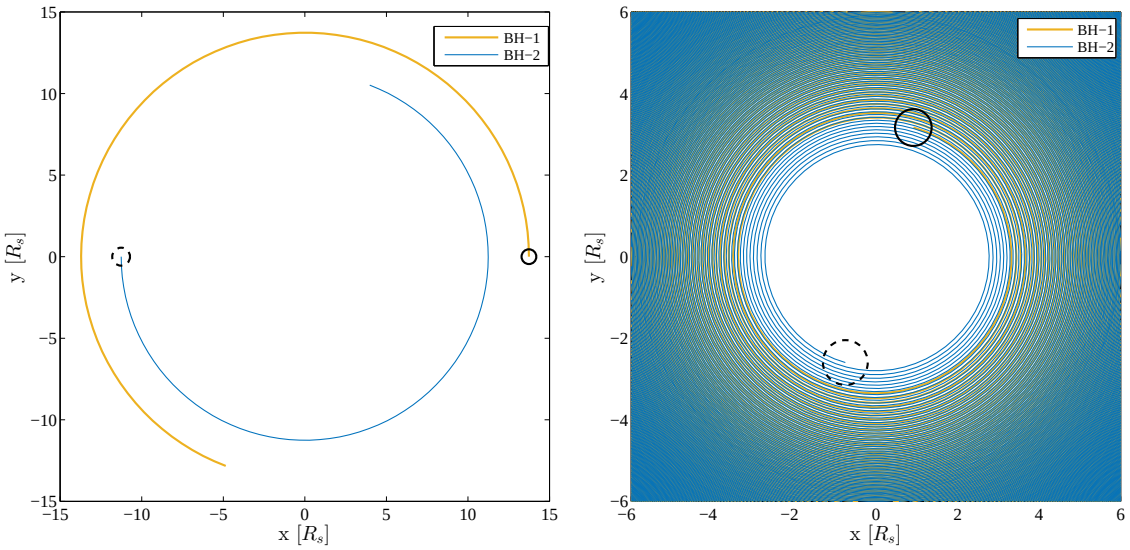

Figure 2.2: Trajectories of individual black holes of GW150914 from $r_0 = 50M$ to $r^{\rm initial} = 12M$ obtained by PN equations. The x-y axes are scaled in Schwarschild units $R_s = 2M \approx 206$ km. The circles refers to the two event horizon of two black holes (dotted being the bigger black hole). The plot on the left is for the first orbit starting at a binary separation of r_0. The plot on the right is for orbital separation at $r^{\rm initial}$. The BBH made 356 orbits around the center of mass from r_0 to $r^{\rm initial}$. The total time spent by BBH in this plot is $\Delta t = 537576M \approx 185$s.

r_0. For follow up NR simulations in LIGO, it is important to get spin orientation at $r^{\rm initial}$ that are consistent with observations. This demands an additional trial and error routine.

Initial Time Slice: Once we have the initial data of GW150914 in PN regime (weak-field limit), the next task is to convert the parameters $\Lambda(r = r^{\rm initial})$ into a spatial hypersurface γ_{ij} at the start of NR simulation time $t = t^{\rm initial}$. On γ_{ij}, the two black holes are the "two punctures", separated by a distance $r = r^{\rm initial}$. These punctures have a boundary of $r_{1,2} = 2m_{1,2}$, forming a *local* apparent horizon. These punctures possess the initial velocity computed earlier using PN equations. At this stage, we are ready to evolve our initial spacetime of BBHs using Einstein's Equations. This step requires running simulations supercomputer, as described in next section.

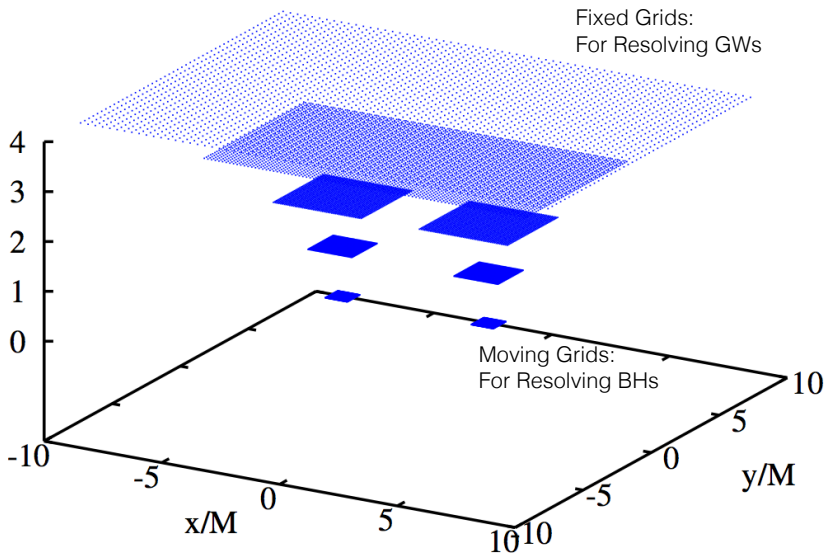

Figure 2.3: Refinement levels in a NR simulation. The finest grids are moving and resolve the black holes. The fixed grids resolve the radiation zone. Image credit: James Healy [67]

2.4 Running on Supercomputers

Our goal is to evolve the initial spacetime of BBH parameters $\Lambda(r = r^{\text{initial}})$ to the end stage of a single black hole $\Lambda(r = 0) = \Lambda_F$ using the full Einstein's Equations decomposed in 3+1 framework. For these, we adapt the BSSN formalism which transforms equation 1.1 into four evolution equations (spatial hypersurface, extrinsic curvature, lapse function, shift vector) and two constrain equations (momenta, Hamiltonian). Solving these 6 physical quantities at each time step dt is essentially the heart of NR simulation and demands extensive computing resources. In running a NR simulation of BBH, the requirement for computing resources is dictated by four factors - (i) length of the simulation (r^{initial}), (ii) resolution of the simulation (size of the black hole, radius of extraction of GWs), (iii) the symmetries we can impose (trajectories of the black holes) and (iv) the output we demand from our simulation (shapes of black hole horizon and GW radiation).

i. Limits on Binary Separation: For the NR relativity infrastructure presented in this thesis, the biggest computing limitation arises from the length of the simulation. TheBBH that the author conducted typically start at binary separation $r^{\rm initial} = 11M$. Based on the intrinsic parameters of BBH $\Lambda(r)$, these simulations last for $t \sim 2000M$. For 192 cores on STAMPEDE, an average speed of our such simulation is $8M$/hour. Therefore, each BBH simulation takes two weeks of wall-time and about $40,000$ SUs. For this binary separation, the BBH coalescence will last for ~ 8 orbits, i.e. ~ 15 GW cycles. Therefore, the usability of these simulations for a GW search is limited to cases of BBH systems with masses comparable or higher to GW150914 (in comparison, for the second BBH detection GW151226, the LIGO detectors observed over 50 orbits).

ii. Choosing Numerical Resolution: Our requirement numerical resolution depends on the choice of intrinsic parameters $\Lambda(r)$ (see figure 2.4), among them the most crucial being the BBH mass-ratio $q = m_1/m_2$. Our NR infrastructure utilizes Adaptive Mesh Refinement (AMR) scheme. We typically set 10 refinement levels, each scaling with

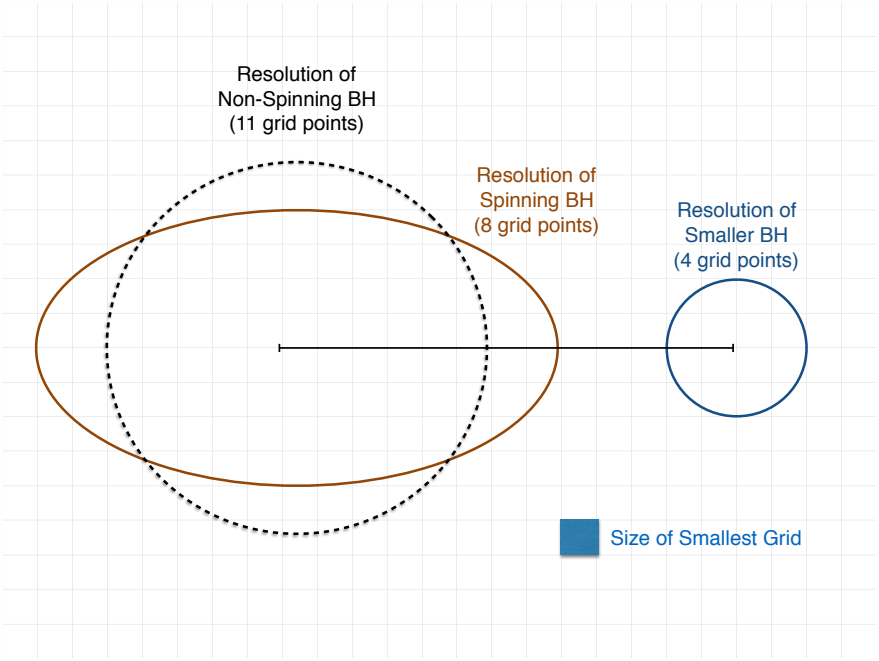

Figure 2.4: Resolving individual black holes in a numerical relativity simulation based on their mass-ratio and spins

powers of 2 of finest grid size, $r_{\rm Res} = 0.2M$. These refinements levels cover two zones - the moving grids which resolve the black holes during their evolution, and the fixed ones that resolve the outgoing gravitational radiated during evolution. The grid sizes in the these two zones are described in figure 2.3. We typically expect to have 100 grid points across the diameter of the smallest black hole. For BBH simulation of equal masses ($q = 1$), in the normalized units the radius of each black hole is $R_1 \sim m_1 \sim 0.5M$. Therefore, the finest resolution of $M/100$ will suffice. Compare that to an unequal BBH with mass-ratio $q = 10$, it will need a finest resolution $M/550$. This increase in resolution will cost ~ 5 times more computing resources. Similarly, a spinning black hole also requires higher resolution as it posses an elongated horizon shape, meaning the distance between poles has shrunk and needs more grid points to resolve compared to a non-spinning black hole.

iii. Role of Symmetries: A BBH system of equal-mass and no-spin is confined in the orbital plane. Furthermore, the trajectory mirror in the four quadrants of x-y plane. We can utilize these symmetry to substantially reduce the grid points of resolving a BBH across our 3D simulation cube. For BBH with unequal masses and/or spins aligned with angular momentum, the black holes are sill confined in the orbital plane, along with a π-symmetry around the x-axis. It is only in case of BBHs with precessing spin that the black holes start wobbling above the orbital plane, and all the symmetries are broken. Hence, a NR simulations of precessing-spin BBH utilizes a factor of 8 more computing resources. Also, as the memory per core is tripled, we typically require 320 cores to run precessing spin simulation. The most computationally expensive simulations are of BBHs that are both, of unequal masses and with precessing spins. This part of parameter space is of utmost importance to GW astronomy as all the approximant models fail to predict GWs from unequal-mass precessing case [21].

iv. Choosing our Outputs: To obtain accurate description of emitted GWs from evolution of BBHs on our simulations, we require extracting the outgoing radiation at

multiple shells. Based on the resolution in radiation zone, we determine the choice of such shells, as typically we wish to get the farthest radius. Each such shells adds to our computing memory. Also, to investigate the 'local' dynamics of black hole in strong-gravity, we utilize various modules, such as computing the horizon shapes for tracking the mass and spins of black holes, the spacetime grid. All these additions scale our computing resources.

2.5 Post-Processing Stage

We stop the simulation once the final black hole relaxes to a stable equilibrium, i.e., there is no more 'ringing' of the black hole. After that we turn our efforts towards the post-processing of the various output from our simulation. We design these post-processing tools based on the physics we wish to dissect regarding the BBH coalescence. In this section we highlight some of the most relevant simulation output that aid gravitational wave astronomy. These quantities are generated by utilizing the GEORGIA TECH POST-PROCESSING TOOLKIT [67, 68]

2.5.1 Gravitational Waveform

Our primary goal behind conducting a NR simulation is to extract the most accurate gravitational waves, h, emitted from BBH coalescence. For that, we first need to extract the Weyl Scalar Ψ_4 [69] at spatial and temporal infinity. As the size of simulation grid is finite, we conduct the extraction on a fiduciary sphere of radius R in the source frame of the simulation such that the initial orbital angular momentum of the binary, $\vec{L}^{\rm initial}$, is pointing in the positive z-direction joining the poles of the sphere. This Ψ_4 is further decomposed into spin-weighted spherical harmonics as,

$$\boxed{\Psi_4(t;\Theta,\Phi) = -\frac{1}{R}\sum_{\ell,m} A_{\ell m}(t) e^{i\phi_{\ell m}(t)}\, {}_{-2}Y_{\ell m}(\Theta,\Phi)} \tag{2.1}$$

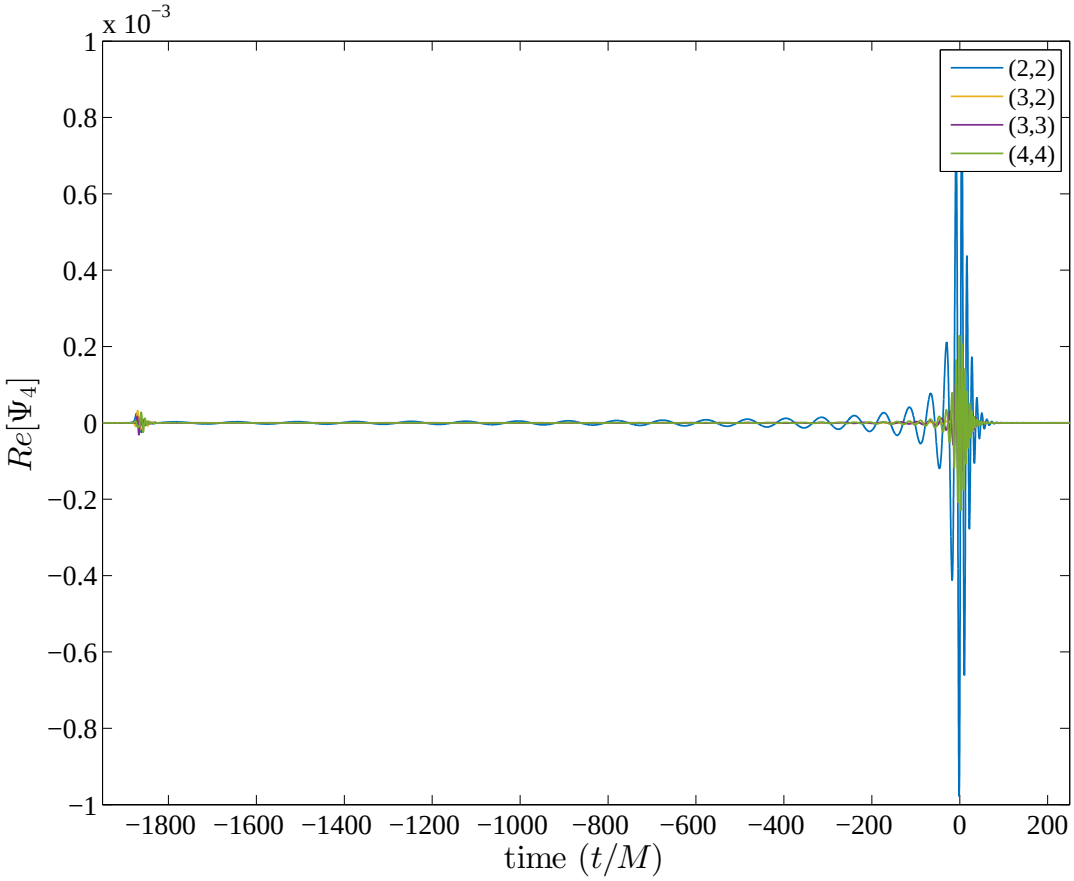

Figure 2.5: Evolution of Ψ_4 at an extraction radius $R = 75M$ for the NR simulation of GW150914. Different harmonic modes of radiation are shown.

with both $A_{\ell m}$ and $\phi_{\ell m}$ real functions of time. This decomposition of Ψ_4 gives rise to the terminology "GW modes" in the literature. The most important output of our NR simulations is a time-series of Ψ_4 for each radiated mode between $\ell = 2 : 8$, $m = -\ell : \ell$, extracted for multiple fiduciary sphere of radius R. The accuracy of extraction on each R is determined by the resolution of our simulation grid. For the simulation of GW150194, we have plotted Ψ_4 for different modes in figure 2.5 at an extraction radius $R = 75M$.

The features of Psi_4 as shown in figure 2.5 are consistent with BBH of any initial parameter:

i. The peak of Ψ_4 corresponds to the BBH merger.

ii. The most dominant mode across the evolution is $(\ell, m) = (2, \pm 2)$.

iii. There is a junk radiation at the beginning, because we have suddenly initiated gravitational radiation on spacetime (in reality the GWs were emitting for millions of orbits). So we have to artfully window this initial junk.

The Weyl scalar Ψ_4 relates with the gravitational waves and its polarization through a double time integration:

$$\boxed{h = h_+ - ih_\times = -\int_{-\infty}^{t}\int_{-\infty}^{t'} \Psi_4 \, dt' dt''} \tag{2.2}$$

The above equation demands the GW be extracted at $R \to \infty$. This means we need to extract Ψ_4 at infinity for *each mode* and then compute GWs using eq. 2.5.1. In the NR simulations described in this thesis, we typically extract all the modes of Ψ_4 at $R = 75M$, and use an analytic expression to extrapolate it to infinity. The gravitational waveform for our GW150914 simulation is showcased in figure 2.6. This waveform was directly used in identifying GW150914 as a binary black hole merger (see chapter 8). The effect of sky-location and higher modes is showcased in figure 2.7.

Scaling of Gravitational Waveform to Physical Masses As noted earlier, all our BBH simulations are conducted in units of total-mass of the binary, i.e., $M = 1$. Therefore. the GW strain obtained in our simulations can be renormalized for any mass of BBHs, from stellar to super-massive range. The limit on the usability of NR waveform depends on how many orbits we evolve.

For the case of a massive BBH system like GW150194, only 6 GW cycles or 3 inspiral orbits were recorded by LIGO. However, in the case of a lighter BBH system, GW151226, LIGO recorded over 100 cycles (remember GW frequency scales inversely with mass). The current sensitivity of LIGO permits detection of GWs starting a minimum frequency, $f_{\rm low} = 30{\rm Hz}$.

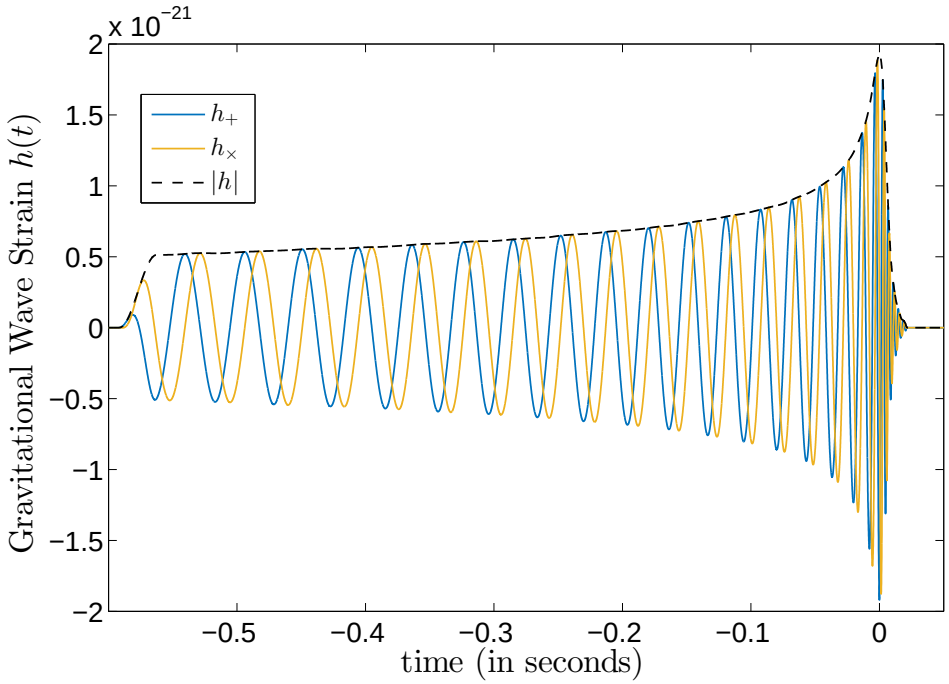

Figure 2.6: Gravitational wave strain $h(t)$ computed from the NR simulation of GW150914. The strain utilizes all the radiated modes of Ψ_4 ($\ell = 2 : 6$) and extracted at $R \to \infty$. To get the physical units, the strain is scaled for a total mass $70M_\odot$ and source placed in an optimal sky-location (north pole) at a distance of 450 Mpc. Both the $+$ and $\times$ polarization are stated, as well as the amplitude of waveform $|h|$. The x-axis are scaled in the physical units of time and centered around the instance of BBH merger. Notices, the LIGO detectors needed a minimum sensitivity of $\delta l/l \sim 10^{-21}$ to detect this signal

.

In our normalized units of total-mass, the frequency corresponding to the first GW cycle is measured by a quantity $M\omega$, where ω is half of the orbital frequency of BBH. The quantity $M\omega$ is referred in the literature to denote the length of a NR simulation of BBH. It relates with the physical mass of the binary as,

$$M = 3.23 \times 10^4 M_\odot \left(\frac{M\omega}{f_{\rm low}}\right) \tag{2.3}$$

Our simulation of GW150914 lasted for 10 orbits before merger (20 GW cycles) after we removed the initial junk radiation. It had a corresponding $M\omega = 0.04$; and therefore the current generation of LIGO can use this simulation for binary of total mass $\geq 45M_\odot$. Once the LIGO reaches its design sensitivity, the lowest frequency it can detect will be

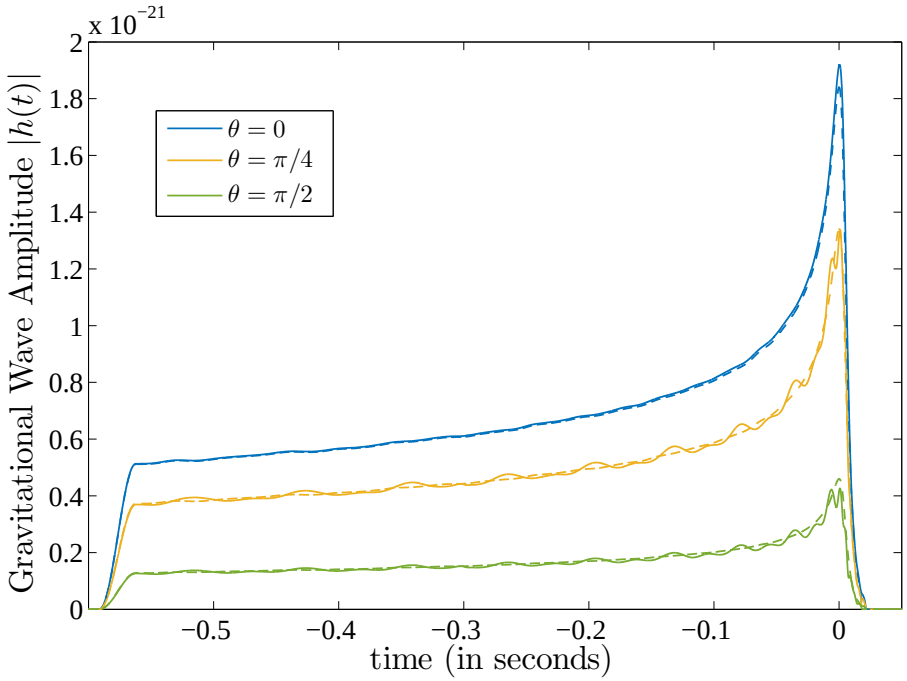

Figure 2.7: Gravitational wave amplitude obtained from NR simulation of GW150914 at different sky-locations values at polar angle θ (0 implies directly above the detector). Here dashed lines refer to amplitude obtained from dominant modes $\ell = 2, m = 2$, while straight lines refer to all combination of modes upto $\ell = 2 : 6$. Notice that when system is pointing at an angle $\theta > 0$, the higher modes show more features, hence allowing us to break degeneracy in the parameter space of the system

$f_{\rm low} = 10$Hz. Hence, the GW cycles from this simulation will be restricted for binaries $\geq 150 M_{\odot}$. As we noted that these simulations are expensive, it is recommended to start new NR simulation at higher binary separation $r^{\rm initial}$, as they can be cataloged to be utilized in future detectors for search of BBH systems similar to GW150914.

2.5.2 Extracting Radiated Energy and Momentum

By observing a gravitational waveform at infinity, one cannot easily infer the dynamics during the evolution of BBHs. However, by utilizing the radiated information from Ψ_4, one can derive the dynamical features of BBH coalescence. We list below the four most relevant dynamical quantities to GW astronomy which can obtained from the output of our simulation [70]. The time evolution of these quantities can be only computed only by

running a full NR simulation till BBH merger. In figure 2.8 and 2.9, we showcase evolution of these quantities in the case of our simulation of GW150914.

i. **Radiated Energy** $E_{\rm rad}$ provides us quantitative understanding of the fraction of total mass being converted into GWs at different stages of BBH coalescence. For building approximate models of GWs, this quantity provides the distribution of radiated energy in different modes (ℓ, m) and the relation of radiated with the intrinsic parameters $\Lambda(r)$ of BBHs. As noted in figure 2.8, about 90% of total-energy in GWs is released during the BBH merger. During the coalescence, GW150914, lost $\sim 3M_{\odot}c^2$ of its total mass as GWs.

ii. **Peak Luminosity** dE/dt corresponds to the power emitted in GWs when two black holes collide. This information helps us to compare BBH coalescence with other extremely energetic in the universe, such as gamma-ray bursts. As shown in the subplot pf figure 2.8, the merger of BBHs in GW150914 released 4×10^{56} erg/s as GWs, making it one of the most energetic astrophysical event ever recorded.

iii. **Evolution of Total Angular Momentum** $\vec{J}$ indicates the direction of emitted GWs. In the case of spin-orbit precession of BBHs, the direction of $\vec{J}$ changes with time. Tracking this quantity helps to gain insights into the non-linear aspects of precession (See chapter 4). As GW15014 had spin components $(\vec{S}_{1,2})$ only in the direction of orbital angular momentum $(\vec{L})$, the direction of total angular momentum $(J = L+S)$ remains fixed across the evolution. The system loses $\sim 10^{44}$J s of angular momentum across evolution (see the left plot in figure 2.9).

iv. **Linear momentum.** We conduct our simulations in frame such that the center of mass is always at the origin. However, with each orbit, the system is slowly losing its linear momentum via GWs. The direction of the linear momentum that is retained within the system is dependent on the initial configuration of BBH. Hence, once two black hole merge, the final black hole (BH) possesses these remaining momenta and

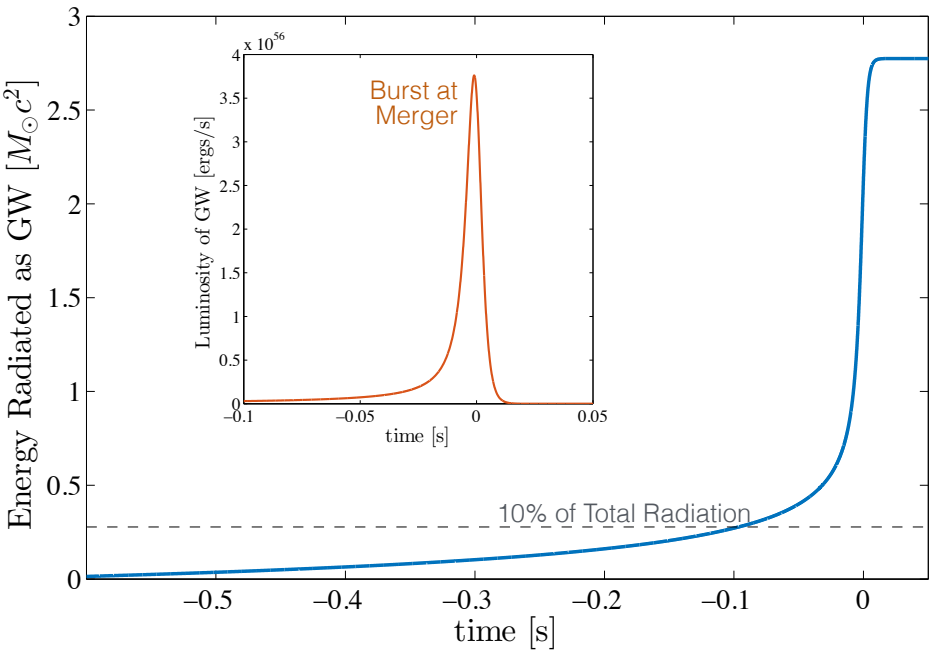

Figure 2.8: Radiated energy and luminosity derived from ψ_4 of the NR simulation of GW150914

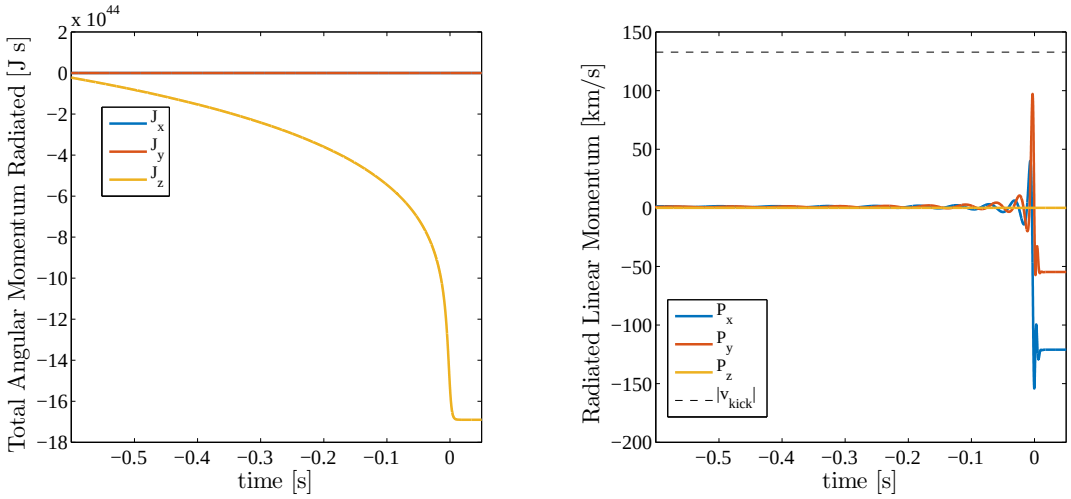

Figure 2.9: Radiated total angular momentum (left) and linear momentum (right) derived from ψ_4 of the NR simulation of GW150914

gets 'kicked' from the center of mass. This kick is a product of the highly non-linear dynamics during BBH merger (see the plot on the right in figure 2.9). n astrophysics, these allows to infer if individual black holes, that may have formed through stellar or

super-massive BBH, get kicked from its host environment. This kick is also referred as the 'recoil velocity' and is often regarded as one of most important result from NR towards astrophysics community [**Healy:2014yta.**, 55, 71, 72, 73] In the simulation of GW150914, we noticed a kick of the remnant black hole of ~ 140 km/s.

2.5.3 Information Regarding Individual Black Holes

The radiated quantities defined in the previous section give us information about the BBH dynamics as a whole at infinity. The advantage the NR simulation is that we can track the non-linear dynamics just outside the horizon of two black holes. This means we can track the evolution of all 15D of initial parameters (black hole masses, theirs spin vectors, their relative position, their momenta). Below we highlight the three important quantities:.

v. **Trajectory of Black Hole:** One of the modules we utilize in our simulation is the `ShiftTracker`. It accurately tracks the position of two black holes all the way until merger. Using the output from these module, we can track the relative positions, velocity and acceleration of individual black holes in the simulation frame. For gravitational astronomy, this helps infer the speed of black hole collision and time of merger for generic configuration of BBH. Information regarding the trajectory of our GW150914 simulation is shown in figure 2.10. Notice, that right before the mergers, the relative velocity of two black holes is 40% speed of light. Other than BBH, no other astrophysical phenomena we are aware of in which we objects of such heavy mass ($\sim 35 M_{\odot}$) move at such high speeds.

vi. **Mass of Black Hole:** From a heuristic argument, one can conclude that the masses of individual black holes, m_1 and m_2, remain the same since the time we define the initial data for our step-1 (PN-equations). On the other hand, the system emit GWs and the energy is proportional to $(m_1 + m_2)$. During the evolution, the only way we can determine the rest mass of the black holes is by a module called `Apparent`

`Horizon Finder` [74, 75]. This module allows us to find the *local horizon* of the black holes (not event-horizon) at every iteration of our simulation. Using the shape of the horizon, we can compute both the mass and the spin of individual black holes. This module is computationally is very demanding, and in a typical NR simulation, we utilize it only for one orbit or for every few hundred iterations. The horizon shapes of the two black holes at the start of the simulation is stated in figure 2.11.

vii. **Spin Vector of Black Hole:** Unlike masses, the spin vector of the black holes for a generic initial data will not remain constant throughout the BBH evolution. The only exceptions are when the two initial black holes are non-spinning, and when their initial spins are parallel to the orbital angular momentum. If one intends to cater the NR simulations for a follow-up of BBH candidate in LIGO, it is important to track the information of individual spins for the entire evolution. For practical purpose, we interpolate the spin information from apparent horizon to obtain approximate spin vectors for rest of the BBH evolution. We do so by utilizing the positions black holes and formula for `Isolated Horizon` [74].

2.5.4 Parameters of Remnant Black Hole

The end stage of a BBH merger is a remnant BH (also referred as 'final BH'). This remnant BH can be described by a family of 7D of intrinsic parameter (mass, spin vector, recoil velocity), and expressed in a compact form $\Lambda_F = \Lambda(m_F, \vec{\chi_F}, \vec{v_F})$.

The value of these parameters strongly depend on our choice of initial 8D parameters of BBH $\Lambda(r)$. Because rest mass is converted into GWs, the mass of the remnant BH is always smaller than the initial BHs. The spin of remnant BH, however, can be more or less than the initial net spin. When the initial two black holes have no spin, the remnant BH will still spin at 60% of its maximum capacity. The spin vector of remnant BH may point in the direction other than initial total angular momentum. Both masses and spin of

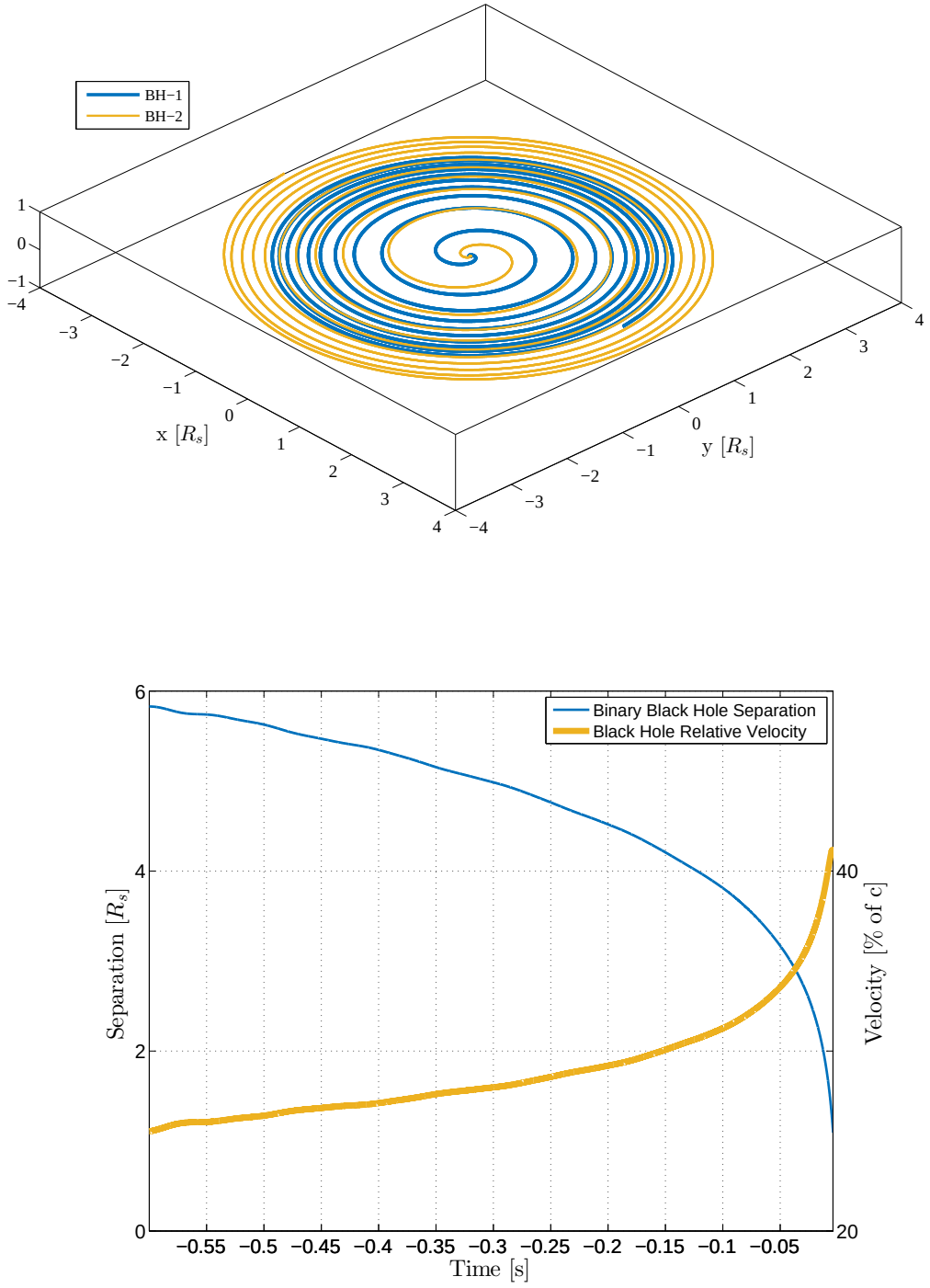

Figure 2.10: Trajectories of individual black holes, orbital separation and relative speed obtained from the NR simulation of GW150914.

remnant BH are computed using the module `Apparent Horizon Finder`. We run this module till the time remnant BH has reached equilibrium, i.e. the ringdown stage

is over. The recoil velocity of remnant BH is obtained by computing radiated linear momentum described earlier. From our NR simulation of GW150914, we obtain the remnant parameters $m_F = 0.96M^{\text{initial}}$ and $|\vec{\chi_F}| = 0.67$. The horizon shape of the final black hole at the end of our simulation is stated in figure 2.11.

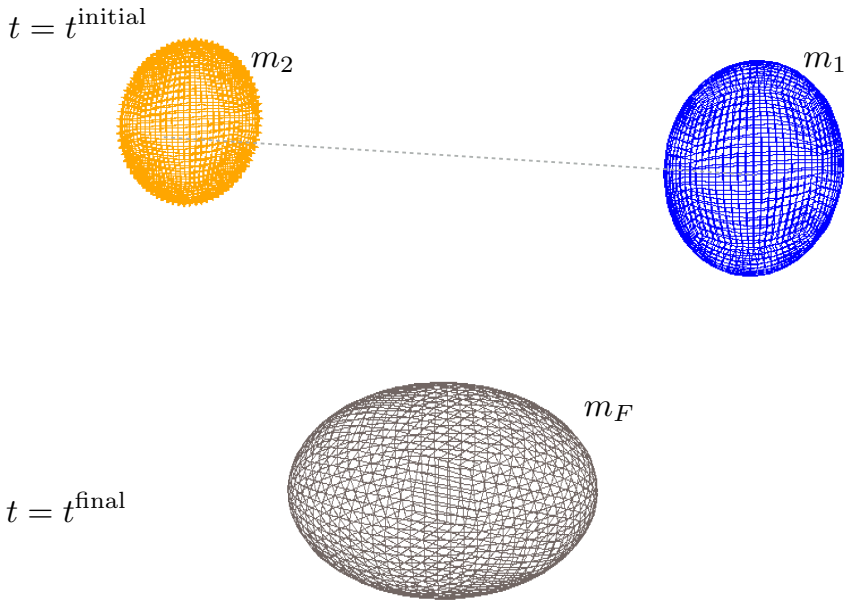

Figure 2.11: Apparent horizon shapes of the black holes for the NR simulation of GW150914. The two black holes at top form the binary at the start of the simulation, the black hole at bottom is the remnant at the end of our simulation at the start of the simulation and remnant black hole at the end of the simulation

Chapter 3

GEORGIA TECH CATALOG OF BINARY BLACK HOLE SIMULATIONS

Overview

This chapter introduces a catalog of gravitational waveforms from the bank of simulations by the numerical relativity effort at Georgia Tech, several of which are conducted by the author. Currently, the catalog consists of 452 distinct waveforms from more than 600 binary black hole simulations: 128 of the waveforms are from binaries with black hole spins aligned with the orbital angular momentum, and 324 are from precessing binary black hole systems. The waveforms from binaries with non-spinning black holes have mass-ratios $q = m_1/m_2 \leq 15$, and those with precessing, spinning black holes have $q \leq 8$. The waveforms expand a moderate number of orbits in the late inspiral, the burst during coalescence, and the ringdown of the final black hole. Examples of waveforms in the catalog matched against the widely used approximate models are presented in section 2.3. In addition, the author has tested predictions of the mass and spin of the final black hole by phenomenological fits against the results from the simulation bank. The Georgia Tech catalog is publicly available at einstein.gatech.edu/catalog. Simulations from this catalog have been directly utilized for studies presented in chapter 4, 5 and 8 (see figure 3.1). This chapter is an overview of the work published in [21].

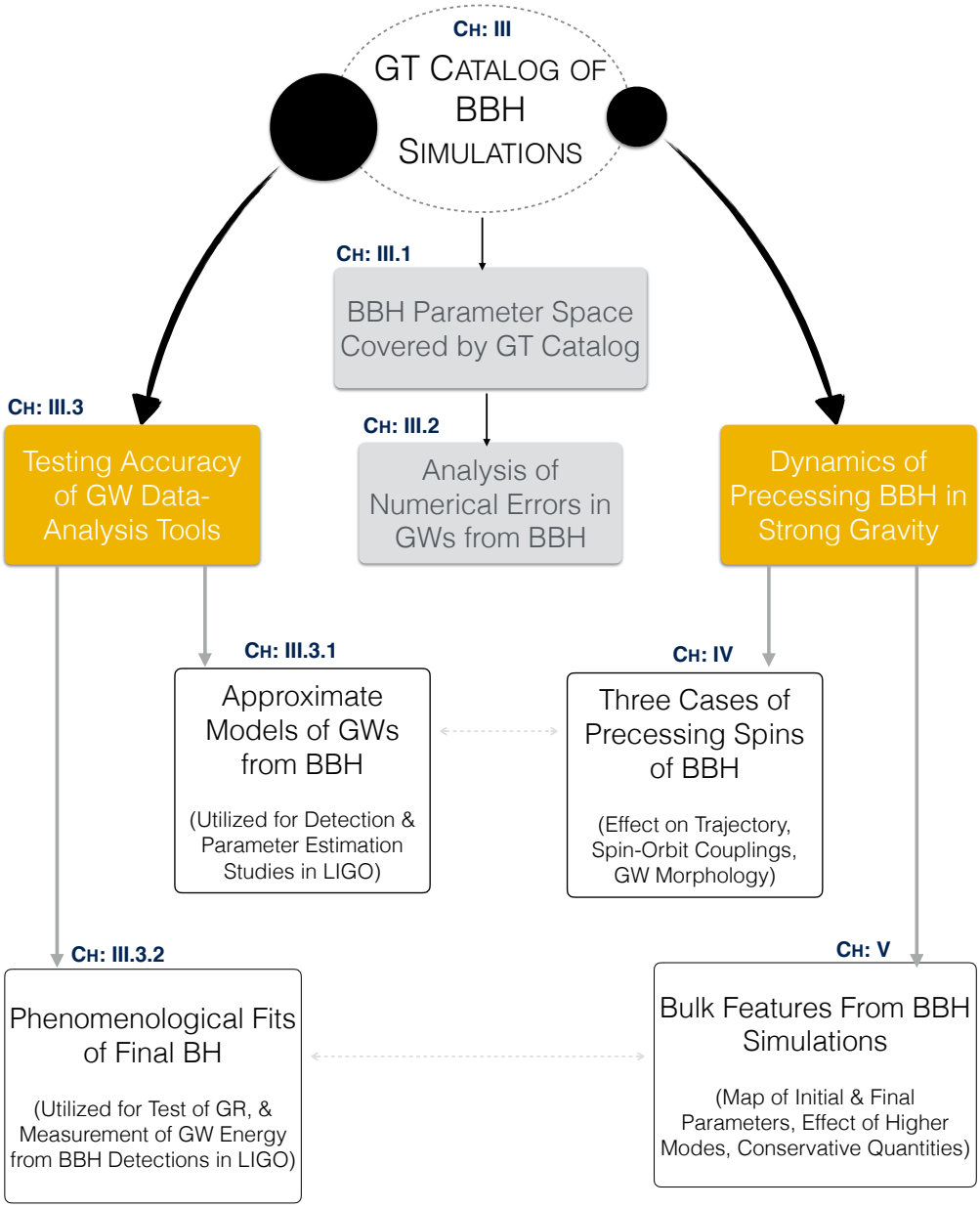

Figure 3.1: Flowchart showing the applications of GT Catalog to GW data-analysis (Chapter 3) and investigating dynamics of BBH in extreme gravity (Chapter 4, 5)

Introduction

The goal of this chapter is to formally introduce the Georgia Tech (GT) catalog of GW waveforms. Currently, the catalog consists of 452 distinct waveforms from a bank of more

than 600 BBH simulations produced by the NR effort at GT. Among the 452 waveforms, 128 are from binary systems with BHs non-precessing spins, i.e. no spins or spins such that they are parallel (aligned, or anti-aligned) with the orbital angular momentum $\vec{L}$); and, 324 waveforms are from generic spin configuration that lead to precessing BBH systems (see Figure 3.2). The catalog probes mass-ratios of $q \leq 15$ for binaries with non-spinning BHs and $q \leq 8$ for binaries with precessing, spinning holes. The waveforms cover a moderate number of GW cycles in the late inspiral, the merger of the binary, and ends with the ring-down of the final BH.

The waveforms are given in terms of an adjustable mass scale (the total mass $M = m_1 + m_2$ of the BBH system); and, therefore, they can be rescaled for both ground and space-based GW detectors. In this paper, we focus the discussion on the relevance of the catalog to data analysis for ground detectors such as Laser Interferometer Gravitational Wave Observatory (LIGO).

Within the sensitivity window of LIGO and Virgo [39] ($10 - 1000$ Hz) the waveforms in the catalog can be in general used in two ways. For binary systems with masses $M \geq 60\, M_\odot$, as in GW150914, the binary system is observed for less than half a dozen GW cycles before merger. A substantial fraction of the waveforms in the GT catalog expand this dynamical range. They can thus be applied directly in analysis massive BBH mergers.On the other hand, for binary systems with $M \leq 60\, M_\odot$, more cycles are needed for detection and parameter estimation [76, 77, 78, 79]. Our catalog also includes waveforms with enough cycles to help improve Effective One Body Approach (EOB) [80] and IMR (Inpiral, Merger, Ringdown) [81] waveform models.

The chapter is organized as follows: Section 3.1 describes the parameter space and some of the key features of the GT catalog. Section 3.2 includes a discussion of the errors in phase and amplitude of the extracted GWs. Section 3.3.1 compares a few of the waveforms in the catalog with the`SEOBNRv2` and `IMRPhenomPv2` waveform models. Section 3.3.2 compares the parameters of remnant BH, namely mass and spin, with the

phenomenological fits [82, 83]. Conclusions are given in Sec. 3.3.2.

3.1 BBH Parameter Space Covered by GT Catalog

The initial data for each simulation in the catalog are fully characterized by a set of 15 parameters: BH masses m_1, m_2, spins $\vec{\chi}_1$, $\vec{\chi}_2$, momenta $\vec{P}_1$, $\vec{P}_2$, and the binary separation r. We select code units such that $M = m_1 + m_2 = 1$. The waveforms are classified into two main types: Non-precessing and Precessing. Non-precessing waveforms are subdivided into two sub-types: Non-spinning if the BHs in the binary are not spinning, and Aligned-Spin if their spins are parallel with the orbital angular momentum $\vec{L}$ (spins of black hole that are anti-aligned and parallel to $\vec{L}$ are put under the class of aligned-spin). The precessing waveforms are also subdivided into two sub-types: Equal Mass and Unequal Mass. Table 3.1 summarizes this classification.

The catalog can be found at einstein.gatech.edu/catalog. Each of the 452 waveforms in the catalog have a unique identifier of the form `GTXXXX`. The catalog is organized by folders. Each folder contains the following information:

- Initial parameters of BBH system
- Parameter file of the simulation
- BH trajectories
- Mass, spin and gravitational recoil of the final BH
- Radiated energy, linear momentum and angular momentum
- Ψ_4 decomposed in spin-weighted spherical harmonics with $\ell \leq 8$ and different extraction radii
- The waveforms are available in `HDF5` format with meta-data as stated in [84, 85].

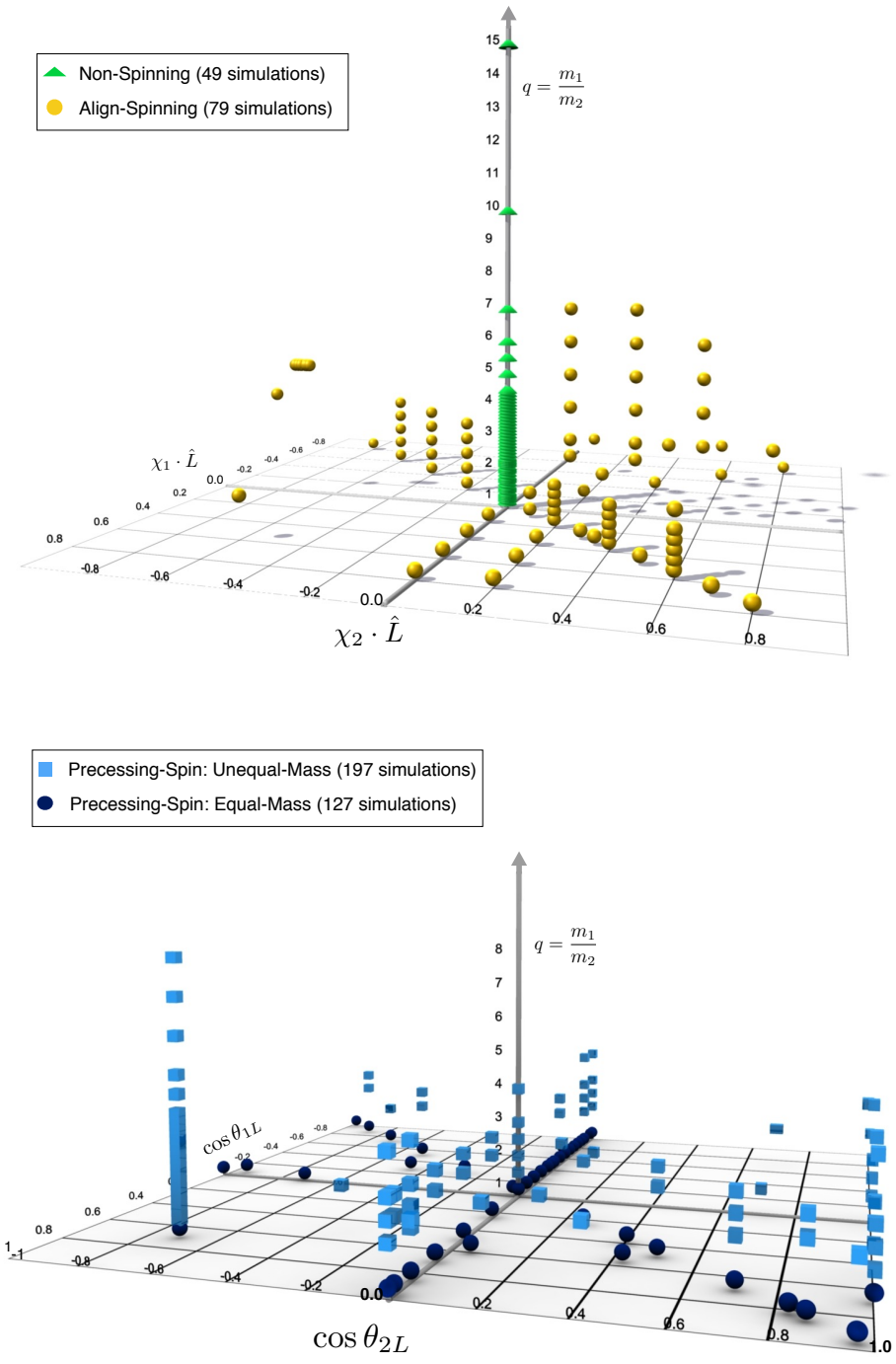

Figure 3.2: Coverage of binary black hole parameter space by the GT catalog. The vertical axis in both plots denotes the mass ratio q. The plot on the left is for non-spinning and aligned-spin systems, and on the right for precessing binaries.

Figure 3.2 provides a general sense of the parameter space covered by the catalog. The vertical axis in both plots denotes the mass ratio q. The plot in the left is for non-spinning

and aligned-spin systems. Therefore, the axis in the plane are given in terms of $\vec{\chi}_{1,2} \cdot \hat{L}$ in order to capture both the spin magnitude and orientation for each BH. The plot on the right in Figure 3.2 describes the precessing runs. The axis in the plane are given in this case in terms of the $\hat{\chi}_{1,2} \cdot \hat{L}$, namely the spin orientation relative to the orbital angular momentum.

Type	Sub-type	Simulations
Non-Precessing	Non-Spinning	49
	Aligned-Spins	79
Precessing	Equal-Mass ($q = 1$)	127
	Unequal-Mass ($q \neq 1$)	197

Table 3.1: GT catalog waveform classification

The scatter plot in Figure 3.3 shows $|\vec{\chi}_F|$, the magnitude of the spin of the final BH, as a function of the percentage of total mass radiated, i.e. $(1 - M_F/M) \times 100\%$. Notice that binary systems with high final BH spin radiate the most energy. On the other hand, configurations that leave behind a slowly rotating BH radiated very little.

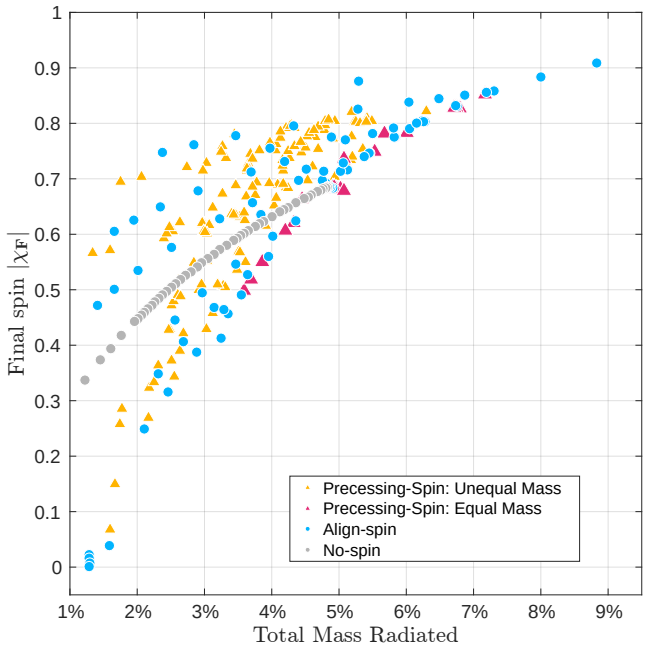

Figure 3.3: Magnitude of the spin of the final BH $|\vec{\chi}_F|$ as a function of the percentage of total mass radiated, i.e. $(1 - M_F/M) \times 100\%$

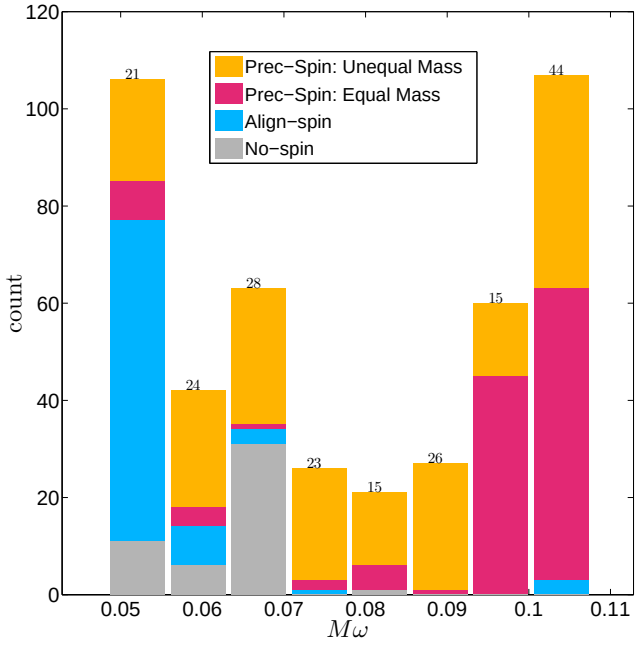

Figure 3.4: The histogram showing the distribution of the $M\omega$. For Advanced LIGO, the x-axis limit scales to $[50, 110]\ M_{\odot}$ as range of minimum total mass M. The numbers on the top of each bar corresponds to the total unequal-mass precessing simulations in the stated range.

The histogram in figure 3.4 show the distribution $M\omega_{orb}$ where ω_{orb} the orbital frequency (half of gravitational-wave frequency). The NR waveforms presented the catalog include the early phase of the simulation that is contaminated with the junk radiation in the initial data. The segment of the waveform with orbital frequencies $\leq M\omega_{orb}$ should hence be ignored. For a given low-frequency cutoff of a GW detector, f_{min}, the waveform can be scaled to a minimum total mass as $M = k\,(M\omega_{orb}/f_{min})$, where $k = 3.23 \times 10^4$. From figure 3.4 it can be inferred the catalog includes a large number of waveforms with less than four GW cycles. These are basically BBH plunges. They are nonetheless useful for studies of quasinormal ringing and gravitational recoil. Waveforms with between five to ten GW cycles are suitable to investigate BBH with massive BH such as GW150914.

The choice of initial BBH parameters in the catalog has been based on the science goals that we wished to investigate in the fully nonlinear regime. For example, the dense parts

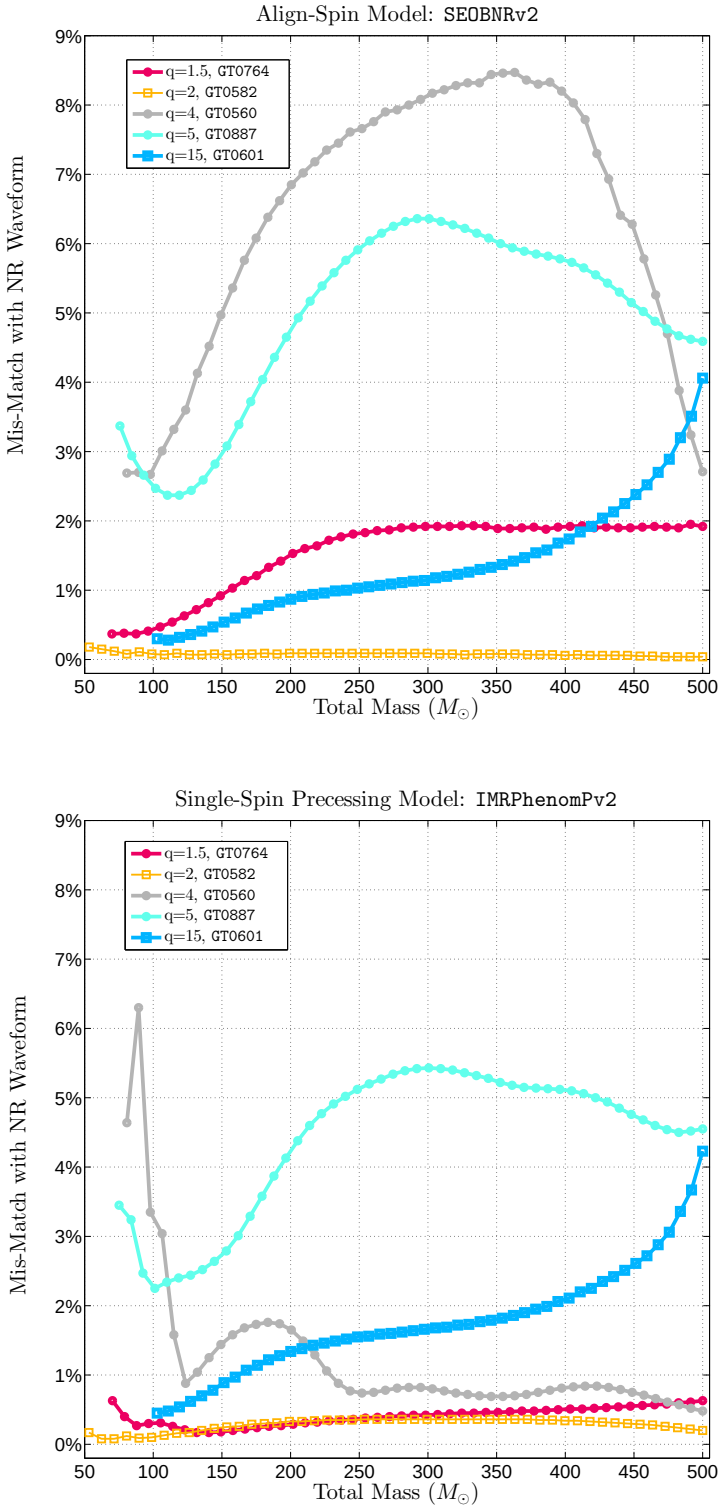

Figure 3.5: Mismatches of NR waveforms in Table 3.4 with approximant GW models.

in non-spinning parameter space from mass-ratio $q = 1 : 4.5$ were used in analyzing GW ringdown frequency [86]. While many of the precessing simulations with $q \leq 4$ were used for investigating the effect of orientation and higher-order modes [87]. On an average, the current simulation placing in the catalog is good representation of the generic BBH parameter space.

Some of the highlights in the catalog are: The largest mass-ratio is $q = 15$ for a non-spinning BBH (`GT0601`), while for precessing BBH $q = 8$ (`GT0886`). The maximum spin for the merging BH is $|\chi_{1,2}| = 0.8$. The most extreme spin for the remnant BH is $|\chi_F| = 0.9048$, corresponding to 8.826% of the total-mass M radiated in GWs (`GT0424`) (see Figure 3.3). The maximum total angular momentum radiated is $\sim 100\%$ for a system of align-spin BBH which results in Schwarzschild-like remnant BH (`GT0770`). The maximum GW cycles in our simulation corresponds to 27.5 for align-spin (`GT0612`) and 21.5 for precessing-spin systems (`GT0468`).

3.2 Analysis of Numerical Errors in BBH Simulations

To give a general sense of the accuracy of the waveforms, we select two cases in the catalog: one with BH spins aligned with the orbital angular momentum and another with precessing BHs (`GT0582` and `GT0560` cases respectively in the catalog, see next Section). Figure 3.6 summarizes the accumulated numerical errors in the GW strain, $h(t)$, from combined $\ell = 2 : 6, m = -\ell : \ell$ radiated mode. The left panels show the results for the aligned-spinning case `GT0582`, and the right panels for the precessing-spin case `GT0560`. Top row panel depicts the strain $h(t)$. The middle and bottom panels show accumulated errors in phase and amplitude for each of the available resolutions, four resolutions for `GT0582` and three for `GT0560`. For each resolution, the errors are computed against a waveform obtained from Richardson extrapolation to the continuum using the available resolutions.

Tables 3.2 and 3.3 summarizes the errors in phase and amplitude are also reported for early inspiral and reference frequency $M\omega = 0.2$ (near merger). The error-analysis

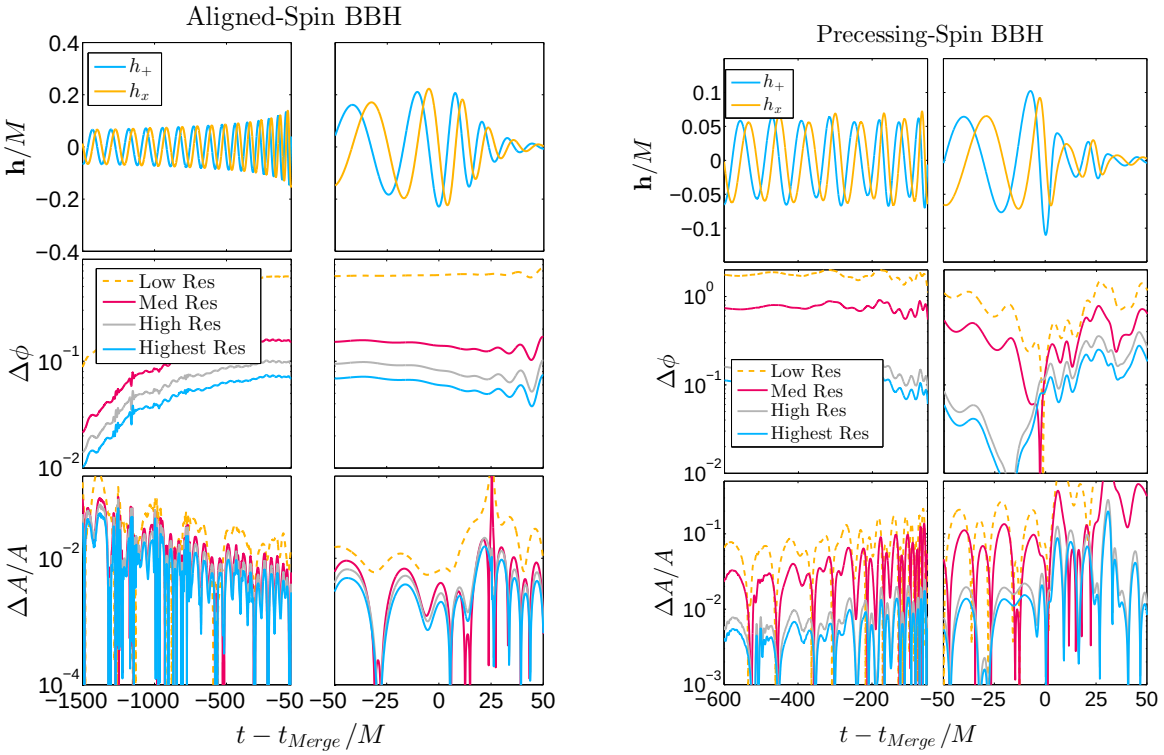

Figure 3.6: Numerical errors in the amplitude and phase of the GW strain, $h(t)$, for $\ell = 2:6, m = -\ell:\ell$ radiated modes. Left panels show results for the `GT0582` case and right panels for the `GT0560`. Top panels depicts the strain $h(t)$ at face-on location from detector. The middle and bottom panel shows the errors in phase and amplitude, respectively.

BBH Type	Mismatch from Finite Resolution	Mismatch from Finite Extraction
Aligned-Spin	2.9×10^{-6}	7.4×10^{-5}
Precessing-Spin	3.1×10^{-4}	4.7×10^{-4}

Table 3.2: Numerical errors in GW strain for GT catalog due to finite computational grid. Here mismatch are computed for the advance LIGO noise curve. The numbers refer to the waveforms showcased in figure 3.6.

	Errors in GW-strain:			
BBH Type	$\Delta A/A\|_{Ins}$	$\Delta\phi\|_{Ins}$	$\Delta A/A\|_{Ref}$	$\Delta\phi\|_{Ref}$
Aligned-Spin	5.8×10^{-4}	1.0×10^{-2}	3.7×10^{-2}	6.8×10^{-2}
Precessing-Spin	3.6×10^{-3}	1.1×10^{-1}	1.2×10^{-3}	2.6×10^{-2}

Table 3.3: Typical numerical errors in phase and amplitude of GW strain for GT catalog. The numbers refer to the waveforms showcased in figure 3.6.

is similar to the one reported in [46]. The mismatches are computed between two finite numerical grid resolutions and finite waveform extraction radius (R in Eq. 4.2). These match calculations involve advanced LIGO noise curve and total-mass of BBH scaled at $70M_{\odot}$ (comparable to GW150914).

As majority of our simulations have resolutions comparable to High or Highest for a given initial data of BBH system, i.e. number of grid points across black hole horizon and resolution in the waveform extraction region are similar, the systematic errors quoted in table **??** and in figure **??** are fairly representative of our entire catalog. The quoted errors are in agreement with the error analysis conducted on multiple simulations from this catalog earlier in [46]. For future space-based gravitational wave detectors, the required accuracy in amplitude-phase evolution is more than what can be currently achieved by numerical relativity simulations (see [88]).

3.3 Testing Accuracy of GW Data- Analysis Tools

3.3.1 Approximate Models of GWs from BBH

Next we compare a few of the waveforms in the catalog with two recent and well-known approximate waveforms. The binary parameters of the selected waveforms are given in Table 3.4, and the corresponding strains $h(t)$ for the two cases (`GT0582` and `GT0560`) are show in Figure 3.6. The cases were chosen to probe highly distinct regions of parameter space.

The two approximate waveform models we use to compare our NR waveforms are: i) a time-domain model for non-precessing, aligned-spin systems, derived from the effective-one-body formalism (referred to as `SEOBNRv2`) and ii) a phenomelogical frequency-domain model for single-spin, precessing systems (referred to as `IMRPhenomPv2`). Both of these approximate models were used in the detection and parameter-estimation analysis of GW150914.

For each waveform in Table 3.4, we compute their mismatch with both SEOBNRv2 and IMRPhenomPv2, where the mismatch is given by

$$\text{mismatch} = 1 - \max_{t_0,\,\phi_0} \frac{(h_1|h_2)}{\sqrt{(h_1|h_1)(h_2|h_2)}}, \tag{3.1}$$

where the inner product is given by

$$(h_1|h_2) = 4\text{Re}\int_{f_{\min}}^{\infty} \frac{\tilde{h_1}(f)\tilde{h_2}^{*}(f)}{S_h(f)}\,\mathrm{d}f\,. \tag{3.2}$$

The maximization in the mismatch (3.1) is over the initial arrival time and phase. In Eq. (3.2), $S_h(f)$ is the noise power spectral density of the detector, and asterisks denote complex conjugation. The integral is evaluated from some minimum frequency $f_{\min}$, below which there is no appreciable contribution to the integrand due to the noise spectrum. We set as low-frequency cutoff $f_{\min} = 30\,\text{Hz}$ and use a noise spectrum representative of advanced LIGO in its early configuration. To evaluate mismatch, both the waveforms, NR and the approximant models, are projected to the same optimal sky-location and orientation.

Figure 3.5 shows the mismatches for the NR waveforms in Table 3.4 with SEOBNRv2 and IMRPhenomPv2. The mismatch is computed for different values of total mass of BBH systems, starting from BBH systems with mass similar to GW150914 to intermediate mass BBH range for current generation of GW detectors. The NR waveform includes all the higher harmonics (as stated in eq. 4.2) from $\ell = 2$ to 6; however, the approximant waveform includes only radiated mode $\ell = 2$, $m = 2$, which will be dominant for the chosen optimal sky-location and orientation.

For the aligned spins with low-mass ratio, both models have a very strong agreement with NR waveform. For the non-spinning BBH with mass-ratio of $q = 15$, which represents an astrophysical intermediate-mass ratio inspiral BBH system, both SEOBNRv2 and IMRPhenomPv2 have a growing mismatch at high total mass. For such high masses,

ID	Type	q	$\vec{\chi}_1$	$\vec{\chi}_2$
GT0764	prec-spin	1.5	(0.6,0,0)	(0,0,0.6)
GT0582	aligned-spin	2	(0,0,-0.15)	(0,0,0.6)
GT0560	prec-spin	4	(-0.6,0,0)	(-0.6,0,0)
GT0887	prec-spin	5	(0.42, 0, 0.42)	(-0.42, 0, -0.42)
GT0601	non-spin	15	$(0, 0, 0)$	$(0, 0, 0)$

Table 3.4: GT BBH simulations used for comparison with approximate GW models. The results are shown in figure 3.5.

the signal in LIGO will be dominated by the merger and ringdown of BBH, and radiated modes beyond the dominant becomes important [89, 86]. Both the models only includes the dominant modes (2,2) and thus there is strong mismatch, even at optimal sky-location.

For the precessing-spin BBH systems, it is expected that SEOBNRv2 will show strong inconsistency with NR simulations as the model is tuned only for aligned-spin systems. The max mismatch we report for SEOBNRv2 in precessing cases, which happens for a system with mass-ratio $q = 4$. In contrast, for the same NR simulation (GT0560), the precessing spin model IMRPhenomPv2 - reports an error up to 6% for lower total mass and drops to less than 1% at higher total mass. Both models agree fairly well with NR simulations for almost equal-mass systems, but for strongly deviate for mass-ratios $q = 5$ and above (where higher radiated modes become important).

3.3.2 Phenomenological Fits of Final BH

As mentioned before, included in the GT catalog is information regarding the mass and spin of the final BH. Over the years, several phenomenological formulas have been proposed that connect the properties (mass and spin) of the remnant BH with the initial parameters of the BHs in the binary. In this section, we concentrate on two of such phenomenological formulas: one from [83], referred as RIT, and the other from [82], referred as BR.

In Figure 3.7, we report the errors the phenomenological formulas incur in predicting the mass and spin of the final BH. The percentage errors are organized according to the

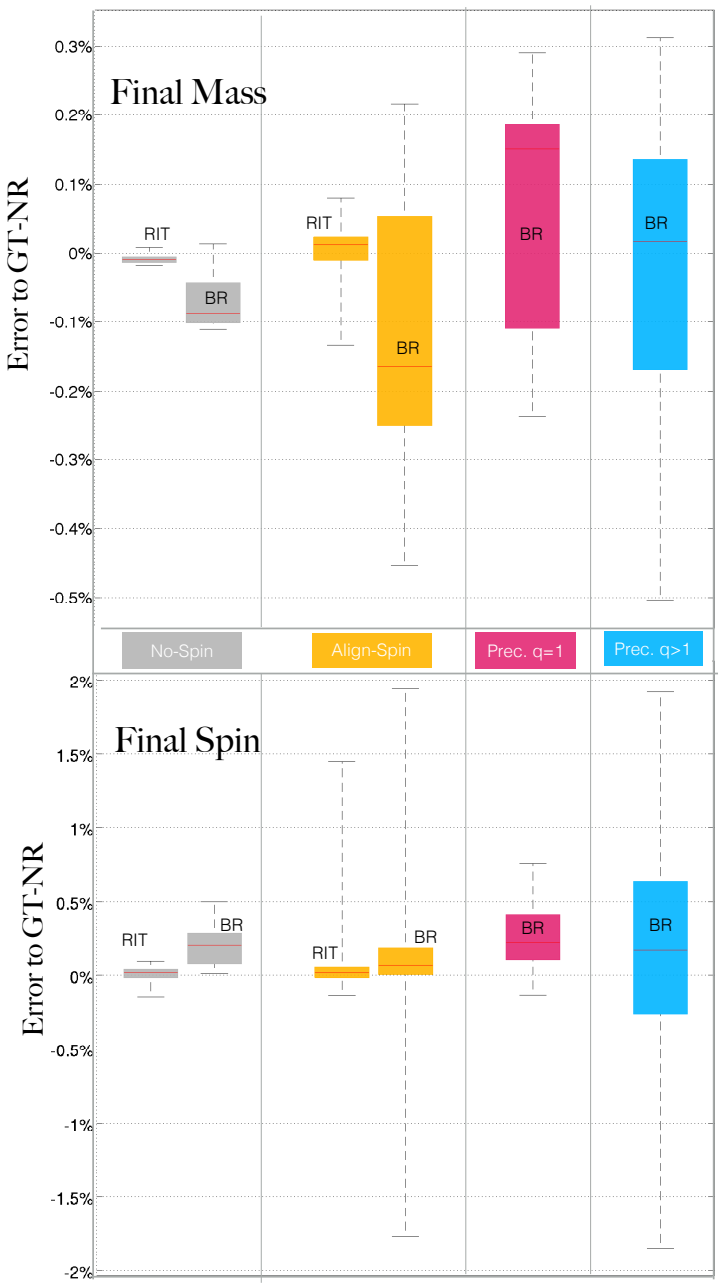

Figure 3.7: Percentage relative errors predicting the mass and spin of the final BH from the `RIT` and `BR` fitting formulas when applied to our catalog. The red line in each box is the median value of the errors. The colored region within each box denote the $25-75$ percentile of relative error in each case.

sub-types in Table 3.1, and they were calculated as $(1 - RIT\ or\ BR/NR) \times 100\%$. Top panels show the errors in the final mass and the bottom for the final spin. The red line in each box is the median value of the errors. On each box, the colored region denotes 75%

of the cases. Notice that, for aligned-spin systems, the spread in errors for the remaining 25% cases (i.e. cases with the largest errors) is quite significant for both formulas. The RIT, valid for non-spinning and align-spinning BBH systems, has an average discrepancy with our catalog of 0.035% for the remnant mass and 0.23% for the remnant spin. The BR formula, valid for all generic BBH configurations, agrees remarkably with all our GT-BBH simulations, and with an average discrepancy of 0.6% for the final mass and 1.6% for the final spin. A recent paper by the authors [90] improves the BR formula for stronger agreements with generic BBH NR simulations.

Conclusion

This chapter introduced the GT catalog of GW waveforms consisting of 452 distinct waveforms from more than 600 spin-aligned and precessing BBH simulations with mass ratios of up to $q = 15$. The waveforms expand a moderate number of orbits in the late inspiral, the burst during coalescence, and the ring-down of the final black hole. A significant fraction of the waveforms have enough GW cycles that can be used in improving phenomenological or EOB models. The waveforms are also useful for tuning the phenomenological formulas describing the remnant black hole. Most of the waveforms can be used directly in connection with analysis of massive BBH binaries such as GW150914 and for conducting tests of general relativity that require knowledge of both the inspiral and ringdown stages. The GT catalog complements and enhances the catalog recently introduced by the SXS collaborations [91]. The GT catalog contains waveforms of the higher modes and will serve as repository of future waveforms, including those from double neutron star and mixed binary mergers.

Chapter 4

DYNAMICS OF MASSIVE, PRECESSING BINARY BLACK HOLES

Overview

This chapter summarizes the investigations conducted by the author to dissect the dynamics of the later stages of a precessing binary black hole systems in extreme gravity using numerical relativity simulations. For ground based GW detectors, the simulations showcased here corresponds to astrophysical sources heavy-stellar to intermediate mass range of black hole mergers (total mass $50 \sim 10^3 M_{\odot}$). With the current sensitivity of LIGO-like experiments, we can detect such massive BBH mergers up to cosmological distances of redshift 1. Following the discussion from the previous chapters, we restate the need for the supercomputer simulations of the Einsteins Equations to understand the morphology of GWs emitted during coalescence of precessing-spins of BBH (section 4.1). To provide a glimpse into the reach behavior of spin-spin and spin-orbit precession of BBH systems in non-linear regime (late inspiral, merger, ringdown), we present a case-study for three distinct NR simulations: *mild precession* for BBH system with mass-ratio $m_1/m_2 = 1$, *strong precession* for mass-ratio 8, and *transitional precession* in $m_1/m_2 = 7$ (section 4.2). We diagnosis the unique features of these three cases in terms of orbital dynamics, spin-orbit couplings and radiated GW morphology (section

4.3). Finally, we test the recovery of this NR simulations using the GW data-analysis tool used in LIGO (section 4.4). This work is in under preparation to be published.

Note: Refer to Appendix for definitions of the precessing angles and binary black hole parameters used in this chapter.

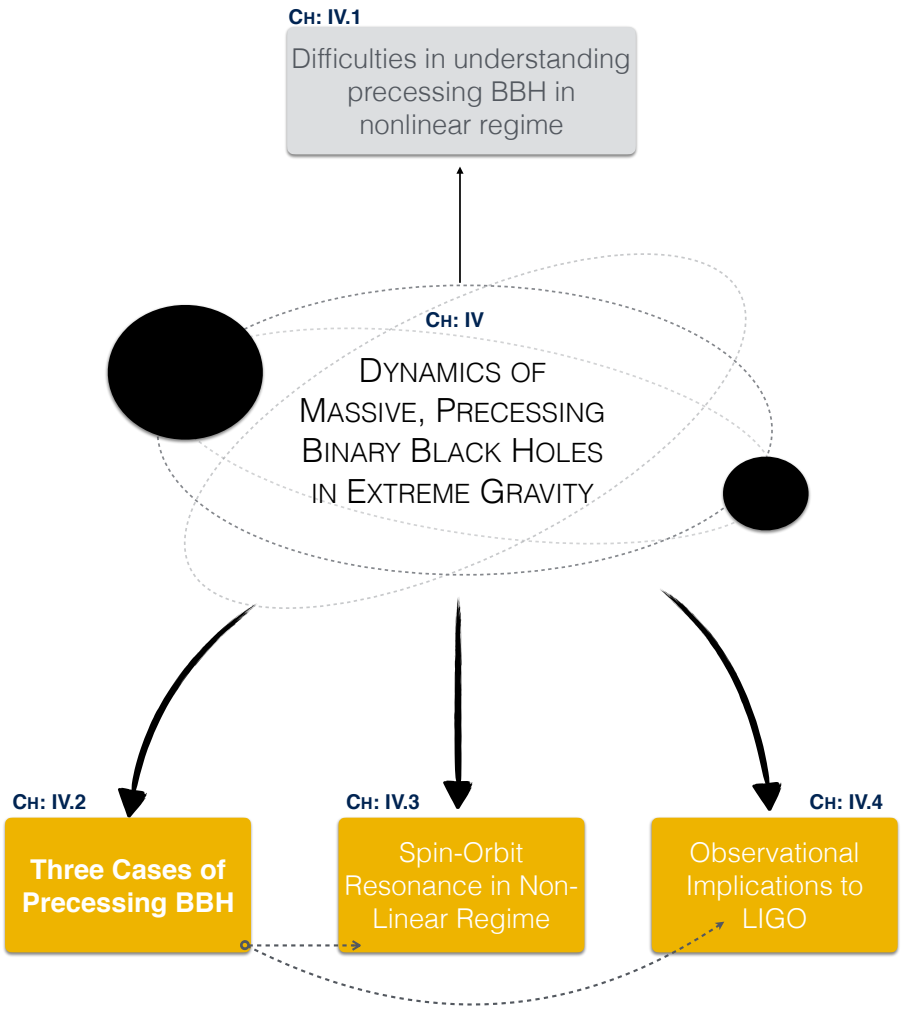

Figure 4.1: Overview of Chapter-4.

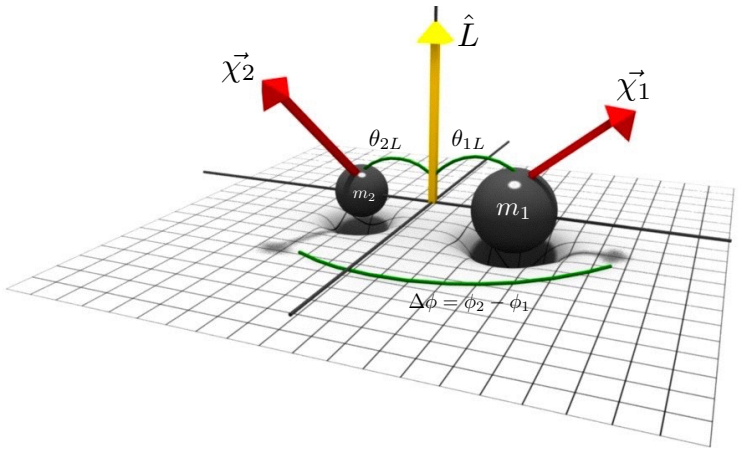

Figure 4.2: Diagrammatic representation of a generic spin configuration of a binary black hole.

Introduction

The dynamics of a BBH coalescence in full General Relativity, as exhibited by the numerical solutions to the Einstein Equations, is strictly dependent on our choice of initial value $Lambda(r)$ (i.e., masses and the spin orientation of the individual BHs at the start of NR simulation). In particular, the morphology of radiated GW has a strong dependence on the polar-components of the spins: θ_{1L}, θ_{2L}, (see figure 4.2)

For any given binary separation r, if $\theta_{1L,2L} = 0$ or π, the dynamics is that of an aligned-spin BBH, which implies the BHs in the binary are confined in the initial orbital plane such that $d\mathbf{S} \cdot \mathbf{L}/dt = 0$ for the entire evolution. This ensures the direction of dominant GW radiation $h_{+,\times}(\ell = 2, m = 2)$ remains fixed in the direction of initial total orbital angular momentum, $\mathbf{J}_i = \mathbf{L}_i + \mathbf{S_1}_i + \mathbf{S_2}_i$. As shown in the previous chapter, this aligned BBH case, defined completely via mass-ratio q, spins χ_{1z}, χ_{2z} and binary separation r, is relatively well investigated by approximate waveform models `Effective-One-Body` and `IMR` models and except heavy mass-ratios are in good agreement with the NR simulations.

But when the initial values of $\theta_{1,2} \in (0, \pi)$, the spin direction of individual BHs are time

dependent, and they couple with orbital angular momentum $\mathbf{L(t)}$ to exhibit a precessing behavior around total angular momentum $\mathbf{J}(t) = \mathbf{L}(t) + \mathbf{S_1}(t) + \mathbf{S_2}(t)$. Based on spin-configurations at the start of NR simulation, precessing-spin can affect dynamics of BBH in much drastic fashion that the in the case of aligned-spin BBH cases.

Understanding the behavior of generic precessing-spin BBH is difficult from both the side of NR simulations as well as modeling it for using approximate GW models. Hence, there has been very limited progress in modeling such systems in extreme gravity, except few cases of mildly precessing spins when mass-ratios are comparable. However, as there is no prior astrophysical constraints on the masses and spins of BBHs we expect to see in ground based GW detectors such as LIGO, we require very accurate waveforms to recover the information about precessing systems [92]. Decoding the parameters of the individual BH's spin are central to our understanding of the formation mechanism of these systems.

4.1 The Many Difficulties With Precessing-Spin BBH

From Numerical Relativity

(i) As we noted in chapter-2, the simulations of BBHs with precessing spins have no symmetry about the orbital plane (as the individual BHs can wobble in the 3D grid). Hence, in NR simulations of precessing-spin BBH, we need to simulate the entire "3D space", which implies about a factor of 8 more computing resources time to run compared to align-spin case.

(ii) The number of cores as well as memory per core is tripled in the case of precessing BBH simulations. Thus, the longer simulations are very difficult to conduct in precessing-spin BBH. In the GT-Catalog, we are restricted to precessing runs with 14 orbits before merger (24 GW cycles).

(iii) For high-mass ratio precessing system, additional resolution is required to capture the dynamics of the smaller BH. More number of grid points are required around this

smaller BH as the horizon is elongated due to spin.

(iv) The extraction sphere where GWs are decomposed into different harmonics is kept fixed, and thus not correspond to the coordinate system of simulation frame. For example, the dominant GW radiation, $h_{+,\times}(\ell = 2, m = 2)$ points in the direction of total angular momentum $\mathbf{J}(t)$, which is in the case of precessing-spin BBH systems is not pointing at the "poles" of the extraction sphere. Thus the ideal frame to capture GWs from precessing systems requires to be in the co-moving frame.

From Modeling and LIGO Data Analysis

(v) In align-spin system, except the magnitude of orbital angular momentum $\mathbf{L}$, none of the initial data quantities change with time. But in precession, barring mass-ratio, all the quantities get coupled due to their dependence on $(\theta_1, \theta_2, \phi)$.

(vi) The dominant GW radiation, $h_{+,\times}(\ell = 2, m = 2)$, captures only partial of the radiated energy from precessing-spin BBH systems. To accurately analyze the behavior of pressing-spin BBH, the waveform needs to include higher harmonics at least up to $(\ell = 4, m = -\ell : \ell)$. The current generation of approximant models do not have well-modeled higher modes for generically precessing BBH systems

(vii) Not having such approximant waveform models affect in our BBH search in two ways : detection and parameter estimation. For the match-filtering search, the template bank are build using models with align-spin and dominant modes $(\ell = 2, m = 2)$. Hence if a true signal is edge-on or of higher mass-ratio, then the template bank is recovering only partial of the signal in the noise, which if below our detection thresholds would imply that this event is missed.

(viii) In the parameter estimation studies of BBH candidates in LIGO, on which based our astrophysical understanding of the systems as well as test of GR, the lack of accurate

GW model for precessing-spin BBH means we are unable to break the degeneracy in the parameter space.

(ix) To model the higher modes of radiation beyond just $(\ell = 2, m = 2)$, particularly in the case of precessing-spin BBH is very complex, as it demands tracking the direction of radiated modes as a fuction of time, which in turn depends strongly on our choice of initial parameters.

(x) To further model the dynamics of BBH with precessing spins, one needs an understanding of how spin-spin and spin-orbit coupling dictates the dynamics in extreme non-linear regime (late inspiral). The information about these quantities from Post-Newtonian Regime has not to be well tested.

(xi) Dynamics of of BBH systems for isotropic distribution of $(\theta_1, \theta_2, \Delta\phi)$ in Post-Newtonian regime have shown that after the course of fairly long evolution (~ 1000 cycles), no particular values are favored (like we expect from *Spin-Orbit Resonance*). This implies that as of current astrophysical understandings, all possible spin configuration are equally likely for such massive BBH systems.

4.2 Three Cases of Precession

To demonstrate, the rich behavior of precessing BBH systems, we present a case-study of three distinct precessing configurations, noted in figure 4.3 and listed in table 4.1.

- The first case (C-1) has the intrinsic parameters (mass-ratio, spins) similar to the first detection of BBH merger from GWs, GW150914. This precessing BBH systems lies in part of parameter space where approximate models of GWs well capture the morphology. For such systems the direction of GW radiation remains fairly fixed. Thus, we term this case as **mildly precessing BBH**.

Case	q	$\mathbf{a_{1},}_{i}$	$\mathbf{a_{2},}_{i}$	$\mathbf{J}_i$
C-1	1	$(0.6, 45°, 0°)$	$(0.6, 0°, 0°)$	$(1.19, 5.12°, 0°)$
C-2	8	$(0.6, 45°, 0°)$	$(0.6, 135°, 180°)$	$(0.86, 18.3°, 0°)$
C-3	7	$(0.8, 168°, 152°)$	$(0.0, 0°, 0°)$	$(0.2, 140°, 152°)$

Case	m_F/M_i	$\mathbf{a_F}$	$\mathbf{v_F}$ (km/s)	Cycles
C-1	0.93	$(0.84, 5.23°, 4.2°)$	$(923, 173°, 166°)$	16
C-2	0.97	$(0.72, 17.8°, -1.7°)$	$(676, 9.8°, -4.4°)$	15
C-3	0.99	$(0.24, 148°, 156°)$	$(152, 83.6°, 130°)$	9

Table 4.1: **Three Cases of Precession:** The initial and final parameters of our three test cases of precession is stated. The first two configuration refers to, what is known in literature as, *simple precession*, while the last case is of *transitional precession* (notice the direction of initial $\mathbf{J}$ and $\mathbf{a_F}$). Here the vectors are listed as (magnitude, polar angle measured from +Z-axis, azimuthal angle measured from +X-axis)

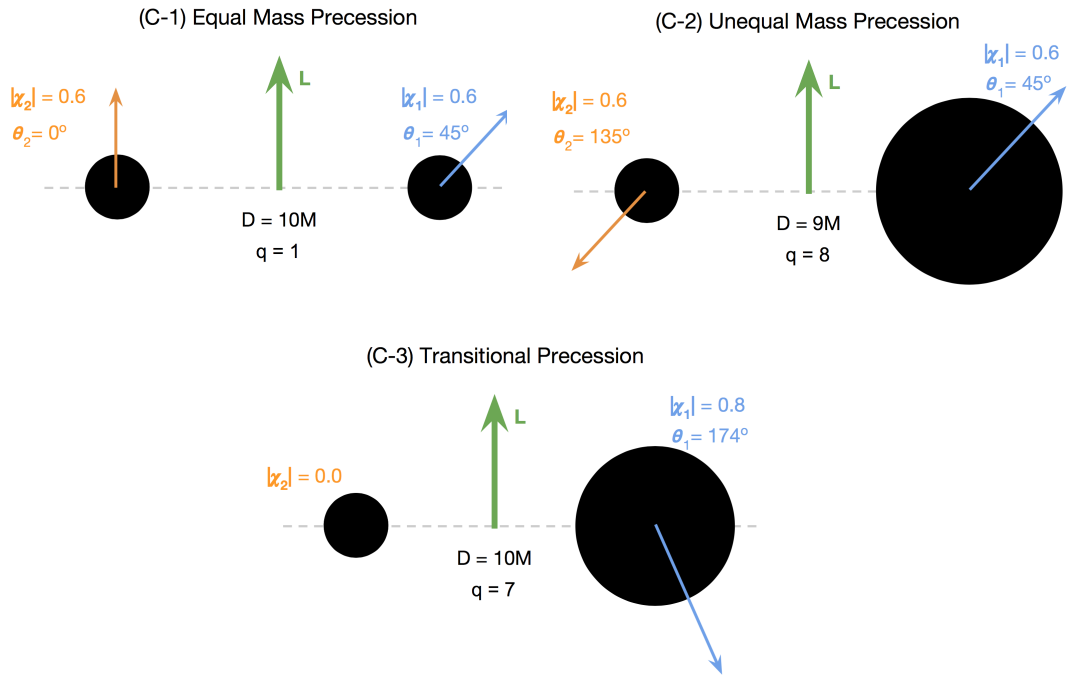

Figure 4.3: Diagrammatic representation of the spin and mass-ratio configuration of three cases

- The second case (C-2) has the intrinsic parameters such the mass distribution is very unequal, and spin on the bigger BH dominates the dynamics. This precessing BBH systems lies in part of parameter space where approximate models of GWs fail to

capture the morphology. In such systems, there is a strong wobbling of BHs around the orbital plane, thus affection the direction of GW radiation. Thus, we term this case as **strongly precessing BBH**.

- The third case (C-3) is a special configuration [93] where initially theBH spins are pointing in the opposite direction of angular momentum such that the total angular momentum $|\mathbf{J}| \sim 0$. As the spin magnitude does not change with time evolution in BBH but the orbital angular momentum is lost as GWs, the direction of J eventually flips and points in the direction of S. Such systems are called **transitionally precessing BBH**.

Below we describe for these three cases the (i) trajectories of the BHs, and (iii) GW morphology and (iii) distribution of energy in higher harmonics. The evolution of the individual BH spin compared and radiated total angular momentum is discussed in the section 4.3 on spin-orbit coupling.

Trajectories

Just based on the trajectory of individual BHs in binary, we can learn a great deal about the dynamics in extreme gravity as well as the morphology of emitted GWs. But the instantaneous position of BHs in binary is a coordinate dependent quantity. In a NR simulation there are three preferred frames of computing the trajectories:

- *simulation frame:* This also called the Center of Mass (CoM) frame. Here the origin of coordinate system is CoM. This is typically frame which is referred in the visualization of BBH simulations.

- *remnant frame:* Here the coordinate system is arrange such that the z-axis is pointing in the direction of the spin of the final BH. For an observer in CoM frame, the remnant frame also has a velocity component as the final BH has a recoil velocity. This frame

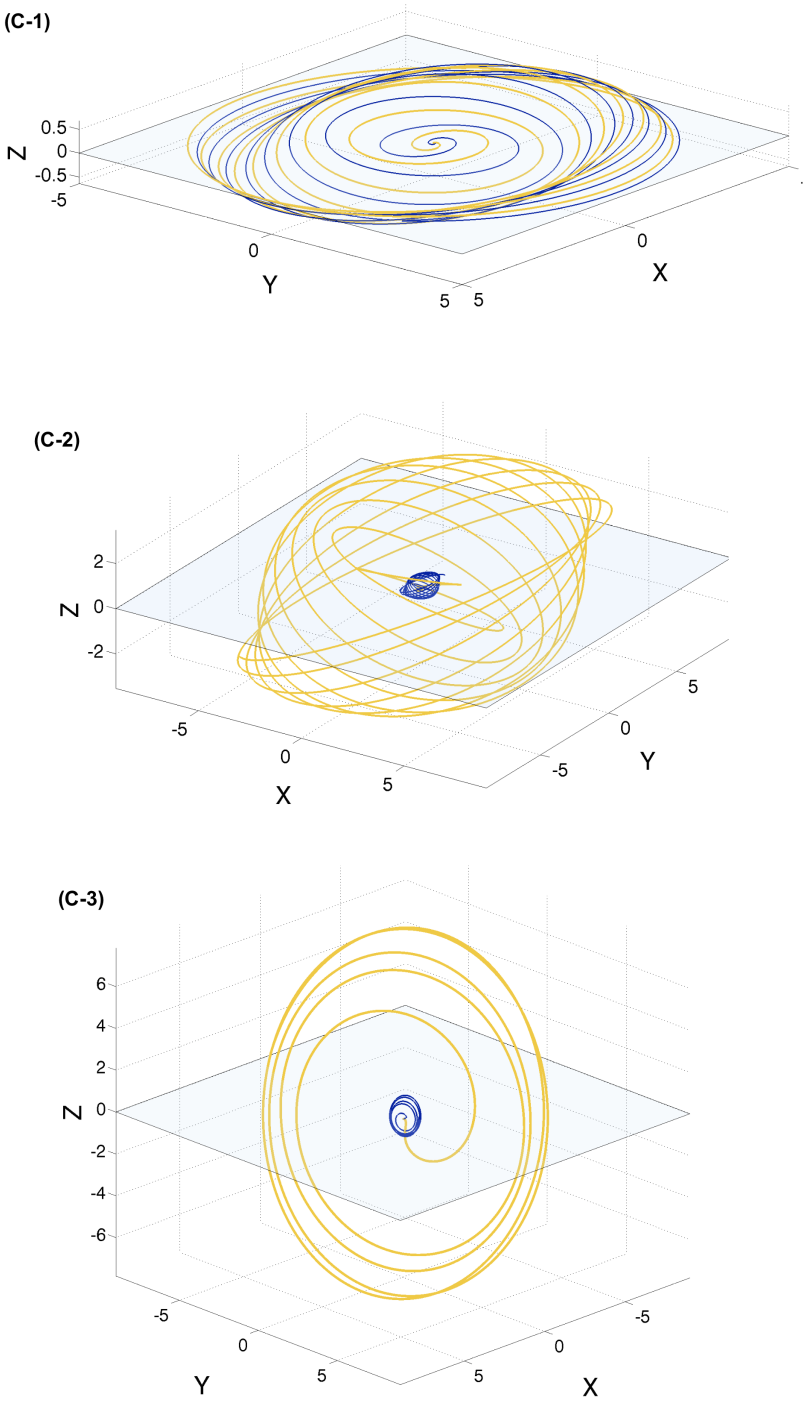

Figure 4.4: **Trajectories of BBH:** In the inertial frame of initial total angular momentum, $\mathbf{J}_i = \mathbf{J}(t = 0)$, the trajectories of BBH of cases C-1 (top), C-2 (center) and C-3 (bottom) is shown. The yellow lines refer to trajectory of smaller BH, blue line refers to trajectory of bigger BH. Notice that the direction of $\mathbf{J}(t = 0)$, from where most energy is radiated, is perpendicular to the plane at $z = 0$ for the first two cases.

is still ideal while extracting GW from a BBH coalescence as the direction of spin of final BH is approximately similar to that of initial total angular momentum.

- *corotating frame:* This coordinate system is important when dealing with precessing BBH. Here we compute corotating angles so that we are in the frame of orbital plane. In this frame, the binary always has aligned spin geometry and hence can be modeled using conventional techniques. When extracting GW from precessing BBH coalescence, we first extract all the modes in these frame. We then switch to either the simulation frame or remnant frame to diagnose the precessing behavior.

The trajectories of configurations of (C-1), (C-2) and (C-3) in the remnant frame are shown in figure 4.4. The plane at z=0 refers for the direction of radiation from GWs. In the case of transition precession (C-3), one can notice the final BH is pointing almost perpendicular to the evolution of orbital angular momentum. Also, notice the "wobbling" of the orbital plane in the z-direction. In descending order, the "wobbling" goes as, (C-2) $>$ (C-3) $>$ (C-1) $\sim$ non-precessing BBH.

This wobbling of the orbits, meaning the precession of orbital angular momentum $\mathbf{L}$ impacts the direction of radiated modes of GWs. If the system is placed at some sky-orientation other than optimal, these wobbling results in changing inclination angle of the system. So when such BBH is merging in the sensitivity band of LIGO, the changing inclination angle impacts the SNR recorded by the detectors.

GW Morphology and Higher Harmonics

Unveiling the coordinate-independent dynamics of a BBH system requires analyzing the gravitational radiation at spatial and temporal infinity. The gravitational radiation from the source (i.e. BBH), is an-isotropic with angular dependence typically recast into spin weighted-2 spherical harmonics, ${}_{-2}Y_{\ell m}(\theta, \phi)$, such that the Weyl scalar ψ_4 is given by equation . In a typical NR simulation, $\psi_4(t, \theta, \phi)$ is extracted at multiple arbitrary radii (dependent on the resolution of computational grid) and then extrapolated to infinity.

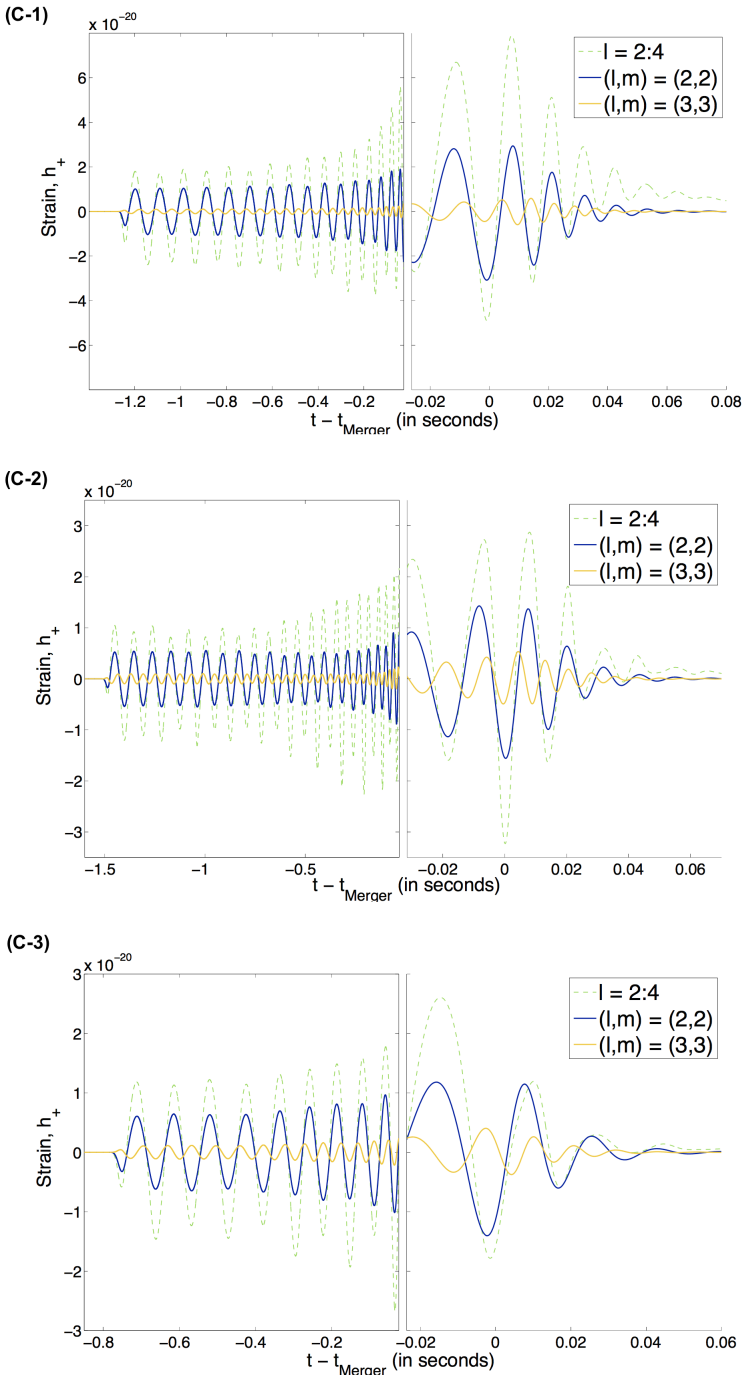

Figure 4.5: **Gravitational-Wave Polarization:** For the BBH source at distance $D = 100$ Mpc, total binary mass $M_{Tot} = 200M_{\odot}$ and sky location face on with LIGO detector, the GW strain of plus-polarization for C-1 (top), C-2 (center), and C-3 (bottom) is showcased for multiple radiated modes: $\ell = 2 : 4, m = -\ell : \ell$ (dashed green), $\ell = 2, m = 2$ (blue), $\ell = 2, m = 2$ (blue), $\ell = 3, m = 3$ (yellow). Note that energy in dominant mode, $\ell = 2, m = \pm 2$ is twice that of shown in $\ell = 2, m = 2$.

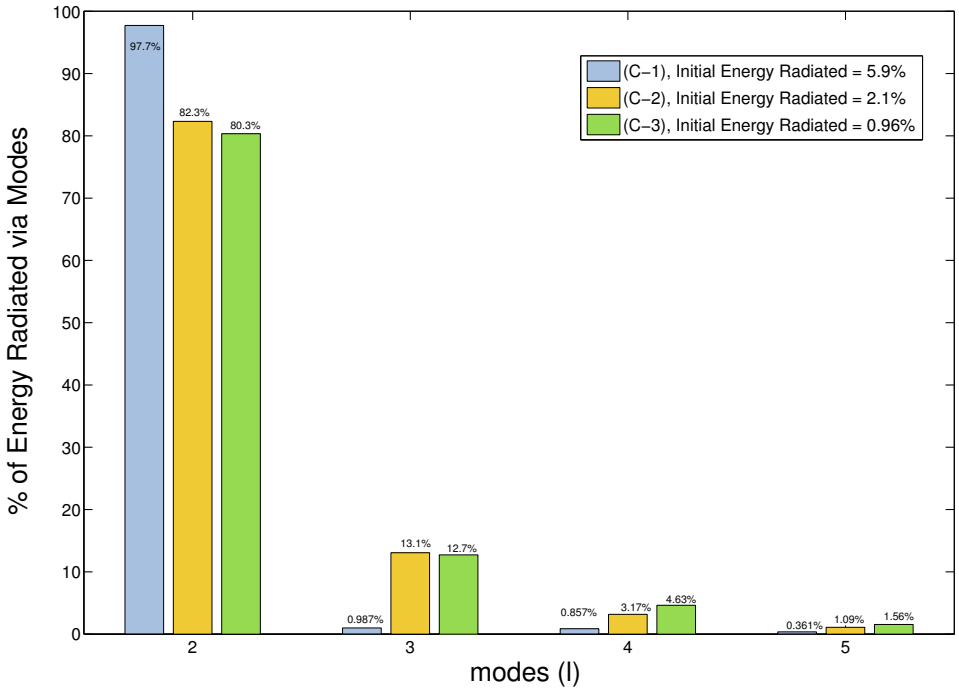

Figure 4.6: **Energy Radiated in dominant modes**: For the test cases (C-1)-blue , (C-2)-yellow, (C-3)-green, the radiated energy in corotating frame is shown for dominant modes $m = \pm\ell$ for $\ell = 2 : 5$. The total radiated energy (stated in legend) is obtained $\sum_{\ell=2}^{6} E_{RAD}(\ell, m)$.

The dominant mode of radiation is $\ell = 2$. For non-precessing systems, the direction of dominant mode $\ell = m = 2$ remains always perpendicular to the orbital plane. With precessing BBH systems the orbital plane is no longer fixed in a plane, complicating the dependence of radiation through ℓ; and, therefore, the direction of the binary in relation to the gravitational-wave detector has more effect.

Work has been carried out [94, 95] to analyze precessing waveform in a less arbitrary frame, the *corotating frame*. The corotating frame follows the direction of dominant radiation, so that BBH configuration mimics a non-precessing configuration. The advantage of such a frame of reference is that the orbital angular momentum of BBH always points at north pole of extraction sphere. Hence, while extracting dominant modes such as $\ell = m = 2$, in corotating frame we get the most accurate value for magnitude of radiated

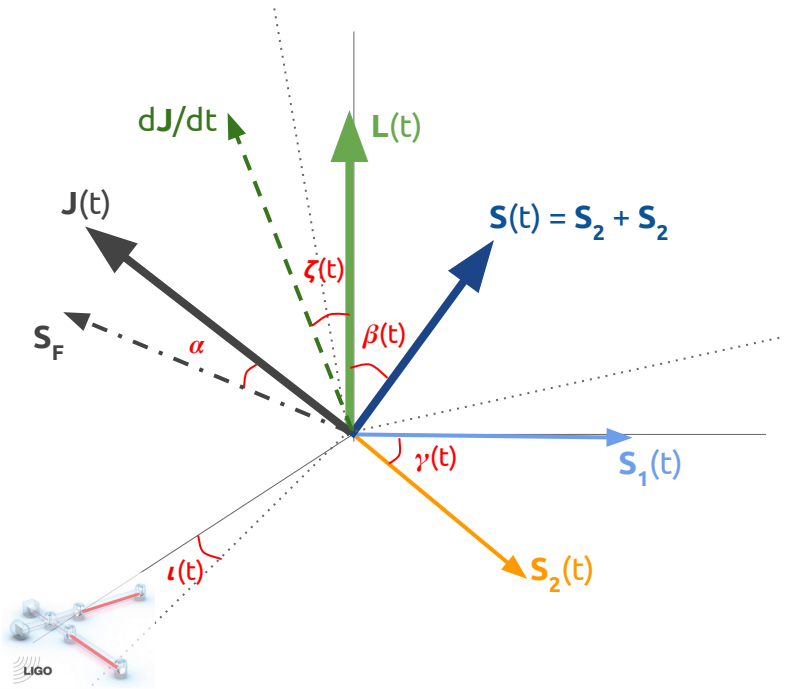

Figure 4.7: Angles between intrinsic parameters of BBH that impact the non-linear behavior and observation of the systems with precessing spins.

quantities such as total-energy radiated, E_{RAD}.

Evolution of Spins and Angular Momentum

In figure 4.5, we show the morphology of GW strain in the simulation frame for the three cases of precession. Each NR simulation is scaled to a physical mass of $200M_{\odot}$. The radiated energy in higher harmonics ($\ell > 2$) gets stronger as (C-3) $>$ (C-2) $>$ (C-1) $\sim$ non-precessing BBH. We also show the distribution of radiated energy for dominant modes in figure 4.6. Notice that in equal-mass precession, over $\sim 98\%$ of radiation is carried in $(\ell, m) = (2, \pm 2)$. However, for cases (C-2) and (C-3), there is a significant increase in energy radiated from $(\ell, m) = (3, \pm 3)$ and $(4, \pm 4)$. Also, notice the total energy emitted in GW is much less in (C-3) and (C-2) compared to (C-1), even though they spent longer time in the inspiral stage, especially (C-2).

4.3 Spin-Orbit Coupling in Non-Linear Regime

With the GW in hand, we can investigate the following questions. How and where did the angular momentum leave the system? How strong was spin-orbit coupling? From the initial data alone, can we predict the final state of simulation, in particular recoil velocity and final spin? For non-precessing system, many of these questions are straightforward to answer as one can ignore spin-orbit coupling. For precessing systems, these same questions are much harder to answer and require additional study. In the context of our three case studies, (C-1), (C-2), and (C-3), we investigate these questions and analyze the various physical quantities stated in figure 4.7.

On an extraction sphere at $r = 75M$ in the default simulation frame we track the following quantities whose unit vectors are labeled in figure 4.8:

- Individual spins: $\mathbf{S_1}(t)$ and $\mathbf{S_2}(t)$
- Total angular momentum:
  $\mathbf{J}(t) = \mathbf{J}(t_0) - \int_{t_0}^{t} \frac{d\mathbf{J}(\tau)}{d\tau} d\tau$
- Orbital angular momentum:
  $\mathbf{L}(t) = \mathbf{J}(t) - \mathbf{S_1}(t) - \mathbf{S_2}(t)$
- Angular momentum radiated: $\frac{d\mathbf{J}(t)}{dt}$
- Total Spin: $\mathbf{S}(t) = \mathbf{S_1}(t) + \mathbf{S_2}(t)$

The quantities $\mathbf{S}$, and consequently $\mathbf{L}$, can be defined only up to the *merger* (in our analysis we set $r = 2M$ as fiducial marker for merger), at that time the individual BHs are lost. The radiated quantity, $d\mathbf{J}/dt$, is extracted through merger until the end of ringdown and hence one can compute $\mathbf{J}(t = \infty) \equiv \mathbf{S_F}$. In all the cases, the loss of total angular momentum from the system is closely aligned with evolution of orbital angular momentum. Except in the case of (C-3), the direction of total angular momentum remain fairly constant.

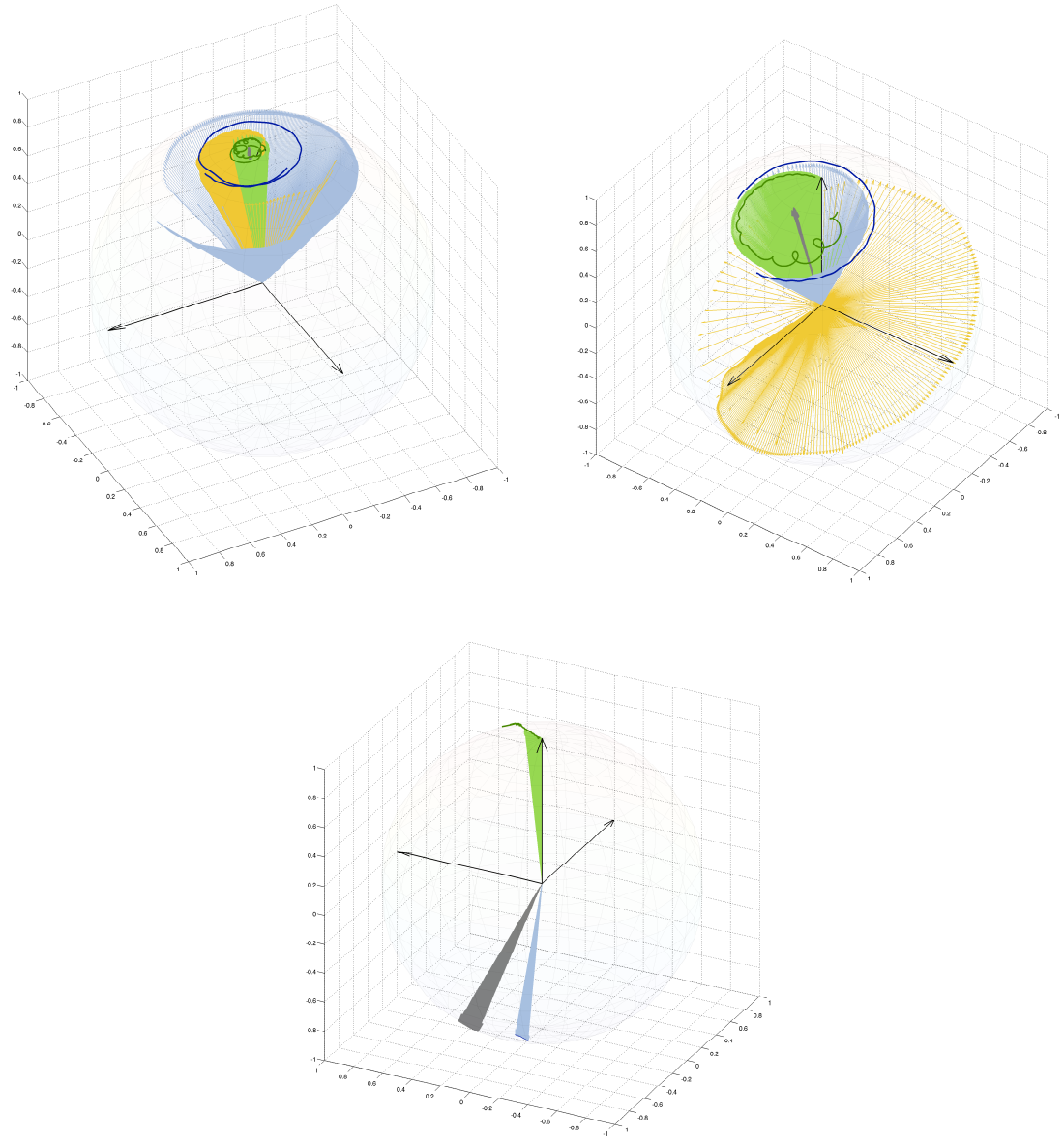

Figure 4.8: **Evolution of Radiated Quantities:** The dynamics of the three cases , C-1 (top-left), C-2 (top-right), and C-3 (bottom), on a particular extraction sphere for $\psi_4(r = 75M)$ is shown. The orbital angular momentum $\mathbf{L}$ (green arrows) and spins $\mathbf{S_1}$, $\mathbf{S_2}$ (blue and yellow vectors) and $\mathbf{S} = \mathbf{S_1} + \mathbf{S_2}$ (blue thick line) are plotted from start of the run (at $D = 10M$) till merger (at $D = 2M$). The total angular momentum $\mathbf{J}$ (grey arrows) and averaged radiated angular momentum $\frac{-d\mathbf{J}}{dt}$ (thick green line) are plotted from the start until the system relaxes to its final BH configuration. Note that the direction of dJ/dt and $L(t)$ remain nearly parallel until merger.

Evolution of Angles

To further analyze precession in the paper, we define *distance (r) dependent* angles (see figure 4.7)

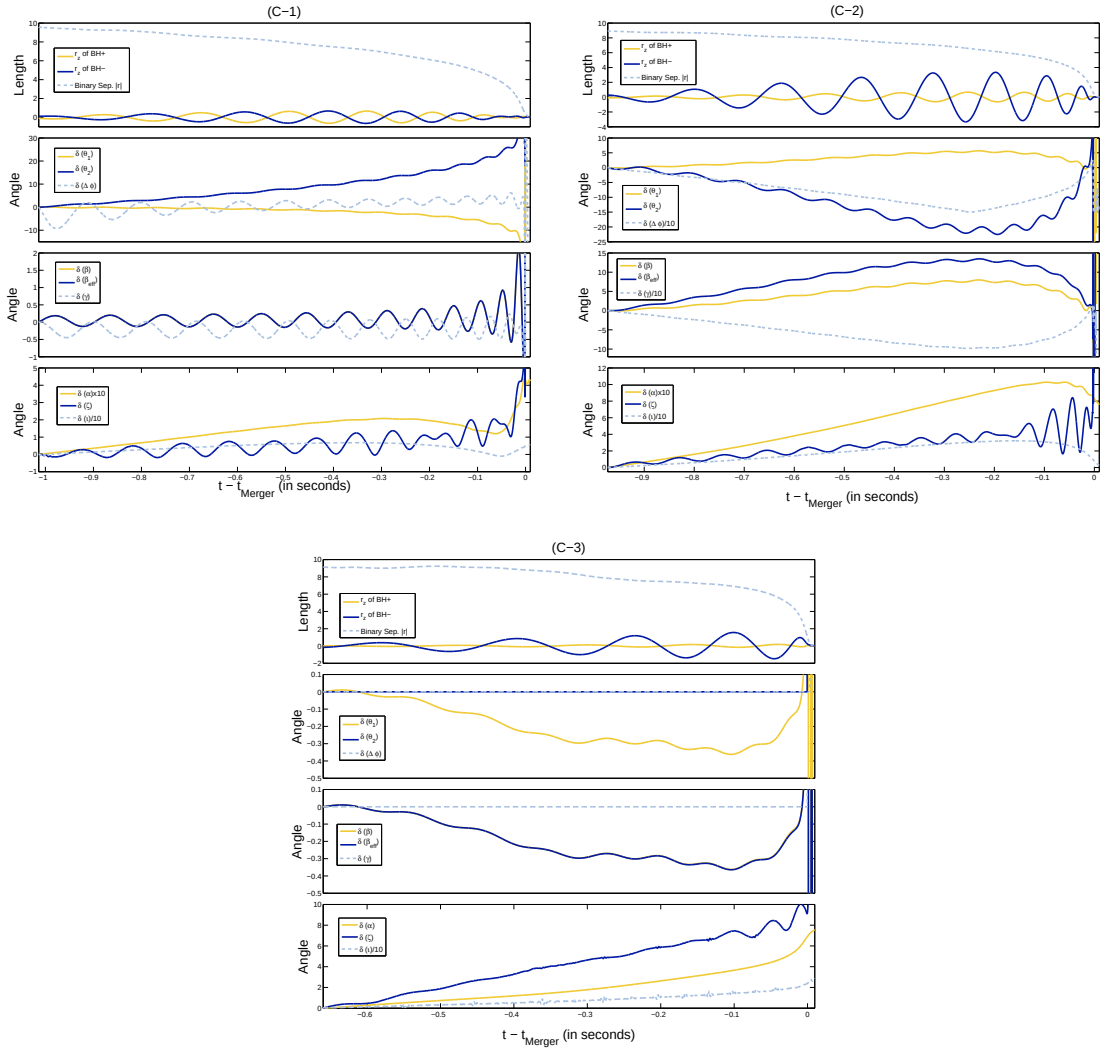

Figure 4.9: For configurations (C-1), (C-2), (C-3), the evolution of angles is stated from the start of the simulation (after first cycle that gets rid of junk radiation) to *merger*. The first row refers to the binary separation, and the z-coordinates of the two BHs. The second row refers to the change in spin geometry angles : $\delta(\theta_1), \delta(\theta_2), \delta(\Delta\phi)$. The third row refers to conservation angles: $\delta(\beta), \delta(\beta_{EF}), \delta(\gamma)$. The fourth row refers to angles that affect detection : $\delta(\iota), \delta(\zeta), \delta(\alpha)$. Notice the varying y-axis scale and scaling of the quantities in the legends of rows 2-4.

- $\alpha(r) \equiv$ Angle between total angular momentum, $\mathbf{J} \equiv \mathbf{L} + \mathbf{S_1} + \mathbf{S_2}$ and final spin $\mathbf{S_F}$ (or final total angular momentum at $r \sim 0$)

- $\beta(r) \equiv$ Angle between orbital angular momentum $\mathbf{L}$ and total spin, $\mathbf{S_{Tot}} = \mathbf{S_1} + \mathbf{S_2}$

- $\beta_{EF}(r) \equiv$ Angle between orbital angular momentum $\mathbf{L}$ and effective spin [96],

$\mathbf{S_{EF}} = (1+q)\mathbf{S_1} + (1+\frac{1}{q})\mathbf{S_2}$

- $\gamma(r) \equiv$ Angle between both the spins $\mathbf{S_1}$ and $\mathbf{S_2}$
- $\zeta(r) \equiv$ Angle between between orbital angular momentum $\mathbf{L}$ and radiated angular momentum $-\dot{\mathbf{J}}$.
- $\iota(r) \equiv$ The change in orbital inclination angle

For our precessing configurations (C-1), (C-2), (C-3), we investigate time evolution of change in precessing angles $\delta(\angle(t)) = \angle(t) - \angle(t_0)$ where $\angle = \theta_1, \theta_2, \Delta\phi, \beta, \beta_{EF}, \gamma, \iota, \zeta, \alpha$. The evolution of these angles are depicted in figure 4.9.

For equal-mass precession case of (C-1) (figure 4.9), $\theta_{1,2}$ diverge as merger approaches but $\Delta\phi$ settles at a constant value prior to merger. The angles γ and β ($= \beta_{EF}$ for $q = 1$), remain fairly well conserved, varying from their mean values by only 0.5° until the last cycle. The angles that impact GW modeling, namely α and ζ, change by a negligible amount of 0.5° and 2°. Although the value of α is fairly small, notice how it rises to a secondary peak before it reaches its maximum value during merger. This indicates the binary had over one cycle of precession before merger of $\mathbf{J}(t)$ around $\mathbf{J}(t=0)$, as seen in the left plot of figure 4.8. The value of orbital inclination, ι, changes by $\sim 10^\circ$ during the coalescence time of this simulation (in physical units corresponds to 1 second for $M_{Tot} = 200 M_\odot$).

For unequal-mass precession case of (C-2), it is interesting to note the direction of spins drastically diverges away from its initial configuration, but the configuration returns to the initial state just before merger. The deviation of spins from orbital angular momentum is proportional to the mass-ratio, $\delta(\theta_1) \sim q\ \delta(\theta_2)$. The deviation of spin-spin coupling, as captured in $\delta(\gamma)$ and $\delta(\Delta\phi)$ is of the order 100°. The spin-orbit coupling, as noted in $\delta(\beta)$ is 6°, while the equivalent conservation quantity from PN equations. $\delta(\beta_{EF})$ deviates 10°. In almost all cases, $\delta(\beta) < \delta(\beta_{EF})$. The behavior of α, ζ and orbital-inclination ι remains same as (C-1), but the effect is scaled by a factor of 5.

For the transitional precession case of (C-3) (figure 4.9), when $|\mathbf{a_2}| = 0$, the only definable angle from the spin geometry is $\theta_1 = \beta = \beta_{EF}$. This angle experiences a negligible change over the course of evolution ($\delta(\beta) \sim 0.4$). The change in orientation of total angular momentum α however is quite substantial (up to $\sim 10^\circ$) compared to the cases (C-1), (C-2). One can also notice there is a monotonic deviation of $-\dot{\mathbf{J}}$ from $\mathbf{L}$ as noted in $\delta(\zeta)$. The change in orbital inclination is about 30°.

4.4 Future Work

As noted in the section so far, these three cases exhibit different dynamics and GW morphology. In this section, we quantify the observational impact of these three cases for a GW detector like LIGO. The work is currently being pursued, and following investigations are being conducted:

- As noted in Chapter 3, the case (C-2) and (C-3) were beyond the parameter space of agreement between NR and approximate models of GWs that only contained dominant modes $(\ell = 2, m = 2)$.

- Recently, a new set of precessing GW models have been developed that contain higher harmonics. We are testing the agreement between these three cases with the new models for a variety of sky-locations and orbital inclinations.

- We are quantifying on whether the disagreement changes dramatically with total-mass of the BBH (as was the behavior reported in Chapter 3).

- Regardless of the disagreement between these cases and approximate models, it is important to note if this system can be recovered in LIGO using the standard machinery of match-filtering search with align-spin templates, as well error in the recovered parameters of the systems.

Chapter 5

APPLICATIONS OF INFORMATION VISUALIZATION TO GENERAL RELATIVITY

5.1 Motivations

The simplest configuration of a two-body problem in General Theory of Relativity is that of BBH that are gravitationally bound with each other. This BBH system radiate information about their initial state ($\Lambda(r)$ represented with 8D parameter space) by emitting gravitational waves, until they reach an equilibrium state of a single, boosted, spinning black hole (Λ_F represented by 5D parameter space). The exact evolution of the BBH systems can be understood only by solving the Einstein Equations - set of 10 highly non-linear, parabolic, partial differential equations - on some of world's fastest supercomputer. Practically, as only a finite number of such simulations can be performed on supercomputers, it is important understand the how BBHs "lose hair" from the pre-merger stage (8D) to the post-merger state (5D).

In this chapter, the author applies techniques from information visualization to find trends in the non-linear dynamics of a binary black hole coalescence. The goal is to extract meaningful features that leads to a deeper understanding of extreme gravity and enhances tools for gravitational wave data analysis. Using the 452 numerical relativity simulations of binary black holes from the Georgia Tech Catalog (Chapter 3), we explore the bulk features between the input and output of these simulations (see figure 5.1 for conceptual overview). This is the first direct application of information visualization to General Relativity.

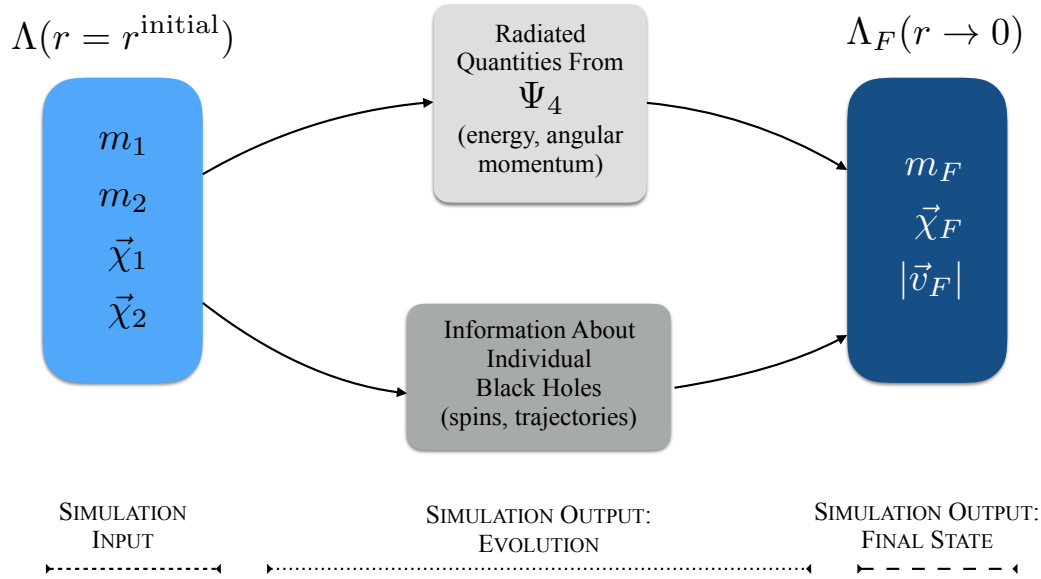

Figure 5.1: Map between input data, ouput and final state for a generic binary black hole simulation in numerical relativity

We begin our investigation by finding patterns between the initial parameters of binary black holes $\Lambda(r)$ and parameters of the remnant black hole Λ_F (section 4.2). We classify in to three cases (i) when both the black holes have no spins (ii) when the spins of black holes are aligned with angular momentum (iii) when black holes have precessing spins.

We extend the studies conducted in chapter 4 for the spin-orbit coupling in the three cases of precessing spin BBHs to an entire library of 350+ precessing-spin simulations from Georgia Tech Catalog. For all these simulations, we compute the deviations of various angles that lead to the complex behavior of precessing BBH. Our preliminary studies find physical quantities that are conserved all the way to the merger stage of binary black hole coalescence, thus providing a new parameter to model gravitational waveforms (section 4.3). The analysis is computed for two classes of precession, (a) when binary black holes have equal mass (b) when binary black holes have unequal masses.

The work is in under preparation to be published.

5.2 Patterns Between Pre- and Post-Merger States of Binary Black Holes

For all the 452 simulations from the Georgia Tech Catalog of BBHs, we create a table with the following columns:

- 8 columns for initial data of our BBH simulation $\Lambda(r = r^{\rm initial})$,
- 5 columns for parameters remnant black hole Λ_F,
- a column for total energy radiated during BBH evolution by using all the modes (ℓ, m) of Ψ_4, and
- a column for total energy radiated through dominant modes $(\ell = 2, m = \pm 2)$

This gives a table with 452×16 entries. Our goal is to find a trends in this table. For this we apply the technique of parallel coordinates. Based on the value of spins of BBHs, we showcase parallel coordinates plots between the entries of table from figure 5.2 to 5.4. The insights we gain from these plots regarding the non-linear dynamics of BBH is mentioned below.

i. Binary Black Holes With No Spin: From the parallel coordinate plot in figure 5.2, we note that with the increase in mass-ratio $q = m_1/m_2$ from 1 to 3 of BBHs, the recoil velocity of the remnant black hole monotonically increases (blue lines). Beyond $q > 3$, the recoil velocity starts to drop (orange lines). A highly unequal BBH system of $q = 10$ has same recoil velocity as an almost equal system $q = 1.5$. This trend is purely a result of non-linear dynamics of binary black holes and cannot have been noted before conducting these simulations. Few more linear trends can be noted between mass-ratio and the spin of the remnant black hole $\chi_F = a_F$. The higher the q, the lower the final spin. Similarly, the fraction of energy emitted in dominant modes drops linearly as we increase q. This effect

signals that beyond mass-ratio 3, we cannot rely on approximate models of gravitational waves that do not incorporate higher harmonics.

ii. Binary Black Holes With Align Spin: Compare to the results we obtain in non-spinning BBHs, we are now adding two more dimensions in our input. We compress the spins into a single dimension parameter space of effective spins ($a_{\mathrm{Eq,z}}$) [1]. Just adding more input axis in the parallel coordinates complicates the trends (see figure 5.3). Few linear trends do glaringly stand out. Such as, with the increase in mass-ratio q the fraction of energy emitted in dominant modes drops linearly. This is interesting as the total-energy radiated depends much strongly on our choice of effective spins. The higher the effective spin, means higher the total angular momentum in the system and this will make BBHs orbit for longer time before merger; therefore more number of GW cycles and ultimately more total-energy is released. The effective spin also has an interesting correlation with the spin of the remnant black holes. Notice, for a particular combination of mass-ratio and low effective spin, we can produce a non-spinning Schwarschild black hole as a remnant (black thick line).

iii. Binary Black Holes With Precessing Spins: Compared to the non-spinning black holes, we have now added 6 more dimensions to the input of our simulations. This is where most of the map between the input and output parameters gets most entangled to find any trends. However, just as was the case in align-spin BBH, we can still compress the precessing sping information in the quantity effective spin. The trends that stand out are the one we already notices in aligned spin case.

[1] sum of the component of spins in the z-direction and weighted by mass-ratio

5.3 Conservative Quantities in Binary Black Holes With Precessing Spins

From all the 350 simulation of BBHs with precessing spins that scattered across the initial parameter space $\Lambda(r)$ in the Georgia Tech Catalog, we intend to find a common link between all of them. We apply the following methodology:

- For each simulation, we compute the evolution of 8 distinct angle that dictate the dynamics of precessing BBHs(described in figure 4.2 and 4.7) .
- We then compute a standard deviation for each of these angles. The only exception being the direction of final spin which is computed at the last iteration of our simulation.
- We divide our parameter space into two categories of initial parameter: simulation with (a) equal-masses, and (b) unequal masses. Within these, we make a further subset based on the azimuthal angle of initial configuration of two spins: $\Delta\Phi = \phi_2 - \phi_1 = 0$ (spins pointing in same direction) and $\Delta\Phi = \pi$ (spins pointing in opposite direction).
- In the parallel coordinate plots shown in figure 5.5 (equal mass BBH) and in figure 5.6 (unequal mass BBH), we exhibit a comparison between the deviation of the 8 distinct angles.

In both figure 5.5 and 5.6, the axes are almost arranged from left to right in the increasing order of their deviations. So the least deviations occurs for the direction of radiation , while the most changes occur in the azimuthal angles $\Delta\Phi$. For an equal-mass BBHs, the orbits do not wobble much ι but in unequal masses deviations can be as high as 20 degrees. The most surprising insights are for the angle between two spins γ. In the case of equal-mass, γ is the most conserved quantity across the evolution, which applies there

is a strong spin-spin coupling even in extreme gravity. While for unequal mass BBHs, the spin-spin coupling does not hold. An other important insight is gained in the spin-orbit coupling, captured by the quantity β (angle between net spin and orbital angular momentum). For both, unequal and equal mass BBHs, β does not deviate beyond 5 degrees.

Therefore, to a good approximation $d\beta/dt \sim 0$ and spin-orbit coupling is conserved in strong gravity regime for BBH regardless of our choice of initial parameters $\Lambda(r)$. For $q = 1$, the quantity $d\gamma/dt \approx 0$ and hence we can conclude a strong spin-spin coupling.

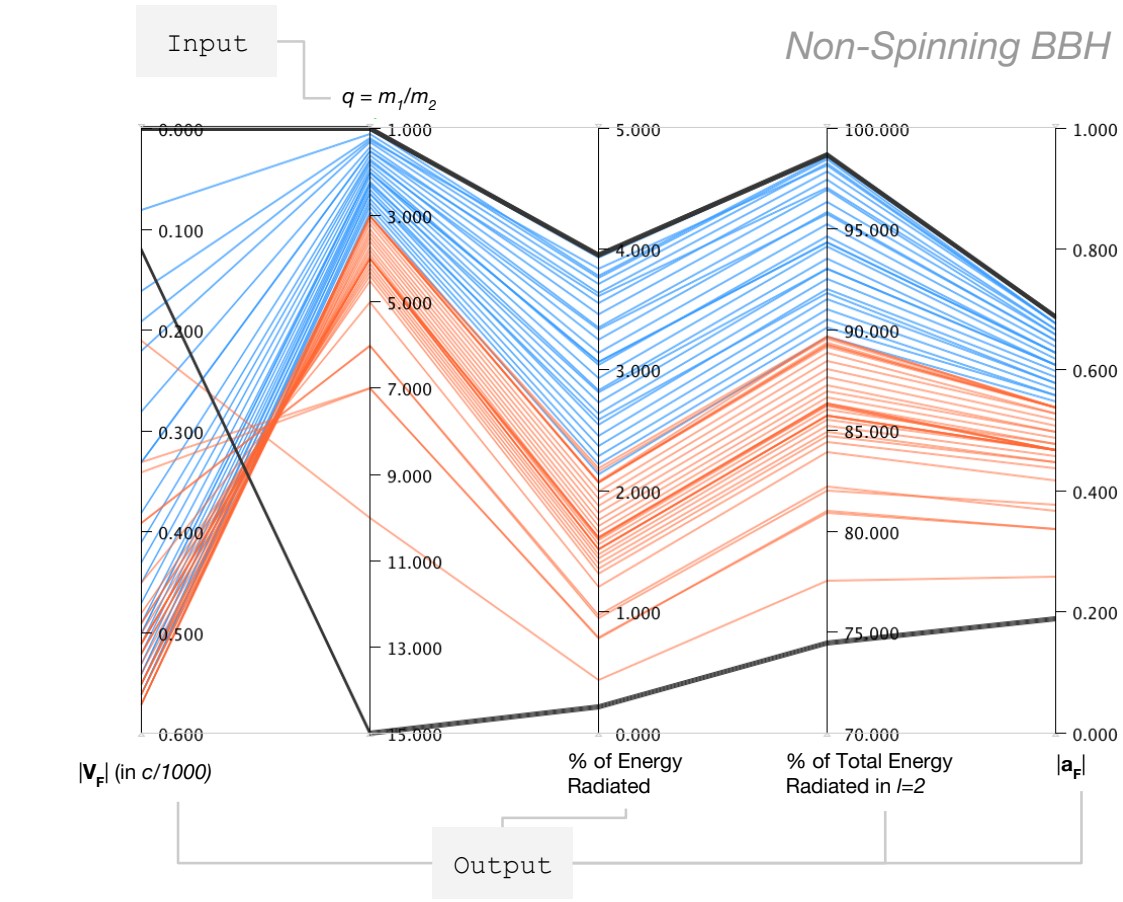

Figure 5.2: Parallel coordinate plot between initial and final values of non-spinning binary black hole simulations. The only input parameter of importance in these simulations is mass-ratio $q = m_1/m_2 \geq 1$ (axis 2 from left). There are four outputs - recoil velocity remnant black hole as a thousandth fraction of speed of light $|v_F|$ (axis-1), energy radiated in all the modes (axis-3), fraction of total energy radiated in dominant modes (axis-4) and final spin of remnant black hole $|a_F|$ (axis-5). The two thick black lines refer to our limits on q. The color refer to the correlation between q and $|v_F|$

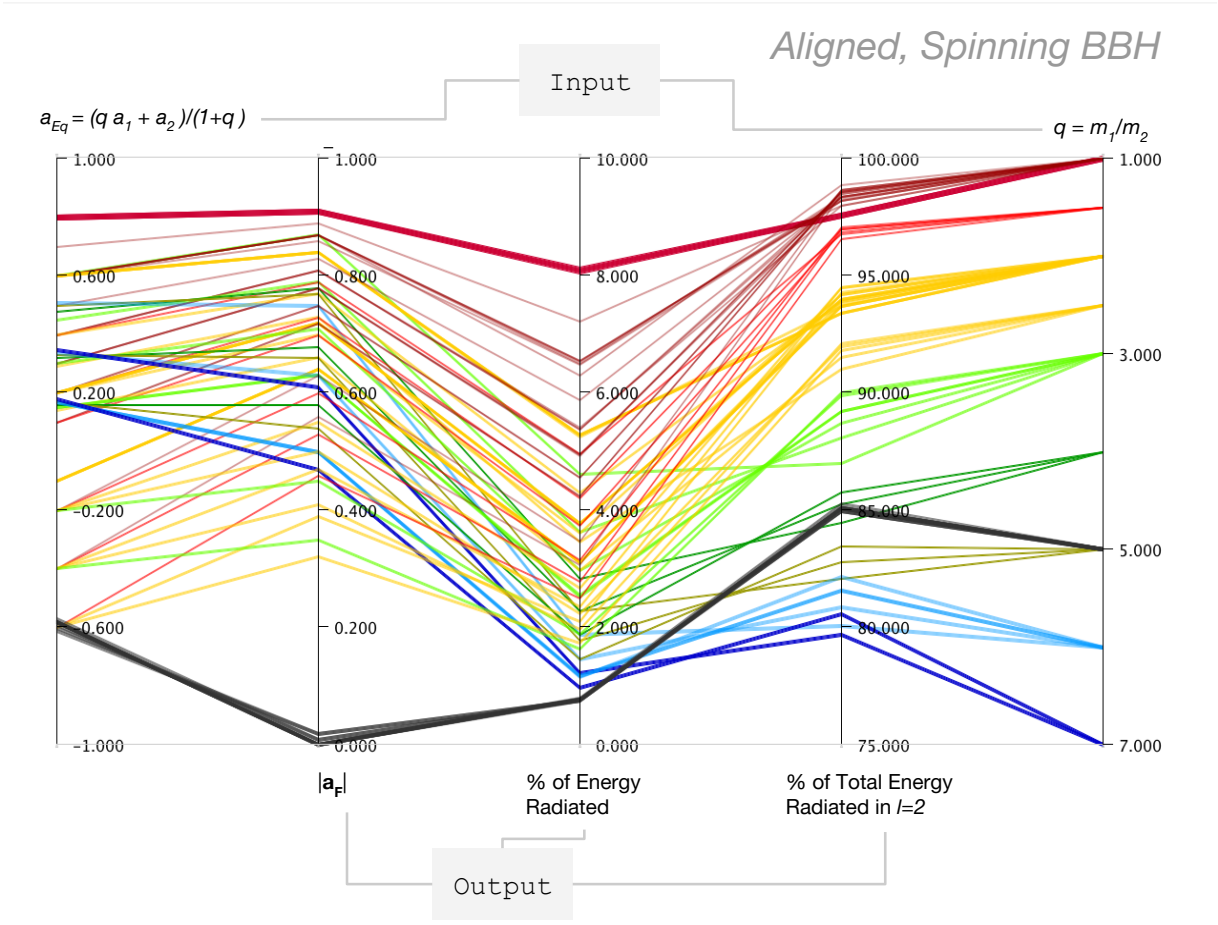

Figure 5.3: Parallel coordinate plot between initial and final values of aligned-spinning binary black hole simulations. The input parameter of these simulations are the effective spins $a_{\rm Eq}$ (axis 1) and mass-ratios $q = m_1/m_2 \geq 1$ (axis 5 from left). There are three outputs - energy radiated in all the modes (axis-3), fraction of total energy radiated in dominant modes (axis-4) and final spin of remnant black hole $|a_F|$ (axis-2). The two thick lines refer to our limits on final spins in these set of simulations. The color refer to the value of mass-ratio q.

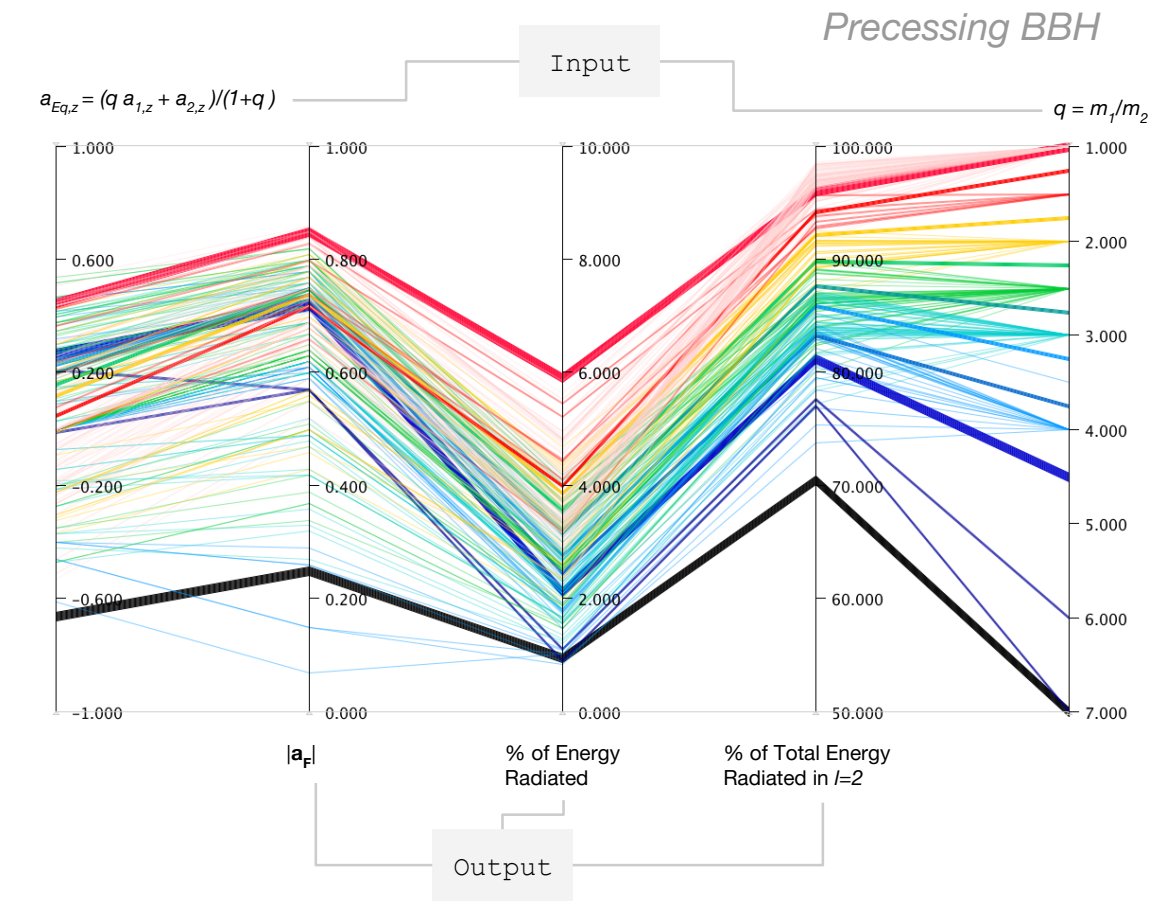

Figure 5.4: Parallel coordinate plot between initial and final values of precessing-spins binary black hole simulations. The input parameter of these simulations are the effective spins $a_{\rm Eq}$ (axis 1) and mass-ratios $q = m_1/m_2 \geq 1$ (axis 5 from left). There are three outputs - energy radiated in all the modes (axis-3), fraction of total energy radiated in dominant modes (axis-4) and final spin of remnant black hole $|a_F|$ (axis-2). The two thick lines refer to our limits on radiated energy from these set of simulations. The color refer to the value of mass-ratio q.

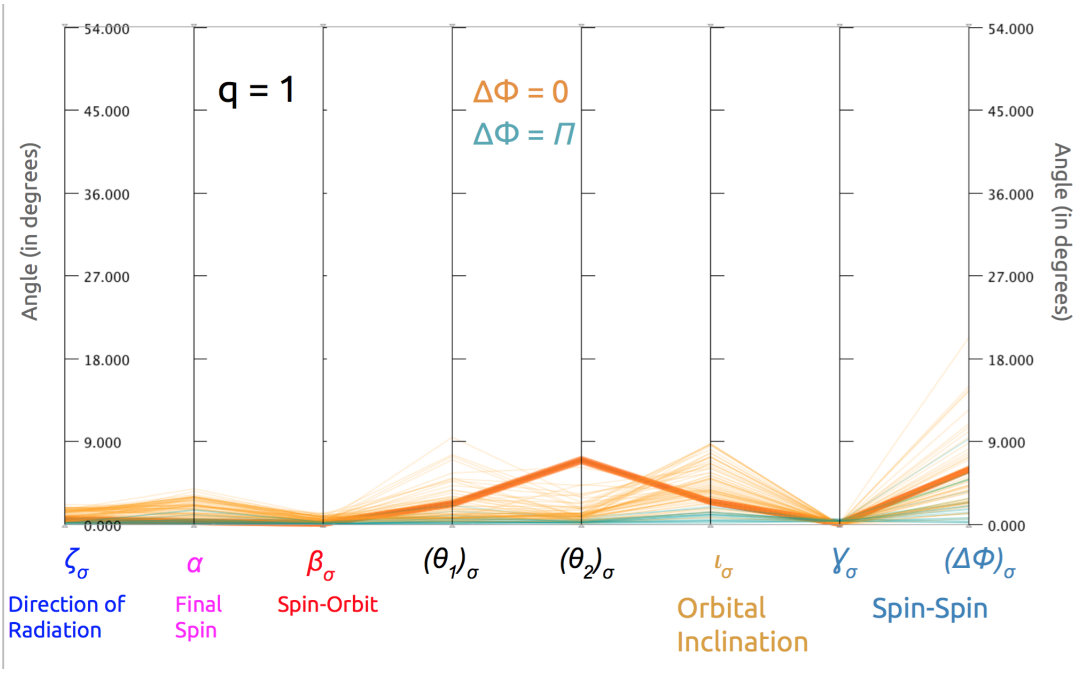

Figure 5.5: Parallel coordinate for the standard deviation of the evolution of 8 distinct angles that govern dynamics of an equal mass, precessing spins binary black holes. The colors refer to the azimuthal angles between the spins at the start of the simulation.

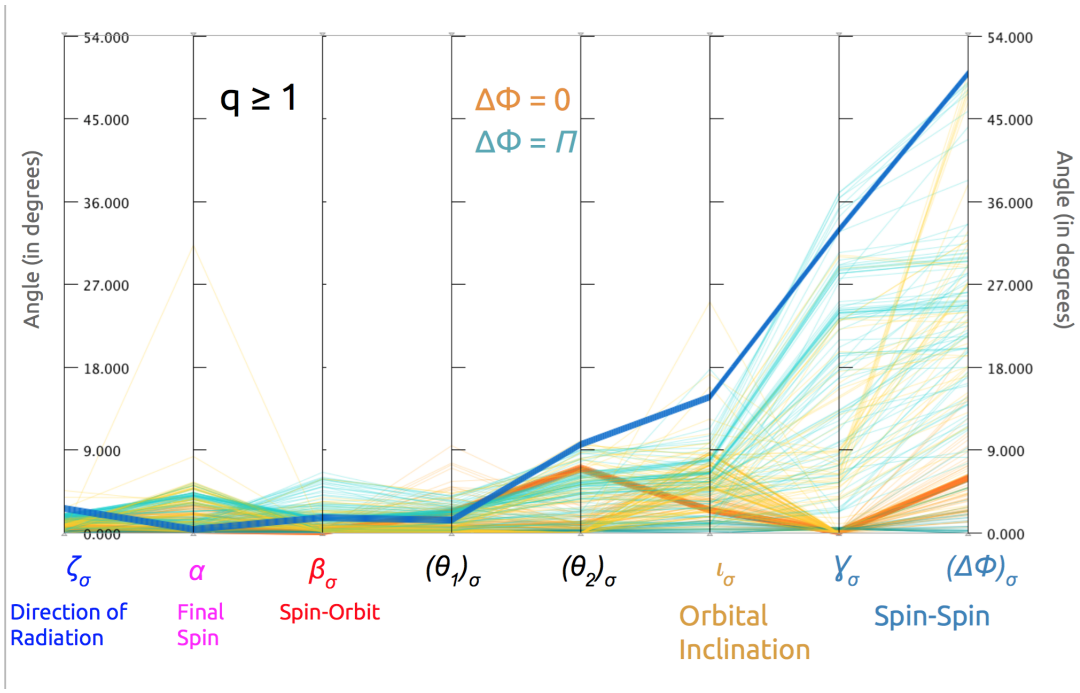

Figure 5.6: Parallel coordinate for the standard deviation of the evolution of 8 distinct angles that govern dynamics of an unequal mass, precessing spins binary black holes. The colors refer to the azimuthal angles between the spins at the start of the simulation.

PART II

BINARY BLACK HOLES IN LIGO

Chapter 6

TRANSIENT BURST SEARCH OF BINARY BLACK HOLES IN LIGO

Overview

This chapter demonstrates the search for transient gravitational wave burst from a binary black hole merger that the author conducted in the two LIGO detectors (see figure 6.3 for a conceptual overview). In section 6.1, we lists the differences between this approach compared to the conventional matched-filtering searches of gravitational waves from compact binary coalescence. This thesis utilizes the COHERENT WAVE BURST (CWB) algorithm [42], which can search for a generic transient burst of gravitational waves, independent of its astrophysical source (section 6.3). By using the data from the the first science observation run of Advanced LIGO (September 2015 - January 2016), the author designed a special configuration of CWB, optimized to search for binary black hole system of total mass $\geq 50M_{\odot}$. The impact of this special configuration in reducing the background rate of noise events from the LIGO data is narrated in section 6.4. We then describe the steps to compute the sensitive volume of our search to detect a binary black hole systems with 90% confidence (section 6.5). The entire process described in this chapter constitutes of what is called the'closed-box studies', i.e. we have not looked at the coincident data from two LIGO detectors to determine if a true binary

black hole merger is measured.

In Chapter 7, we utilize this special configuration in determining our readiness and threshold to detect binary black hole merger for varying intrinsic parameters (masses, spins). In Chapters 8 and 9, we discuss the 'open-box results' from the first science run of LIGO, i.e. the binary black holes of astrophysical origins we did and didn't detect using the search described in this chapter.

All the statements made here are in author's personal capacity and not an official statement on the search result from the LIGO Scientific Collaboration and Virgo Collaboration.

6.1 Binary Black Hole Searches in LIGO

Based on the intrinsic parameters of BBH (masses, spins), the LIGO detectors will either measure all four stages of coalescence (early to late inpiral, merger and ringdown) or just the merger. We exhibit few such cases for the design sensitivity of LIGO detectors in figure 6.2. Also, the maximum energy in BBH coalescence is released during the merger of two black holes. Thus, based on the corresponding GW frequency for BBH merger, we can get an order of estimate on the range of total-mass of BBH that our searches are sensitive in LIGO. Notice, that **all BBH mergers of interest to our search have merger frequency less than $\sim$500 Hz**.

There are broadly two classes of techniques to detect GWs from a binary black hole coalescence in a network on GW experiments.

I. **Modeled, Matched-Filtering Search:** In this case, you start with a large pool of GW morphology that correspond to variety of intrinsic parameters of a BBH coalescence. Then, you try to find a point in your bank/pool that provides a maximum match with a coincident chunk of time in the LIGO data from both the detectors.

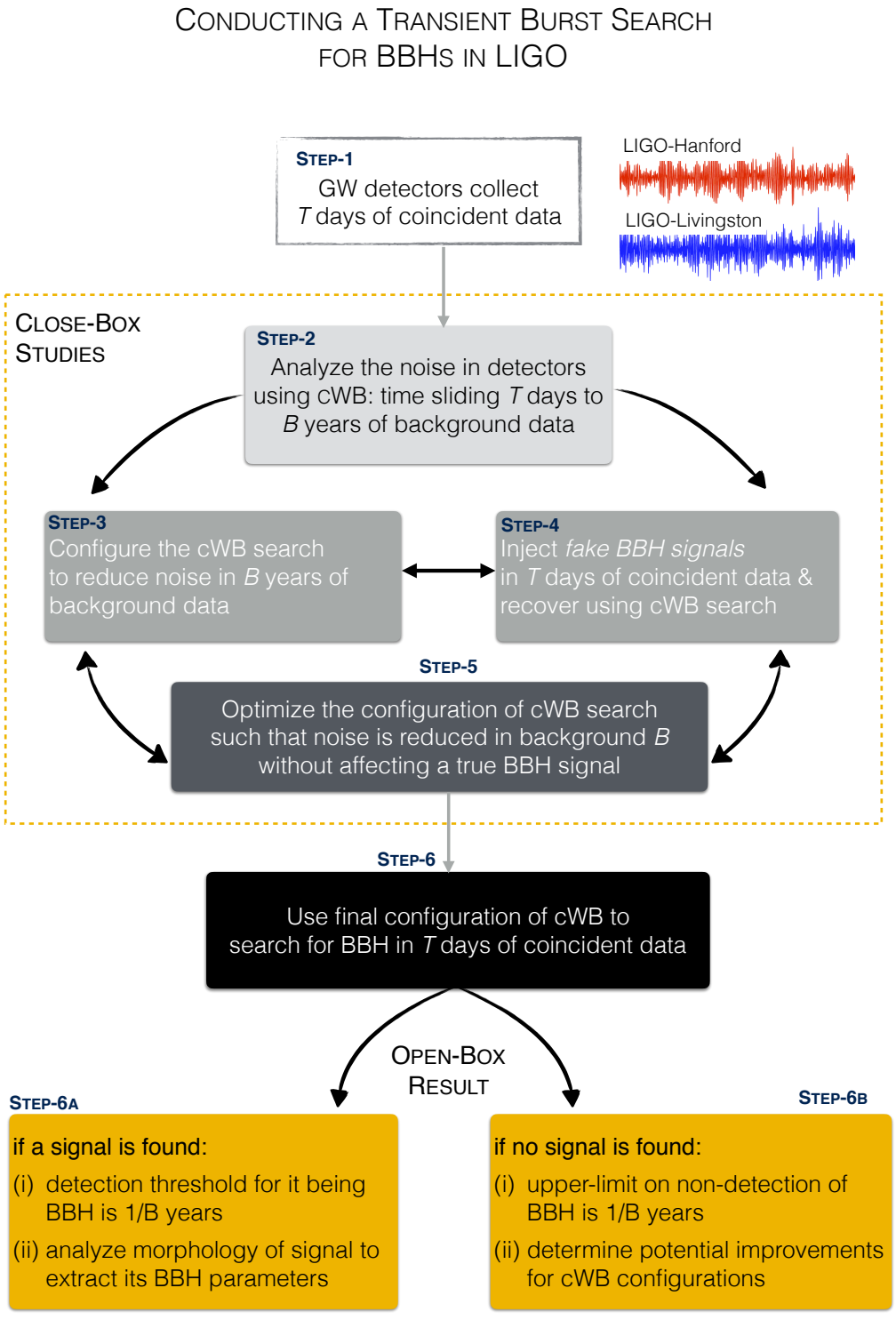

Figure 6.1: Steps involved in conducting a transient gravitational wave search for binary black hole merger

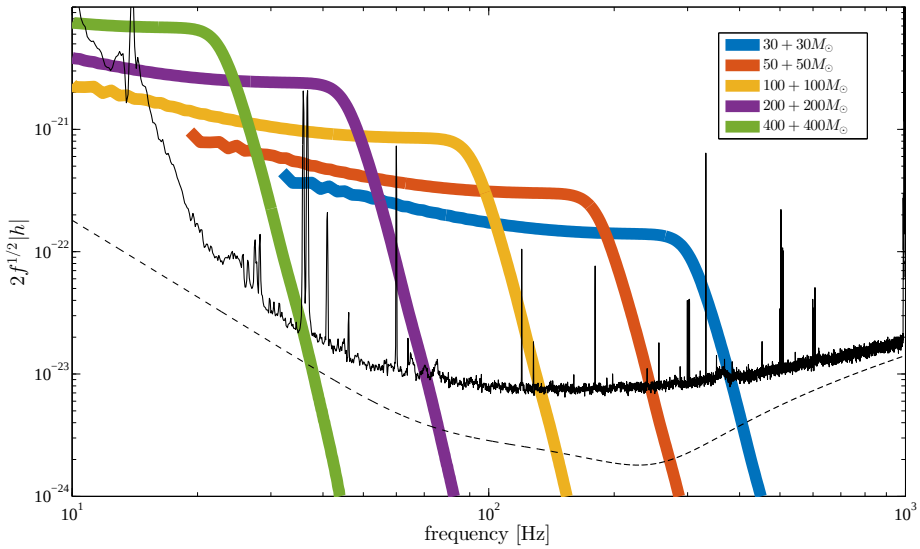

Figure 6.2: Fourier frequencies of an binary black hole waveform of different total masses. The two black holes are non-spinning and of equal masses. Binary is placed at an optimal orientation and at a distance of 1 Gpc. The BBH waveform is obtained from the Georgia Tech Numerical Relativity catalog. The noise curves refer to the sensitivity of Advanced LIGO during first observation run (black line), and for its design stage (dashed lines).

II. **Unmodeled, Transient Burst Search:** In this case, you look for an excess of power that is coherently measured in both the LIGO detectors. Here, there is no assumption whether the access power is a from a binary black hole or a supernova or a random person is vandalizing both the LIGO detector with a tiny needle, at the same instance of time of a millisecond accuracy.

By construct, method-I is more efficient in looking for BBHs as, *a priori*, it assumes to know the morphology of signal it is in hunting for. However, as we noted in chapter-3 that there are parts of BBH parameter space which can be modeled only by conducting NR simulations of BBHs. A typical template bank in matched filtering search for GWs require $\sim 250,00$ distinct points scattered across the BBH parameter space. For obvious reasons we cannot conduct NR simulations for all those points, the matched-filtering searches are fundamentally constrained to a limited parts of BBH parameter space where approximate models of GWs can be trusted. An astrophysical BBH with parameters that cannot be

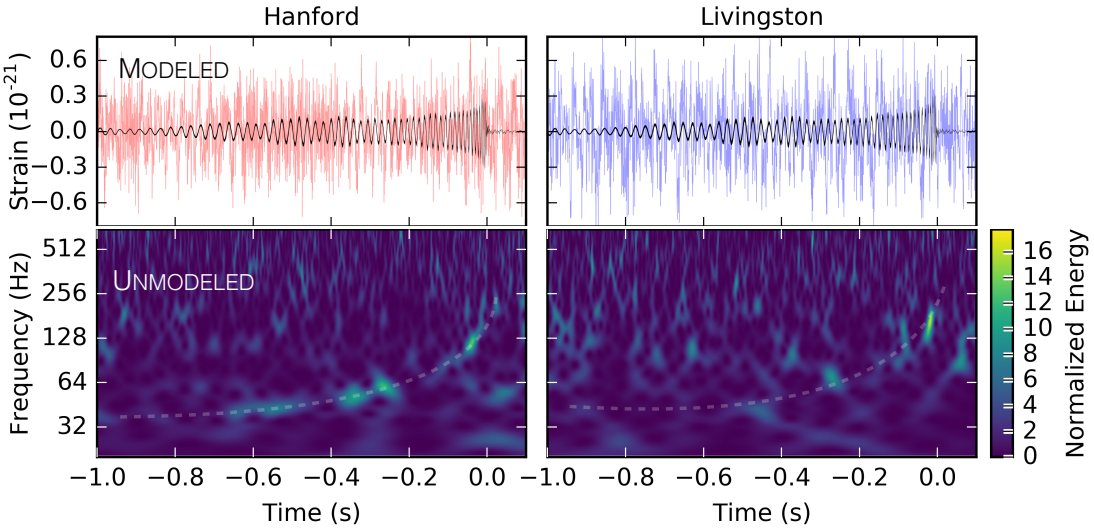

Figure 6.3: Difference between a modeled and unmodeled search of gravitational waves from binary black holes merger. Image credit: [97]

modeled will thus be completely missed by such modeled searches. This is where we find the science case for unmodeled, transient burst search of BBH.

As we describe in this chapter, method-II can be optimized such that it is more sensitive towards a BBH merger compared to other generic transient bursts. Even in the parameter space where one can accurately model GWs, the transient search is as likely, or in cases more likely, to pick up a true GW signal for a massive BBH than method-I. At a conceptual level, this has to do with method-I being better at differentiating background noise from a short-duration GW signal [98]. A sketch on sensitivity of both methods for different total-mass of BBH is shown in figure 6.4.

Currently in LIGO, there are three distinct transient burst algorithms [99], and two matched-filtering algorithms [44] that hunt for GWs from BBH mergers. In this thesis, we focus only on one of these algorithms, COHERENT WAVE BURST, which was also the first to detect GW150914.

The transient burst search of BBH, like most other GW searches, is efficient only when both the LIGO detectors are observing at the same instance, i.e. it requires *coincident detection*. As the environmental and instrumental conditions at each LIGO site dictates the

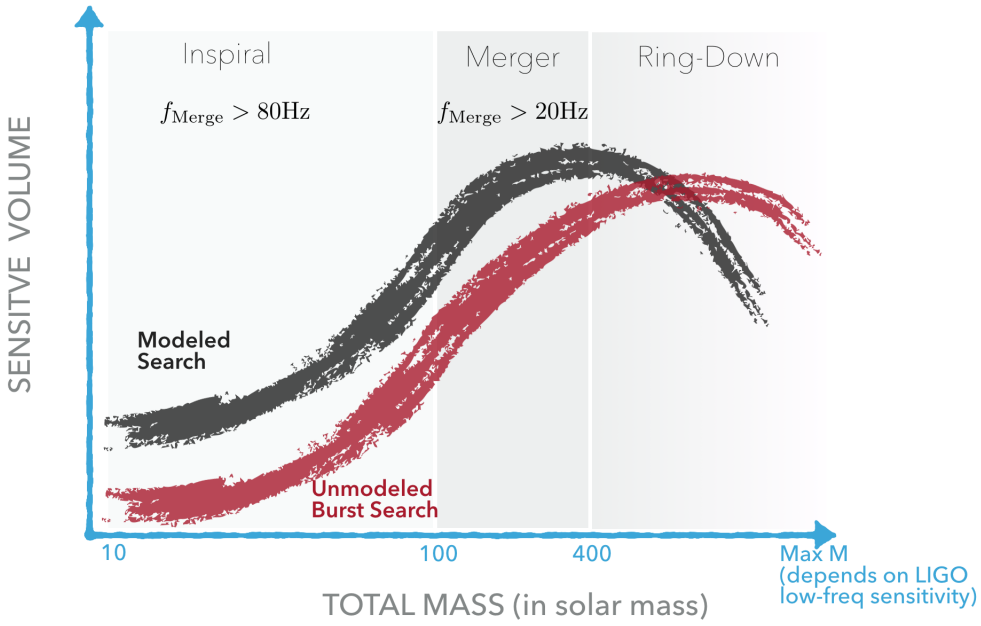

Figure 6.4: A heuristic sketch of binary black hole sensitivity for matched-filtering vs. transient burst search in a LIGO-like experiment. At higher total-mass, only the merger and ringdown signal is within the sensitivity band.

observation time, the coincident time between two detectors in only a fraction of the over all time it is up and running. In context of this thesis, we focus our analysis on the inaugural observation period of the upgraded Advanced LIGO detectors.

6.2 First Science Observation Run of Advanced LIGO

After 5 years of upgrade, the two Advanced LIGO detectors in Hanford and Livingston begun their collection of scientific data, referred formally as the First Observation Run (O1), between September 14, 2015 to January 19, 2016. Out of these 128 calendar dates, the two detectors had a total coincident data collection of 51.3 days.

The LIGO data refers to the measurement of strain, $\delta L/L$, at both the Hanford and Livingston sites. The structure of the LIGO data is thus simply two columns: the GPS time and the corresponding strain at that instance. We have such time series for each of the two LIGO detectors. The GW frequencies that the LIGO detectors in were sensitive during O1

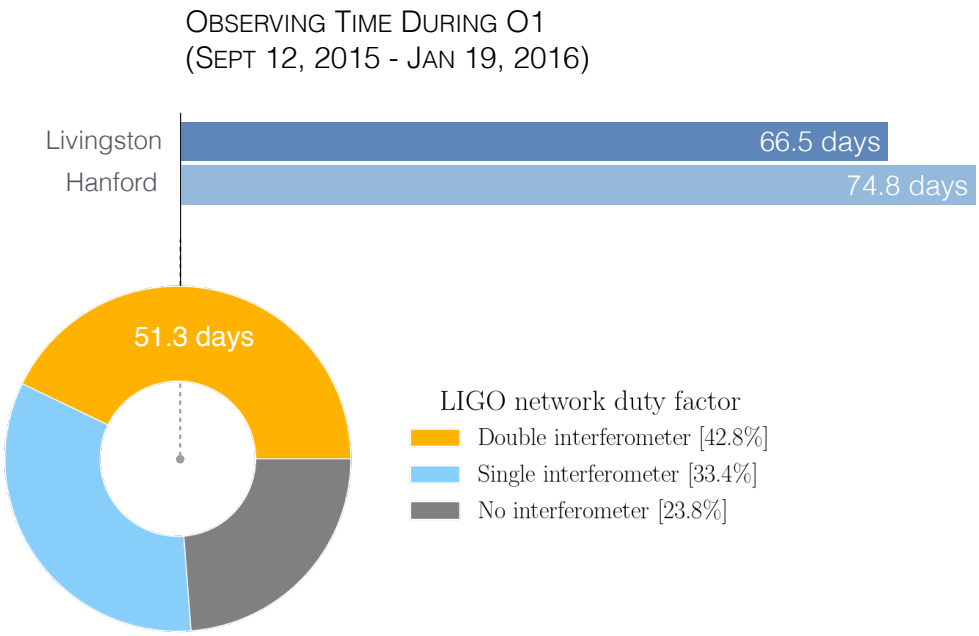

Figure 6.5: Total observation time in during the first science run of Advanced LIGO. Pie-chart obtained from the online summary pages of LIGO detector characterization studies.

to ranged between $16 \sim 2000$ Hz.

Within the LIGO detector, there are about 100,000 monitors tracking different environmental and instrumental sources of noise that couple with data. Based on the information from these monitors, we articulately remove chunks of data that are corrupted by know source of loud noises (usually referred as *glitches*). At the end of this exercise, the final observational data we utilized in our transient burst search was of $\mathbf{T} = \mathbf{44.8}$ days. Figure 6.5 summarizes the calculations for total observation time.

6.3 Overview of Coherent Wave Burst Algorithm

The basic idea of the Coherent Wave Burst (cWB) algorithm is to (I) convert the data from individual GW detectors into a time-frequency power map (II) look for a *coherent signal* which is present in both the detectors and that it stands out against a threshold of background noise in the data (III) reconstruct the morphology of signal and output relevant

parameters to aid GW data analysis. There are two class of cWB searches:

A. *online (or low-latency)*, which can detect GW signal within minutes after it is recorded in LIGO detectors. This is uitlized in sending information about the signal to the astronomy partners so they can look for electromagnetic counterpart of GW detectors.

B. *offline*, which provides the higher significance of a GW signal in data that may or may not have detected priory by online search.

In the context of this thesis, the cWB algorithm is configured for an offline search for BBH signal in a coincident data from network of LIGO detectors at Hanford and Livingston.

6.3.1 Input and Output

cWB Inputs . The primary input is the data of strain from both the LIGO detectors. At an intermediate stage, one can include further details regarding the data quality. Also, we need to define configuration of our search, i.e. tuning based on noise in the data and the type of signal we are looking at. The configuration utilized for BBH search is provided in next subsection.

cWB Outputs . If a coherent signal is found in the LIGO data, the algorithm will (a) construct time-frequency map, (b) reconstruct the morphology of GW signal (c) estimate the location of this signal in sky (important for electromagnetic follow up of the potential detection) (d) measure the likelihood (signal-to-noise ratio) (e) chirp-mass of the signal (this is most relevant to know whether signal is BBH or a black hole-neutron star). For the online searches of cWB, within few minutes it summarized all these outputs on a web-page (called Coherent Event Display. In figure 6.6, we showcase the outputs of cWB for GW150914 obtained from offline search of BBH.

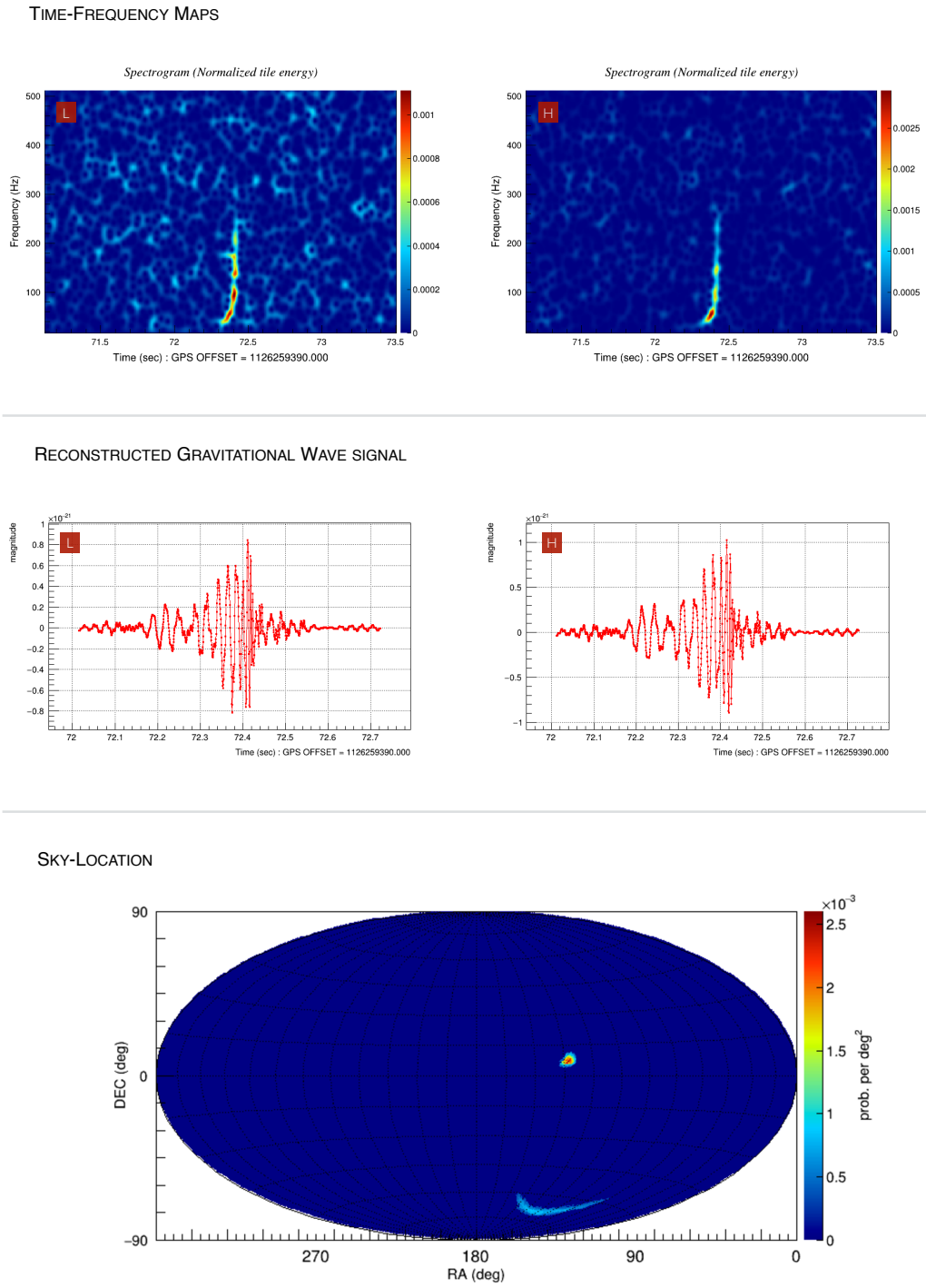

Figure 6.6: Output of cWB for GW150914 with the search configuration defined in this chapter. 'L' and 'H' refer to output specific to the two LIGO detectors. Images obtained from the report page generated by cWB algorithm.

6.3.2 Search Configurations

Our goal is to configure cWB algorithm such that it is robust to detect BBH mergers of $50\ M_{\odot}$. Thus, we tune the algorithm to (a) pick coherent signals of expected behaviors from BBH coalescence, and (b) separate the signal from background noise. Broadly, stage-a is called production cuts (i.e, we apply this as our initial input), and stage-b is defined as post-production cuts (i.e, we apply at an intermediate stage of the analysis as it involves some level of trial-error).

Beyond the default production and post-productions cuts that are included in cWB algorithm, for our transient search of BBH of total mass $\geq 50M_{\odot}$, we apply the following noteworthy changes:

Production Cuts .

i. *Frequency Range:* We limit our search for coherent signal only within this range of frequencies between **16-512 Hz** in LIGO data. We do not expect to detect BBH mergers in the current sensitivity of LIGO beyond these frequencies.

ii. *Polarization Constraints:* We look for coherent signals whose GW polarization obeys chirality. A GW from BBH coalescence have a fixed phase difference between the two polarization.

iii. *Frequency Resolution:* The lowest frequency we can resolve is within the bin of 2Hz. We avoid further scaling down of resolution, as otherwise our background noise will be dominated by the large population os low frequency (¡30 Hz) glitches from LIGO data.

Post-Production Cuts .

iv. *Blip Glitches:* We apply a cut to remove the blip glitches that tend to notice in LIGO data above 60 Hz. The cause of these glitches is rather unknown.

v. *Line Glitches:* We apply a cut to remove the line glitches that are noticed in LIGO data around 60 Hz.

vi. *Chirp Morphology:* We apply a cut to keep only those signals where we can notice a chirpy behavior in reconstructed signal.

vi. *Central frequency:* We apply a further scale down our on frequency range, such that the frequency corresponding to BBH merger is within the range of $24 - 256$ Hz. This means a ringdown can continue beyond the 256 Hz and still be detectable by cWB.

6.4 Estimating Background Rate of Noise Events in LIGO

The coincident LIGO data that we use in our final analysis has been cleaned through most identifiable glitches. However, there still a background residual of noise events of unknown sources, which has *a random chance* to affect our GW search for BBH. So, the most important stage of our analysis relies in quantifying the *probability* of the background noise that limit our transient burst search for BBH. From a statistical terminology, this is the procedure to compute the False Alarm Rate (FAR) of BBH detection.
In the `cWB` infrastructure, we do this in four steps:

i. **Non-Zero Lag:** By utilizing the two $\mathbf{T = 46.3}$ days of data stream from O1, corresponding to LIGO Hanford and Livingston sites, we artificially time-shift to create a coincident data of $B \approx 1,100$ years. A schematic diagram of this procedure is shown in fig 6.7. The time-shift is done such that none of the original coincident GPS times are matched together. This 1,100 years of artificial coincident data is now our background residual to estimate noise.

ii. **Event Trigger Generation (Production Cuts):** Based on our choice of configurations (see section 6.3 - production cuts), we find event that are coherent in our 1,100 years of background. A coherent event in this background will, by design,

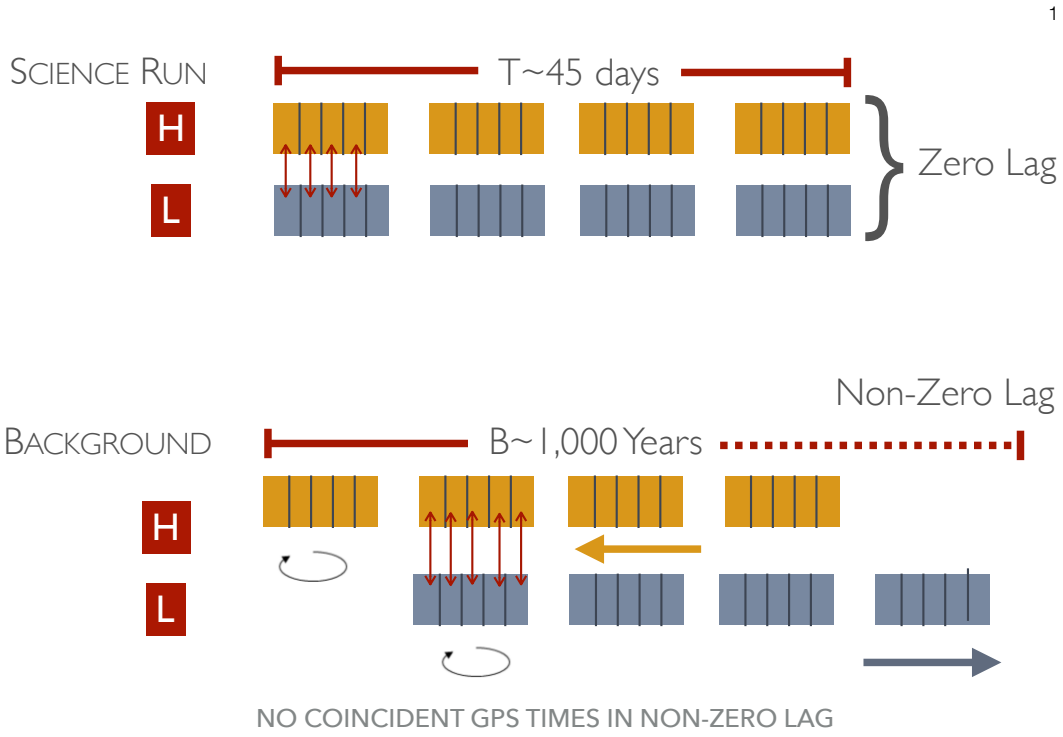

Figure 6.7: A representative diagram for generating artificial time shifting in cWB algorithm. Zero-lag is the coincident data $T = 44.8$ days during O1. Non-zero lag is the artificial time-shifting to generate a background of $B = 1,100$ years using coincident data of length T. A true gravitational wave signal lies in zero-lag, while non-zero lag is used for estimating rate of background noise.

refer to separate GPS times in both the LIGO detectors. But this provides us with a true representation of noise occurring in the LIGO detector that has a probability of occurring coincidentally and being identified as a GW candidate by our search. In figure 6.8 (top-left plot), we show the distribution of such coherent events found in our background noise as a function of the GPS time in Livingston for the entire O1. The center-left plot of figure 6.8 shows the same distribution as a function of frequency. Notice, the glitches are of SNR $= 2 \times \rho \sim 80$.

iii. **Classifying Coherent Triggers (Post-Production Cuts):** As it is clear from the distribution of coherent events (figure 6.8 left column), we need to remove the very loud events that are corrupting our background at different instances and

frequencies. However, we simply cannot put an arbitrary post-production cuts based on frequencies and SNR, as we risk removing a true BBH signal from our T days of coincident data. This last step may demands us to to further tune our post-production cuts based on the BBH signal are intending to detect. This is the topic of next section.

iv. **Computing False Alarm Rate:** In GW searches, FAR defines the statistical significance of a detection (the requires standard is $> 4\sigma$.) This quantity is dependent on the strength of the signal, i.e. if a GW signal is low of SNR, it will look more like the background. If a signal is of SNR higher than the background, the probability of it being a coincident glitch gets lower. The lower limit of SNR at which we can distinguish the signal from background is decided by strength of our production and post production cuts. We typically quote the Inverse of FAR (iFAR) in the units of seconds or years. Our improvement in iFAR from from the production and post-production cuts is demonstrated in bottom panel of figure 6.8. Notice, the cleaning of background glitches has improve our significance to detect a BBH signal of $\rho = 8$ (SNR=16) by iFAR of month to 1,000 years.

6.5 Impact of Background Noise on Binary Black Hole Search

Ideally, we want to configure cWB such that we reduce all the background noise and yet do not lower our sensitivity to detect binary black holes. However, the instrumental glitches (example blip glitches) have morphology very close to a binary black hole merger with anti-align spins (see figure 6.9). Therefore, we have to artfully decide our post-production cuts.

In this section, we demonstrate the effect of our post-production cuts on our threshold to detect a generic BBH signal (masses, spins). We do this in three steps - injecting simulated BBH waveform, recovering them using the cWB algorithm configured for transient burst search of BBH and computing an average volume and distance to which we can detect

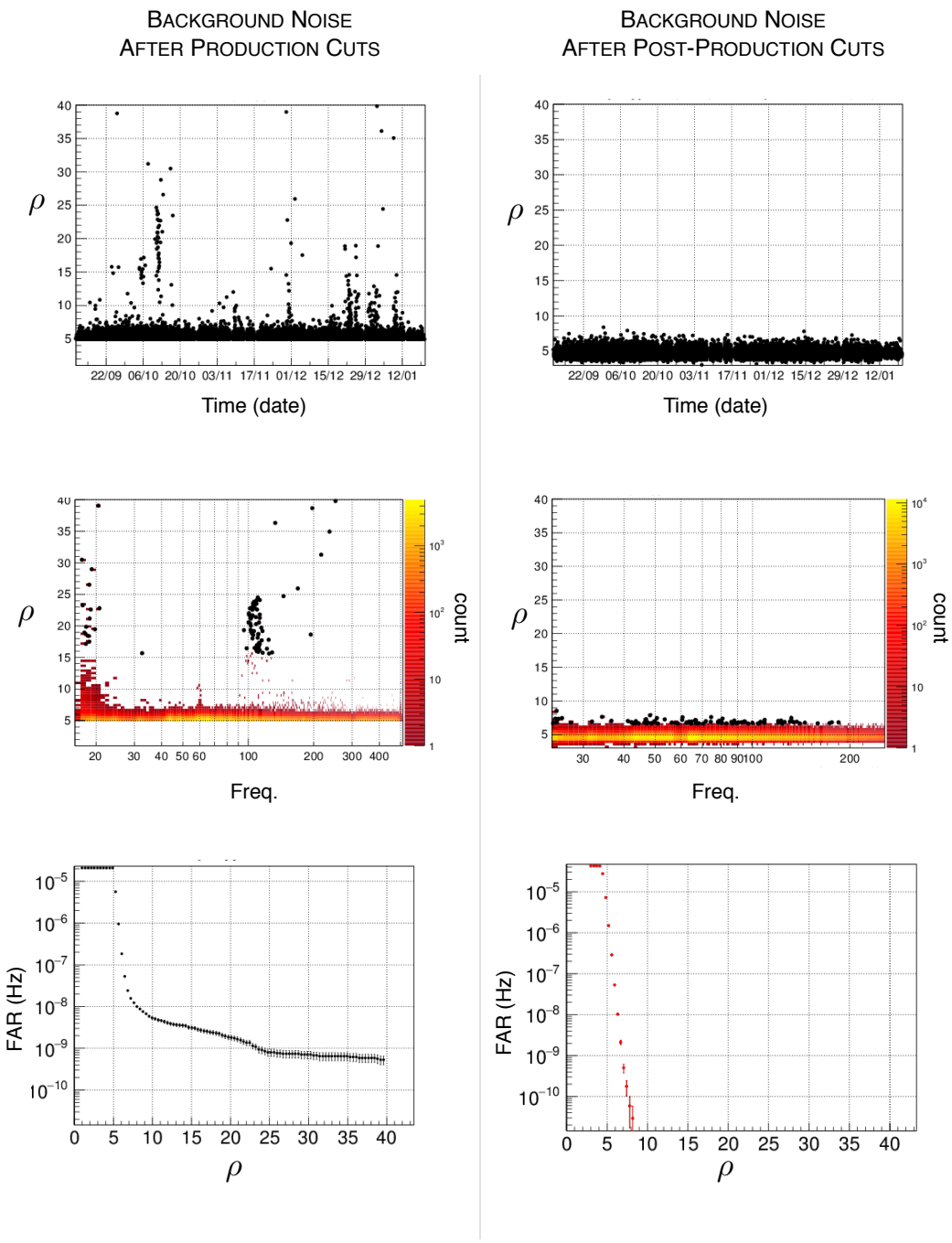

Figure 6.8: Estimating rate of background noise in O1. The left column refers to quality of 1,100 years of background after applying production cuts, while right column is the background after post-production cuts. Both these cuts are mentioned in section 6.3.2. The first row is a measure of ρ (half of SNR) of glitches as a function of GPS time in Livingston. The second row is ρ vs. the frequency range. The third row represents the False Alarm Rate as function of ρ. Images obtained from the report page generated by cWB algorithm.

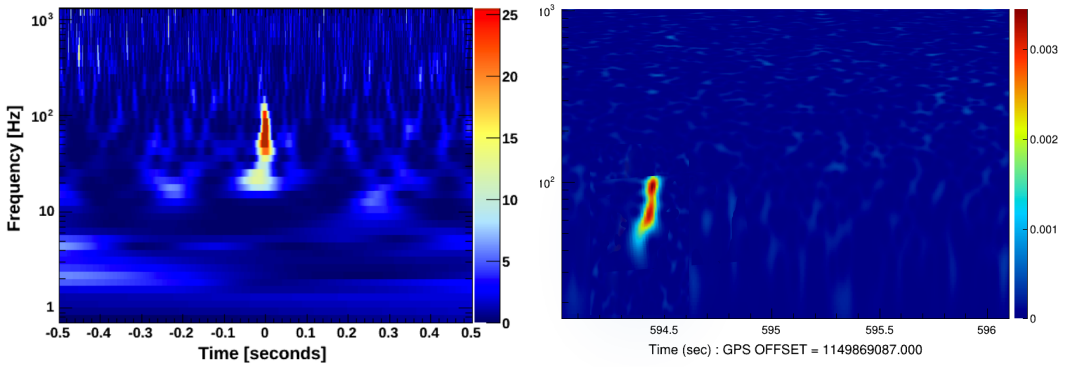

Figure 6.9: A blip glitch (left) compared to a heavy mass binary black hole system with anti-align spins (right). Image for blip glitch obtained from [100], while time-frequency map of binary is from from cWB report page.

these systems. Summary of these steps are provided below.

Injecting Simulated Binary Black Holes: The full parameter space for detecting a signal from BBH system is quite extensive. The intrinsic parameters of the source itself is 8D (masses m_1, m_2, and dimensionless spins $\mathbf{S_1}, \mathbf{S_2}$ of the two BHs), while there are additional four extrinsic parameters that significantly affect detection efficiency - distance to the source D, sky-location (θ, ϕ) and orientation of the BBH with respect to LIGO detectors ι. For a given range of BBH parameters - individual black hole masses (m_1, m_2) and spins $(\vec{\chi}_1, \vec{\chi}_2)$ - that we are interested in determining sensitivity, we 'inject' them in our coincident data of O1 and then recover using cWB algorithm with production cuts defined in the previous chapter. The injection set is generated such that signals are placed for random distribution over all possible sky-locations, while the orientation ι is uniformly distributed between 0 and π. The distance of BBH injections are scaled uniformly between a range of $D(r)$, where typically r_i is few Mpc and r_f is few Gpc. On an average, we generate $N_{\text{inj}} \sim 10,000$ injections for each combination of masses and spins. Figure 6.10 gives an overview of this step.

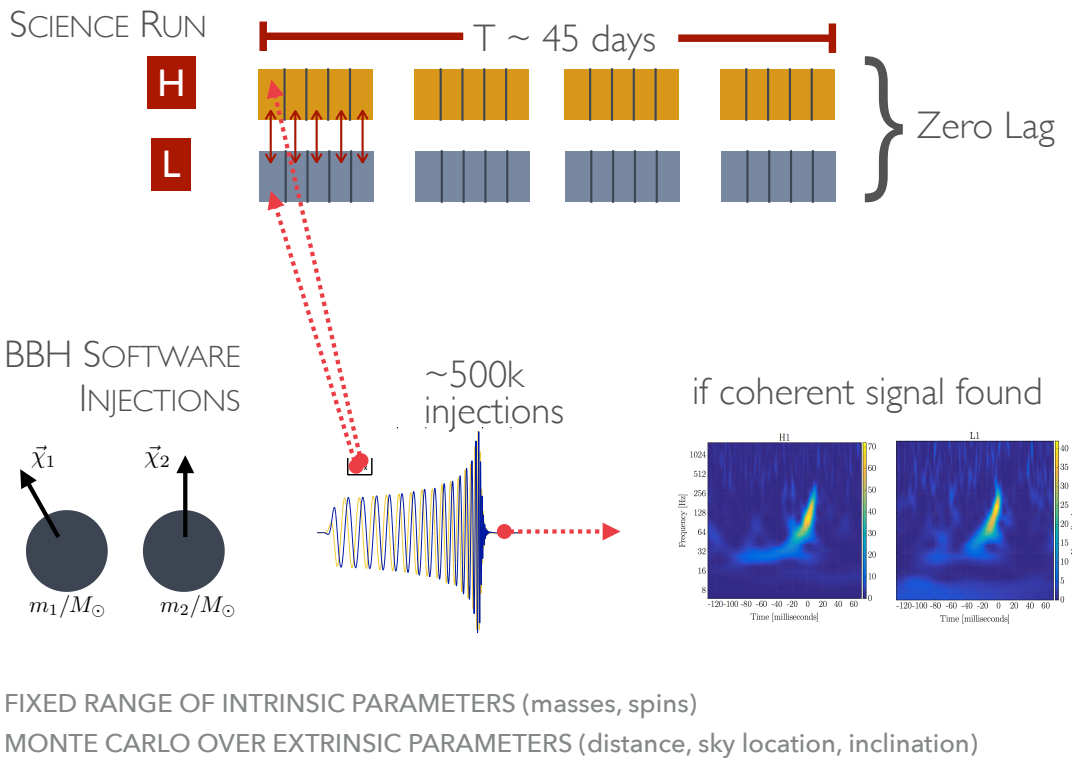

Figure 6.10: Simulated injections of binary black holes of generic masses and spins in the coincident (zero-lag) data of O1. The cWB algorithm then looks for the simulated signals just like an actual search. If a signal is found, an output page as shown in figure 6.6 is generated. The time-frequency map displayed here is from [101].

Computing Sensitive Distance: Based on the our production parameters, we recover a fraction of the injected signals. The recovery is dependent on the strength of GWs measured in the LIGO band and intrinsic BBH parameters (masses, spins). For example, an aligned, maximally spinning, binary black hole system will release the most energetic GWs, but in LIGO band the sensitivity of such system is dictated by their total-mass. We compute the sensitivity of our transient binary black hole search in following steps (highlighted in figure 6.11):

- Out of the $N_{\rm inj}$ injected signals, only a fractional $N_{\rm rec}$ will be recovered based on the production parameters.

- We then apply the same post-production cuts, which we have previously applied to

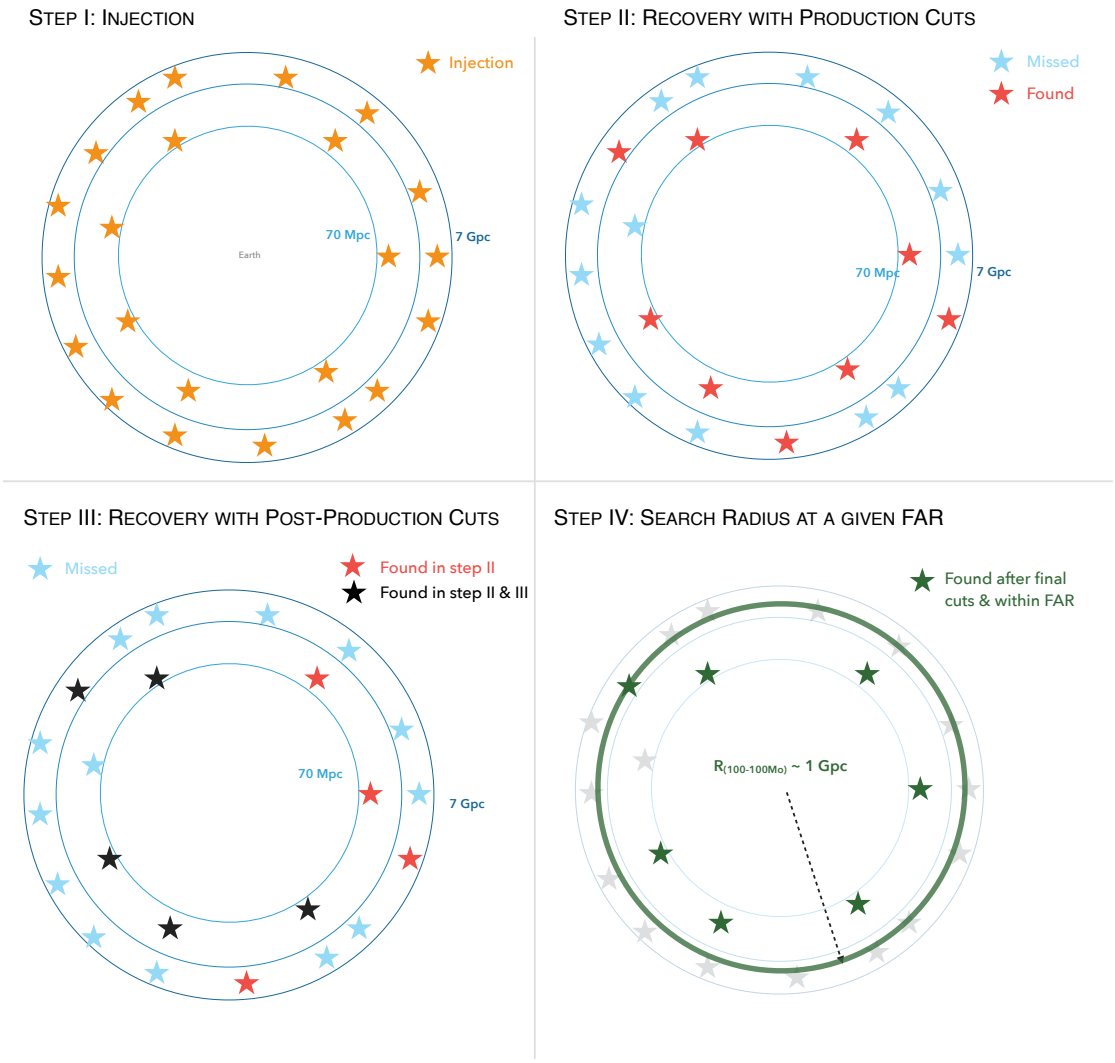

Figure 6.11: Diagrammatic representation of the steps involved for computing sensitive distances for injected binary black hole waveform.

clean the background. Based on trial-and-error, we determine if the post-productions cuts are too strict, and affect our recovery of the injected signals.

- Based on the final choice for post-production cuts, we count the recovery of signals over range of distances $D(r)$. In this step we are essentially reporting our search volume to detect BBH merger for a range of signal-to-noise ratios. To compute the

volume from recovered signal at different distances, we use the expression:

$$V(m_1,\ m_2,\ \vec{\chi}_1,\ \vec{\chi}_2,\ \eta) = \sum_i 4\pi r_i^2 \left(\frac{dN_{\rm rec}}{dr} dr_i\right)^{-1} \tag{6.1}$$

- The quantity η in the above equations refers to significance to which we can separated the recovered signal from the background noise. This essentially implies labeling each recovered injection with a False Alarm Rate (FAR). The higher the signal-to-noise ratio, the lower measure of FAR and thus higher the threshold of detection. A standard threshold for deciding the limit of signal-to-noise ratio we can detect is FAR of 1 per year.

- Finally, based on our total observation time T, and the volume that we span at a given FAR, we can compute the average distance, or as mentioned in the literature the *sensitive distance*, to which our search can detect BBH signals of the mass and spin parameters defined in the injection set.

$$D_{\langle VT\rangle} = \left(\frac{3\langle VT\rangle}{4\pi T}\right)^{1/3} \tag{6.2}$$

Chapter 7

SENSITIVITY TO DETECT BINARY BLACK HOLE COALESCENCE

Overview

Based on the machinery described in previous chapter for injecting and recovering simulated signals, in this chapter demonstrates the author demonstrates the distance to which the transient burst search of gravitational waves can detect binary black hole coalescence. This is a part of the 'closed-box' studies, i.e. we use this distance measurement to interpret our ability of detection before looking at the actual coincident signal in the data from the two LIGO detectors. The search distance will strictly depends on the masses and spin of the two black holes. Therefore, the author computed sensitivity for two classes of binary black holes based on total-mass (i) stellar to heavy-stellar of $20 \sim 100 M_{\odot}$ (section 7.3), and (ii) intermediate mass black holes of $50 \sim 600 M_{\odot}$ (section 7.2). As the sensitivity is also dependent on the quality of LIGO data, the author repeated this investigations for various instances of time segments - from the early test engineering runs in 2015, the begin few days of First Observation Run, to the entire 45 days of coincident data from September, 2015 - January 2016. While a resident fellow at LIGO Livingston Observatory, the author conducted hardware injections of intermediate mass black hole binaries, and their recovery with low-latency transient burst searches

is also highlighted (section 7.4).

The combination of search sensitivity and recovery of hardware injections dictates our readiness to detect gravitational waves from binary black holes of astrophysical origins.

All the statements made here are in author's personal capacity and not an official statement on the search result from the LIGO Scientific Collaboration and Virgo Collaboration.

7.1 Quoting Sensitivity Towards a Gravitational Wave Source

For a given power spectral density (also called noise curve) of a gravitational wave detector, one needs to compute its sensitivity for a gravitational wave source. The sensitivity is quoted as a measure of distance to which we can detect a source beyond a threshold of background noise. In context of binary black hole systems, there are three measures of 'distance' that are usually quoted in the literature.

Horizon Distance (D_H) This is similar to the luminosity distance defined in astrophysics. For a given noise curve, we can measure the maximum distance for which we can detect a binary system with signal-to-noise ratio, $\rho = 8$. This value of ρ is a minimum threshold for detection. By quoting 'maximum distance', we are assuming the binary is optimally oriented with respect to the position of detector (i.e., face-on inclination and sky-location). The horizon distance provides a general idea on the parameter space of binary black hole we can detect for a given gravitational wave experiment (see figure 7.1).

Angle-Averaged Range (R) After computing the horizon distance, one can further compute the average radius of our sensitive volume. This requires averaging over all angular patches. The relation between horizon distance and angle-averaged range can be described as $R = (1/f(\mathrm{z}))D_H$, where $f(\mathrm{z})$ is a redshift dependent scaling factor. At z=0, $f = 2.26$.

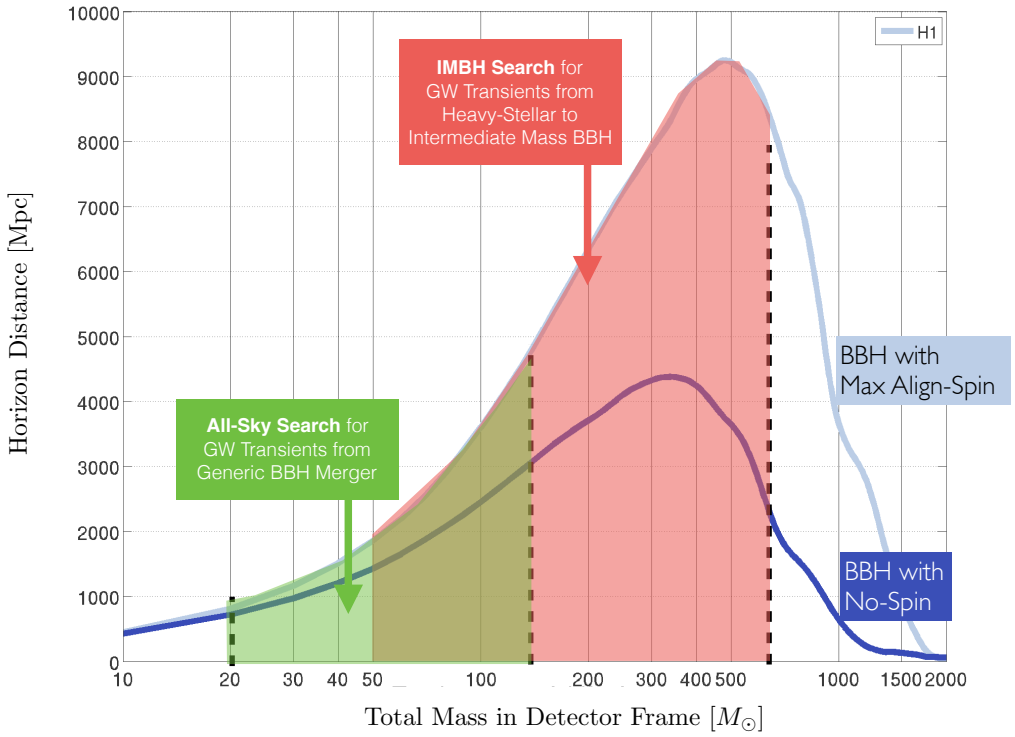

Figure 7.1: Horizon distance for binary black hole systems during First Observation Run of Advanced LIGO. Thetwo curves refer to horizon distance for binaries with equal masses of individual black holes (no-spin, and maximally align spin). The sensitive total-mass range for two distinct transient burst searches are highlighted.

Sensitive Distance $(D_{\langle VT\rangle})$ This is the value we primarily quote in determining our search radius and upper-limits for detecting a GW source. The sensitive distance is a search technique dependent quantity, i.e. for BBH systems of same parameters, the matched-filtering search will report a different $D_{\langle VT\rangle}$ than transient burst search. The details for computing search distance are quoted in previous chapter and in equation 6.5-6.5.

Notice the hierarchy in quoting a distance to which we can detect a binary black holes: $D_H > R > D_{\langle VT\rangle}$. There are two separate transient burst searches using cWB algorithm in LIGO are configured to hunt for binary black hole systems . The total-mass range of target for each search is highlighted in figure 7.1.

7.2 Sensitive Distance for Heavy-Stellar to Intermediate Mass Binary Black Holes

During the First Observation Run of Advanced LIGO (September 12, 2015 - January 19, 2016), the Coherent Wave Burst (cWB) algorithm was configured to conduct an offline, high-significance search for gravitational waves from binary black hole coalescence within total-mass range $50 - 600 M_{\odot}$. In astrophysics, this total mass range corresponds between heavy stellar to intermediate mass black hole binaries. Therefore, we will refer this configuration of transient burst as the `IMBH Search`.

The procedure of determining the production and post-production cuts for this search is elaborated in chapter 6. As an example to the text of section 6.5, in this section we detail the steps to compute search sensitivity in the mass-range. This is done in three stages: Step-1 involves injecting a set of simulated BBH waveforms, step-2 involves recovering these signals using cWB and step-3 determines the sensitive distances $(D_{\langle VT \rangle})$ for various combinations of masses and spins of BBH at a given threshold of inverse false rate.

Injection Set: We limit our test injections to cases when the spins of each black-holes are aligned with the orbital angular momentum of the BBH system. The injection set is uniformly distributed between $M = m_1 + m_2 \in [20, 150] M_{\odot}$ and mass-ratio $m_1/m_2 = 1:10$ (see the red dots in top-left and bottom panel of figure 7.2). Furthermore, we uniformly distribute the z-components of spin vectors of individual BHs across their full range, $|\mathbf{S_{1,2}}| \in [0, 0.99]$ (see top-right figure 7.2). These BBHs injections are placed uniformly in volume within the range 2 Mpc to 6 Gpc. The entire injection set is uniformly placed across the 45 days of coincident data of O1 with a gap of 15 seconds between each waveform. The injection set consists of $N_{\rm inj} \approx 350,000$ waveforms of BBH. The BBH waveforms analyzed in this study have been generated using the approximate model `SEOBNRv2`. The model accounts only for the dominant radiated modes, $(\ell = 2, m = 2)$ of

gravitational waves.

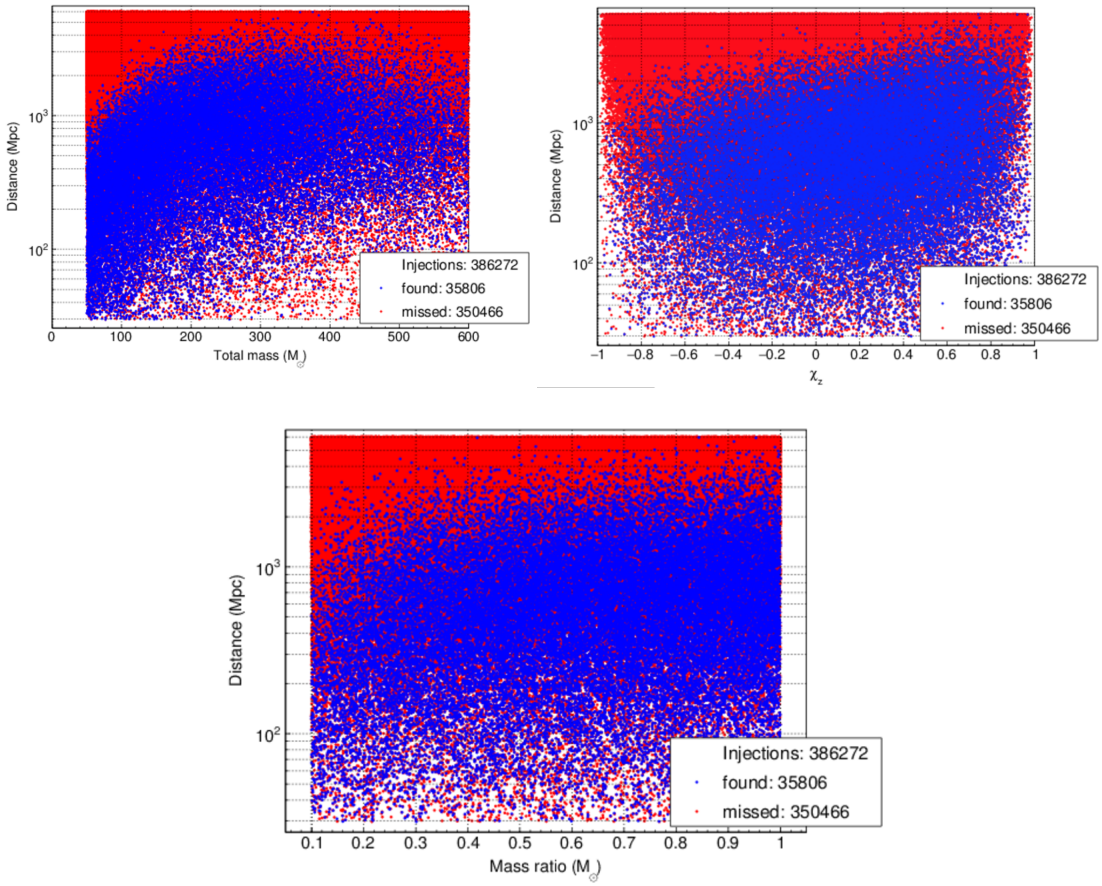

Figure 7.2: Recovery of simulated injections of binary black holes using cWB algorithm configured for the `IMBH Search`. The plot on the top demonstrates the missed-found injections for total-mass vs. distance, while bottom plot refers to effective spin vs. distance. Red are the missed injections and blue are the recovered signals by this search. About 1/10th of 350,000 simulated injections of binary black holes are recovered. The plots have been generated using the CBC_PLOTS plugin within cWB infrastructure.

Recovered Injections: The missed and found BBH injections (after post-production cuts) for the range of total mass and spins are highlighted in figure 7.2. The distance to which we recover signals peaks around a binary total-mass of $\sim 400 M_{\odot}$, with the farthest detected BBH ranging all the way to 6 Gpc. However, as we increase the total mass, the number of recovered injections decreases. Many nearby high mass BBH signal seems to be eliminated by our production and post-production cuts. The strictest cut happens due to our

removal of blip glitches which take the morphology of short BBH mergers (see figure 6.9). The BBH spins have a similar effect on recovery. For anti-align systems ($\chi_z < -0.6$), we miss nearby events. Its only the mass-ratio $q = m_1/m_2$ where recovery of nearby injection remains fairly constant. As expected, with higher mass-ratio ($1/q = 0.1$), the recovery drops.

Sensitive Distance: In figure 7.3, we showcase the sensitive distance $D_{\langle VT\rangle}$ to which we can detect heavy stellar to intermediate-mass BBHs with high confidence. There are various correlations one can notice between $D_{\langle VT\rangle}$ and the dynamics of BBH we observe in NR simulations. The total mass of BBH strongly dictates the sensitive distance. Binaries with equal masses of black holes can be seen the farthest (1619 Mpc for $200 + 200M_\odot$), while an unequal mass distribution for same total mass drops sensitivity by a factor of 3 (igure 7.3 - top-plot). Also, notice the symmetry in sensitive distance for different combination of masses of black holes. A total of mass of $300M_\odot$ has same effective distance as a binary with $500M_\odot$. While the sensitivity for an equal-mass $50+50M_\odot$ system is same as that for a higher asymmetric system of $500+50M_\odot$. There are more number of GW cycles in LIGO band for higher mass-ratio, but the energy released during merger is less, thus transients burst searches notice a drop of sensitivity. Also, for a high total-mass of BBH ($\geq 100M_\odot$), the spins can boost the sensitivity by a factor of 3. At lower total mass ($\leq 100M_\odot$), the effect of spin is quite marginal. For BBH with anti-align spins ($\chi_z < -0.6$), a $100M_\odot$ system has same likelihood of detection as a $600M_\odot$ system. The farthest GW source we can with this transient burst search is a $400M_\odot$ BBH with align spins $\chi_z > +0.6$, all the way up to 1.79 Gpc.

In conclusion, during the First Observation Run of Advanced LIGO, the `IMBH Search` can detect binary black holes between 50 to $600M_\odot$ up to an average distance of 1 Gpc, and with a high significance of inverse False Alarm Rate of 1000 years (see figure 7.4).

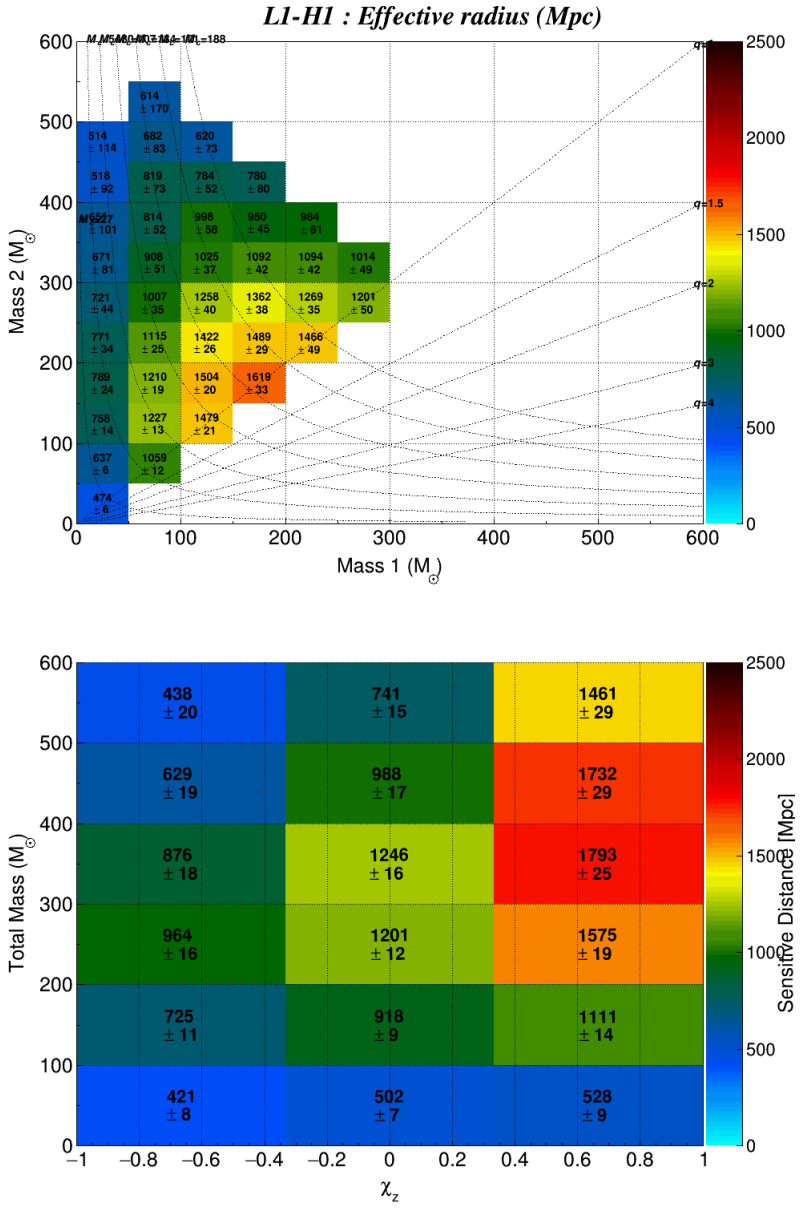

Figure 7.3: Search distance for binary black holes using cWB algorithm configured for the `IMBH Search`. The plot on the top demonstrates the search distance as a function of individual black hole masses (m_1, m_2), while bottom plot refers to search distance as a function of effective spin χ_z and total-binary mass M. Colors indicate the values of search distance at an Inverse False Alarm Rate of half year. The error bars depends on the ratio of missed and found injections. The plots have been generated using the CBC_PLOTS plugin within cWB infrastructure.

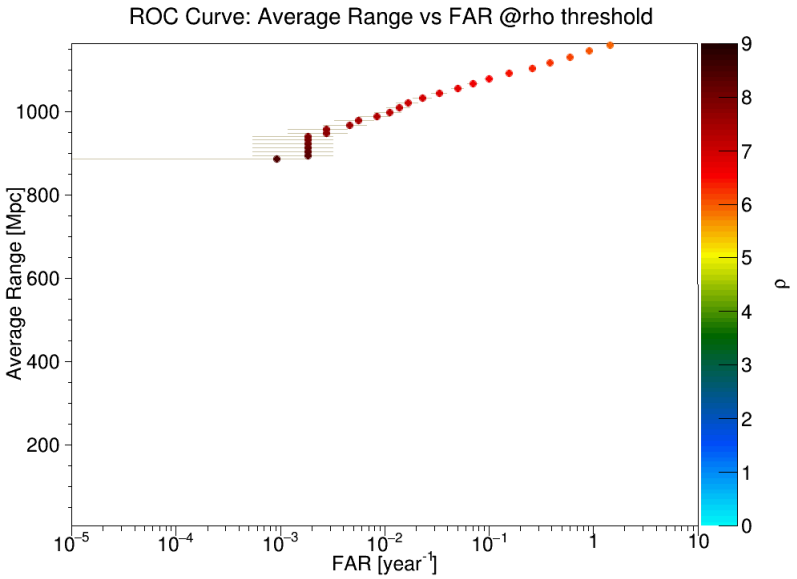

Figure 7.4: Average sensitive distance as a function of false alarm rate for binary black holes systems using cWB algorithm configured for the `IMBH Search` for heavy-stellar to intermediate mass black hole mergers in the total mass-range $50 - 600 M_{\odot}$. The plots have been generated using the CBC_PLOTS plugin within cWB infrastructure.

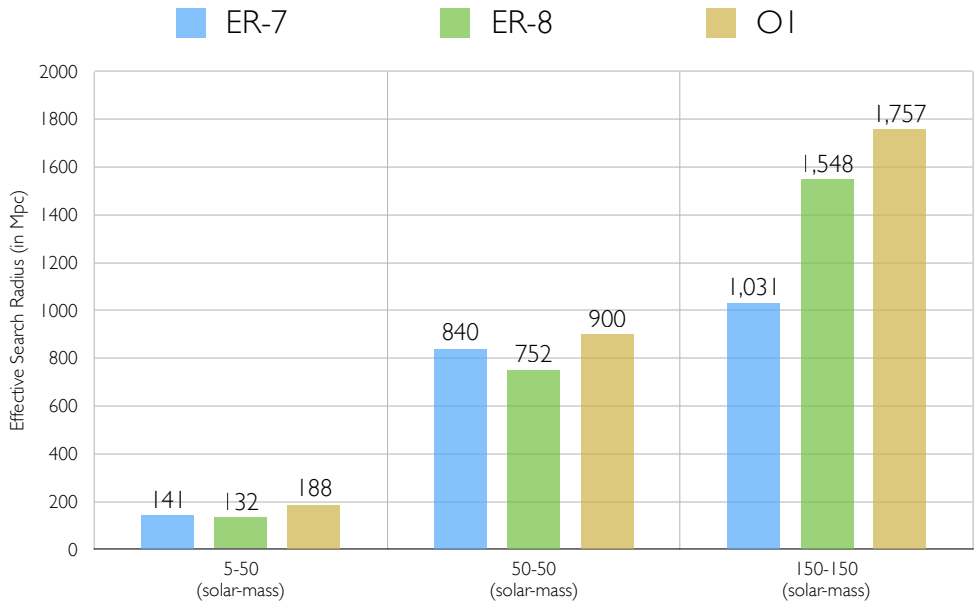

Figure 7.5: Sensitive distance to binary black holes computed using cWB algorithm at different operational stages of in LIGO data between June 2015 to January 2016.

7.2.1 Impact of Data Quality on Sensitive Distance

The studies demonstrated in the `IMBH Search` were configured in keeping in mind the sensitivity the Advanced LIGO detectors during the First Observation Run (O1). Before the start of the official data collection period of O1, the LIGO detectors go through engineering runs where efforts are made to improve the sensitivity as well as identify sources of instrumental noises. From a perspective of GW data analysis, the coincident data from engineering runs provide an early assessment for the sensitivity that our searches have to configured. During the seventh and eight engineering run during the summer of 2015 (ER-7 and ER-8), we injected the simulated waveform of BBH for three distinct mass bins, which were representative of the range of systems from stellar to intermediate mass black holes. The sensitive distance from these injections from ER-7 to ER-8 to O1 are shown in figure 7.5. Notice, the improvement in sensitivity impacted the most towards intermediate mass black holes of total mass $300M_{\odot}$. This implies, the most improvement occurred from ER-7 to O1 was in reducing the constant sources of low frequency noise in LIGO.

7.3 Sensitive Distance Towards a Generic Binary Black Holes

During the First Observation Run of Advanced LIGO (September 12, 2015 - January 19, 2016), the Coherent Wave Burst (cWB) algorithm was configured to conduct an *all-sky* search (offline, high significance) for gravitational wave sources that lie within the frequency spectrum from 32 to 1024 Hz [99]. These search is not fine tuned to look for a particular astrophysical source, but in principle, can catch a binary black hole coalescence. In this section, we determine the sensitive distance to which the *all-sky* search can detect stellar binary black hole systems of generic parameters of masses and spins. In particular, we want to understand our threshold of search radius for BBHs within total-mass range $20 - 150M_{\odot}$.

The procedure is similar to the one listed in earlier chapter: step-1 involves deciding

production and post-production cuts to clean a background, step-2 involves injecting a set of simulated BBH waveforms, and step-3 involves recovering these signals using cWB and determining the sensitive distances ($D_{\langle VT \rangle}$) for various combinations of masses and spins of BBH.

Injection Set: Similar to the studies presented earlier for heavy stellar to intermediate mass black hole binaries, we limit our test injections to cases when the spins of each black-holes are aligned with the orbital angular momentum of the BBH system and waveforms have been generated using the approximate model `SEOBNRv2`. The model accounts only for the dominant radiated modes, ($\ell = 2, m = 2$) of gravitational waves. We divide our BBH injections into three bins of mass-ratios q such that $q = m_2/m_1 \in \{1, 2, 4\}$. For each injection bin, BBH waveform are generated such that total mass M of the binary is uniformly distributed between $M = m_1 + m_2 \in [20, 150] M_\odot$ (see top panel of figure 7.6). Furthermore, in each of the three injection bins, the spin vectors of individual BHs are uniformly distributed across their full range, $|\mathbf{S_{1,2}}| \in [0, 0.99]$ (see top bottom of figure 7.6). Each injection bin has a random distribution over all possible sky-locations, while the orientation ι is uniformly distributed between 0 and π. The distance of BBH injections are scaled uniformly based on their "chirp-distance" $D_c (\propto \mathcal{M}_c)$ within the range 2 Mpc to 1.25 Gpc (corresponding Euclidean distance D is 5 Mpc to 3.5 Gpc) . The three injections bins are uniformly placed across the 45 days of coincident data of O1 with a gap of 15 seconds between each waveform. Therefore, the entire injection set consists of about 460,000 waveforms of BBH.

Recovered Injections: In figure 7.6, we highlight the missed and recovered BBH injections (after post-production cuts) for our range of total mass and spins. The distance to which we recovery signals is fairly linear with the total-mass of the systems. For a BBH system of total-mass $20 M_\odot$, the farthest we can recover a signal is at 500 Mpc, while for $150 M_\odot$ we can recover upto 3 Gpc. The BBH spins have a similar effect on recovery. For

BBH with anti-align spins ($\chi_z < -0.6$), we barely recovery beyond 1 Gpc, but for BBH with no-spin or aligned spin ($\chi_z > 0.0$) we start recovering signals beyond 2 Gpc.

Sensitive Distance: In figure 7.7, we showcase the sensitive distance $D_{\langle VT\rangle}$ to which we can detect generic stellar BBHs with high confidence. There are various correlations one can notice between $D_{\langle VT\rangle}$ and the dynamics of BBH we observe in NR simulations. The higher the total mass of BBH, the further the distance we can detect the systems. Binaries with equal masses of black holes can be seen the farthest (1318 Mpc), while an unequal mass distribution drops sensitivity by 40% (top-plot). There are more number of GW cycles in LIGO band for higher mass-ratio, but the energy released during merger is less, thus transients burst searches notice a drop of sensitivity. Also, for a high total-mass of BBH ($\geq 100M_{\odot}$), the spins can at most impact 30%. At lower total mass ($\leq 40M_{\odot}$), the effect of spin is quite marginal. Just like mass-ratio, higher the spin implies more number of GW cycles in LIGO band. But the energy released during merger depends strongly on mass of the system, and thus the additional cycles does marginal improvement in for cWB algorithm

In conclusion, during the First Observation Run of Advanced LIGO, the transient burst search was ready to detect stellar binary black hole systems of masses $20 - 150M - \odot$ up to an average distance of ~ 500 Mpc.

7.4 Hardware Injections of Intermediate Mass Black Holes

Before the start of the Second Observing Run (December 2016 - Current), the author conducted hardware injections of intermediate mass binary black holes waveform in the two LIGO detectors. Each of these signals go in the actual hardware, and a photon calibrator 'shakes' the end-mirrors with the same frequency it will in case of an actual gravitational waveform coming from astrophysical black holes of the injected parameters. Therefore, the LIGO data now contains a fake GW strain. This is different than the

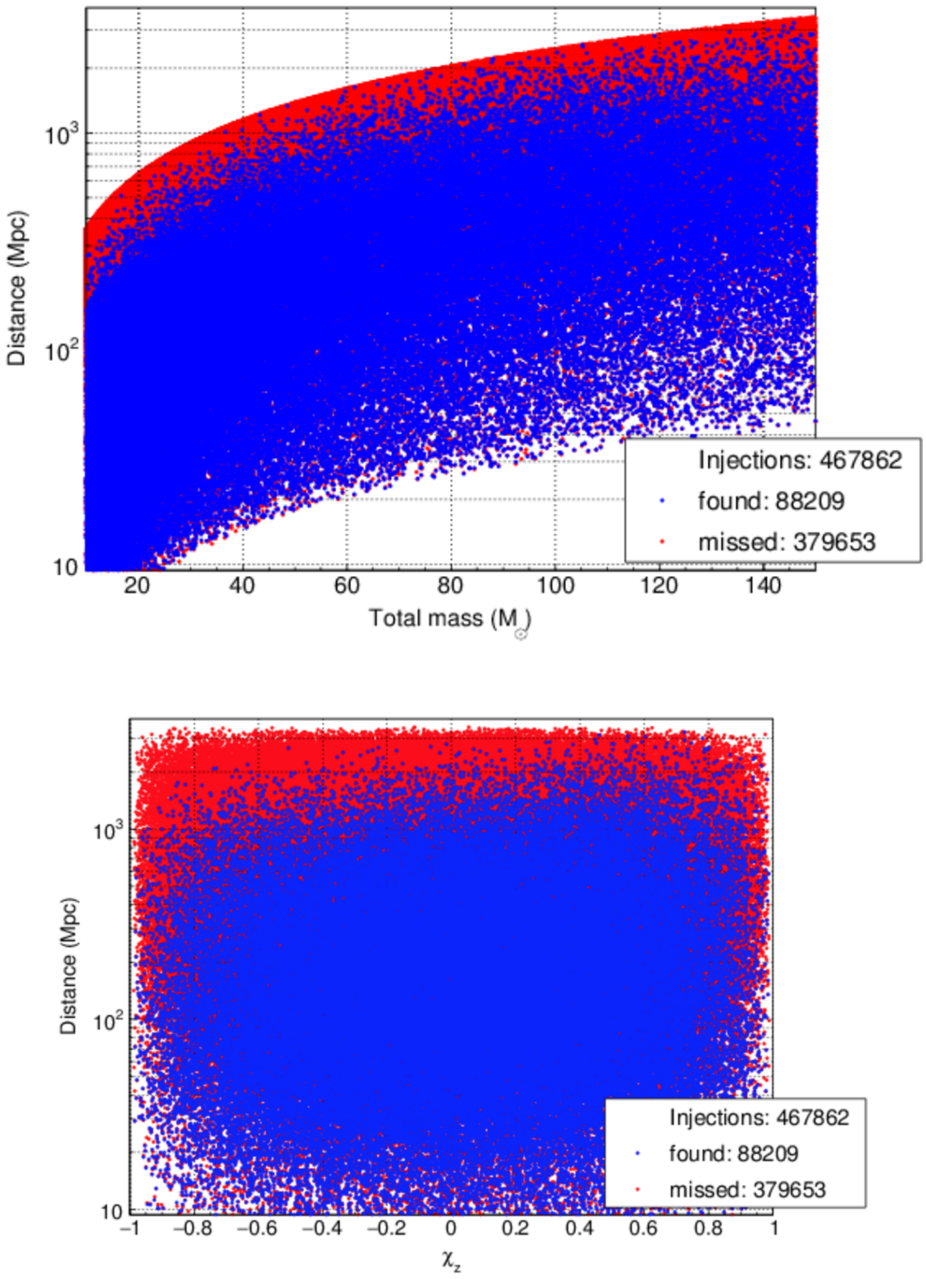

Figure 7.6: Recovery of simulated injections of stellar binary black holes using the *all-sky* search of cWB. The plot on the top demonstrates the missed-found injections for total-mass vs. distance, while bottom plot refers to effective spin vs. distance. Red are the missed injections and blue are the recovered signals by this search. About 1/5th of 460,000 simulated injections of binary black holes are recovered. The plots have been generated using the CBC_PLOTS plugin within cWB infrastructure.

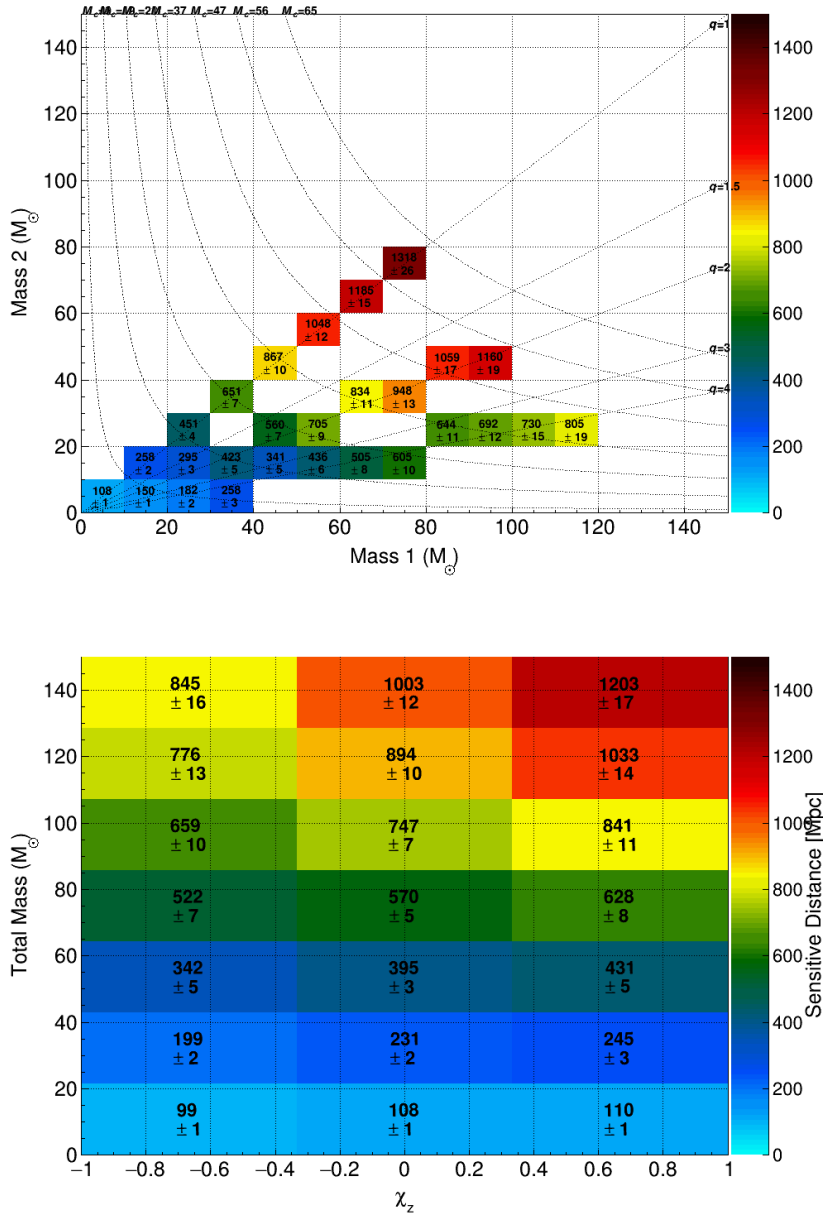

Figure 7.7: Search distance to stellar binary black holes using the *all-sky* search of cWB. The plot on the top demonstrates the search distance as a function of individual black hole masses (m_1, m_2), while bottom plot refers to search distance as a function of effective spin χ_z and total-binary mass M. Colors indicate the values of search distance at an Inverse False Alarm Rate of half year. The error bars depends on the ratio of missed and found injections. The plots have been generated using the CBC_PLOTS plugin within cWB infrastructure.

simulated injections we conducted in the earlier sections of this chapter, where the BBH waveforms were added on top of the LIGO data. These hardware injections are coordinated

such that they are coincidentally injected in both the LIGO sites - Hanford and Livingston at the same instance of time. Such hardware injections provides an unique opportunity to understand the coupling on instrumental noise with the binary black hole search. This study was conducted while being the LIGO Scientific Collaboration Fellow at LIGO Livingston.

Figure 7.8 showcases the two hardware injections of heavy-mass binary black hole waveform and its recovery using low-latency cWB algorithm. Both these systems are different in terms of waveform morphology and their potential astrophysical origins. The first injected signal was an intermediate mass binary of two $50M_{\odot}$ black holes of a signal-to-noise ratio (SNR) of 24. The low-latency cWB algorithm recovered this signal within few minutes of injections and reconstructed the potential GW waveform morphology.

The second injected signal was an intermediate mass ratio inspiral of two non-spinning black holes with masses $5M_{\odot}$ and $100M_{\odot}$ with a signal-to-noise ratio (SNR) of 12. This is a fairly weak signal for transient burst searches like cWB. Yet, these signal was well recovered and with reconstructed morphology noticeably similar to injected signal.

With these sucessful hardware injections, we can conclude that a binary black hole coalescence of intermediate-masses $\geq 100M_{\odot}$ can be detected using the transient burst searches in LIGO.

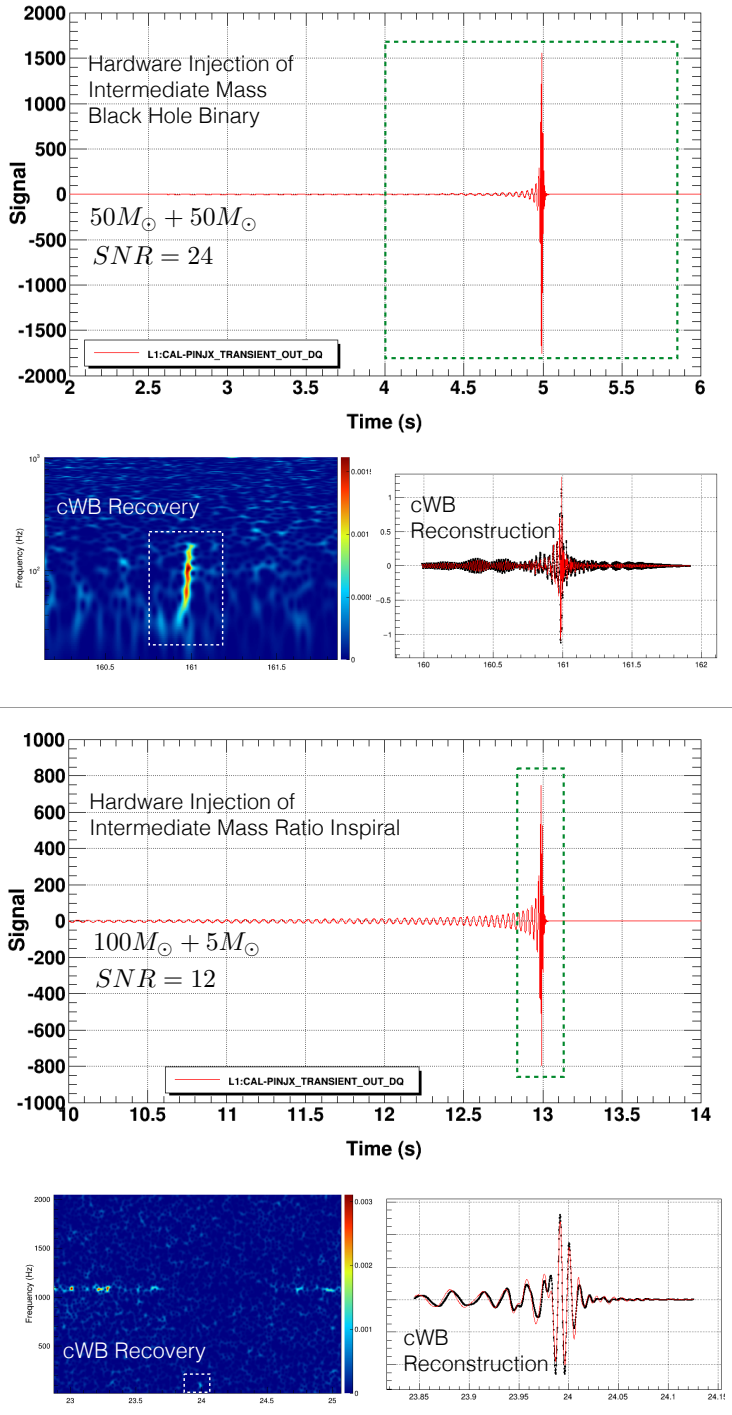

Figure 7.8: Hardware injections of two distinct types on intermediate mass black hole systems in Advanced LIGO and recovery using low-latency transient burst search. Dotted green line shows the region of the injected signal reconstructed by cWB. Time-frequency maps and reconstructed signal obtain from cWB report pages.

PART III

BINARY BLACK HOLES IN THE UNIVERSE

Chapter 8

GW150914: ROLE IN THE FIRST GRAVITATIONAL WAVE DETECTION

Overview

On the early morning of September 14, 2015, the LIGO detector in Livingston, LA recorded a transient burst of excess power in the data. A similar signal was recorded 10ms later in the LIGO detector at Hanford, WA. This transient signal was first picked by the low-latency COHERENT WAVE BURST algorithm (see figure 8.2). On February 11, 2016 we announced this signal as the first direct detection of gravitational waves, the first observation of binary black hole coalescence in the universe and the final long standing confirmation of Albert Einstein's General Theory of Relativity in extreme gravity. This chapter highlights the studies the author conducted in confirming this historic detection, officially labeled GW150914, as a binary black hole merger.

The organization of this chapter is shown in figure 8.1. Section 8.1 showcases the numerical relativity simulations of binary black holes the author conducted as a followup to GW150914, as well as the simulations from Georgia Tech Catalog of binary black hole waveforms that were directly utilized for the first detection. In section 8.1.1, we demonstrate the comparison between these numerical relativity simulations with the reconstructed signal of GW150914 from transient burst searches. In section 8.1.2, we highlight the direct

comparison of our simulations with the data from two LIGO detectors at the instance when GW150914 was recorded. Finally, in section 8.2, I reevaluate the search sensitivity of offline transient burst searches to have detected GW150914 with the required significance.

All the statements made here are in author's personal capacity and not an official statement on the search result from the LIGO Scientific Collaboration and Virgo Collaboration.

8.1 Numerical Relativity Simulations

From the parameter estimation studies and the best matching template to the LIGO data, the intrinsic parameters of GW150914 were narrowed towards a $\sim 70M_{\odot}$ binary of two equal mass black holes, and their spins in the direction of orbital angular momentum either being either zero or exactly canceling each other. There was very little evidence of spins in the orbital plane. These results were obtained by the approximate models for gravitational waveform of binary black holes.

The primary goal of conducting NR simulations was to shed light on the parameters of GW150914 beyond the reach of the models. This meant utilizing gravitational waveform from NR BBH simulations, which contained higher harmonics of radiation, as well as provided accurate description in parts of parameter space where models were known to be limiting. Based on the possible range of parameters of GW150914, the author conducted 4 follow-up simulations, whose initial parameters are reported in table 8.1. An NR simulation with the exact parameters of `GT0901` was reported in the two primary figures in the detection paper of GW150914 [91]. The visualization of the simulation `GT0901` was widely for educationa d public outreach of GW150914 (see the poster in figure 8.3).

The first physical quantity to assert that GW150914 is a possibleBBH candidate was the chirp-mass of the binary as measured by the transient burst search. By tracking the

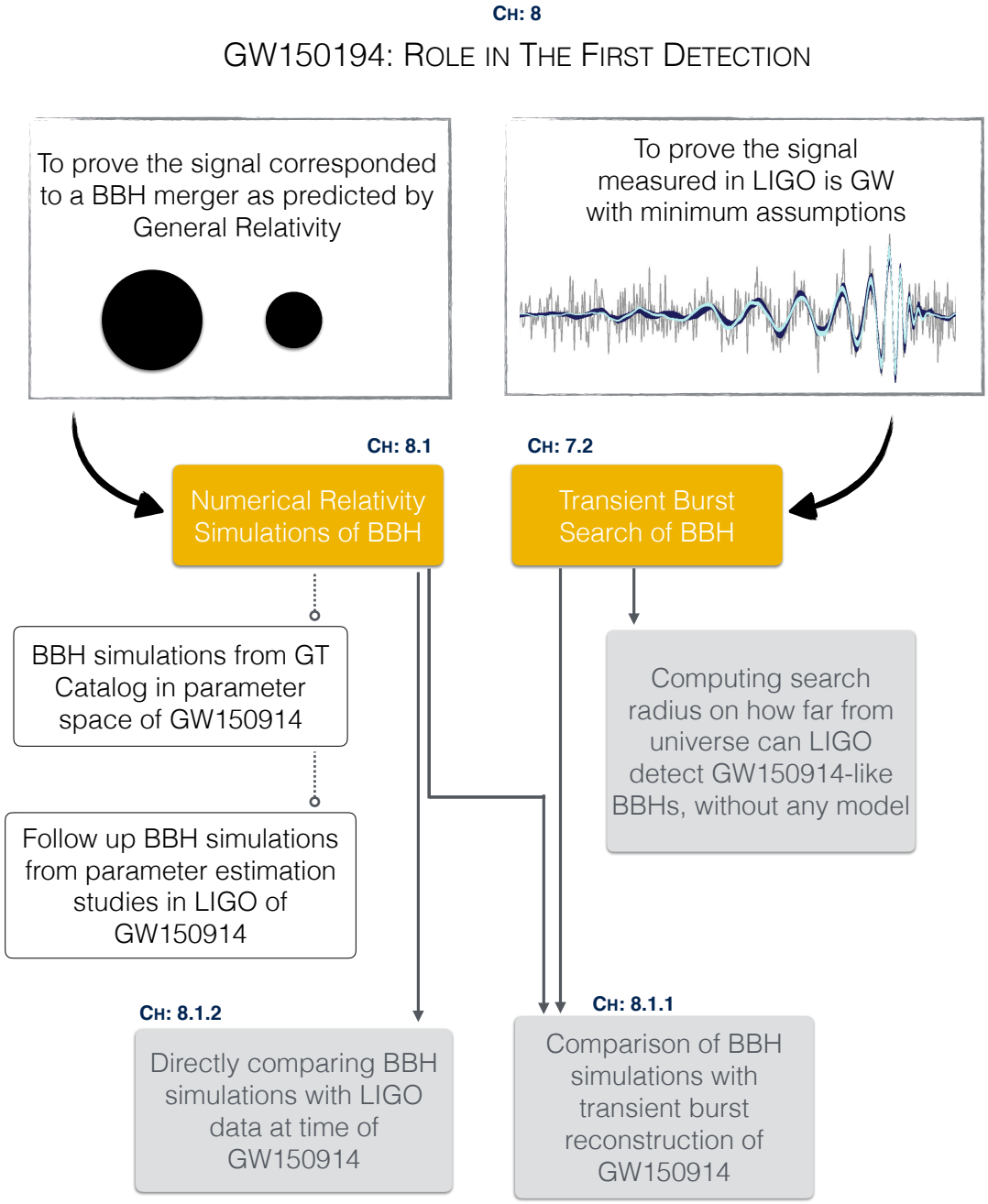

Figure 8.1: Overview of this chapter.

Row	GT-ID	m_1/m_2	$\vec{\chi_1}$	$\vec{\chi_2}$	GW-cycles	SU
1	GT0898	1.2	(0,0,0)	(0,0,0)	17	40k
2	GT0901	1.22	(0,0,0.33)	(0,0,-0.44)	17	40k
3	GT0899	1.19	(0,0,0.42)	(0,0,-0.38)	18	40k
4	GT0900	1.2	(0.4,0,0)	(0.4,0,0)	14	55k

Table 8.1: Numerical relativity simulations of binary black holes conducted as a followup on GW150914.

frequency evolution of the reconstructed signal of GW150914, chirp mass of this system was recorded as $\mathcal{M}_c = \eta^{3/5} M \approx 30 \pm 5 M_\odot$. from the Georgia Tech Catalog of NR

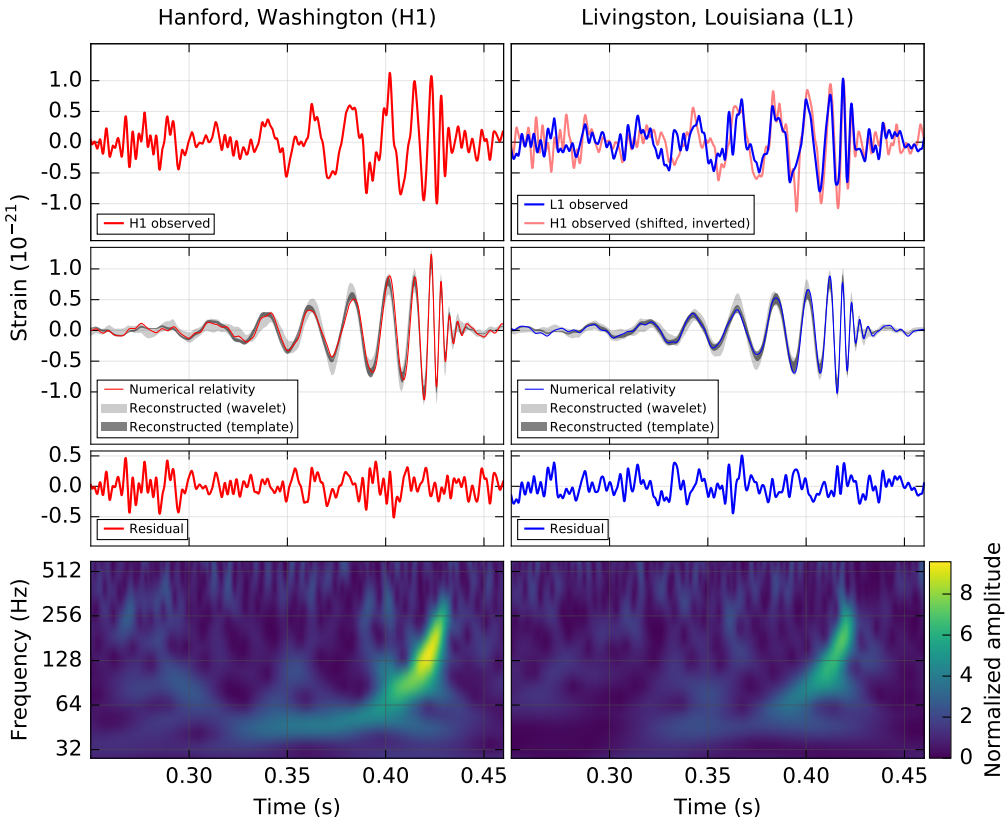

Figure 8.2: GW150914 as observed in the LIGO detectors. The top panel is the measured GW strain. The bottom panel is the time-frequency map as computed by transient burst searches. The middle plot is a comparision between the reconstructed waveform and numerical relativity simulations. [20]

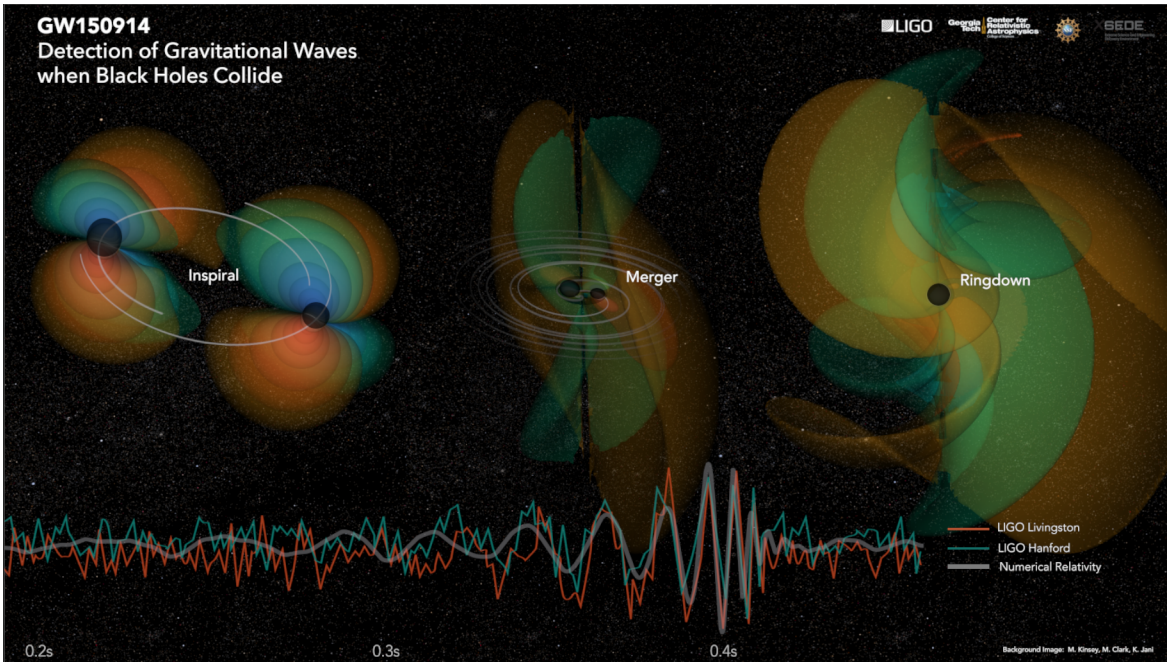

Figure 8.3: Visualization of GW150914 for `GT0901`. Image Credit: M. Kinsey, M. Clark, K. Jani for the Georgia Tech NR Group.

simulations of BBH, there were already 187 simulations that could be scaled in the chirp-mass range of GW150914 (see figure 8.5). Among these, 67 were BBH simulations with precessing spins. These were of utmost interest as the approximate models did not offer much insights regarding evidence of the precession of GW150914. Also, unlike the NR simulations, the models did not have accurate description of gravitational waveform for high-mass ratio systems.

Apart from filtering NR simulations based on chirp-mass, a total of 406 simulations from Georgia Tech catalog were used for direct comparison studies with the LIGO data at the instance of GW150914. These waveform ranged for BBH with parameters ranging for mass-ratios $1:15$ and were distributed for generic orientations of spins. Figure 8.4 summarizes the initial parameters of these simulations from Georgia Tech catalog.

With an exact description of Einstein's Equations, obtained from over 5 million hours of computing resources spent on simulating binary black holes, as our primary tool, the next task was to find the best matching parameter of simulation with the signal GW150914. The

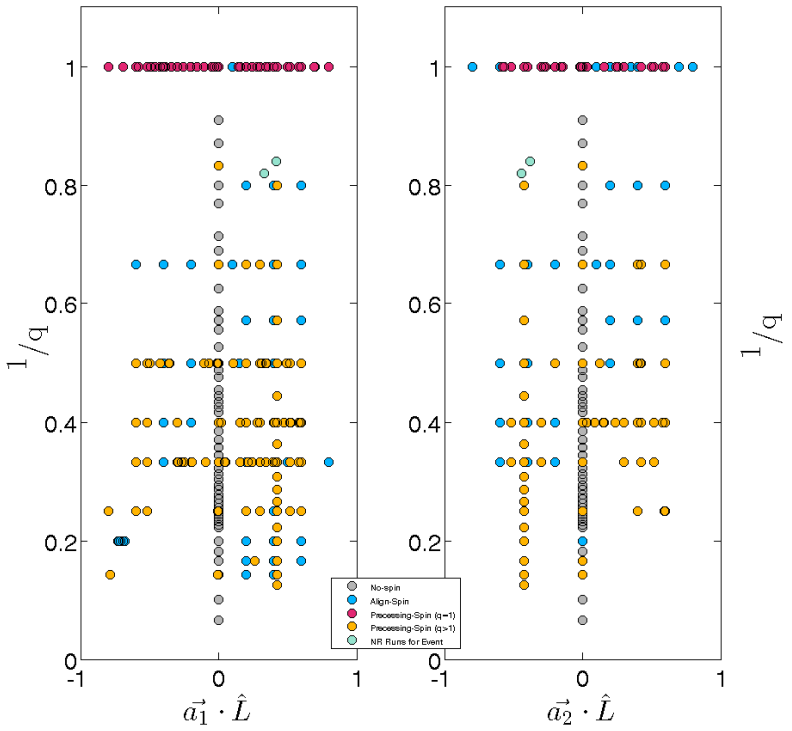

Figure 8.4: Distribution of initial parameters Georgia Tech NR simulations utilized to directly compare with the LIGO data from GW150914.

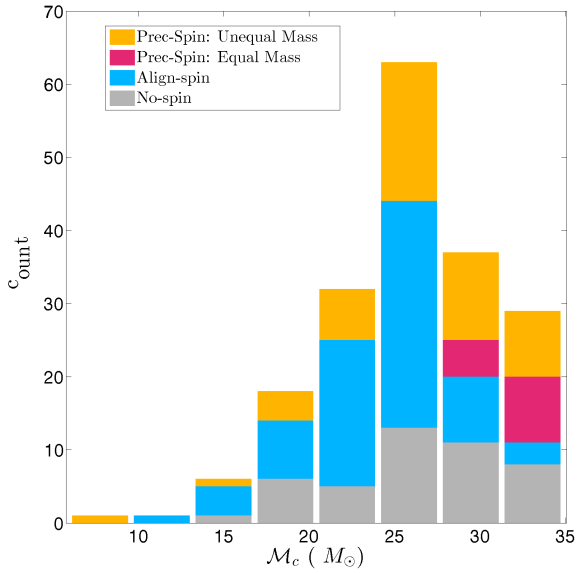

Figure 8.5: Histogram of Georgia Tech NR simulations for minimum salable chirp-masses in the range of GW150914. Any NR waveforms of $\mathcal{M}_c \leq 35 M_\odot$ can be scaled for GW150914.

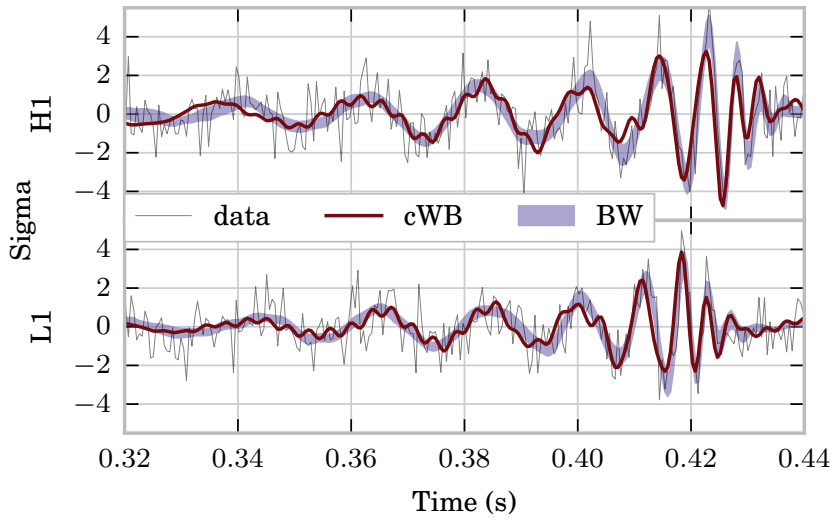

Figure 8.6: Reconstructed signal of GW150914 in both the LIGO detectors from the two transient burst searches - COHERENT WAVE BURST (cWB) and BAYESWAVE. The light grey lines refer to the strain measured in LIGO.

next two section highlights these efforts.

8.1.1 Comparison with Reconstructed Signal From Transient Burst Search

As we noted in Chapter 5, the COHERENT WAVE BURST (cWB) algorithm finds a coincident signal in the two data stream from LIGO detectors, without using any model. One of the outputs of cWB is the reconstructed signal at both the detectors. Unlike the matched-filtering search, the reconstruction is a true representation of all the coherent energy recorded by the LIGO detectors. The reconstructed signals are available within few minutes of detection by the low-latency search. The reconstructed signal from offline transient burst search of GW150914 for both the detectors is highlighted in figure 8.6. Two independent transient burst searches - cWB and BayesWave (BW), independently reconstructed the signal. The reconstruction from cWB is a point estimate, while BW produces a set of reconstructions around the median value.

The next task is to find an NR waveform ($h_{\rm NR}$) that has the closest representations with these reconstructed waveforms ($s_{\rm rec}$). This is done in two steps:

(i) we first define a network match between the reconstructed waveform in two detectors

$d =$ H, L, with the NR waveform. This is essentially computing a noise-weighted an inner product between two waveform morphology and maximizing over time and phase. The expression for such network match is:

$$\mathcal{N} = \frac{\sum_d \max_{t_0,\phi_0}(s^d_{\rm rec}|h_{\rm NR})_d}{[\sum_d (h_{\rm NR}|h_{\rm NR})_d]^{1/2}[\sum_d (s^d_{\rm rec}|s^d_{\rm rec})_d]^{1/2}} \tag{8.1}$$

(ii) We then compute the corresponding Fitting Factor (FF), which requires maximizing the value of network match $\mathcal{N}$ for all values of total-mass and orbital inclination.

As a companion study to the detection paper of GW150914, we computed such fitting factor for 104 distinct NR simulations from Georgia Tech Catalog, as well as the four followup simulations highlighted earlier. Each waveform was ranked based on their FF for the reconstruction from cWB and BW. The comparison between NR and reconstructed waveform is highlighted in figure 8.7, and the inferred parameter of total mass and chirp-mass in table 8.2. The key results of this study were:

- The highest ranked NR waveform (`GT0901`) was consistent with other parameter estimation studies, thus enhancing our confidence in the intrinsic values of the BBH system GW150914.

- NR simulations from patches of parameter space like high-mass ratios, highly aligned or anti-aligned spins, gave low matches, thus confirming GW150914 is indeed an almost equal-mass BBH with spin identically canceling each other.

- The two independent reconstructions of GW150914 obtained using cWB and BW algorithm gave similar results.

- We proved GW150914 was a binary black hole merger as predicted by Einstein's General Relativity by utilizing no assumption regarding the source.

	cWB	BW	LALInference
Max Match with NR	87%	95%	-
Total Mass $M_\odot$	$66.4 - 74.8$	$67.9 - 75.7$	$66 - 75$
Chirp Mass $M_\odot$	$27.8 - 33.0$	$27.4 - 32.6$	$28 - 32$

Table 8.2: Total mass and chirp-mass of GW150914 obtained from the numerical relativity comparison with reconstructed waveforms from transient burst searches (cWB and BW), and similar values obtained from conventional parameters estimation studies using approximant models (LALInference)

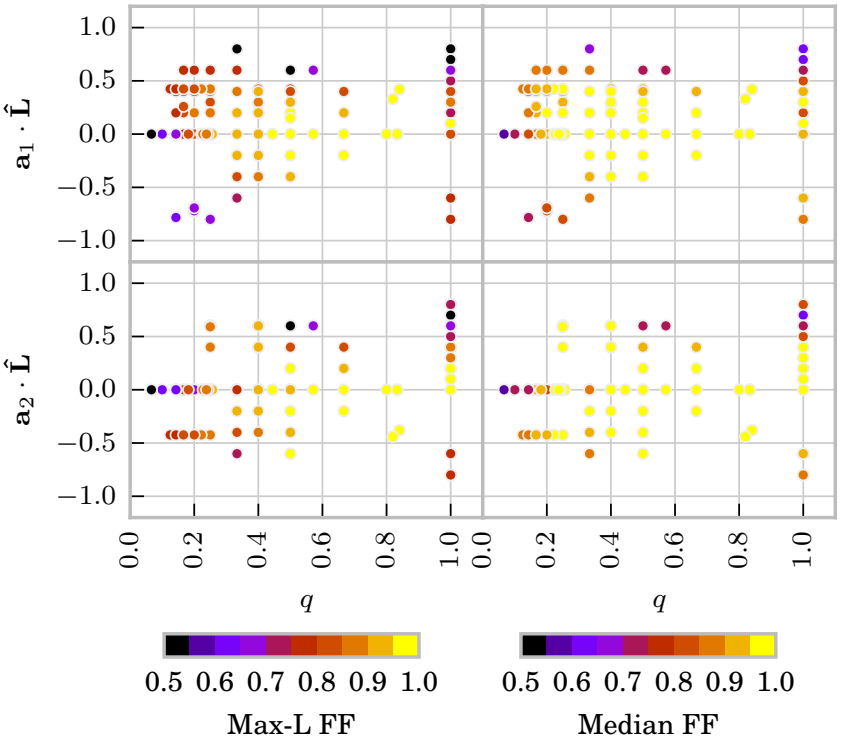

Figure 8.7: Fitting factors between NR waveforms and the reconstructed waveform from COHERENT WAVE BURST (left) and BAYESWAVE (right). Each dot is a distinct NR simulation from the Georgia Tech Catalog. A total of 104 such BBH simulations are showcased in this plot. The x-axis represents mass-ratio of NR simulation, while the two y-axes refers to the component of spin aligned with the orbital angular momentum at the start of NR simulation. Color refers to the scale of FF - yellow being best match, black being list match.

8.1.2 Direct Comparison with LIGO Data

Instead of reconstructed waveforms obtained from transient burst search, we can, in principle, directly compare NR waveforms with the data in the LIGO detectors. Usually,

the GW signal is deeply buried in the noise, which limits our ability to conduct such direct, and therefore we rely on reconstructed signals. In the case of GW150914, the signal was sufficiently loud that such direct comparison can be performed. With this study, we eliminated all possible biases in constraining the parameters of binary black hole system GW150914, which may have otherwise resulted due to our assumptions in modeling of gravitational waveform or search techniques. The studies concluded the result is in agreement with the parameters quoted in table 8.2 [43].

In figure 8.8, we showcase the comparison between 900+ NR waveforrm from multiple research groups with the gravitational wave strain measured in the LIGO data at the GPS time of GW150914. Among the plotted simulation, about half of them are from the Georgia Tech Catalog showcased in chapter 3.

8.2 Estimating Sensitive Distance Based on Chirp-Mass

The only intrinsic parameters of binary black hole (BBH) that is reported as an output of the Coherent Wave Burst (cWB) algorithm is the chirp-mass $\mathcal{M}_c$ [1] of the system. As stated in chapter 6, the cWB algorithm computes chirp-mass based on the reconstructed waveform for a coherent GW signal measured in the two LIGO detectors. The chirp-mass is a tricky quantity, as for a fixed value we can have a large parameter space for the masses of individual black holes (see figure 8.9).

After the online (low-latency) search of cWB reported a possibility of BBH system of $\mathcal{M}_c \approx 30M_\odot$ (later confirmed as the first detection, GW150914), the author conducted offline (high-significance) studies to investigate the impact of the chirp-mass and individual black hole masses on the distance at which we can detect the system. The machinery to conduct these studies has been quoted in chapter 6 and 7.

The goal of this exercise was to essentially confirm if the transient burst search was sensitive enough to detect a GW150914 signal. At the time of this study, the two LIGO

[1] $\mathcal{M}_c = (m_1 m_2)^{3/5}/(m_1 + m_2)^{1/5}$

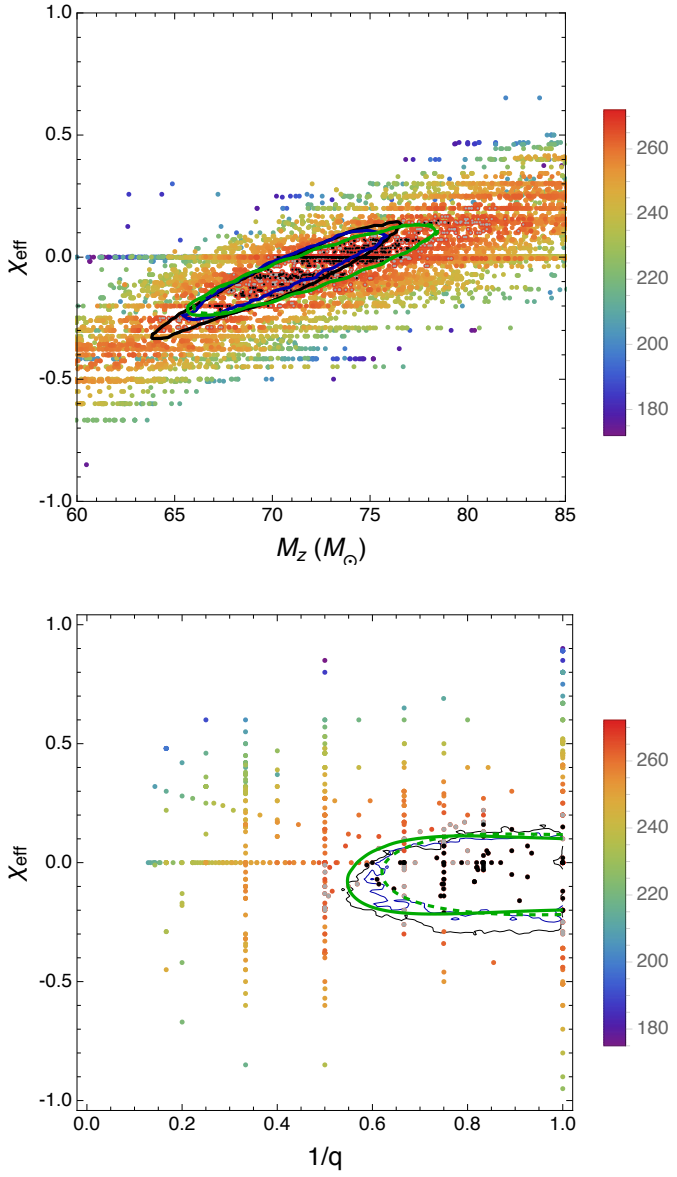

Figure 8.8: Direct comparison of NR simulations with the strain data from the LIGO detector at the GPS time of GW150914. Each dot is a distinct NR simulation from four different groups. There are 406 BBH simulations from the Georgia Tech Catalog in this plot. The plot on the top highlight the values of effective spin and total mass of GW150914 as constrained using this study. The plot on the bottom highlight the values of effective spin and mass-ratio of GW150914 as constrained using this study. The colors refer to a likelihood parameter of match between NR waveform and LIGO data (black being the highest match, orange being a medium match, purple being the least match). The black contour lines refer to the constrain obtained from an independent parameter estimation study. The blue and green contour lines refer to the constraints obtained through this study. Image credit: Richard OShaughnessy [43].

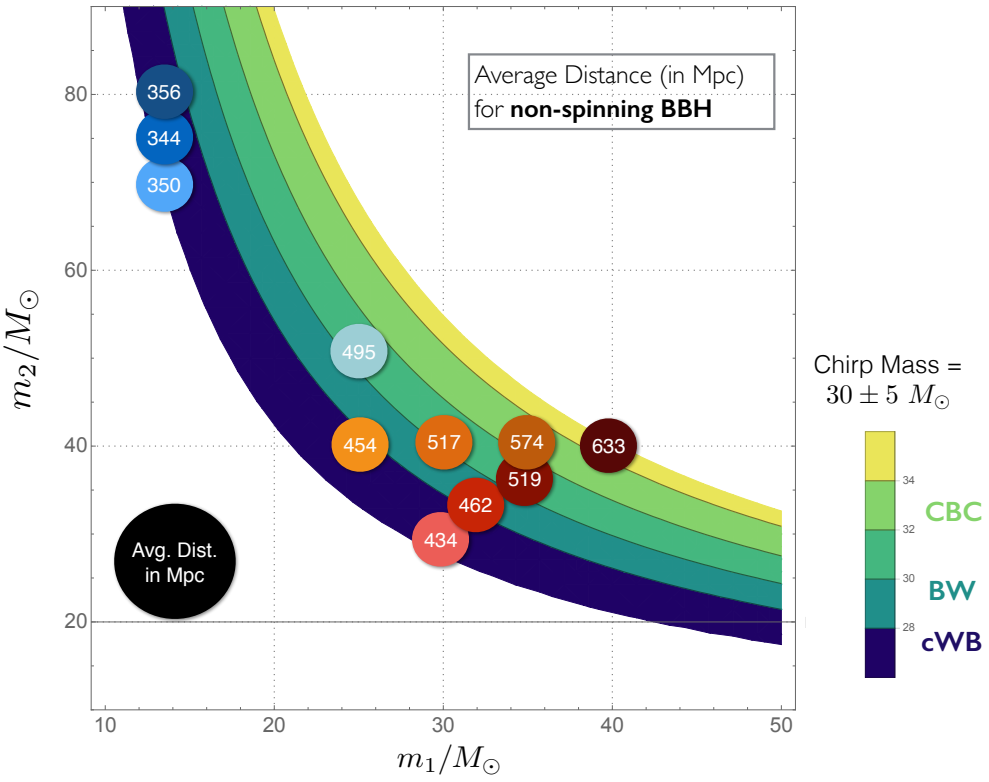

Figure 8.9: Possible values for the masses of individual black holes of GW150914 for the recorded chirp-mass by three different algorithms (cWB, BW, CBC). Circles highlight the sensitive distance to which we can detect these systems using the cWB algorithm

detectors had collected 15 days of coincident data since the start of First Observation Run (September 12 - October 15, 2016). Two studies were conducted as part of the investigation:

i. Injecting BBH signals of different individual black holes masses that are centered around $\mathcal{M}_c = 30 \pm 5 M_\odot$ (see figure 8.9 for the results). About 15,000 non-spinning BBH signals were injected for different values of m_1, m_2. The aim of this study was to obtain a quick overview on the distance to the source of GW150914. If the GW signal originated from the collision of two black holes of $\sim 30 M_\odot$ (as was the case that was confirmed later), then the maximum distance would have been about 450 Mpc for it to be detected by cWB.

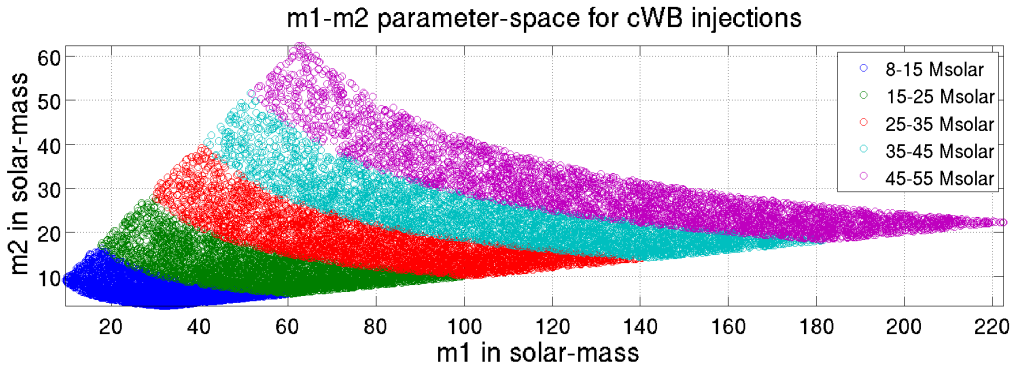

Figure 8.10: The parameter space of BBH injections in five chirp-mass bins are shown.

ii. Injecting BBH signals in five different bins of chirp-mass, ranging from $\mathcal{M}_c = 8M_\odot$ to $55M_\odot$ (figure 8.10). The aim for this was more comprehensive - to understand the detection threshold of cWB across ranges of individual black hole mass, including the accuracy with which it reports chirp-mass (see figure **??** for the results). Notice, that for lighter systems (low $\mathcal{M}_c$), the search distance remains fairly indifferent to the singificance at which we are quoting the numbers, i.e. the False Alarm Rate (FAR). However, at higher chirp-mass, the sensitivity is strongly dependent on FAR. A standard to quote the search distance is FAR per 1 year. The cWB algorithm had an average search sensitivity for a BBH system with chirp-mass $25 - 35M_\odot$ up to 400 Mpc. This was a confirmation that indeed it can detect a system like GW150914 with the current configuration.

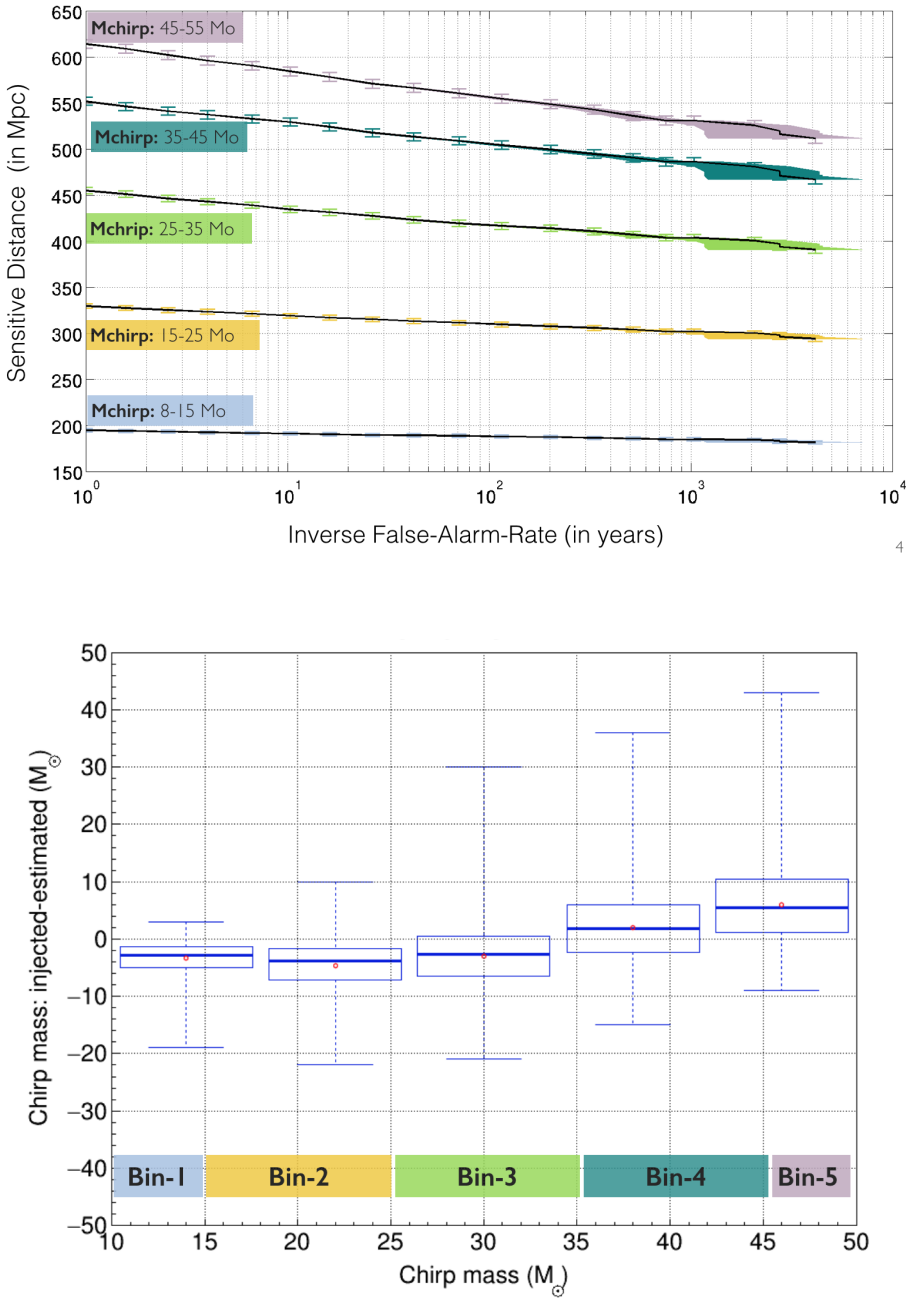

Figure 8.11: Effective chirp-mass on the sensitive distance as recovered by transient burst search. The center plot showcase the sensitive distance for each bin. The bottom plot displays the error between injected and recovered chirp mass of BBH with cWB algorithm.

Chapter 9

SEARCH FOR INTERMEDIATE MASS BLACK HOLE BINARIES IN THE FIRST SCIENCE RUN OF ADVANCED LIGO DETECTORS

Overview

The two Advanced LIGO detector in their first observational run (September, 2015 - January, 2016) had sensitivity to detect binary black hole mergers up to total-mass of $\sim 600M_{\odot}$ for an average all sky search radius of ~ 1 Gpc. The author developed the `IMBH` transient burst search in LIGO (Chapter 6, 7) to hunt for binary black holes within total mass range $50-600M_{\odot}$, for mass-ratios ≤ 10 and maximally aligned and anti-aligned spins. In this chapter, we report the non-detection of gravitational-waves from any heavier binary black hole merger than the one recorded earlier as heavy-stellar mass system, GW150914. An independent matched-filtering (modeled) search was also configured in the similar total-mass space and obtained similar results of non-detection. The discussion in this chapter is confined to the results from transient burst search, which the author conducted since the start of the engineering runs of Advanced LIGO. Based on this non-detection, we put astrophysical constraints on intermediate mass black hole binary mergers up to cosmological distance of redshift ~ 1. The most stringent limit on the rates is measured to be less than 0.88 Gpc^{-3}yr^{-1} for a merger of two individual $100M_{\odot}$ black holes at

the 90% confidence level. This is a factor of $\sim$ 1000 improvement in the observable search volume for intermediate mass black hole mergers compared to the last joint science run of LIGO and Virgo detectors. We discuss the astrophysical implications of this non-detection and explore the rates of such massive mass black hole mergers in the future observing runs of the Advanced detector network.

The chapter is organized as follow: section 9.1 describes the scope of this search, section 9.2 summarizes the configuration of transient burst search, section 9.3 describes upper limits on rates for varying mass-ratios and spins, in section 9.3.1 we highlights the importance of numerical relativity and higher modes in the future search, in section 9.4 we briefly sketch the astrophysical implications.

This work is currently is unpublished and under embargo [102]. The results highlighted in this chapter are done in collaboration with the IMBH WORKING GROUP *in LIGO. All the statements made here are in author's personal capacity and not an official statement on the search result from the LIGO Scientific Collaboration and Virgo Collaboration.*

9.1 Scope of The Search

The first observing run (O1) of the Advanced LIGO detectors took place from September 12, 2015 to January 19, 2016, with a total observation time of 44.8 days. The detectors were sensitive up to lowest frequency of 10 Hz, which sets a maximum detectable chirp-mass of BBH coalescence to $\sim$ $800M_{\odot}$ [103]. The only two GW events reported so far from O1 were BBH mergers GW150914 [20] and GW151226 [97], with an estimated chirp-mass in source frame to be $28.1M_{\odot}$ and $8.9M_{\odot}$ respectively. The corresponding component masses of the black holes in these systems are consistent with stellar evolutionary scenarios

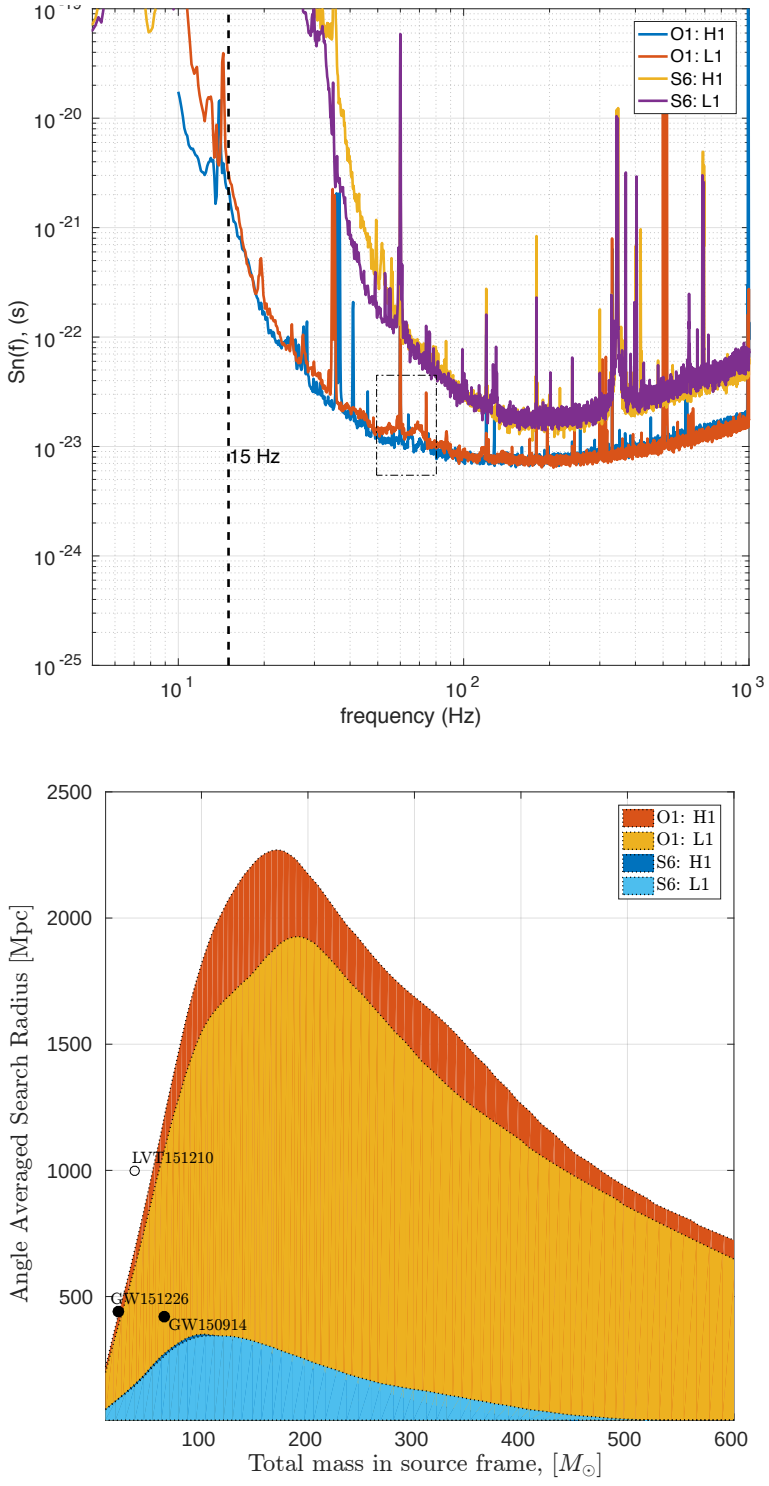

Figure 9.1: Horizon distances at optimal orientation for equal-mass BBH systems with a detection threshold of SNR=8 in O1. Comparison curves are also given for the previous S6 run.

[104], and both BBH systems merged at relatively nearby distance of ~ 450 Mpc [105, 47]. As GWs from BBH mergers will continue to dominate this era of gravitational-wave astronomy [105, 106], strongest astrophysical constraints can now be provided regarding the formation and growth of BHs beyond the stellar scenarios, in particular on the existence of intermediate mass black holes in our universe.

The mergers of such intermediate mass black holes is the most energetic GW sources for the Advanced LIGO and Virgo detectors and set the maximum horizon distance of a ground-based GW detector network (see 9.1). The last joint science searches of LIGO and Virgo detector had the detection sensitivity up to ~ 900 Mpc. In that comparison, the Advanced LIGO in its design sensitivity can reach up to horizon distances of ~ 10 Gpc [103]. The maximum detectable total-mass for an intermediate-mass black hole (IMBH) binary system is dictated by the the low frequency cutoff chose for the data processing in GW searches. The noise spectrum of O1 allowed frequencies ≥ 24 Hz [101], which corresponds to detectable IMBH binary mergers of total-masses $\leq 600 M_{\odot}$.

There are two independent search techniques that look for BBH systems in the LIGO-Virgo data: *matched-filtering searches*, which relies on best-match of signal with a BBH waveform models [105, 107]; and *unmodeled transient searches*, which looks for access of coherent power in the detector network. Match-filtering searches are efficient when BBH inspiral dominates signal morphology, while transient searches can identify burst-like signals beyond reach of approximate waveform models . In O1, both these searches looked for BBH mergers in the total-mass range of $\leq 100 M_{\odot}$ (and $\leq 150 M_{\odot}$ in burst search) and independently reported GW150914 with comparable significance [41, 107], while GW151226 was detected with higher significance by match-filtering searches [105].

In the previous IMBH binary searches in LIGO-Virgo data [108, 109], only unmodeled transient method was used to put limits on upper limit on merger rates of intermediate-mass black holes. For O1, a new separate search was inaugurated where both modeled and unmodeled methods produced independent data-processing which were specifically tuned

for robust detection of IMBH binary in the broadest intrinsic binary parameter space in LIGO-Virgo searches (masses: $m_1 + m_2 \in [50, 600] M_\odot,\ m_1/m_2 \leq 10$, spins:$\chi_{1z}, \chi_{2z} \in [-0.9, 0.9]$). The results presented in this paper are the combined statistics from both search technique. We report no that binary black hole larger than GW150914 was detected in O1. We use this non-detection to put the 90% upper limit on mergers of IMBH binary.

9.2 Search Technique

The unmodel transient search of IMBH binary uses the Coherent Wave Burst (cWB) algorithm [42]. This algorithm computes excess of coherent energy in the time-frequency decomposition between network of detectors and outputs a reconstructed signal of GWs. As this reconstruction of signal is agnostic to the modeling of the astrophysical source, this algorithm can be tuned for search of massive to eccentric binary black holes mergers [110, 111], supernovae explosions and binary neutron star mergers [112]. The binary black hole merger GW150914 was first picked up by an automated search using the cWB algorithm [113].

The version of the cWB code in the IMBH binary search is similar to the one used for GW150914 [41] and an all-sky search for lower mass binary black holes [99]. The tuning specific to the current IMBH binary search are, (i) data processing between $24 - 256$ Hz (within which resides binary $\geq 50 M\odot$) (ii) chirality constraint in the polarization of signal, so the algorithm is more robust in picking GW corresponding to coalescence of a binary (iii) less stringent post-production cuts to remove glitches, as signal from heavy-mass binary systems ($\geq 200 M_\odot$ LIGO records only merger-ringdown), possesses morphology similar to glitches.

For the IMBH binary search in O1, the cWB algorithm was used to produce a background set events of $\sim$ 1100 years by artificial time-slicing the 44.15 days of coincident data. This background set was used in finalizing the tuning such that the search was sensitive for binary black holes in total-mas range $50 - 600 M_\odot$. The only coincident

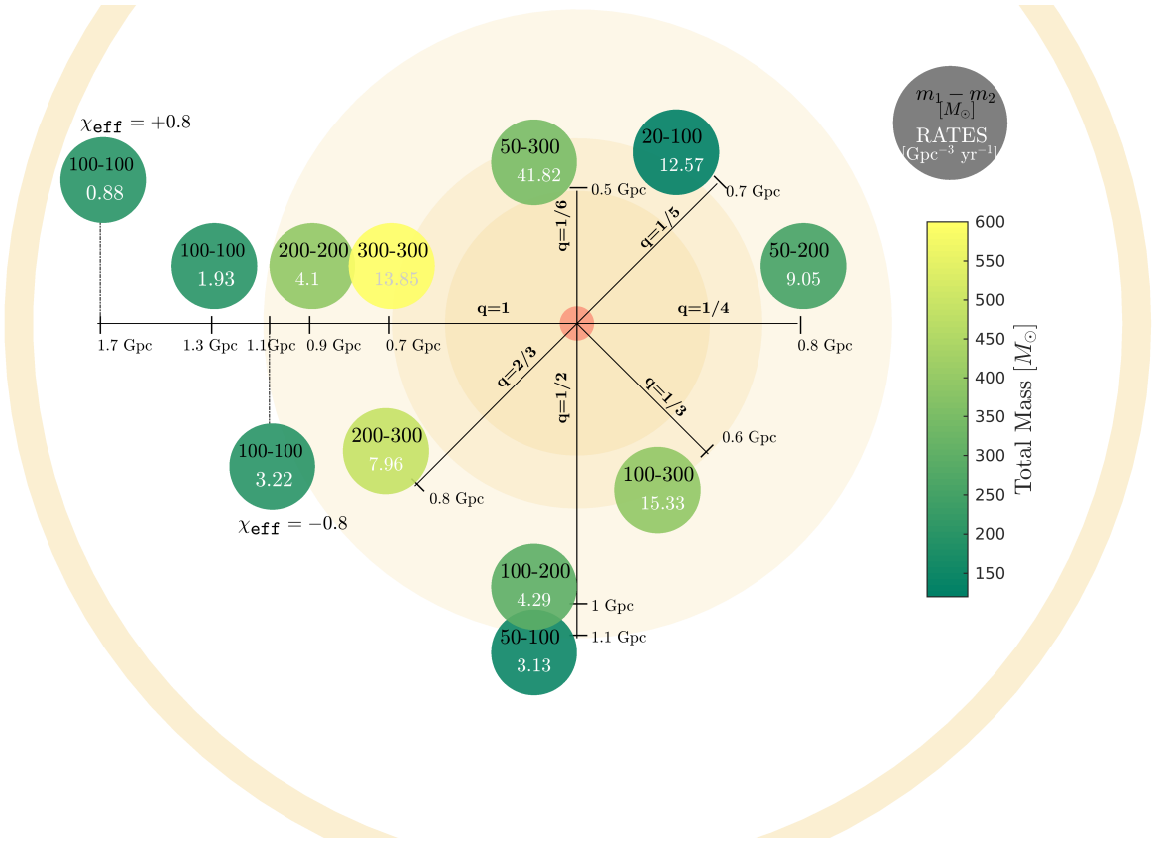

Figure 9.2: Search range in Gpc and 90%-confidence rate density upper limits in $\mathrm{Gpc}^{-3}\,\mathrm{yr}^{-1}$ for IMBH binary mergers in the first science run of Advanced LIGO. Each circle represents an all-sky injection of IMBH binary with component masses (m_1, m_2) and their corresponding upper limit rates. The lines represent constant mass-ratios $q = m_1/m_2$. The impact of spin (χ_{eff}) in search sensitivity is reported for 100–100$M_\odot$ system. For comparison, the binary neutron star search range is reported as the red circle at center. All reported quantities are in the source frame.

signal found in the O1 data of the two LIGO detectors using these specific cWB tuning was GW150914, with a p-value of 1.15×10^{-5}. This confirms that no binary black hole apart from GW150914 and LVT151012, has been detected in the O1 by unmodel searches. The background produced by cWB was utilized to compute the 90% upper-limit for IMBH binary mergers for unmodel search.

9.3 Upper-Limits on Merger Rates

This search spanned the largest sensitive volume to hunt for IMBH binaries than any other GW searches conducted so far. As we did not find any signal in the binary mass-range $\geq 100M_{\odot}$ during O1, this allows us to put constrains on the existence of such systems in the universe. We compute the upper-limits on the merger rates of IMBH binaries by utilizing the sensitive distance for a give intrinsic parameter of BBH and the total-time observation time during O1.

The procedure to compute sensitive distance is similar to the one described in chapter 6 and 7. We begin by injecting simulated BBH signal in the O1 data and recover these signals by utilizing the cWB algorithm with the configuration stated in the section 9.2. As the parameter space of IMBH binaries is fairly broad, we intend to get estimates on upper-limits of merger rates for only 12 'points' of parameter space of BBH masses and spins $(m_1, m_2, \chi_{\rm eff})$. We highlight these 12 points in figure 9.2. For each point, we inject about 100,000 simulated waveforms across the O1 data.

From the recovery of these injections by cWB algorithm, we compute sensitive distance $D_{\langle VT\rangle}$ for each of these 12 points. Our threshold to measure $D_{\langle VT\rangle}$ is for false alarm rate (FAR) of $\sim yr^{-1}$. The value of FAR is chosen based on the loudest coherent event found in our search which is not a GW detection. As the loudest event found in our search was GW150914, we pick FAR corresponding to the second loudest event. Based on the total observation time of O1 T_0 and sensitive distance, we then compute the spacetime volume $\langle VT\rangle \propto \left((D_{\langle VT\rangle})^3\, T_0\right)$ surveyed by our search for each of the 12 points of IMBH. Finally, we compute the rate of binary black hole merger with 90% confidence as following:

$$R_{90\%} = -\frac{\ln 0.1}{\langle VT\rangle} = \frac{2.303}{\langle VT\rangle}\,, \tag{9.1}$$

We quote this merger rates of BBHs in the units per cubic Gpc per year ($\mathrm{Gpc}^{-3}\,\mathrm{yr}^{-1}$).

9.4 Discussions

To compute our estimates on $R_{90\%}$, we inject BBH signals for 10 distinct points of masses m_1, m_2. For the case of $100 + 100M)_{\odot}$, we also inject BBH with aligned and anti-aligned spins. The results are highlighted in figure 9.2. Our maximum sensitive distance is 1.7 Gpc for a IMBH merger of two $100M_{\odot}$ black holes with aligned spin $\chi_{\rm eff} = +0.8$. For the black hole with similar masses but no spin can lower our sensitivity by 25%, while if the spins are anti aligned $\chi_{\rm eff} = -0.8$, we lose 72% of detection volume.

Our estimates on the rate of IMBH mergers are inversely related to sensitive volume. Therefore, our constraints on the existence of $100 + 100M_{\odot}$ an IMBH binary with aligned spins is $0.88\ \mathrm{Gpc}^{-3}\ \mathrm{yr}^{-1}$, and for with for same IMBH mass with anti-aligned spins $3.22\ \mathrm{Gpc}^{-3}\ \mathrm{yr}^{-1}$. Notice, the latter case has a comparatively higher value for merger rate. This does not imply the chances of LIGO detecting an anti-aligned spin IMBH merger is higher than that of an aligned or non-spinning IMBH. The rate is simply a statistical measure of constraints we report based on our sensitive volume. The lower our sensitivity, the weaker are our constraints, and therefore higher the estimates on $R_{90\%}$,

For a merger of two IMBHs of $300M_{\odot}$, our sensitive distance drops to 0.7 Gpc and $R_{90\%} = 13.85\ \mathrm{Gpc}^{-3}\ \mathrm{yr}^{-1}$. From all the injection sets show in figure 9.2, our lowest sensitivity is for a merger of an unequal mass binary, composed of a $50M_{\odot}$ stellar black hole and a $300M_{\odot}$ IMBH. Our estimates on the merger rates for this system is $41.82\ \mathrm{Gpc}^{-3}\,\mathrm{yr}^{-1}$.

Effect of Higher Modes: The numbers stated in figure 9.2 have been computing using gravitational waveforms from an approximate model (`SEOBNRv2`). As we shown in chapter 3, these model deviates from the GWs we obtained from NR simulations, especially for systems with high mass rations and total mass in the range of IMBH. Not including higher modes reduces the the total signal strength, and thus directly impact our sensitive distance and volume. In an ongoing study, the author repeated the analysis of previous section by injecting gravitational waveforms that contain higher harmonics (approximate

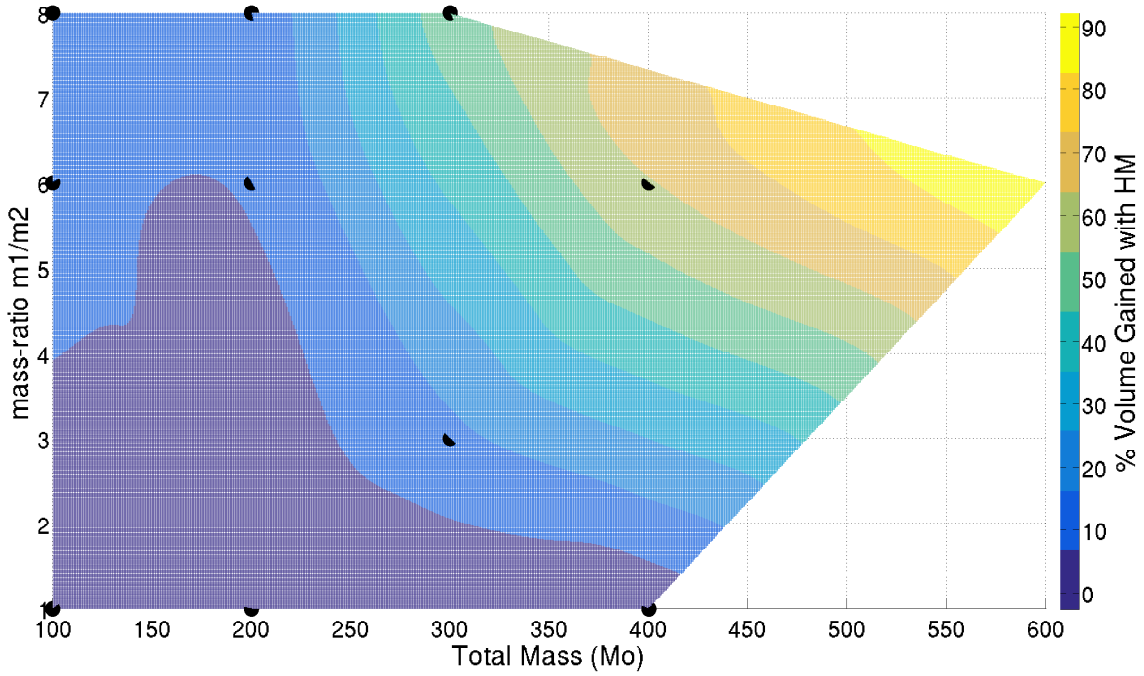

Figure 9.3: Increase in sensitive volume it the total mass range of intermediate mass black holes while utilizing gravitational waveforms with higher harmonic modes of radiation $\ell > 2$.

model: `EOBNRHM`). For IMBH binaries of total-mass $\geq 400M_{\odot}$ and mass-ratios ≥ 4, we gain 50% greater detection volume by including higher modes.

9.5 Astrophysical Implications of Results

The first detection of BBHs from GWs, GW150914, produced a remnant black hole of $\sim 70M_{\odot}$. This is the highest black hole mass recorded so far from the stellar evolution. Therefore, it is to fair hypothesize a population of black holes with similar or higher masses in the universe. As we highlighted in chapter 1, the mass of black holes can be divided in three bins based on their astrophysical origins,: (i) stellar black holes ($\sim 10M_{\odot}$), (ii) intermediate mass black holes (iii) super-massive black holes ($\sim 10^6 M_{\odot}$). Of these, the observational evidence and formation mechanism of i and ii have been fairly well understood. The theoretical motivations for astrophysical populations of intermediate mass

black holes have resulted from the mass gap that exist between between stellar and super-massive scales. In the literature, there are three primary formation scenarios proposed for formation of IMBHs [102]:

- from the collapse of the very first generations of stars in our universe, Population III, [114]
- from dynamical captures between stellar black holes and/or regular stars in dense stellar environment [115], and
- from an accretion of gaseous disk by a stellar black hole [116]

Independent of the formation mechanism, we can expect an IMBH to form a coalescing binary with a corresponding stellar black hole ($\leq 50M_{\odot}$) or an another IMBH ($\geq 100M_{\odot}$. Based on the results we discussed in earlier section and showcased in figure 9.2, we can constrain the coalescence-rate density, $R_{90\%}$, of IMBH binaries in the universe. Our stringiest constraints are $R_{90\%} = 0.88\,\mathrm{Gpc}^{-3}\,\mathrm{yr}^{-1}$ for IMBH binaries of total mass $200M_{\odot}$. For comparison, our lowest estimates on rates for coalescence of stellar BBH in the mass range of GW150914 and GW151226 is $9\,\mathrm{Gpc}^{-3}\,\mathrm{yr}^{-1}$ [44].

Therefore, our studies conclude that the existence of an IMBH in a binary is much rarer than that of a stellar BBH system. During the second science run (December 2016-current), we expect Advanced LIGO to be $\sim\ 20\%$ more sensitive for IMBHs than the results we present here from O1. If we continue to keep getting null results on IMBH binaries from our searches, then it strongly hints towards a real mass gap between stellar and super-massive black holes. However, a single detection from our search can provide an unambiguous confirmation on the existence of IMBHs in our uinverse.

Chapter 10

BINARY BLACK HOLES IN THE NEXT GENERATION OF GRAVITATIONAL WAVE EXPERIMENTS

Overview

In this era of gravitational wave astronomy, one of the most promising astrophysical source is intermediate mass black hole binary. The current generation of ground based gravitational wave experiments such as Advanced LIGO and Virgo have sensitivity to detect these astrophysical sources up to redshift ~ 1 and total-masses up to $\sim 10^3 M_\odot$. There is no unambiguous evidence of black holes at such masses and therefore their detection with gravitational waves can add valuable information to black hole formation channels. These sources also provide a unique opportunity to test general relativity in the multiband gravitational wave spectrum of space-based experiments (LISA) and next generation of ground-based experiments (Einstein Telescope, Cosmic Explorer).

In this chapter, the author demonstrates the sensitivity of binary black holes in this inaugural decade of gravitational wave astronomy, and the challenges that lie from the front of modeling and data analysis. This is currently an ongoing work [117].

10.1 Motivations

The detection of gravitational waves from the coalescence of black holes has inaugurated the era of gravitational wave astronomy. With two confirmed stellar BBH detection, GW15014 [**Abbott:2016blz**] and GW151226 [97], in the inaugural observation run of the Advanced LIGO detectors, our ground-based gravitational wave experiments have reached a sensitivity to detect $\sim$10 black hole mergers in a year of coincident data [105]. The inferred mass-spin parameters of GW150914 have already pushed our astrophysical inferences regarding formation mechanism of BBHs, while the non-detection of binary neutron stars and black hole-neutron star mergers have eliminated some of the most optimistic models [118]. Arguably, the most promising astrophysical source for this decade in the gravitational wave band is IMBH [119, 117].

During the first observation run, the two LIGO detectors were most sensitive for black hole mergers of total-mass $\sim 200M_{\odot}$. Compared to science observation runs during Initial LIGO (S5, S6), the search volume to detect such massive BBHs is a factor ~ 1000 more with the current sensitivity. Recent electromagnetic observations have found potential candidates of black holes in the IMBH mass-range [35, 34], however there is still no strong evidence of their existence, and no known signature of them forming a coalescing binary. If a gravitational wave signal is found in this mass range, it will be the strongest evidence on the existence of IMBHs, while a non-detection will provide the stringiest limit on the rate of mergers of such IMBHs that are potentially occurring in globular clusters within few Gpc. Therefore, gravitational wave astronomy promises the first cosmological survey of black holes between the stellar and super-massive scales.

10.2 A Science Case For Next Detectors

For the network of upcoming ground-based detectors of similar sensitivity as Advanced LIGO (by 2018: Virgo, 2019: KAGRA, 2023: LIGO-India), it has been shown that we

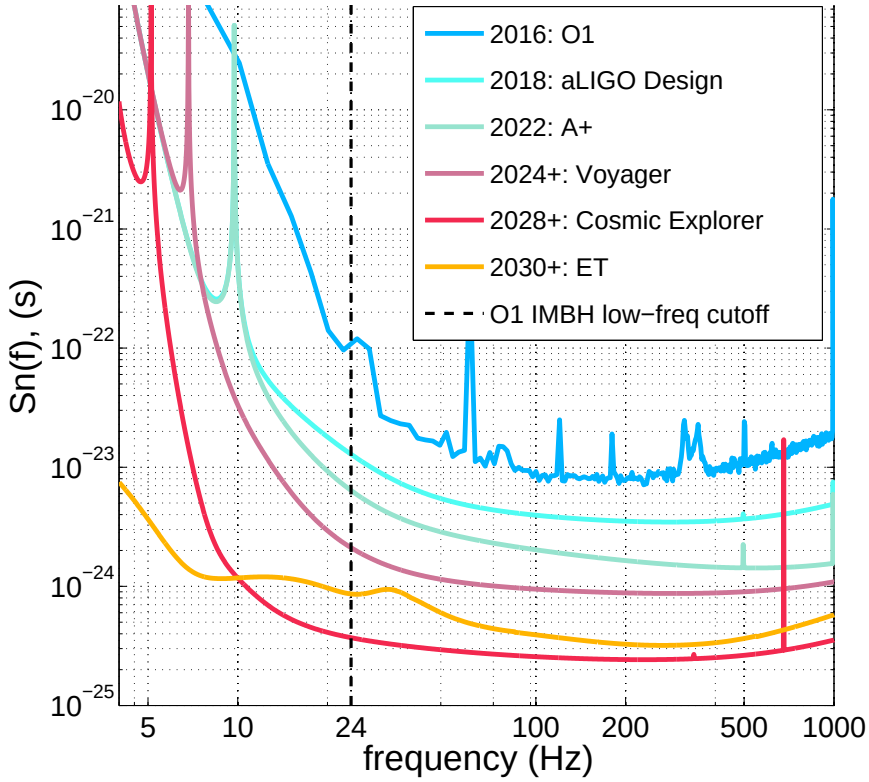

Figure 10.1: Sensitivity curves of the current and proposed ground-based gravitational wave experiments. Details about the listed experiments can be found in [120]. Timeline of the experiments are speculative.

substantially improve our estimates on sky-location and mass-spin of IMBH sources [121]. Further, the maximum mass of an BBH we can detect in a ground-based gravitational wave experiment is dictated by the low-frequency noise ($\leq$ 30 Hz for the current stage of Advanced LIGO, ref figure 10.1). In the coming decade, the planned upgrades in the network of LIGO detectors (2022: A+) and the proposed next-generation of ground-based gravitational wave experiments (Voyager, Cosmic Explorer, Einstein Telescope) are focused on reducing the low frequency noises ($10 \sim 30$ Hz). In these detectors, the sensitivity at ~ 10 Hz will be higher than our current best limits in the 'sensitivity bucket' at 100 Hz (see figure 10.1).

The enhanced sensitivity for gravitational waves at low frequency directly impacts the total-mass of BBH mergers that we can observe, as well pushes our over all signal-to-noise

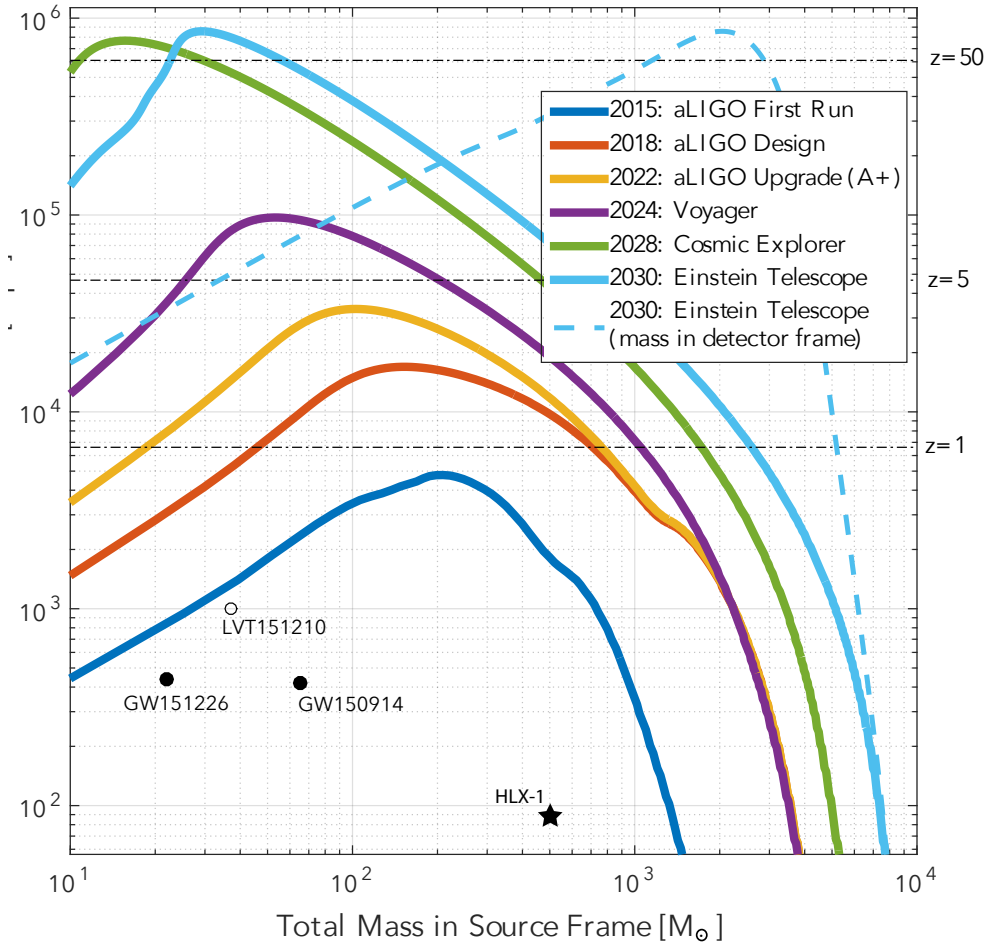

Figure 10.2: Horizon distance for equal-mass, non-spinning binary black hole systems in the current and proposed ground-based gravitational wave experiments. Here 'aLIGO First Run' refers to sensitivity of Advanced LIGO during detection of GW150914. The total-mass is computed in the source frame of BBH by taking into account the redshift corrections (dashed line is to interpret mass measured in detector frame). Circles refer to the remnant black holes produced from the binary black hole events published from the First Observation Run of Advanced LIGO (O1). The star refers to an intermediate mass black hole candidate from electromagnetic observations.

ratio. By 2022, we expect to probe mergers of IMBH binaries of total-mass $\sim 10^4 M_\odot$, and up to cosmological distances of red-shift $\sim$5 (see figure 10.2).We expect the peak of mergers of intermediate mass binary black holes occur in our cosmic history around red-shift of 3. Thus, a non detection of IMBH merger in the next few years can severely

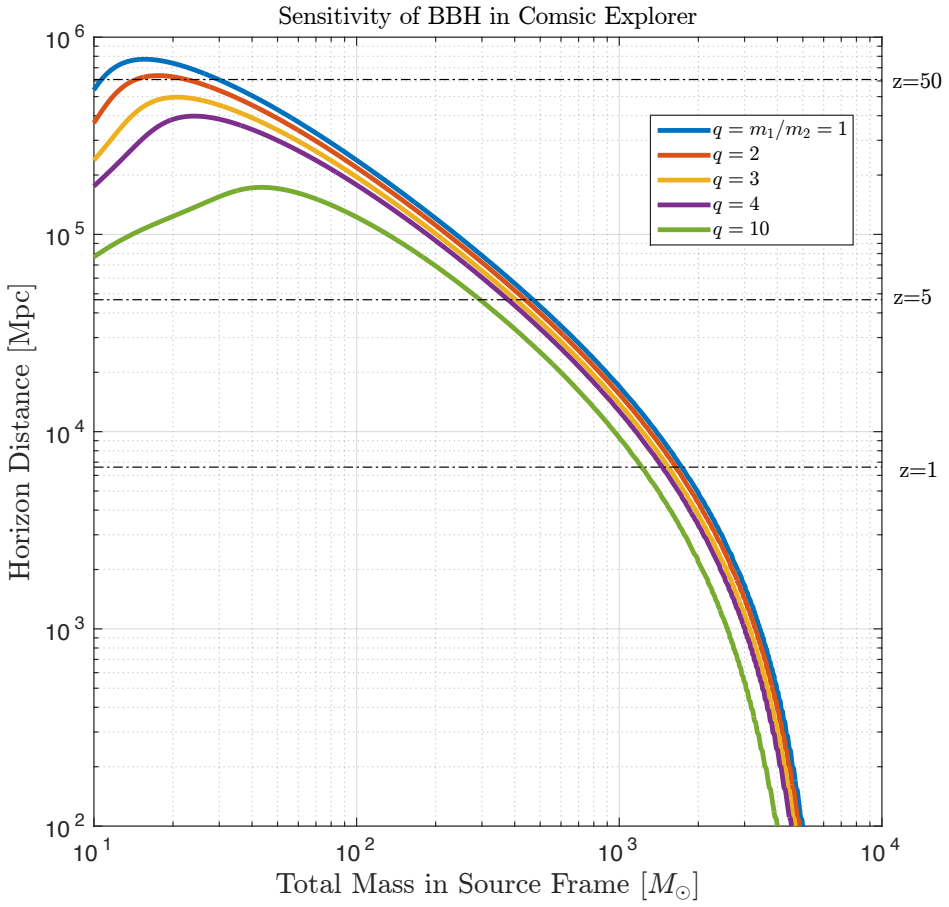

Figure 10.3: Horizon distances in Cosmic Explorer (2028+) for binary black holes with unequal masses. The plot is an extension of the sensitivity studies of Cosmic Explorer show in figure 10.2.

constrain the coalescence rate we expect to see in milli-Hz frequency band of space-detector such as LISA.

On the other hand, a gravitational wave detection of an IMBH merger in the ground-based detectors confirms a population of astrophysical sources we expect to dominate in the LISA band. In an era when both LISA and LIGO-like detectors are simultaneously hunting for cosmic gravitational waves, these IMBH binaries will be of special interest, as we expect to first see their coalescence in space detectors, and then their merger and ringdown in ground detectors. These allows an unique opportunity to test General Relativity ('no-

hair' theorem, mass of graviton) by independently measuring the pre- and post-merger parameters of the binary [122, 123].

An earlier study by the author shown that the initial orbital position of the three LISA satellites can be configured such that we alter the average sensitivity for specific parts in sky [124]. Therefore, we can purposefully 'blind' the known sources of background noise (binary white dwarf), while enhance our sensitivity for the globular clusters that we expect to be the hive of IMBH binaries.

10.3 Challenges From Gravitational Wave Data Analysis

The scenarios of observable IMBHs in gravitational wave band can be classified depending on their astrophysical environments and evolutionary stage. In the coming decade, we expect ground based gravitational wave experiments to potentially detect one of these three cases of IMBH systems:

- `CASE-A`: merger of two IMBHs, where mass of each black hole is $\sim 10^2 M_\odot$ [125]
- `CASE-B`: coalescence of a stellar black hole or a neutron star with an IMBH (mass-ratios $\geq 10 - 100$, see figure 10.3)
- `CASE-C`: ringdown from a perturbed IMBH ($\sim 10^3 M_\odot$) [126]

In all these cases, the conventional template bank based matched-filtering searches of gravitational waves [107] may prove limiting as,

- the radiated energy from such high-mass IMBH systems are not accurately modeled by approximate gravitational waveform [21],
- the gravitational waves from IMBHs in the ground-based detectors are of transient nature (total signal size $\sim$0.1s), and

- the low frequency gravitational waves emitted from IMBHs overlap with the seismic noise limit of ground-based experiments.

Therefore, an optimized search of gravitational waves from IMBHs in this future detectors will require a holistic framework, where (i) data-analysis techniques, (ii) modeling of the astrophysics and (iii) understanding of the instrumental noise, each demand coordinated efforts.

Interface with Electromagnetic Observations and Cosmological Simulations: The current IMBH searches in Advanced LIGO spans the largest parameter space compared to any other astrophysical binary source (total-mass: $50 \sim 10^3 M_{\odot}$, mass-ratios ≤ 10, align-spin configurations, zero eccentricity). However, this still does not cover all the possible parameter space of IMBH, and we are practically limited by computing resources. Providing inferences about parameters of IMBH and their astrophysical environments from,

- potential IMBH candidates observed in x-ray with *Chandra*, *XMM Newton*, as well their followup in broad electromagnetic band by *Hubble Space Telescope* [33], and
- *N*-body simulations of star clusters [127], and cosmological simulations of sub-parsec resolution

will boost the efforts for gravitational wave modeling and data-analysis tools. For example, if eccentricity is exhibited in dynamical captures forming IMBH binaries (`CASE-A`) or if neutron star is a favored component (`CASE-B`), then one can push numerical relativity efforts in modeling of such astrophysical sources [26], and develop algorithms to detect such distinct gravitational wave morphology, which are currently not accessible to template bank search [111].

Future Work: A systematic investigation on the impact of intrinsic parameters of IMBHs (mass-ratio and spins) on the detection sensitivity for all the proposed ground-based detectors (example shown for Cosmic Explorer in figure 10.3) is being currently pursued. Further, we will make a quantitative assessment on our search volume and merger rates in these detectors compared to the numbers obtained in current IMBH search in LIGO (chapter 9).

Chapter 11

CONCLUSION AND SUMMARY

The work presented in this thesis spanned from the investigation of a binary black hole (BBH) evolution - inspiral, merger, rigndown - in extreme gravity, to developing an observational search for gravitational waves from the coalescence of BBHs, to, finally, confirming the very first coincident signal recorded in the two LIGO detectors as a direct detection of gravitational waves (GWs) from a BBH merger of cosmic origins.

The theoretical studies were conducted by solving the Einstein's Equations in the numerical relativity simulations on **supercomputers** (Part I); the observational search was performed for GWs of transient nature in the data from Advance **LIGO** since mid-2015 (Part II); and these combined learning were applied in enhancing our astrophysical understanding of stellar and intermediate mass BBHs in the **universe** (Part III).

By showcasing the example of the first BBH detection, GW150914, in Chapter 2, we provide a recipe to conduct numerical relativity simulations of generic BBH systems and post-processing of the simulation output (see figure 11.1). As we expect to routinely observe BBHs in this era of gravitational wave astronomy, in Chapter 3 we present the publicly available Georgia Tech Catalog of numerical relativity simulations (einstein.gatech.edu/catalog). With 452 distinct simulations, this catalog spans a large intrinsic parameter space for BBHs, from mass-ratios $m_1/m_2 \leq 15$ to generic spin orientation of individual black holes. Most of the simulations from this catalog were directly utilized in constraining the astrophysical parameters of the first BBH detection, GW150914 (Chapter 8). Further, we demonstrated three applications of this catalog for

understanding of the dynamics of BBHs in extreme gravity and enhancing tools for GW data-analysis: (i) accessing the accuracy of approximate GW models utilized in detection and parameter estimation of BBH coalescence in LIGO, as well as of phenomenological fits of remnant black hole that tests General Relativity (Chapter 3), (ii) dissecting the complex behavior on BBHs with precessing spins, and shedding light on spin-spin and spin-orbit coupling between black holes (Chapter 4), and (iii) making a case for information visualization techniques to decode non-linear dynamics in General Relativity (Chapter 5).

Prior to the detection of BBHs in the First Observation Run (O1) of Advance LIGO (from September 12, 2015 - January 19, 2016), our constraints on the astrophysical parameters of these sources were fairly poor. Also, as we noted in Chapter 3, the approximate models of gravitational waveforms agree with the numerical relativity solutions for only a range of parameters. Therefore, the strategy the author adopted was to hunt for GWs in LIGO without adding any assumptions on the expected morphology of the signal from coalescing BBH. This methods fall under a broad class of transient burst searches of GWs, as they primarily rely on detecting a sudden excess of coherent power in a coincident data from a network of detectors. The algorithm we utilized to conduct the search for BBHs in ~ 45 days of coincident LIGO data, COHERENT WAVE BURST (cWB), was also the first to detect GW150914. In Chapter 6, we provide a high level overview on the steps involved in optimizing cWB to search for BBH mergers in O1 within GW frequency range of $16-512$ Hz. The most crucial an computationally intensive step in running cWB is to utilize coincident data of O1 produce an artificial data stream of $\sim 1,100$ years and estimating rate of background noise occurring from environmental and instrumental glitches at the two LIGO sites. After listing a set of production and post-production cuts of cWB to clean this background, we discuss in detail in Chapter 7 our sensitivity to detect BBH in the total mass range $20-600M_{\odot}$. Astrophysically, this corresponds to BBH composed of stellar and intermediate mass black holes. In doing so, we narrate the machinery of injecting simulated BBH signals in O1, recovering them

using cWB and thereafter computing the sensitive distance $D_{\langle \mathrm{VT} \rangle}$ of our search for a given intrinsic parameter of BBH (masses, spins). We demonstrate that during O1, the cWB search the author configured had an average detection radius of ~ 1 Gpc for intermediate mass BBH and ~ 0.5 Gpc for stellar BBH at a significance of false alarm rate 1 per 100 years. To understand the coupling of instrumental noise with GWs from intermediate mass black hole binaries, we also showcase the hardware injections that the author conducted at the LIGO detectors while being a resident fellow on site. Both the Chapters 6 and 7 are part of the 'closed-box' studies, i.e. we conduct them to tune our search for GWs before biasing ourselves by looking for a coincident GW in the LIGO data.

On September 14, 2015, the low-latency search of cWB (agnostic to any astrophysical source) detected a coincident GW trigger in both the LIGO detectors. The chirp-mass measured by cWB reconstruction of this signal, $\mathcal{M}_c = 30 \pm M_\odot$, indicted the source had to be a merger of some heavy BBH system. During the initial period, the intrinsic parameter of this potential BBH system (masses, spins) remained unknown. Therefore, we took 104 of BBH simulations from the Georgia Tech Catalog in this chirp-mass range and compared with the reconstructed signal. Four more targeted simulations worth about 150k SUs were also conducted as followups. As we shown in Chapter 8, the result from our study were pointing the signal was matching a BBH system of two almost equal-mass black holes, with their net spins canceling in the direction of orbital angular momentum. Our estimates on the individual black hole mass and spins were consistent with other independent parameter estimation studies conducted using approximate GW models. As no assumption about the source went in the reconstruction of the signal with transient burst search, and as our numerical relativity simulations were the exact solution of Einstein's Equations, this study provided a strong, independent check on GW150914 being a BBH merger as predicted by General Relativity. A similar comparison with numerical relativity waveforms was repeated on the GW strain recorded by two LIGO detectors at the GPS time of GW150914. In this study, 406 simulations from the Georgia Tech Catalog were utilized, and the results were

found to be consistent with the parameters we obtained with the reconstructed waveform. With both these studies, the first detection of BBH portrayed the strong role that numerical relativity will go on to play in this era of gravitational wave astronomy. Further, for a variety of combinations of BBH parameters, we computed the sensitive distance for cWB configured to search for GWs from BBH merger. This provided an estimate that for binary of two $30M_{\odot}$ black holes, the farthest we could have detected using transient burst search was $\sim$ 450 Mpc. These distance estimates were in agreement with other independent parameter estimation studies.

During O1, the two LIGO detectors had their maximum sensitivity for a merger of two $100M_{\odot}$ black holes, with horizon radius up to ~ 5 Gpc. This was our primary motivation in searching for GWs in O1 from the mergers of intermediate mass black hole binaries (Chapter 9). As showcased in the 'closed-box' studies in Chapter 7, we had a strong readiness to detect BBH in the mass range $50 - 600M_{\odot}$, mass-ratio $1 - 10$ and generic spins. However, the cWB search we configured did not find any BBH system other than GW150914 in O1. These non-detection were utilized to provide the upper-limit on the rate of intermediate mass black hole binaries in the universe with 90% confidence. The most stringent limit was measured as 0.88 Gpc^{-3}yr^{-1}, which is a factor of 1000 improvement compared to the similar limits quoted from the earlier observation of LIGO (2010 and before).

As all the three GW candidates that were found in O1 were consistent with BBH coalescence, with two of them, GW150914 and GW151226, being confirmed with 5σ-confidence, BBHs now occupy the status of most promising sources in this inaugural decade of GW astronomy. In Chapter 10, we highlight the sensitivity of BBH in the stellar and intermediate mass range ($\leq 10^4 M_{\odot}$) for all the proposed next generation of ground-based GW experiments. By 2022, our sensitivity to detect intermediate black holes will reach cosmological distances of red-shift ~ 3. A detection or non-detection of these systems by then puts a strong constraints on the astrophysical population we expect in the

ground-based GW detectors such as LISA.

In conclusion, the end-to-end investigation of binary black hole systems provided in this thesis sets the narrative for the holistic and collaborative approach demanded in terms of modeling, data-analysis and understanding of instrumental noise for searching exotic astrophysical sources in this era of gravitational wave astronomy. The analysis presented in this thesis can be naturally extended for future ground and space-based GW experiments, and the results narrated may further the inferences regarding the formation mechanism of black holes in our universe and in testing of theories beyond General Relativity. Welcome to the new age of astronomy!

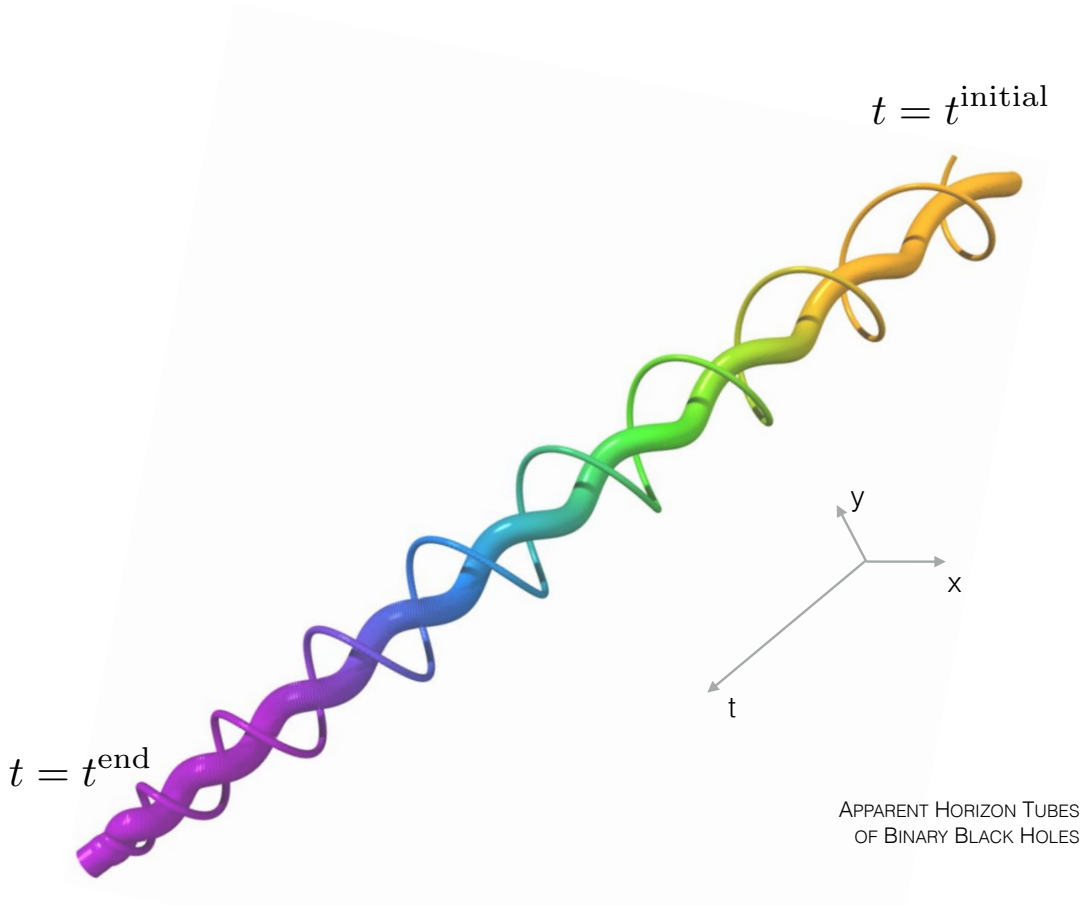

Figure 11.1: Apparent horizon tubes of a binary black hole system from the start to end of a numerical relativity simulation. The data has been obtained from the the Georgia Tech Catalog.

Appendices

Appendix A

GLOSSARY OF BINARY BLACK HOLE PARAMETERS

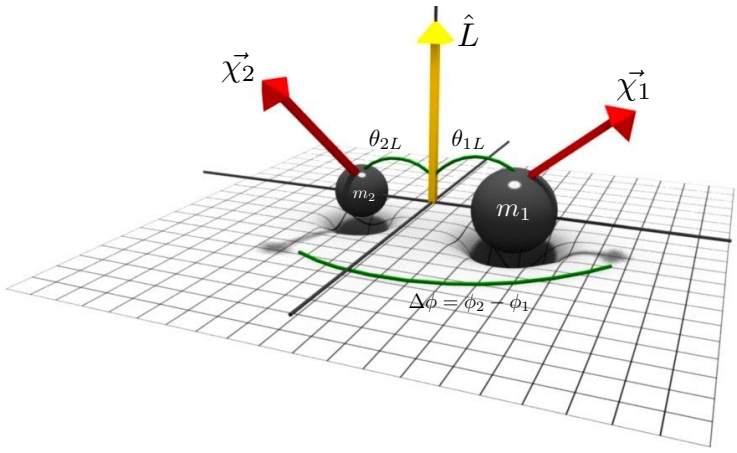

Figure A.1: Diagrammatic representation of a generic spin configuration of an relevant components of binary black hole in numerical relativity simulations.

A note on Initial Data of BBH for NR simulations: Chapter 2,3

- $M \equiv m_1 + m_2 \equiv 1$ for all NR BBH simulations
- m_1 := mass of bigger black hole (BH)
- m_2 := mass of smaller BH
- $\mathbf{S_1}$:= spin vector of bigger BH
- $\mathbf{S_2}$:= spin vector of smaller BH

- $\mathbf{p_1}$:= linear momentum of bigger BH
- $\mathbf{p_2}$:= linear momentum of smaller BH
- $\mathbf{r_1}$:= position of BH-1 from center of mass
- $\mathbf{r_2}$:= position of BH-2 from center of mass

A note about typical initial data of quasi-circular BBH: Chapter 2,3

- The center of mass of BBH is the origin of the coordinate systems
- The BHs are placed in the grid such that $\mathbf{r_{1,2}}$ have only x-components. So the separation between two BHs can be defined as $b = r_{1x} - r_{2x}$.
- The linear momentum are set such $\mathbf{p_1} = -\mathbf{p_2}$ and the momentum has only x-component

A note about spins: Chapter 2,3,4

- $\mathbf{a_1} \equiv \mathbf{S_1}/m_1^2$:= dimensionless spin vector of bigger BH
- $\mathbf{a_2} \equiv \mathbf{S_2}/m_2^2$:= dimensionless spin vector of smaller BH
- $|\mathbf{a_{1,2}}| \in [\mathbf{0}, \mathbf{1}]$:= these dimensionless spins are the Kerr-parameters of each BH, with 0 being non-spinning BH, and 1 being maximally spinning BH.

A note about angular momentum: Chapter 4,5

- $\mathbf{L_N} \equiv (\mathbf{r_1} \times \mathbf{p_1}) + (\mathbf{r_2} \times \mathbf{p_2})$:= Newtonian Orbital Angular Momentum of BBH
- $\mathbf{J} = \mathbf{L} + \mathbf{S_1} + \mathbf{S_2}$:= Total Angular Momentum of BBH
- $\mathbf{J}$ can be computed using two ways (i) by measuring evolution of $\mathbf{L}$ and $\mathbf{S}$, which we will refer as $\mathbf{J_N}$ (ii) computing it directly from the radiated GWs, which we will refer as $\mathbf{J_R}$

- Note $\mathbf{J_N} \neq \mathbf{J_R}$.
- Similarly, $\mathbf{L_N} \neq \mathbf{L_R}$, where $\mathbf{L_R} = \mathbf{J_R} - \mathbf{S_1} - \mathbf{S_2}$.

A note about parameters of the remnant / final BH : Chapter 2,3,4,5

- m_F := mass of the final BH.
- $\mathbf{S_F}$:= spin of the final BH
- $|\mathbf{a_F}| = |\mathbf{S_F}|/m_F^2 \leq [0, 1]$:= dimensionless spin of the final BH
- Note, spin and mass of remnant BH can be computed using two methods (i) by measuring the shape of apparent horizon (more accurate) (ii) by measuring the radiated energy and total angular momentum from GW
- $\mathbf{v_F}$:= kick / velocity of the final BH. This quantity can be computed only from radiated GWs

Note about radiated quantities we can obtain from ψ_4 (i.e. GWs): Chapter 4,5 .

- Look for formula from the Alcbr.. paper.
- E_{RAD} := Binding energy radiated as GWs.
- $\dot{E}$:= Luminosity in GWs. Time integration of this quantity gives E_{RAD}
- $d\mathbf{J}/dt$:= Radiated total angular momentum. Time integration of this quantity gives $\mathbf{J_R}$.
- $d\mathbf{p}/dt$:= Radiated linear angular momentum. Time integration of this quantity provides information about $\mathbf{v_F}$.
- All the radiated quantities are dependent on radius of extraction. The true values of these quantities are defined at infinity.

A note about reduced mass and spin: Chapter 4,5

- $q \equiv m_1/m_2 \geq 1$:= mass-ratio of BBH
- $\eta = q/(1+q)^2$:= symmetric mass-ratio of BBH
- $\chi_{eff} \equiv \left(\frac{\mathbf{S_1}}{m_1} + \frac{\mathbf{S_2}}{m_2}\right) \cdot \hat{\mathbf{L}}_\mathbf{N} = (q\, a_{1z} + a_{2z})/(1+q) \in [-1, 1]$:= effective spin
- χ_p := in-plane spin (re-look at definition)

A note on intrinsic components of spin used for studying BBH precession: Chapter-4

- $\theta_{1L} \equiv \cos^{-1}\left(\hat{\mathbf{a}}_\mathbf{1} \cdot \hat{\mathbf{L}}\right)$:= polar angle between spin of BH-1 and the orbital angular momentum.
- $\theta_{2L} \equiv \cos^{-1}\left(\hat{\mathbf{a}}_\mathbf{2} \cdot \hat{\mathbf{L}}\right)$:= polar angle between spin of BH-2 and the orbital angular momentum.
- $\phi_1 \equiv \sin^{-1}\left(\hat{\mathbf{a}}_\mathbf{1} \times \hat{\mathbf{L}}\right)$:= azimuthal angle between spin of BH-1 and the orbital angular momentum.
- $\phi_2 \equiv \sin^{-1}\left(\hat{\mathbf{a}}_\mathbf{2} \times \hat{\mathbf{L}}\right)$:= azimuthal angle between spin of BH-2 and the orbital angular momentum.
- $\Delta\phi = \phi_2 - \phi_1$:= Typically used in literature to differentiate two types of spin-orbit coupling. $\phi = 0$ and $\phi = \pi$.
- Note: The coordinates are set such that +z-direction corresponds to $\theta_{1L,2L} = 0$ and +x-direction corresponds to $\phi_{1,2} = 0$. If either of the black holes are not spinning, then $\theta_{1L,2L} = \phi_{1,2} =$ NaN.

A note on various angles used in studying spin-orbit coupling of BBH: Chapter-4

- $\alpha(r) \equiv$ Angle between total angular momentum, $\mathbf{J} \equiv \mathbf{L} + \mathbf{S_1} + \mathbf{S_2}$ and final spin $\mathbf{S_F}$ (or final total angular momentum at $r \sim 0$)

- $\beta(r) \equiv$ Angle between orbital angular momentum $\mathbf{L}$ and total spin, $\mathbf{S_{Tot}} = \mathbf{S_1} + \mathbf{S_2}$
- $\beta_{EF}(r) \equiv$ Angle between orbital angular momentum $\mathbf{L}$ and effective spin [96], $\mathbf{S_{EF}} = (1+q)\mathbf{S_1} + (1+\frac{1}{q})\mathbf{S_2}$
- $\gamma(r) \equiv$ Angle between both the spins $\mathbf{S_1}$ and $\mathbf{S_2}$
- $\zeta(r) \equiv$ Angle between between orbital angular momentum $\mathbf{L}$ and radiated angular momentum $-\dot{\mathbf{J}}$.
- $\iota(r) \equiv$ The change in orbital inclination angle

REFERENCES

[1] A. Einstein, "The field equations of gravitation," Sitzungsber. K. Preuss. Akad. Wiss., p. 696, 1915.

[2] A. Einstein, "Uber einen die erzeugung und verwandlung des lichtes betreffenden heurischen gesichtpunkt," Ann. Phys., vol. 17, pp. 132–148, 1905.

[3] A. Einstein, "Approximative integration of the field equations of gravitation," Sitzungsber. K. Preuss. Akad. Wiss., p. 688, 1916.

[4] E. Conover, "Einstein's milestones," Science, vol. 347, no. 6226, pp. 1085–1097, 2015. eprint: http://science.sciencemag.org/content/347/6226/1085.full.pdf.

[5] K. Schwarzschild, "On the gravitational field of a mass point according to einstein's theory," Abh. Konigl. Preuss. Akad. Wissenschaften Jahre 1906,92, Berlin,1907, vol. 1916, 1916.

[6] R. P. Kerr, "Gravitational field of a spinning mass as an example of algebraically special metrics," Phys. Rev. Lett., vol. 11, pp. 237–238, 5 1963.

[7] D. Finkelstein, "Past-future asymmetry of the gravitational field of a point particle," Phys. Rev., vol. 110, pp. 965–967, 4 1958.

[8] C. V. Vishveshwara, "Generalization of the "schwarzschild surface" to arbitrary static and stationary metrics," Journal of Mathematical Physics, vol. 9, pp. 1319–1322, Aug. 1968.

[9] C. V. Vishveshwara, "Stability of the schwarzschild metric," Phys. Rev. D, vol. 1, pp. 2870–2879, 10 1970.

[10] C. V. VISHVESHWARA, "Scattering of gravitational radiation by a schwarzschild black-hole," Nature, vol. 227, no. 5261, pp. 936–938, Aug. 1970.

[11] S. Chandrasekhar, "The maximum mass of ideal white dwarfs,", vol. 74, p. 81, Jul. 1931.

[12] K. Thorne and W. Press, "Gravitational-wave astronomy," Annual Review of Astronomy and Astrophysics, vol. 10, no. 1, pp. 335–374, 1972. eprint: http://dx.doi.org/10.1146/annurev.aa.10.090172.002003.

[13] R. Weiss, "Electromagnetically coupled broadband gravitational antenna," Quarterly Report of the Research Laboratory for Electronics, MIT Report, 1972.

[14] P. Laguna and D. Shoemaker, "Numerical stability of a new conformal-traceless 3 + 1 formulation of the einstein equation," Classical and Quantum Gravity, vol. 19, pp. 3679–3686, Jul. 2002. eprint: gr-qc/0202105.

[15] W. Tichy, B. Brügmann, and P. Laguna, "Gauge conditions for binary black hole puncture data based on an approximate helical killing vector,", vol. 68, no. 6, 064008, p. 064 008, Sep. 2003. eprint: gr-qc/0306020.

[16] F. Pretorius, "Evolution of binary black-hole spacetimes," Phys. Rev. Lett., vol. 95, p. 121 101, 12 2005.

[17] M. Campanelli, C. O. Lousto, P. Marronetti, and Y. Zlochower, "Accurate evolutions of orbiting black-hole binaries without excision," Phys. Rev. Lett., vol. 96, p. 111 101, 11 2006.

[18] J. G. Baker, J. Centrella, D.-I. Choi, M. Koppitz, and J. van Meter, "Gravitational-wave extraction from an inspiraling configuration of merging black holes," Phys. Rev. Lett., vol. 96, p. 111 102, 11 2006.

[19] R. W. P. Drever, F. J. Raab, K. S. Thorne, R. Vogt, and R. Weiss, " laser interferometer gravitational-wave observatory (ligo) technical report," 1989.

[20] B. P. Abbott and et al., "Observation of gravitational waves from a binary black hole merger," Physical Review Letters, vol. 116, no. 6, 061102, p. 061 102, 2016. arXiv: 1602.03837 [gr-qc].

[21] K. Jani, J. Healy, J. A. Clark, L. London, P. Laguna, and D. Shoemaker, "Georgia tech catalog of gravitational waveforms," Classical and Quantum Gravity, vol. 33, no. 20, p. 204 001, 2016.

[22] R. Arnowitt, S. Deser, and C. W. Misner, "Dynamical structure and definition of energy in general relativity," Physical Review, vol. 116, pp. 1322–1330, Dec. 1959.

[23] T. W. Baumgarte and S. L. Shapiro, "On the numerical integration of Einstein's field equations," Phys. Rev. D, vol. 59, p. 024 007, 1999.

[24] J. Healy, T. Bode, R. Haas, E. Pazos, P. Laguna, D. M. Shoemaker, and N. Yunes, "Late inspiral and merger of binary black holes in scalar-tensor theories of gravity," Classical and Quantum Gravity, vol. 29, no. 23, 232002, p. 232 002, Dec. 2012.

[25] T. Bode, T. Bogdanovic, R. Haas, J. Healy, P. Laguna, et al., "Mergers of supermassive black holes in astrophysical environments," Astrophys.J., vol. 744, p. 45, 2012.

[26] M. Clark et al., "Bowen-york-type initial data for binaries with neutron stars,", vol. 94, no. 6, 064058, p. 064 058, Sep. 2016. arXiv: 1606.04881 [gr-qc].

[27] S Chandrasekhar, The mathematical theory of black holes, ser. Oxford classic texts in the physical sciences. Oxford: Oxford Univ. Press, 2002.

[28] S. E. Woosley, A. Heger, and T. A. Weaver, "The evolution and explosion of massive stars," Rev. Mod. Phys., vol. 74, pp. 1015–1071, 4 2002.

[29] H. Sana, E. Gosset, and C. J. Evans, "The massive star binary fraction in young open clusters ii. ngc 6611 (eagle nebula)," Monthly Notices of the Royal Astronomical Society, vol. 400, no. 3, p. 1479, 2009. eprint: /oup/backfile/Content_public/Journal/mnras/400/3/10.1111/j.1365-2966.2009.15545.x/2/mnras0400-1479.pdf.

[30] P. Mszros and M. J. Rees, "High-entropy fireballs and jets in gamma-ray burst sources," Monthly Notices of the Royal Astronomical Society, vol. 257, no. 1, 29P, 1992. eprint: /oup/backfile/Content_public/Journal/mnras/257/1/10.1093/mnras/257.1.29P/2/mnras257-029P.pdf.

[31] S. Gillessen, F. Eisenhauer, S. Trippe, T. Alexander, R. Genzel, F. Martins, and T. Ott, "Monitoring stellar orbits around the massive black hole in the galactic center," Astrophys. J., vol. 692, pp. 1075–1109, 2009. arXiv: 0810.4674 [astro-ph].

[32] P. A. Crowther, S. M. Caballero-Nieves, K. A. Bostroem, J. Maíz Apellániz, F. R. N. Schneider, N. R. Walborn, C. R. Angus, I. Brott, A. Bonanos, A. de Koter, S. E. de Mink, C. J. Evans, G. Gräfener, A. Herrero, I. D. Howarth, N. Langer, D. J. Lennon, J. Puls, H. Sana, and J. S. Vink, "The r136 star cluster dissected with hubble space telescope/stis. i. far-ultraviolet spectroscopic census and the origin of he ii λ1640 in young star clusters,", vol. 458, pp. 624–659, May 2016. arXiv: 1603.04994 [astro-ph.SR].

[33] N. A. Webb, D. Barret, O. Godet, M. Servillat, S. A. Farrell, and S. R. Oates, "Chandra and swift follow-up observations of the intermediate-mass black hole in eso 243-49,", vol. 712, pp. L107–L110, Mar. 2010. arXiv: 1002.3625 [astro-ph.HE].

[34] D. R. Pasham, T. E. Strohmayer, and R. F. Mushotzky, "A 400-solar-mass black hole in the galaxy m82,", vol. 513, pp. 74–76, Sep. 2014. arXiv: 1501.03180 [astro-ph.HE].

[35] S. A. Farrell, N. A. Webb, D. Barret, O. Godet, and J. M. Rodrigues, "An intermediate-mass black hole of over 500 solar masses in the galaxy eso243-49,", vol. 460, pp. 73–75, Jul. 2009. arXiv: 1001.0567 [astro-ph.HE].

[36] T. L. S. Collaboration, "Advanced ligo," Classical and Quantum Gravity, vol. 32, no. 7, p. 074 001, 2015.

[37] B. Iyer and et al., "Ligo-india technical report no. ligo-m1100296," 2011.

[38] T. Accadia et al., "Virgo: a laser interferometer to detect gravitational waves," JINST, vol. 7, P03012, 2012.

[39] F. Acernese et al., "Advanced virgo: a second-generation interferometric gravitational wave detector," Class. Quant. Grav., vol. 32, no. 2, p. 024 001, 2015. arXiv: 1408.3978 [gr-qc].

[40] T. A. Prince, P. Binetruy, J. Centrella, L. S. Finn, C. Hogan, G. Nelemans, E. S. Phinney, B. Schutz, and LISA International Science Team, "Lisa: probing the universe with gravitational waves," in American Astronomical Society Meeting Abstracts, ser. Bulletin of the American Astronomical Society, vol. 38, Dec. 2006, p. 990.

[41] The LIGO Scientific Collaboration and the Virgo Collaboration, "Observing gravitational-wave transient gw150914 with minimal assumptions," Physical Review D, vol. 93, no. 12, 122004, p. 122 004, Jun. 2016. arXiv: 1602.03843 [gr-qc].

[42] S. Klimenko et al., "Method for detection and reconstruction of gravitational wave transients with networks of advanced detectors," Phys. Rev., vol. D93, no. 4, p. 042 004, 2016. arXiv: 1511.05999 [gr-qc].

[43] The LIGO Scientific Collaboration and the Virgo Collaboration, "Directly comparing gw150914 with numerical solutions of einstein's equations for binary black hole coalescence," Phys. Rev. D, vol. 94, p. 064 035, 6 2016.

[44] B. P. Abbott et al., "Binary black hole mergers in the first advanced ligo observing run," Phys. Rev., vol. X6, no. 4, p. 041 015, 2016. arXiv: 1606.04856 [gr-qc].

[45] B. Aylott, J. G. Baker, W. D. Boggs, M. Boyle, P. R. Brady, D. A. Brown, B. Brügmann, L. T. Buchman, A. Buonanno, L. Cadonati, J. Camp, M. Campanelli, J. Centrella, S. Chatterji, N. Christensen, T. Chu, P. Diener, N. Dorband, Z. B.

Etienne, J. Faber, S. Fairhurst, B. Farr, S. Fischetti, G. Guidi, L. M. Goggin, M. Hannam, F. Herrmann, I. Hinder, S. Husa, V. Kalogera, D. Keppel, L. E. Kidder, B. J. Kelly, B. Krishnan, P. Laguna, C. O. Lousto, I. Mandel, P. Marronetti, R. Matzner, S. T. McWilliams, K. D. Matthews, R. A. Mercer, S. R. P. Mohapatra, A. H. Mroué, H. Nakano, E. Ochsner, Y. Pan, L. Pekowsky, H. a. P. Pfeiffer, D. Pollney, F. Pretorius, V. Raymond, C. Reisswig, L. Rezzolla, O. Rinne, C. Robinson, C. Röver, L. Santamaría, B. Sathyaprakash, M. A. Scheel, E. Schnetter, J. Seiler, S. L. Shapiro, D. Shoemaker, U. Sperhake, A. Stroeer, R. Sturani, W. Tichy, Y. T. Liu, M. van der Sluys, J. R. van Meter, R. Vaulin, A. Vecchio, J. Veitch, A. Viceré, J. T. Whelan, and Y. Zlochower, "Testing gravitational-wave searches with numerical relativity waveforms: results from the first numerical injection analysis (ninja) project," Classical and Quantum Gravity, vol. 26, no. 16, 165008, p. 165 008, 2009. arXiv: 0901.4399 [gr-qc].

[46] I. Hinder et al., "Error-analysis and comparison to analytical models of numerical waveforms produced by the nrar collaboration," Class. Quant. Grav., vol. 31, p. 025 012, 2014. arXiv: 1307.5307 [gr-qc].

[47] B. P. Abbott et al., "Properties of the binary black hole merger gw150914," Phys. Rev. Lett., vol. 116, no. 24, p. 241 102, 2016.

[48] ——, "Tests of general relativity with gw150914," Phys. Rev. Lett., vol. 116, no. 22, p. 221 101, 2016.

[49] A. Taracchini et al., "Effective-one-body model for black-hole binaries with generic mass ratios and spins," Phys. Rev., vol. D89, no. 6, p. 061 502, 2014. arXiv: 1311.2544 [gr-qc].

[50] M. Pürrer, "Frequency domain reduced order model of aligned-spin effective-one-body waveforms with generic mass ratios and spins," Phys. Rev. D, vol. 93, p. 064 041, 6 2016.

[51] S. Khan, S. Husa, M. Hannam, F. Ohme, M. Pürrer, X. J. Forteza, and A. Bohé, "Frequency-domain gravitational waves from nonprecessing black-hole binaries. ii. a phenomenological model for the advanced detector era," Phys. Rev. D, vol. 93, p. 044 007, 4 2016.

[52] P. Schmidt, M. Hannam, and S. Husa, "Towards models of gravitational waveforms from generic binaries: a simple approximate mapping between precessing and non-precessing inspiral signals," Phys. Rev., vol. D86, p. 104 063, 2012. arXiv: 1207.3088 [gr-qc].

[53] M. Hannam, P. Schmidt, A. Bohé, L. Haegel, S. Husa, F. Ohme, G. Pratten, and M. Pürrer, "Simple model of complete precessing black-hole-binary gravitational waveforms," Phys. Rev. Lett., vol. 113, p. 151 101, 15 2014.

[54] J. Healy, P. Laguna, and D. Shoemaker, "Decoding the final state in binary black hole mergers," Class. Quant. Grav., vol. 31, no. 21, p. 212 001, 2014. arXiv: 1407.5989 [gr-qc].

[55] F. Herrmann, I. Hinder, D. Shoemaker, and P. Laguna, "Unequal mass binary black hole plunges and gravitational recoil," Class. Quant. Grav., vol. 24, S33–S42, 2007.

[56] B. Vaishnav, I. Hinder, F. Herrmann, and D. Shoemaker, "Matched filtering of numerical relativity templates of spinning binary black holes," Phys.Rev., vol. D76, p. 084 020, 2007. arXiv: 0705.3829 [gr-qc].

[57] J. Healy, J. Levin, and D. Shoemaker, "Zoom-whirl orbits in black hole binaries," Phys. Rev. Lett., vol. 103, p. 131 101, 2009.

[58] L. Pekowsky, R. OShaughnessy, J. Healy, and D. Shoemaker, "Comparing gravitational waves from nonprecessing and precessing black hole binaries in the corotating frame," Phys.Rev., vol. D88, no. 2, p. 024 040, 2013. arXiv: 1304.3176 [gr-qc].

[59] Einstein Toolkit home page:http://www.einsteintoolkit.org.

[60] G. Allen, T. Goodale, and E. Seidel, "The cactus computational collaboratory: Enabling technologies for relativistic astrophysics, and a toolkit for solving pdes by communities in science and engineering," in 7th Symposium on the Frontiers of Massively Parallel Computation-Frontiers 99, New York: IEEE, 1999.

[61] E. Schnetter, S. H. Hawley, and I. Hawke, "Evolutions in 3D numerical relativity using fixed mesh refinement," Class. Quant. Grav., vol. 21, pp. 1465–1488, 2004.

[62] S. Husa, I. Hinder, and C. Lechner, "Kranc: A mathematica application to generate numerical codes for tensorial evolution equations," Computer Physics Communications, vol. 174, pp. 983–1004, Jun. 2006.

[63] J. M. Bowen and J. W. York Jr., "Time-asymmetric initial data for black holes and black hole collisions," Phys. Rev. D, vol. 21, no. 8, pp. 2047–2056, 1980.

[64] M. Ansorg, B. Brügmann, and W. Tichy, "A single-domain spectral method for black hole puncture data," Phys. Rev. D, vol. 70, p. 064 011, 2004.

[65] S. Husa, M. Hannam, J. A. González, U. Sperhake, and B. Brügmann, "Reducing eccentricity in black-hole binary evolutions with initial parameters from post-newtonian inspiral," Phys. Rev. D, vol. 77, p. 044 037, 2008.

[66] W. Tichy and P. Marronetti, "A simple method to set up low eccentricity initial data for moving puncture simulations," Phys. Rev. D, vol. 83, p. 024 012, 2011. arXiv: 1010.2936 [gr-qc].

[67] J. Healy, "The final state from generic binary black hole coalescence: mass, spin, and gravitational recoil," PhD thesis, Penn State, 2009.

[68] L. London, "On gravitational wave modeling: numerical relativity data analysis, the excitation of kerr quasinormal modes, and the unsupervised machine learning of waveform morphology," PhD thesis, Georgia Tech, 2015.

[69] C. Reisswig, N. T. Bishop, D. Pollney, and B. Szilagyi, "Characteristic extraction in numerical relativity: binary black hole merger waveforms at null infinity," Class. Quant. Grav., vol. 27, p. 075 014, 2010.

[70] M. Ruiz, M. Alcubierre, D. Núñez, and R. Takahashi, "Multiple expansions for energy and momenta carried by gravitational waves," General Relativity and Gravitation, vol. 40, no. 8, pp. 1705–1729, 2008.

[71] F. Herrmann, I. Hinder, D. M. Shoemaker, P. Laguna, and R. A. Matzner, "Binary black holes: spin dynamics and gravitational recoil," Phys. Rev., vol. D76, p. 084 032, 2007. arXiv: 0706.2541 [gr-qc].

[72] F. Herrmann, I. Hinder, D. Shoemaker, P. Laguna, and R. A. Matzner, "Gravitational recoil from spinning binary black hole mergers," Astrophys. J., vol. 661, pp. 430–436, 2007. arXiv: gr-qc/0701143.

[73] F. Herrmann, I. Hinder, D. Shoemaker, and P. Laguna, "Unequal mass binary black hole plunges and gravitational recoil," Classical and Quantum Gravity, vol. 24, S33–S42, Jun. 2007. eprint: arXiv:gr-qc/0601026.

[74] O. Dreyer, B. Krishnan, D. Shoemaker, and E. Schnetter, "Introduction to isolated horizons in numerical relativity," Phys. Rev. D, vol. 67, no. 2, 024018, p. 024 018, Jan. 2003. eprint: gr-qc/0206008.

[75] O. Dreyer, B. Krishnan, D. Shoemaker, and E. Schnetter, "Introduction to isolated horizons in numerical relativity," Phys. Rev. D, vol. 67, p. 024 018, 2 2003.

[76] B. Abbott and the LIGO Scientific Collaborations, "Search for gravitational waves from galactic and extra-galactic binary neutron stars," Physical Review D, vol. 72, no. 8, pp. 082 001–+, Oct. 2005.

[77] B. Abbott and the LIGO Scientific Collaboration, "Search for gravitational waves from binary black hole inspirals in LIGO data," Physical Review D, vol. 73, no. 6, pp. 062 001–+, Mar. 2006.

[78] The LIGO Scientific Collaboration, "Search for gravitational waves from binary inspirals in s3 and s4 ligo data," Physical Review D, vol. 77, no. 6, pp. 062 002–+, Mar. 2008. arXiv: 0704.3368.

[79] B. P. Abbott et al., "Search of s3 ligo data for gravitational wave signals from spinning black hole and neutron star binary inspirals," Physical Review D, vol. 78, no. 4, pp. 042 002–+, Aug. 2008. arXiv: 0712.2050.

[80] Y. Pan, A. Buonanno, L. T. Buchman, T. Chu, L. E. Kidder, H. P. Pfeiffer, and M. A. Scheel, "Effective-one-body waveforms calibrated to numerical relativity simulations: Coalescence of nonprecessing, spinning, equal-mass black holes," Phys. Rev. D, vol. 81, p. 084 041, 8 2010.

[81] P. Ajith, M. Hannam, S. Husa, Y. Chen, B. Bruegmann, et al., "Inspiral-merger-ringdown waveforms for black-hole binaries with non-precessing spins," Phys. Rev. Lett., vol. 106, p. 241 101, 2011.

[82] E. Barausse, V. Morozova, and L. Rezzolla, "On the mass radiated by coalescing black-hole binaries," Astrophys.J., vol. 758, p. 63, 2012. arXiv: 1206.3803 [gr-qc].

[83] J. Healy, C. O. Lousto, and Y. Zlochower, "Remnant mass, spin, and recoil from spin aligned black-hole binaries," Phys.Rev., vol. D90, no. 10, p. 104 004, 2014. arXiv: 1406.7295 [gr-qc].

[84] P. Schmidt, I. W. Harry, and H. P. Pfeiffer, "Reduced-order spline interpolation: enabling fast and efficient usage of numerical relativity waveforms in ligo data analysis," In Prep, 2016.

[85] P. Galley Chad R.and Schmidt, "Reduced-order spline interpolation: enabling fast and efficient usage of numerical relativity waveforms in ligo data analysis," In Prep, 2016.

[86] L. London, D. Shoemaker, and J. Healy, "Modeling ringdown: beyond the fundamental quasinormal modes," Phys. Rev., vol. D90, no. 12, p. 124 032, 2014.

[87] R. O'Shaughnessy, J. Healy, L. London, Z. Meeks, and D. Shoemaker, "Is j enough? comparison of gravitational waves emitted along the total angular momentum direction with other preferred orientations," Phys.Rev. D, vol. 85, p. 084 003, 2012. arXiv: 1201.2113 [gr-qc].

[88] L. Lindblom, B. J. Owen, and D. A. Brown, "Model waveform accuracy standards for gravitational wave data analysis," Phys. Rev., vol. D78, p. 124 020, 2008. arXiv: 0809.3844 [gr-qc].

[89] J. Caldern Bustillo, S. Husa, A. M. Sintes, and M. Prrer, "Impact of gravitational radiation higher order modes on single aligned-spin gravitational wave searches for binary black holes," Phys. Rev., vol. D93, no. 8, p. 084 019, 2016.

[90] F. Hofmann, E. Barausse, and L. Rezzolla, "The final spin from binary black holes in quasi-circular orbits," Astrophys. J., vol. 825, no. 2, p. L19, 2016.

[91] A. H. Mroué, M. A. Scheel, B. Szilágyi, H. P. Pfeiffer, M. Boyle, D. A. Hemberger, L. E. Kidder, G. Lovelace, S. Ossokine, N. W. Taylor, A. Zenginoğlu, L. T. Buchman, T. Chu, E. Foley, M. Giesler, R. Owen, and S. A. Teukolsky, "Catalog of 174 binary black hole simulations for gravitational wave astronomy," Physical Review Letters, vol. 111, no. 24, 241104, p. 241 104, Dec. 2013.

[92] J. Caldern Bustillo, P. Laguna, and D. Shoemaker, "Detectability of gravitational waves from binary black holes: impact of precession and higher modes," 2016. arXiv: 1612.02340 [gr-qc].

[93] T. A. Apostolatos, C. Cutler, G. J. Sussman, and K. S. Thorne, "Spin-induced orbital precession and its modulation of the gravitational waveforms from merging binaries," Physical Review D, vol. 49, no. 12, p. 6274, 1994.

[94] R. O'Shaughnessy, B. Vaishnav, J. Healy, Z. Meeks, and D. Shoemaker, "Efficient asymptotic frame selection for binary black hole spacetimes using asymptotic radiation," Phys.Rev., vol. D84, p. 124 002, 2011. arXiv: 1109.5224 [gr-qc].

[95] C. O. Lousto and Y. Zlochower, "Orbital evolution of extreme-mass-ratio black-hole binaries with numerical relativity," Phys.Rev.Lett., vol. 106, p. 041 101, 2011. arXiv: 1009.0292 [gr-qc].

[96] A. Buonanno et al., "Toward faithful templates for non-spinning binary black holes using the effective-one-body approach," Phys. Rev. D, vol. 76, p. 104 049, 2007.

[97] B. P. Abbott et al., "Gw151226: Observation of gravitational waves from a 22-solar-mass binary black hole coalescence," Phys. Rev. Lett., vol. 116, p. 241 103, 24 2016.

[98] S. Mohapatra, Z. Nemtzow, E. Chassande-Mottin, and L. Cadonati, "Performance of a chirplet-based analysis for gravitational waves from binary black hole mergers," J.Phys.Conf.Ser., vol. 363, p. 012 031, 2012. arXiv: 1111.3621 [gr-qc].

[99] B. P. Abbott et al., "All-sky search for short gravitational-wave bursts in the first advanced ligo run," Phys. Rev. D, vol. 95, p. 042 003, 4 2017.

[100] J. Smith, LIGO Detector Characterization Group : https://dcc.ligo.org/public/0119

[101] B. P. Abbott et al., "Characterization of transient noise in advanced ligo relevant to gravitational wave signal gw150914," Classical and Quantum Gravity, vol. 33, no. 13, p. 134 001, 2016.

[102] The LIGO Scientific Collaboration and the Virgo Collaboration, "Search for intermediate mass black hole binaries in the first observing run of advanced ligo detector," To be submitted to ApJ, 2017.

[103] D. V. Martynov et al., "Sensitivity of the advanced ligo detectors at the beginning of gravitational wave astronomy," vol. D93, no. 11, p. 112 004, 2016. arXiv: 1604.00439 [astro-ph.IM].

[104] B. P. Abbott et al., "Astrophysical implications of the binary black-hole merger gw150914," Astrophys. J., vol. 818, no. 2, p. L22, 2016. arXiv: 1602.03846 [astro-ph.HE].

[105] ——, "Binary black hole mergers in the first advanced ligo observing run," 2016. arXiv: 1606.04856 [gr-qc].

[106] ——, "The rate of binary black hole mergers inferred from advanced ligo observations surrounding gw150914," 2016. arXiv: 1602.03842 [astro-ph.HE].

[107] ——, "Gw150914: first results from the search for binary black hole coalescence with advanced ligo," Phys. Rev., vol. D93, no. 12, p. 122 003, 2016. arXiv: 1602.03839 [gr-qc].

[108] The LIGO Scientific Collaboration and the Virgo Collaboration, "Search for gravitational radiation from intermediate mass black hole binaries in data from the second ligo-virgo joint science run," Phys. Rev., vol. D89, no. 12, p. 122 003, 2014. arXiv: 1404.2199 [gr-qc].

[109] B. P. Abbott et al., "Search for gravitational wave ringdowns from perturbed intermediate mass black holes in ligo-virgo data from 2005-2010," Phys. Rev., vol. D89, no. 10, p. 102 006, 2014. arXiv: 1403.5306 [gr-qc].

[110] G. Mazzolo et al., "Prospects for intermediate mass black hole binary searches with advanced gravitational-wave detectors," Phys. Rev., vol. D90, no. 6, p. 063 002, 2014. arXiv: 1404.7757 [gr-qc].

[111] V. Tiwari et al., "Proposed search for the detection of gravitational waves from eccentric binary black holes," Phys. Rev., vol. D93, no. 4, p. 043 007, 2016. arXiv: 1511.09240 [gr-qc].

[112] J. Clark, A. Bauswein, L. Cadonati, H. T. Janka, C. Pankow, and N. Stergioulas, "Prospects for high frequency burst searches following binary neutron star coalescence with advanced gravitational wave detectors," Phys. Rev., vol. D90, no. 6, p. 062 004, 2014. arXiv: 1406.5444 [astro-ph.HE].

[113] B. P. Abbott et al., Phys. Rev. Lett., vol. 116, p. 061 102, 6 2016.

[114] R. Schneider, A. Ferrara, P. Natarajan, and K. Omukai, "First stars, very massive black holes and metals," Astrophys. J., vol. 571, pp. 30–39, 2002. arXiv: astro-ph/0111341 [astro-ph].

[115] M. C. Miller and D. P. Hamilton, "Production of intermediate-mass black holes in globular clusters," Mon. Not. Roy. Astron. Soc., vol. 330, p. 232, 2002. arXiv: astro-ph/0106188 [astro-ph].

[116] N. Leigh, A. Sills, and T. Böker, "Modifying two-body relaxation in n-body systems by gas accretion," Mon. Not. Roy. Astron. Soc., vol. 433, pp. 1958–1965, Aug. 2013. arXiv: 1305.3275 [astro-ph.SR].

[117] K. Jani, A. Aykutalp, and D. Shoemaker, "Astrophysics of bbh populations for upcoming ground-based gravitational wave experiments," To be submitted to ApJ, 2016.

[118] The LIGO Scientific Collaboration and the Virgo Collaboration, "Upper limits on the rates of binary neutron star and neutron-star–black-hole mergers from advanced ligo's first observing run," ArXiv e-prints, Jul. 2016. arXiv: 1607.07456 [astro-ph.HE].

[119] M. Coleman Miller and E. J. M. Colbert, "Intermediate-mass black holes," International Journal of Modern Physics D, vol. 13, pp. 1–64, 2004. eprint: astro-ph/0308402.

[120] The LIGO Scientific Collaboration and the Virgo Collaboration, "Exploring the sensitivity of next generation gravitational wave detectors," ArXiv e-prints, Jul. 2016. arXiv: 1607.08697 [astro-ph.IM].

[121] A. Ghosh, W. Del Pozzo, and P. Ajith, "Estimating parameters of binary black holes from gravitational-wave observations of their inspiral, merger and ringdown," ArXiv e-prints, May 2015. arXiv: 1505.05607 [gr-qc].

[122] A. Sesana, "Prospects for multiband gravitational-wave astronomy after gw150914," Physical Review Letters, vol. 116, no. 23, 231102, p. 231 102, Jun. 2016. arXiv: 1602.06951 [gr-qc].

[123] S. Vitale, "Multiband gravitational-wave astronomy: parameter estimation and tests of general relativity with space- and ground-based detectors," Physical Review Letters, vol. 117, no. 5, 051102, p. 051 102, Jul. 2016. arXiv: 1605.01037 [gr-qc].

[124] K. P. Jani, L. S. Finn, and M. J. Benacquista, "Pointing lisa-like gravitational wave detectors," ArXiv e-prints, Jun. 2013. arXiv: 1306.3253 [astro-ph.IM].

[125] The LIGO Scientific Collaboration and the Virgo Collaboration, "Search for gravitational radiation from intermediate mass black hole binaries in data from the second ligo-virgo joint science run," Phys. Rev. D, vol. 89, p. 122 003, 12 2014.

[126] B. P. Abbott et al., "Search for gravitational wave ringdowns from perturbed intermediate mass black holes in ligo-virgo data from 2005-2010," Phys. Rev. D, vol. 89, p. 102 006, 10 2014.

[127] M. MacLeod, M. Trenti, and E. Ramirez-Ruiz, "The close stellar companions to intermediate-mass black holes,", vol. 819, 70, p. 70, Mar. 2016. arXiv: 1508.07000 [astro-ph.HE].